Signal in the Scatter: Advancing Speckle-Based Optical Sensing for Deep Cerebral Blood Flow Monitoring

Thesis by
Yu Xi (Max) Huang

In Partial Fulfillment of the Requirements for the
degree of
Doctor of Philosophy



CALIFORNIA INSTITUTE OF TECHNOLOGY
Pasadena, California

2026
Defended January 16, 2026

© 2026

Yu Xi (Max) Huang
ORCID: 0009-0000-0165-2084

All rights reserved except where otherwise noted

To my wife, Olivia.

ACKNOWLEDGEMENTS

I started my PhD journey in the shadow of COVID-19, admittedly with little idea of what I was signing up for. I want to thank my professor, Changhuei Yang, for guiding me through the fog from day one. His rigorous principles and high standards defined these last four years. He took a chance on me in a field where I had zero experience, and I am proud to say that I've learned enough to leave behind a few references for those who follow. To push the boundary, even slightly, or to provide a spark for future researchers makes every struggle worth it.

A special thanks goes to Simon Mahler, who worked alongside me for the majority of this thesis. He taught me everything from the basics of optics to the nuances of laser coupling. I know he will thrive at Stevens Institute, and I'm sure he will be a fantastic PI.

To my labmates—Cheng, Ruizhi, Mingshu, Haowen, Steven, Siyuan, Zhengyu, Josh, Ninghe, and Oumeng: thank you for the lunches, the dinners, the clashes in meetings, and the laughter in the postdoc office. You are friends for life, and I value our bond just as much as the research itself.

Thank you to my committee members—Professor Lihong, Professor Jerome, Professor Marandi, and Dr. Charles Liu—for your guidance and for recognizing the value of my work. A special thanks to Charles and the USC team for bridging the gap in our biomedical knowledge.

Finally, to my family. To my mom and dad, for supporting me unconditionally and guiding me through life's complications. To my Shiba Inu, Oka, for being my alarm clock. And to my wife, Olivia, whose love is stronger than any obstacle I have ever faced.

ABSTRACT

This thesis presents the development and application of novel, non-invasive optical techniques for monitoring cerebral blood flow (CBF) and cerebral blood volume (CBV), addressing the critical need for cost-effective and scalable solutions in cerebrovascular health assessment. The research introduces advancements in interferometric speckle visibility spectroscopy (iSVS) and speckle contrast optical spectroscopy (SCOS) to overcome the challenges of signal attenuation and noise when measuring blood flow through the scalp and skull.

The depth sensitivity of these optical methods was first experimentally determined. Using iSVS on phantoms, rabbits, and human subjects, a two-layer decay model was observed as the source-to-detector (S-D) distance was varied, allowing for the quantification of the transition point from superficial to cerebral signal detection. Complementing this, a multi-channel SCOS system was used with temporary occlusion of the superficial temporal artery to experimentally isolate and quantify the influence of scalp blood flow, providing direct evidence of brain-to-scalp signal sensitivity and establishing optimal S-D configurations.

Another primary focus of this work was enhancing the signal-to-noise ratio (SNR) of deep-tissue measurements. A comprehensive theoretical framework for iSVS was developed to evaluate its SNR in the presence of detector noise, confirming its superiority in photon-limited regimes and revealing relaxed constraints on the reference beam. In parallel, a compact, fiber-free SCOS device was engineered, demonstrating a 70-fold increase in signal collection over traditional fiber-based systems with enhanced stability. The SNR for SCOS was further improved through an optimization-based, adaptive noise calibration framework that mitigates artifacts from cerebral blood volume fluctuations, significantly lowering the signal detection threshold for reliable CBF measurement.

Building upon these foundational advancements, the research progressed to clinical applications. The technology's modularity was demonstrated by engineering a portable, six-channel SCOS system for simultaneous, real-time measurements at multiple brain locations. This system was validated in a preliminary study on a patient with traumatic brain injury, demonstrating its potential for characterizing regional cerebrovascular dysfunction by comparing blood flow dynamics against structural MRI data. Furthermore, the compact SCOS device was used to assess

stroke risk in a 50-person cohort by monitoring cerebrovascular reactivity during a breath-holding task; this revealed significant discrepancies between CBF and CBV responses that correlated with risk scores.

PUBLISHED CONTENT AND CONTRIBUTIONS

[1] Simon Mahler et al. “Assessing depth sensitivity in laser interferometry speckle visibility spectroscopy (iSVS) through source-to-detector distance variation and cerebral blood flow monitoring in humans and rabbits”. In: *Biomed. Opt. Express* 14.9 (Sept. 2023), pp. 4964–4978. DOI: 10.1364/BOE.498815.
Y.X.H. participated in the conception of the project, acquiring live animal experimental data and human trials, post processing of the dataset, and construction of phantom.

[2] Yu Xi Huang et al. “Interferometric speckle visibility spectroscopy (iSVS) for measuring decorrelation time and dynamics of moving samples with enhanced signal-to-noise ratio and relaxed reference requirements”. In: *Opt. Express* 31.19 (Sept. 2023), pp. 31253–31266. DOI: 10.1364/OE.499473.
Y.X.H. participated in the theoretical derivation and building the optical system.

[3] Yu Xi Huang et al. “Correlating stroke risk with non-invasive cerebrovascular perfusion dynamics using a portable speckle contrast optical spectroscopy laser device”. In: *Biomed. Opt. Express* 15.10 (Oct. 2024), pp. 6083–6097. DOI: 10.1364/BOE.534796.
Y.X.H. participated in the conception of the project, identifying the observed phenomenon, construction of the system, acquiring experimental and clinical data, and post processing of the dataset.

[4] Yu Xi Huang et al. “Compact and cost-effective laser-powered speckle contrast optical spectroscopy fiber-free device for measuring cerebral blood flow”. In: *Journal of Biomedical Optics* 29.6 (2024), p. 067001. DOI: 10.1117/1.JBO.29.6.067001.
Y.X.H. participated in the conception of the project, construction of the device, acquiring experimental and clinical data, and post processing of the dataset.

[5] Simon Mahler et al. “Portable six-channel laser speckle system for simultaneous measurement of cerebral blood flow and volume with potential applications in characterization of brain injury”. In: *Neurophotonics* 12.1 (2025), p. 015003. DOI: 10.1117/1.NPh.12.1.015003.
Y.X.H. participated in the conception of the project, construction of the device, acquiring experimental and clinical data, and post processing of the dataset.

[6] Yu Xi Huang et al. “Assessing human scalp and brain blood flow sensitivities via superficial temporal artery occlusion using speckle contrast optical spectroscopy”. In: *APL Bioengineering* 9.4 (Oct. 2025), p. 046106. DOI: 10.1063/5.0263953.

Y.X.H. participated in the conception of the project, acquiring experimental and clinical data, and post processing of the dataset.

[7] Ninghe Liu et al. “Optimized cerebral blood flow measurement in speckle contrast optical spectroscopy via refinement of noise calibration”. In: *Opt. Lett.* 50.17 (Sept. 2025), pp. 5382–5385. DOI: 10.1364/OL.570951.
Y.X.H. participated in the conception of the project, acquiring experimental and clinical data, and post processing of the dataset.

TABLE OF CONTENTS

Acknowledgements . . . iv
Abstract . . . v
Published Content and Contributions . . . vii
Table of Contents . . . viii
List of Illustrations . . . xi
List of Tables . . . xiii
Chapter I: Introduction . . . 1
1.1 The critical role of cerebral blood flow in brain health and disease . . . 1
1.2 A survey of modalities for cerebral blood flow measurement . . . 2
1.3 Fundamental principles of speckle-based blood flow measurement . . . 6
1.4 A dichotomy of speckle measurement: temporal and spatial sampling techniques . . . 12
1.5 Positioning the thesis contribution: fundamental advancement and application of iSVS and SCOS . . . 15
1.6 Note on Nomenclature: SVS versus SCOS . . . 17
Note on Nomenclature: SVS versus SCOS . . . 17
Chapter II: Are we measuring the brain? . . . 21
2.1 The fundamental challenge: superficial signal contamination in transcranial optical measurements . . . 21
2.2 Assessing depth sensitivity in iSVS in rabbits and humans . . . 24
2.3 Superficial temporal artery occlusion: a new approach to SCOS sensitivity . . . 39
2.4 The imperative for extended S–D and emerging challenges . . . 61
Chapter III: Signal is the Key . . . 68
3.1 Interferometry! The solution? . . . 69
3.2 Compact speckle contrast optical spectroscopy . . . 87
3.3 Separating CBV and CBF waveforms . . . 104
3.4 Concluding Remarks and Future Directions . . . 115
Chapter IV: From Single-Channel Sensor to Multi-Channel System . . . 125
4.1 Scaling up, from single to multi-channel . . . 126
4.2 System Stability: Power and Thermal Management . . . 131
4.3 Can we detect brain injury? . . . 132
4.4 Multi-Channel System Results: Human Subject Studies . . . 134
4.5 Concluding Remarks on the Multi-Channel System . . . 138
Chapter V: Stroke risk? A stress test for your brain . . . 142
5.1 Introduction to stroke risk and our approaches . . . 142
5.2 Methods to evaluate stroke risk . . . 145
5.3 Breath holding SCOS results . . . 148
5.4 Preventative screening, looking forward and what is next? . . . 157

Chapter VI: Next things to explore 165

LIST OF ILLUSTRATIONS

Number *Page*

2.1 iSVS experimental arrangement and depth sensitivity 26
2.2 iSVS processing pipeline 29
2.3 SVS vs. iSVS blood flow measurement comparison 31
2.4 Blood flow at varying S-D distances for human and rabbit 32
2.5 S-D threshold investigation for human, rabbit, and phantom 35
2.6 S-D threshold and decay rates for subject comparison 37
2.7 Experimental arrangement of the SCOS system for measuring cerebral blood dynamics during superficial temporal artery (STA) occlusion 43
2.8 Typical cerebral blood flow (CBF) time traces during superficial temporal artery occlusion and non-occlusive pressure. 44
2.9 Effects of the superficial temporal artery occlusion on the scalp, skull, and brain blood flows measured from 20 subjects. 47
2.10 Effects of superficial temporal artery occlusion on CBF and CBV. . . 50
3.1 Theoretical comparison between iSVS and SVS by using the SNR and the derived speckle contrast equations. 80
3.2 Experimental arrangment for measuring decorrelation time and SNR for iSVS. 82
3.3 The iSVS and SVS SNR experiment results with rotating diffuser. . . 85
3.4 Compact SCOS Device Design and Application 90
3.5 Compact SCOS processing analysis flowchart for deriving the blood flow from recorded camera images 92
3.6 Experimental signal comparison between fiber SCOS and compact SCOS 95
3.7 Experimental comparison of flow reproducibility between fiber SCOS and compact SCOS 98
3.8 Experimental comparison of stability between fiber SCOS and compact SCOS 99
3.9 Experimental Comparison of Fiber SCOS and Compact SCOS for Blood Flow Measurement 102
3.10 Experimental comparison between fiber and compact SCOS in blood flow measurement on a cohort of five subjects 103

3.11 Compact SCOS Device and BFI Processing Pipeline 106
3.12 Detailed CBF and CBV Waveforms Before and After Optimization . 108
3.13 Comparison of CBF Measurements with Standard and Optimized Processing 113
3.14 Enhanced SCOS Performance Across Varying S-D Separations . . . 114
4.1 Overview of the Six-Channel Wearable SCOS System 127
4.2 Overview of the Six-Channel Wearable SCOS System 129
4.3 In-Vivo Thermal Performance and Comfort Ratings 134
4.4 In-Vivo multi-channel CBF data on various subjects 136
4.5 Quantitative results from multi-channel CBF data between subjects . 137
5.1 Infrared laser cerebrovascular perfusion measures during breath-holding. 148
5.2 Stroke risk assessment via brain perfusion measurements during breath-holding. 150
5.3 Breath-holding features comparison between the low-risk and higher-risk groups. 153
5.4 Flow to volume ratio across different stroke risk groups 158

LIST OF TABLES

Number *Page*

1.1 Updated comparison of different imaging modalities. 4

5.1 Mean and standard deviation of the different features extracted from the breath-holding dataset, comparing the low-risk and higher-risk groups. 156

Chapter 1

INTRODUCTION

This introduction chapter provides essential background on cerebral blood flow and blood volume, establishing why they are critical physiological metrics and surveying the modalities available for their measurement. It then transitions to the core of this thesis: optical methods, explaining how laser light and the phenomenon of laser speckle are leveraged in this process. Finally, the chapter delineates and explores the two primary domains of speckle-based measurement—temporal and spatial sampling—setting the stage for the specific contributions of this research.

1.1 The critical role of cerebral blood flow in brain health and disease

The human brain, despite constituting merely 2% of the body's mass, is an organ of exceptionally high metabolic activity. It commands approximately 15% of the total cardiac output and has virtually no capacity for energy storage or reserve blood flow. This unique physiological profile renders it critically dependent on a continuous and precisely regulated supply of blood to deliver oxygen and energy substrates—primarily glucose—and to clear metabolic waste products. Consequently, the measurement and monitoring of cerebral blood flow (CBF) serve as a vital window into brain function and pathology, offering a powerful biomarker for a wide spectrum of neurological conditions.

The cerebral circulatory system is governed by a sophisticated set of homeostatic mechanisms designed to maintain stable brain perfusion against physiological perturbations. These include: 1) Cerebral Autoregulation (CA), the intrinsic capacity of cerebral blood vessels to maintain constant CBF across a range of systemic arterial blood pressures [1]; 2) Neurovascular Coupling (NVC), the process that locally increases CBF to match the heightened metabolic demands of active neural populations [2]; and 3) Cerebrovascular Reactivity (CVR), the ability of cerebral vessels to dilate or constrict in response to vasoactive stimuli, most notably the partial pressure of arterial carbon dioxide ($PaCO_2$) [3]. Hypercapnia, an elevation in $PaCO_2$, is a potent vasodilator that robustly increases CBF, while hypocapnia induces vasoconstriction.

The integrity of these regulatory mechanisms is paramount; their failure can lead

to severe neurological consequences. Both hypoperfusion (insufficient CBF) and hyperperfusion (excessive CBF) can be profoundly damaging, causing ischemic injury or a breakdown of the blood-brain barrier, respectively. Dysregulation of CBF is a central feature in numerous acute and chronic neurological disorders. In the context of stroke, which poses a significant global health threat, a disruption of blood flow—either through blockage (ischemic) or rupture (hemorrhagic)—is the primary event leading to neuronal death. For traumatic brain injury (TBI), the initial mechanical insult is often followed by a secondary cascade of physiological disruptions, including cerebrovascular dysregulation, edema, and ischemia, which can exacerbate the primary injury. Therefore, monitoring CBF and cerebrovascular health is crucial for risk assessment, early diagnosis, and the management of these conditions.

This necessity has highlighted a significant gap in clinical diagnostics: the absence of a widely accessible, objective measure for neurovascular health, akin to the role of cardiac stress testing in evaluating myocardial ischemia risk. A "cerebral stress test" that could directly and non-invasively probe the functional reserve of the brain's vasculature would represent a paradigm shift in neurological care. Such a test can be realized by subjecting the cerebrovascular system to a controlled physiological challenge and measuring its hemodynamic response. Voluntary breath-holding, for instance, induces a state of transient hypercapnia and hypoxia, directly stimulating CVR and causing cerebral blood vessels to dilate to increase CBF and cerebral blood volume (CBV). The magnitude and dynamics of this response serve as a direct indicator of vascular compliance and health. A healthy, flexible vascular system can readily accommodate this demand, whereas a diseased or atherosclerotic system exhibits an impaired response. By quantifying these dynamic changes, it becomes possible to move beyond passive monitoring and develop a functional assessment of an individual's cerebrovascular reserve, offering a powerful tool for personalized stroke risk stratification and the characterization of brain injuries.

1.2 A survey of modalities for cerebral blood flow measurement

The clinical and scientific imperative to monitor CBF has driven the development of numerous measurement technologies. However, no single existing modality simultaneously satisfies the need for a non-invasive, portable, cost-effective tool that provides high temporal resolution and is sensitive to the microvasculature. To accurately capture the rapid dynamics of cerebral hemodynamics, including the distinct phases of the cardiac cycle such as the systolic peak and dicrotic notch, a temporal

resolution of 20 Hz or higher is desirable. This benchmark reveals a significant multi-dimensional technological gap in the current landscape of neuroimaging and monitoring tools.

Radiological and nuclear imaging techniques, while powerful, are fundamentally limited in this regard. Magnetic Resonance Imaging (MRI) and Computed Tomography (CT) can provide high-resolution structural images and quantitative perfusion maps, but their temporal resolution is limited to a few images per second, precluding real-time monitoring of blood dynamics[4, 5]. Furthermore, these modalities are characterized by high cost, lack of portability, and, in the case of CT and some MRI protocols, the need for ionizing radiation or intravenous contrast agents, making them unsuitable for routine screening or continuous bedside monitoring. Positron Emission Tomography (PET) and Single-Photon Emission Computed Tomography (SPECT) are considered gold standards for absolute CBF quantification but suffer from even poorer temporal resolution, high operational complexity, and reliance on radioactive tracers [6, 7].

Alternative methods offer improved temporal resolution but come with their own distinct limitations. Transcranial Doppler (TCD) ultrasound can measure blood flow with high temporal resolution (typically 50-100 Hz) but is restricted to measuring flow velocity in large basal arteries, not true tissue perfusion in the microvasculature [8]. Its application is further constrained by operator dependency and the inability to penetrate the skull in patients lacking a suitable temporal acoustic window. Electroencephalography (EEG) provides excellent temporal resolution for tracking the brain's electrical activity but is fundamentally incapable of measuring blood flow dynamics directly . It measures a consequence of neural function, not the underlying hemodynamic support.

This survey of existing technologies underscores a clear and unmet need for a tool that can bridge this gap. An ideal solution would be non-invasive, portable, affordable, and capable of providing continuous, high-temporal-resolution measurements of microvascular blood flow. As summarized in Table 1.1, diffuse optical methods are uniquely positioned to address this multi-dimensional challenge.

Modality	**Principle**	**Temporal Resolution**	**Spatial Resolution**	**Penetration Depth**	**Target**	**Invasiveness**	**Portability**	**Cost**
MRI	Nuclear magnetic resonance	Low (0.5-1 Hz)	High (mm)	Whole Brain	Microvasculature	Non-invasive	No	Very High
CT	X-ray attenuation	Low (snapshot)	High (mm)	Whole Brain	Microvasculature	Ionizing radiation	No	High
PET/SPECT	Radioactive tracer decay	Very Low (<0.02 Hz)	Moderate (cm)	Whole Brain	Microvasculature	Radioactive tracer	No	Very High
TCD	Doppler shift of sound waves	High (50-100 Hz)	Very Low (vessel)	Limited (acoustic window)	Macrovasculature	Non-invasive	Yes	Moderate
EEG	Electrical potential measurement	Very High (>100 Hz)	Low (cm)	Whole Brain	Neural Activity	Non-invasive	Yes	Low
NIRS/fNIRS	Light absorption	High (10-100 Hz)	Low (cm)	1.5-3 cm	Microvasculature (CBV, Oxygenation)	Non-invasive	Yes	Low
Diffuse Optics (SCOS/DCS)	Light scattering dynamics	High (20-100 Hz)	Low (cm)	1.5-3 cm	Microvasculature (CBF, CBV)	Non-invasive	Yes	Low

Table 1.1: Updated comparison of different imaging modalities.

High-temporal-resolution methods capable of resolving individual heartbeats reveal a characteristic pulsatile blood flow waveform rich with physiological information. This waveform, analogous to an arterial pressure trace, is composed of distinct features corresponding to different phases of the cardiac cycle. The cycle begins with a rapid systolic upstroke, culminating in the first and typically dominant peak (P1), which corresponds to the rapid ejection of blood from the left ventricle. This is followed by a second peak (P2), which is associated with reflected pressure waves from the peripheral vasculature. After the systolic peak, a small downward deflection known as the dicrotic notch marks the end of systole and the onset of diastole, an event physiologically linked to the closure of the aortic valve and the subsequent brief backflow and pressure wave reflection. The notch is followed by a smaller, third peak (P3) before the diastolic runoff phase continues until the next heartbeat. The relative heights, shapes, and timings of these peaks and notches can serve as valuable markers for cardiovascular health, offering insights into arterial stiffness, vascular compliance, and cerebrovascular resistance [9, 10].

Near-Infrared Spectroscopy (NIRS)

Among optical techniques, Near-Infrared Spectroscopy (NIRS), and its functional application (fNIRS), stands out as a well-established method for non-invasively monitoring cerebral hemodynamics [11]. Like other optical methods, NIRS leverages the "optical window" in the near-infrared spectrum (typically 700-900 nm), where biological tissues like the scalp and skull are relatively transparent. However, NIRS operates on the principle of light absorption rather than the analysis of dynamic light scattering. The primary absorbers, or chromophores, in the brain at these wavelengths are oxygenated hemoglobin (oxyHb) and deoxygenated hemoglobin (deoxyHb), which have distinct absorption spectra.

A typical NIRS system uses light sources, often light-emitting diodes (LEDs), to illuminate the head at two or more different wavelengths. Detectors placed several centimeters away measure the amount of light that has passed through the tissue. By applying the modified Beer-Lambert law, which relates light attenuation to the concentration of absorbing substances, NIRS can quantify the relative changes in the concentrations of oxyHb and deoxyHb.

From these measurements, NIRS provides direct information on two crucial physiological parameters: cerebral oxygenation and cerebral blood volume (CBV). The total hemoglobin concentration (the sum of oxyHb and deoxyHb) serves as a robust

proxy for changes in regional CBV. This makes NIRS a powerful tool for assessing how blood volume and oxygen supply change in response to neural activity (neurovascular coupling) or other physiological stimuli.

However, a fundamental limitation of NIRS is that it does not directly measure cerebral blood flow (CBF). The technique quantifies the amount of blood and its oxygenation state within a tissue volume but provides no information about the velocity or rate of blood movement. While some studies have attempted to derive CBF surrogates from NIRS signals, such as by analyzing the difference between oxyHb and deoxyHb, these are indirect estimations and not a direct measurement of flow dynamics.

The inability of NIRS to directly measure CBF highlights the need for complementary techniques. While CBV is a vital metric, a complete picture of cerebrovascular health requires understanding both the volume of blood present and the rate at which it is being delivered. CBF provides dynamic information that CBV alone cannot capture. For instance, the detailed pulsatile waveform of the cardiac cycle, including features like the dicrotic notch, is clearly discernible in CBF measurements but absent in CBV traces. Furthermore, the ratio of CBF to CBV can serve as a proxy for changes in mean arterial pressure, offering deeper insights into vascular compliance and resistance. Therefore, the simultaneous measurement of both CBF and CBV is necessary for a comprehensive assessment of brain hemodynamics, motivating the use of speckle-based methods that are sensitive to the motion of red blood cells.

1.3 Fundamental principles of speckle-based blood flow measurement

Optical techniques offer a compelling solution to the limitations of conventional CBF monitoring technologies by leveraging the properties of near-infrared light. Within the spectral range of approximately 700 nm to 900 nm, biological tissues exhibit relatively low absorption by water, allowing photons to penetrate several centimeters, including through the scalp and skull. This "optical window" enables non-invasive probing of cerebral tissue.

The fundamental framework underpinning many of these coherent optical techniques is Diffusing Wave Spectroscopy (DWS). Unlike NIRS which utilizes non-coherent illumination sources such as LEDs, DWS is a powerful group of methods that use coherent light, such as that from a laser, to extract information about the dynamics of a scattering medium. When laser light is injected into the head, photons undergo numerous scattering events before a fraction of them emerge at the surface to be col-

lected by a detector. The motion of scattering particles within the tissue—primarily red blood cells—induces fluctuations in the detected light pattern. By analyzing these fluctuations, DWS can quantify the dynamics of the scatterers and, by extension, the rate of blood flow. A key advantage of this approach is its ability to collect a substantial number of photons that have interacted with deep tissue, including the brain, thereby enhancing the signal available for analysis.

To understand how DWS quantifies blood flow, it is essential to grasp the underlying physics of light propagation in tissue and the nature of the resulting optical signal.

The physics of laser speckle

When coherent light, such as from a laser, illuminates an optically rough surface or a scattering medium like biological tissue, the backscattered light forms a random, granular pattern of bright and dark spots. This high-contrast intensity distribution is known as a laser speckle pattern. It is not a form of external noise but rather an inherent and information-rich phenomenon that arises from the interference of many waves of the same frequency that have different phases and amplitudes. The speckle pattern is a direct consequence of the light's coherence and its interaction with the microscopic structure of the medium.

The formation of speckle can be understood by considering that a rough surface or scattering medium is composed of a multitude of individual scattering points. As a coherent wavefront illuminates these points, each one acts as a source of secondary spherical waves. These waves travel along different optical paths to reach an observation plane, such as a camera sensor. Because the light is coherent, these waves interfere with one another. At points where the waves arrive in phase, they interfere constructively, creating a bright spot or "speckle." Conversely, at points where they arrive out of phase, they interfere destructively, resulting in a dark spot. This process is often modeled as a "random walk" in the complex plane, where the resulting electric field at any point is the vector sum of many elementary phasors, each with a random amplitude and phase.

Because the microscopic surface roughness is random, the resulting speckle pattern is also random and must be described statistically. Under ideal conditions—such as illumination with highly coherent, monochromatic, and linearly polarized light, and scattering from a perfectly diffusing surface—the resulting pattern is known as a "fully developed" speckle pattern. For such a pattern, the statistics are well-defined. The probability distribution of the intensity follows a negative exponential

function, which means that dark speckles (low intensity) are the most probable, and the likelihood of observing brighter speckles decreases exponentially.

A crucial metric for characterizing a speckle pattern is the speckle contrast (K). It is defined as the ratio of the spatial standard deviation of the pixel intensities (σ) to their spatial mean (μ) across the pattern: $K = \sigma/\mu$. For a fully developed, static speckle pattern, the theory predicts that the standard deviation of the intensity is equal to the mean intensity, resulting in a speckle contrast of unity ($K = 1$). This represents the maximum possible contrast. If there is any movement of the scattering particles (e.g., red blood cells) during the camera's exposure time, the speckle pattern fluctuates. This causes the pattern recorded on the camera sensor to become blurred, which reduces the spatial standard deviation of the intensity relative to the mean, thereby lowering the speckle contrast. This reduction in contrast is the fundamental principle used to quantify motion and blood flow.

An important characteristic of a speckle pattern is the average size of the individual speckles. Counterintuitively, the speckle size is generally not related to the microscopic structure of the scattering surface itself. Instead, it is determined by the diffraction properties of the optical system used to observe the pattern. When a speckle pattern is imaged by a lens onto a camera sensor, the average speckle size is on the order of the diffraction-limited resolution spot of the lens, which is related to the Airy disk diameter. The speckle size can be approximated by the formula $\frac{\lambda v}{D}$, where λ is the wavelength of the light, v is the distance from the lens to the image plane, and D is the diameter of the lens aperture. This relationship implies that using a smaller aperture (a larger f-number) will produce larger speckles on the detector. This is a critical consideration in designing an optical system, as the speckle size must be appropriately matched to the pixel size of the camera for optimal measurement. It also reveals a potential tradeoff between speckle size and numerical aperture.

Light propagation and depth sensitivity

In a highly scattering medium like biological tissue, the path of individual photons is random. However, the collective behavior of a large number of photons can be described by the diffusion approximation to the radiative transport equation. This model is valid when light undergoes a large number of scattering events, causing its directionality to be randomized, and when observations are made at a distance of at least a few transport mean free paths from the light source. This model predicts that

for a given geometry of a light source and a detector placed on the surface of the head, there is a specific spatial region that is most sensitively probed. This region forms a characteristic "banana-shaped" sensitivity profile connecting the source and the detector.

A critical principle, central to this thesis, is that the mean penetration depth of this sensitivity profile is intrinsically related to the source-to-detector (S-D) separation distance. As the S-D distance increases, the "banana" extends deeper into the tissue. This relationship provides a crucial, non-invasive mechanism for depth selection. By using short S-D distances, one can preferentially measure blood flow in superficial layers like the scalp and skull. Conversely, by employing larger S-D distances (typically >2.5 cm), the sensitivity profile extends sufficiently deep to probe the cerebral cortex, allowing for the measurement of brain blood flow while minimizing signal contamination from overlying tissues. This principle has been experimentally validated through systematic variation of the S-D distance, which reveals a characteristic "double decay" in signal quality corresponding to the transition from scalp/skull to brain layers, and through targeted occlusion of superficial arteries to isolate the scalp-specific signal component.

From photon diffusion to autocorrelation: the theoretical link

The propagation of light through a highly scattering medium like biological tissue is well-described by the diffusion approximation to the radiative transport equation. This model is valid when scattering events are far more probable than absorption events ($\mu_s' \gg \mu_a$) and when observations are made at a distance of at least a few transport mean free paths (l^*) from the light source, where the light's directionality has been randomized. The key parameter in this model is the reduced scattering coefficient, $\mu_s' = \mu_s(1 - g)$, which combines the scattering coefficient (μ_s) and the scattering anisotropy (g) into a single term describing isotropic scattering. The reciprocal of this, $l^* = 1/\mu_s'$, is the transport mean free path, representing the average distance a photon travels before its direction is randomized [12, 13].

The power of Diffusing Wave Spectroscopy (DWS) lies in extending this diffusion concept from describing the propagation of light intensity to describing the propagation of the light's temporal coherence. The temporal electric field autocorrelation function, $g_1(\tau)$, which quantifies the timescale of speckle fluctuations, also propagates through the tissue in a diffusive manner. This process is governed by the correlation diffusion equation, a partial differential equation that is formally analo-

gous to the diffusion equation for light fluence. By solving this equation, one can obtain a theoretical model for the shape of the autocorrelation function measured at a detector, linking it directly to the optical and dynamic properties of the tissue.

The fundamental connection between the physical process of light diffusion and the measured decorrelation time is established by considering the cumulative phase shifts experienced by photons traveling along different paths. The total field autocorrelation function, $g_1(\tau)$, is an integral over the distribution of all possible photon path lengths, $P(s)$. For each path of length s, the decorrelation depends on the mean-square displacement (MSD), $\langle \Delta r^2(\tau) \rangle$, of the scattering particles (red blood cells) and the number of scattering events, which is proportional to s/l^*. This relationship is expressed as:

$$g_1(\tau) = \int_0^\infty P(s) \exp\left(-\frac{1}{3} k_0^2 \langle \Delta r^2(\tau) \rangle \frac{s}{l^*}\right) ds$$

Here, k_0 is the wave number of light in the medium. This equation elegantly ties the macroscopic measurement of decorrelation time to the microscopic physics of particle motion and the statistical nature of photon transport, where longer paths with more scattering events contribute to a faster decay of the correlation.

The specific shape of the autocorrelation decay curve is determined by the nature of the scatterer motion, which is encapsulated in the MSD term, $\langle \Delta r^2(\tau) \rangle$. In the case of single scattering, as in traditional Dynamic Light Scattering (DLS), the decay is a simple function of a single scattering vector, q. However, in the multiple scattering regime of DWS, the decay is an average over many scattering events. Different models of particle motion lead to different functional forms for the decay. For random, Brownian-like motion, the MSD is linear with time, $\langle \Delta r^2(\tau) \rangle = 6 D_B \tau$, where D_B is an effective diffusion coefficient. This leads to a decay that is approximately a single exponential. For more ordered, convective or ballistic motion, the MSD is quadratic with time, $\langle \Delta r^2(\tau) \rangle = \langle v^2 \rangle \tau^2$, which results in a Gaussian decay profile for $g_1(\tau)$.

In the context of blood flow, substantial experimental evidence indicates that a diffusive motion model provides a better fit to the data than a convective one, a phenomenon often attributed to processes like shear-induced diffusion. By adopting the diffusive model ($\langle \Delta r^2(\tau) \rangle = 6 D_B \tau$) and solving the correlation diffusion equation for a given geometry (e.g., a semi-infinite medium), a specific analytical solution for $g_1(\tau)$ is obtained. The decay rate of this function is found to be directly proportional to the effective diffusion coefficient, D_B. This coefficient, which has units of

cm^2/s, thus serves as the quantitative blood flow index (BFI) that is extracted from experimental data. This provides the final, crucial link: by measuring the speckle decorrelation time, we can fit the data to this diffusion-based model to quantify the underlying rate of blood flow.

Ergodicity, autocorrelation, and the Siegert relation

When a coherent laser beam illuminates a scattering medium, the light waves exiting the tissue have traveled along a multitude of different paths. The interference of these dephased but still coherent waves creates a complex, high-contrast, granular intensity pattern known as a laser speckle field. This pattern is a static snapshot of the scatterers' positions at a given moment. Within living tissue, red blood cells are in constant motion, causing the optical path lengths of the scattered photons to change continuously. This leads to rapid temporal fluctuations in the speckle pattern, a process termed decorrelation. The timescale of these fluctuations is directly related to the speed of the scatterers; faster blood flow results in more rapid speckle fluctuations.

DWS techniques rely on a fundamental statistical assumption known as ergodicity. An ergodic process is one where the statistical properties, such as the mean and variance, are the same whether they are averaged over a long period of time for a single instance of the process (a time average) or averaged over many different instances of the process at a single point in time (an ensemble average). This assumption is critical because it allows for practical measurements. For a dynamic speckle field, ergodicity implies that the statistical information contained in the temporal fluctuations of a single speckle is equivalent to the information contained in a spatial snapshot of many independent speckles at one instant. This principle forms the basis for the two distinct methodological branches of DWS [14].

The characteristic timescale of decorrelation is quantified by the field autocorrelation function, $g_1(\tau)$, which is defined as the correlation of the scattered electric field, $E(t)$, with a time-delayed version of itself, $E(t+\tau)$ [14]:

$$g_1(\tau) = \frac{\langle E(t)E^*(t+\tau)\rangle}{\langle I(t)\rangle}$$

The decay time of this function is the field decorrelation time, τ_{field}. A shorter τ_{field} signifies faster dynamics. However, most non-interferometric optical detectors measure intensity, $I(t) \propto |E(t)|^2$, not the electric field directly. The intensity

autocorrelation function, $g_2(\tau)$, is defined as [14]:

$$g_2(\tau) = \frac{\langle I(t)I(t+\tau)\rangle}{\langle I(t)\rangle^2}$$

The crucial link between the measurable intensity correlation and the physically descriptive field correlation is the Siegert relation. It states that for a complex random Gaussian field—a condition met when light is scattered by a large number of independent emitters like red blood cells—the two functions are related by: $g_2(\tau) = 1 + \beta|g_1(\tau)|^2$, where β is an instrumental constant related to the detection geometry and coherence. The Siegert relation is foundational because it allows one to infer the field decorrelation, which directly relates to scatterer motion, from simple intensity measurements. However, this relation can break down under certain conditions, such as when the number of scatterers is low, when there are correlations between scattering events, or in the presence of a strong, non-fluctuating (static) component in the scattered light. Understanding these limitations is key to interpreting DWS data correctly and motivates the development of interferometric techniques that can measure properties of $g_1(\tau)$ more directly.

1.4 A dichotomy of speckle measurement: temporal and spatial sampling techniques

Within the DWS framework, two primary methodologies have emerged for analyzing speckle fluctuations to infer blood flow: temporal sampling and spatial sampling. These approaches differ fundamentally in their detection strategy, data analysis, and instrumentation, each presenting a unique set of advantages and disadvantages. Both methods leverage the principle of ergodicity, but they do so in opposite ways: temporal methods perform a time average on one or a few speckles, while spatial methods perform a spatial average over many speckles at a limited number of time points.

Temporal sampling: diffuse correlation spectroscopy (DCS)

The temporal sampling technique, most commonly known as Diffuse Correlation Spectroscopy (DCS), is a powerful non-invasive method that quantifies deep tissue blood flow by analyzing the temporal fluctuations of scattered coherent light. It operates by measuring the time-evolution of the intensity of a single or a small number of speckles, effectively performing a time-average measurement under the assumption of ergodicity. This approach has been extensively validated against

"gold-standard" techniques like arterial spin-labeled MRI and is widely used in neuromonitoring applications.

A typical DCS system consists of three main components: a long-coherence-length near-infrared (NIR) laser to illuminate the tissue, high-sensitivity single-photon counting detectors (like single-photon avalanche diodes, or SPADs) to record the light, and a digital correlator. Light is delivered to the tissue surface via a source fiber, and the scattered light is collected by one or more single-mode or few-mode detector fibers placed at a specific source-detector separation. The detectors must have a very high sampling rate (typically >100 kHz) to resolve the rapid intensity fluctuations, which are on the order of microseconds. The photon arrival times are then processed by the correlator, either in hardware or software, to compute the temporal intensity autocorrelation function, $g_2(\tau)$.

The core of DCS data analysis involves fitting the experimentally measured $g_2(\tau)$ to a theoretical model derived from the correlation diffusion equation. This equation models the propagation of the electric field's temporal autocorrelation through a multiply scattering medium. The solution depends on the tissue's optical properties (absorption and scattering coefficients) and, crucially, on a model for the scatterers' motion, which is quantified by their mean-square displacement (MSD), $\langle \Delta r^2(\tau) \rangle$. Although blood flow is fundamentally a convective process (directed flow), substantial evidence shows that a diffusive motion model, where $\langle \Delta r^2(\tau) \rangle = 6 D_B \tau$, provides a better fit to experimental data. This apparent contradiction is often explained by phenomena like shear-induced diffusion. The fit yields an effective diffusion coefficient, D_B, which serves as the quantitative blood flow index (BFI) [15].

The shape of the autocorrelation decay curve itself contains information about the nature of the scatterer motion. For instance, classic Brownian motion (a random walk) results in a purely exponential decay for the field autocorrelation function, $g_1(\tau)$. In contrast, more ordered or constrained motion, such as convective flow, can lead to a Gaussian or other non-exponential decay profiles. A key strength of DCS is its ability to measure the full shape of the autocorrelation function, allowing researchers to probe these different motion models and gain deeper insight into the micro-hemodynamics of the tissue.

Despite its power, DCS faces several challenges. The requirement for specialized, high-speed, single-photon counting detectors and correlator electronics makes DCS systems relatively expensive and complex. Furthermore, because it samples only

one or a few speckle modes at a time, its signal-to-noise ratio (SNR) is fundamentally limited by photon-counting statistics, which becomes a significant problem at the large source-detector separations needed for deep brain monitoring. This creates a difficult trade-off between brain specificity and signal quality. To address these limitations, advanced DCS techniques have been developed, including interferometric DCS (iDCS) [16] to reject noise and multi-speckle DCS systems that use arrays of SPADs [17] to improve photon throughput.

Spatial sampling: speckle contrast optical spectroscopy (SCOS)

The spatial sampling technique, known as Speckle Contrast Optical Spectroscopy (SCOS) or Speckle Visibility Spectroscopy (SVS), offers an alternative approach that leverages a spatial ensemble of speckles. Instead of tracking the temporal evolution of a single speckle with a fast point detector, SCOS uses a multi-pixel detector, such as a CMOS or CCD camera, to capture a snapshot of thousands or millions of speckles simultaneously. This method capitalizes on the ergodicity of the speckle field by substituting the time average of DCS with a spatial average over the detector array.

The principle of SCOS relies on the relationship between speckle motion and image blur. The camera's exposure time, T, is intentionally set to be longer than the characteristic speckle decorrelation time, τ_c. During this exposure, red blood cells move, causing the speckle pattern to fluctuate. Faster blood flow leads to more rapid fluctuations, causing multiple independent speckle patterns to be integrated onto a single camera frame. This time-averaging process blurs, or "washes out," the speckle pattern. The degree of this blurring is quantified by the speckle contrast, K, defined as the spatial standard deviation of the pixel intensities (σ) divided by their spatial mean (μ): $K = \sigma/\mu$. Lower contrast indicates more blurring and, therefore, faster blood flow. A Blood Flow Index (BFI) is defined as being inversely proportional to the squared speckle contrast, $BFI \propto 1/K^2$ [18, 19, 20] .

A primary advantage of SCOS is its instrumentation. It can be implemented with cost-effective, commercially available cameras, making SCOS systems significantly more accessible and scalable than typical DCS setups. By integrating the signal over a massive number of speckles simultaneously, SCOS achieves a very high photon throughput. This parallelization often results in a superior signal-to-noise ratio (SNR) compared to single-detector DCS, particularly in the photon-starved conditions encountered when probing deep tissue at large source-detector separa-

tions. This high SNR makes SCOS well-suited for developing portable, wearable, and even multi-channel monitoring devices.

However, the main weakness of SCOS is its profound susceptibility to measurement noise. The calculated spatial variance, σ^2, is a composite of the true flow-related speckle variance and noise contributions from multiple sources, including photon shot noise, camera read noise, and quantization noise. These noise sources are not constant; their contribution to the speckle contrast depends on the mean signal intensity, μ, which itself fluctuates with the cardiac cycle due to changes in blood volume. Consequently, accurate BFI extraction requires a meticulous noise calibration procedure, where the noise contributions are subtracted from the raw measured contrast: $K^2_{flow} = K^2_{raw} - K^2_{shot} - K^2_{camera} - K^2_{quant}$. Any error in this calibration can introduce artifacts that mimic the blood volume signal, severely corrupting the CBF waveform, especially in low-light conditions.

Another fundamental limitation of SCOS is that, by integrating the signal over the exposure time T, it loses the ability to resolve the full shape of the autocorrelation function, $g_2(\tau)$. The speckle contrast measurement provides only a single metric related to the integral of the correlation function, not the function itself. This prevents the analysis of different motion models (e.g., diffusive vs. convective) that is possible with DCS. To address the critical noise issue, advanced techniques like interferometric Speckle Visibility Spectroscopy (iSVS) have been developed. By coherently mixing the weak sample light with a strong reference beam, iSVS amplifies the signal above the camera's noise floor, dramatically improving SNR and enabling accurate measurements even in extremely low-light conditions.

1.5 Positioning the thesis contribution: fundamental advancement and application of iSVS and SCOS

This thesis presents a body of work that forms a logical and strategic research program aimed at systematically overcoming the primary challenges of iSVS and SCOS. The goal is to transform optical diffuse correlation methods from a promising laboratory technique into a robust, accurate, and clinically viable technology for non-invasive cerebrovascular monitoring. This research arc progresses from fundamental scientific validation to practical engineering solutions and culminates in advanced signal processing for clinical-grade accuracy.

First, the foundational premise—that optical methods can non-invasively probe the brain—is experimentally validated. By systematically varying the S-D distance, the

transition point at which cerebral signals become detectable is identified, characterized by a "double decay" curve that differentiates the optical properties of the superficial scalp/skull layers from the deeper brain layer. This is further solidified by a novel experimental paradigm using temporary occlusion of the superficial temporal artery to selectively remove the scalp's blood flow contribution, providing the first direct, in-vivo experimental proof of the depth sensitivity of optical measurements and confirming that larger S-D distances preferentially sample brain tissue.

Having established the principle of depth-resolved measurement, the research next confronts the primary physical limitation of SCOS at large S-D distances: low signal and high noise. In these photon-limited regimes, camera read noise can overwhelm the true speckle contrast signal. To solve this, Interferometric Speckle Visibility Spectroscopy (iSVS) is introduced. By coherently mixing the weak, scattered sample light with a strong, stable reference beam on the camera sensor, the faint signal from the brain is interferometrically amplified above the detector's noise floor. This technique dramatically improves the SNR, enabling accurate decorrelation time measurements in conditions where traditional SCOS would fail, thereby making deep-tissue measurements feasible.

With the physics validated and the SNR problem solved, the focus shifts to clinical translation and practical engineering. Traditional SCOS and iSVS systems often rely on bulky laboratory optics and are highly susceptible to motion artifacts from optical fibers connecting the patient to the detection system. To address this, a new generation of compact, fiber-free SCOS devices is developed. By mounting the laser diode and camera sensor directly on the subject's head in a lightweight, wearable module, these systems eliminate fiber-related motion artifacts and, due to a larger light collection area and numerical aperture, achieve a signal gain of approximately 70-fold over single-fiber SCOS systems. This innovation not only enhances signal stability and quality but also enables the creation of truly portable, battery-powered, multi-channel systems capable of simultaneously monitoring CBF and CBV at multiple distinct brain locations.

Finally, the thesis addresses the critical, and often overlooked, challenge of ensuring measurement accuracy through precise noise calibration. Imperfect subtraction of photon shot noise and camera noise—which are themselves dependent on the fluctuating signal intensity—can introduce artifacts into the calculated CBF waveform that spuriously mimic the CBV signal. To correct this, an innovative optimization-based framework is developed. This algorithm adaptively refines the noise calibration pa-

rameters by iteratively minimizing the correlation between the calculated CBF and CBV waveforms. This intelligent post-processing technique effectively suppresses these artifacts, significantly lowering the signal threshold required for reliable measurements and enhancing the overall robustness and accuracy of the SCOS method, even in the presence of imperfect a priori system characterization.

To demonstrate the clinical utility and potential of this refined SCOS technology, the developed system was deployed in a clinical trial for stroke risk assessment. This study showcased the system's application as a non-invasive tool to monitor cerebral blood flow and volume changes during a physiological challenge—a voluntary breath-hold. The trial involved 50 participants, stratified into low-risk and higher-risk groups for stroke, and revealed significant differences in their cerebrovascular responses. By analyzing the dynamics of blood flow and volume, particularly their ratio, the system provided direct physiological insights that correlated with established stroke risk scores, demonstrating its potential as a cost-effective and scalable tool for early diagnosis and personalized stroke risk management.

Collectively, these contributions represent a comprehensive effort to advance speckle-based optical neuro-monitoring, moving it from a proof-of-concept technique toward a practical, powerful, and accessible tool for clinical diagnostics and neuroscience research.

1.6 Note on Nomenclature: SVS versus SCOS

Throughout this dissertation, the terms *Speckle Visibility Spectroscopy* (SVS) and *Speckle Contrast Optical Spectroscopy* (SCOS) are used. It is important to clarify that these terms refer to the same fundamental optical measurement principle: the analysis of spatial fluctuations (contrast) within a laser speckle pattern to quantify the dynamics of a scattering medium.

The distinction in usage within this document mirrors the chronological evolution of this research and aligns with the specific conventions adopted in the peer-reviewed publications adapted for each chapter. Specifically:

- **SVS** is primarily employed in **Chapter 2** and **Section 3.1**. This terminology aligns with foundational literature regarding Diffusing Wave Spectroscopy (DWS) and is used here specifically in the context of Interferometric Speckle Visibility Spectroscopy (iSVS).

- **SCOS** is primarily employed in **Section 3.2**, **Chapter 4**, and **Chapter 5**. This term is widely adopted in the biomedical optics engineering community and is used here to describe the compact, fiber-free, and wearable sensor architectures developed in the latter stages of this work.

Unless distinct physical modifications are explicitly noted—such as the introduction of a reference beam in iSVS—the underlying physics, signal acquisition strategies, and statistical definitions of the blood flow index remain consistent across both nomenclatures.

References

[1] R Aaslid et al. "Cerebral autoregulation dynamics in humans." en. In: *Stroke* 20.1 (Jan. 1989), pp. 45–52. DOI: 10.1161/01.STR.20.1.45.

[2] Clément Huneau, Habib Benali, and Hugues Chabriat. "Investigating Human Neurovascular Coupling Using Functional Neuroimaging: A Critical Review of Dynamic Models". English. In: *Frontiers in Neuroscience* 9 (Dec. 2015). Publisher: Frontiers. DOI: 10.3389/fnins.2015.00467.

[3] G. J. Bouma and J. P. Muizelaar. "Cerebral blood flow, cerebral blood volume, and cerebrovascular reactivity after severe head injury". eng. In: *Journal of Neurotrauma* 9 Suppl 1 (Mar. 1992), S333–348.

[4] Souraya Elsankari et al. "Cerebrospinal fluid and blood flow in mild cognitive impairment and Alzheimer's disease: A differential diagnosis from idiopathic normal pressure hydrocephalus". In: *Fluids and barriers of the CNS* 8 (Feb. 2011), p. 12. DOI: 10.1186/2045-8118-8-12.

[5] Daniel F. Arteaga et al. "Cerebral blood flow territory instability in patients with atherosclerotic intracranial stenosis". eng. In: *Journal of magnetic resonance imaging: JMRI* 50.5 (Nov. 2019), pp. 1441–1451. DOI: 10.1002/jmri.26737.

[6] Krisztián Szigeti et al. "A novel SPECT-based approach reveals early mechanisms of central and peripheral inflammation after cerebral ischemia". In: *Journal of Cerebral Blood Flow & Metabolism* 35.12 (Dec. 2015), pp. 1921–1929. DOI: 10.1038/jcbfm.2015.174.

[7] Samuel Kuttner et al. "Cerebral blood flow measurements with 15O-water PET using a non-invasive machine-learning-derived arterial input function". eng. In: *Journal of Cerebral Blood Flow and Metabolism: Official Journal of the International Society of Cerebral Blood Flow and Metabolism* 41.9 (Sept. 2021), pp. 2229–2241. DOI: 10.1177/0271678X21991393.

[8] Sushmita Purkayastha and Farzaneh Sorond. “Transcranial Doppler Ultrasound: Technique and Application”. In: *Seminars in neurology* 32.4 (Sept. 2012), pp. 411–420. DOI: 10.1055/s-0032-1331812.

[9] Junichiro Hashimoto, Berend E. Westerhof, and Sadayoshi Ito. “Carotid Flow Augmentation, Arterial Aging, and Cerebral White Matter Hyperintensities: Comparison With Pressure Augmentation”. en. In: *Arteriosclerosis, Thrombosis, and Vascular Biology* 38.12 (Dec. 2018), pp. 2843–2853. DOI: 10.1161/ATVBAHA.118.311873.

[10] “Arterial Pressure Waveforms”. In: *Basic Physiology for Anaesthetists*. Ed. by Christopher Huang, David Chambers, and Gareth Matthews. 2nd ed. Cambridge: Cambridge University Press, 2019, pp. 155–157. DOI: 10.1017/9781108565011.038.

[11] George Themelis et al. “Near-infrared spectroscopy measurement of the pulsatile component of cerebral blood flow and volume from arterial oscillations”. en. In: *Journal of Biomedical Optics* 12.1 (2007). Publisher: SPIE-Intl Soc Optical Eng, p. 014033. DOI: 10.1117/1.2710250.

[12] Steven L. Jacques and Brian W. Pogue. “Tutorial on diffuse light transport”. In: *Journal of Biomedical Optics* 13.4 (July 2008). Publisher: SPIE, p. 041302. DOI: 10.1117/1.2967535.

[13] Zahra Fahimi. “Diffusing-wave spectroscopy in a standard dynamic light scattering setup”. In: *Physical Review E* 96.6 (2017). DOI: 10.1103/PhysRevE.96.062611.

[14] Jian Xu, Ali K Jahromi, and Changhuei Yang. “Diffusing wave spectroscopy: A unified treatment on temporal sampling and speckle ensemble methods”. en. In: *APL Photonics* 6.1 (Jan. 2021). Publisher: AIP Publishing, p. 016105. DOI: 10.1063/5.0034576.

[15] Stefan A. Carp, Mitchell B. Robinson, and Maria A. Franceschini. “Diffuse correlation spectroscopy: current status and future outlook”. In: *Neurophotonics* 10.01 (Jan. 2023). DOI: 10.1117/1.NPh.10.1.013509.

[16] Mingjun Zhao et al. “Interferometric diffusing wave spectroscopy imaging with an electronically variable time-of-flight filter”. en. In: *Optica* 10.1 (Jan. 2023), p. 42. DOI: 10.1364/OPTICA.472471.

[17] Wenjun Zhou et al. “Functional interferometric diffusing wave spectroscopy of the human brain”. en. In: *Science Advances* 7.20 (May 2021), eabe0150. DOI: 10.1126/sciadv.abe0150.

[18] Jian Xu et al. “Interferometric speckle visibility spectroscopy (ISVS) for human cerebral blood flow monitoring”. en. In: *APL Photonics* 5.12 (Dec. 2020), p. 126102. DOI: 10.1063/5.0021988.

[19] David A. Boas and Andrew K. Dunn. “Laser speckle contrast imaging in biomedical optics”. en. In: *Journal of Biomedical Optics* 15.1 (2010), p. 011109. DOI: 10.1117/1.3285504.

[20] Byungchan Kim et al. “Measuring human cerebral blood flow and brain function with fiber-based speckle contrast optical spectroscopy system”. en. In: *Communications Biology* 6.1 (Aug. 2023), p. 844. DOI: 10.1038/s42003-023-05211-4.

Chapter 2

ARE WE MEASURING THE BRAIN?

2.1 The fundamental challenge: superficial signal contamination in transcranial optical measurements

The central premise of non-invasive optical neuro-monitoring is the ability to transmit light through the scalp and skull to probe the physiological dynamics of the underlying cerebral cortex. Techniques based on Diffusing Wave Spectroscopy (DWS), such as Diffuse Correlation Spectroscopy (DCS) and Speckle Contrast Optical Spectroscopy (SCOS), have emerged as powerful modalities for this purpose, offering high temporal resolution measurements of cerebral blood flow (CBF). However, the very nature of this transcranial approach presents a fundamental and critical challenge: any detected optical signal is inherently a composite, influenced not only by the target cerebral tissue but also by the overlying, extracerebral layers.

Photons injected into the head must traverse the scalp, skull, and a layer of cerebrospinal fluid (CSF) before reaching the cerebral gray matter, and they must complete the return journey to be collected by a detector. Each of these anatomical compartments possesses a unique and dynamic vascular network, as well as distinct optical properties (absorption and scattering coefficients). The scalp, in particular, is highly perfused and exhibits a strong pulsatile blood flow signal driven by the cardiac cycle. Consequently, the signal measured at the surface is a weighted average of the dynamics occurring in all tissue layers interrogated by the light. This creates a significant potential for signal contamination, where strong hemodynamic signals from the scalp can mask or be mistaken for the weaker signals originating from the deeper cerebral cortex.

This reality reframes the primary validation challenge for transcranial DWS. The problem is not merely one of signal-to-noise ratio (SNR), where the goal is simply to obtain a clear and robust signal. Rather, it is a more fundamental problem of signal origin. A strong, high-quality pulsatile waveform is of little clinical or scientific value if it predominantly reflects scalp hemodynamics rather than cerebral perfusion. Misinterpreting a change in scalp blood flow—perhaps due to a systemic physiological response or local temperature changes—as a sign of cerebrovascular dysregulation could lead to profoundly erroneous clinical conclusions. Therefore,

for DWS techniques to be accepted as clinically viable tools for monitoring brain health, it is imperative to establish a reliable and quantifiable method for ensuring the anatomical specificity of the measurement.

The principal, non-invasive parameter available to control the mean penetration depth of an optical measurement is the source-to-detector (S-D) separation distance. Intuitively, as the distance between the light source and the detector on the tissue surface increases, photons must travel, on average, along longer and deeper paths to be detected. This relationship provides a crucial mechanism for depth selection. By employing short S-D distances, the measurement can be made preferentially sensitive to superficial layers, while larger S-D distances are required to extend the sensitivity profile deep enough to probe the cerebral cortex. The following sections will provide a rigorous theoretical and experimental examination of this principle, with the ultimate goal of answering the foundational question posed by this chapter's title.

Theoretical foundations: Monte Carlo modeling of photon transport in multi-layered tissue

To theoretically predict and understand how light propagates through the complex, multi-layered structure of the human head, the Monte Carlo (MC) method has been established as the computational "gold standard". Unlike analytical models based on the diffusion approximation, which can be limited by geometry and assumptions, MC simulations offer a flexible and rigorous approach that directly solves the radiative transport equation without approximation. This method provides a powerful predictive framework for optimizing the design of optical systems and for interpreting the signals they measure.

The core principle of the MC method is the computational tracing of the trajectories of millions of individual "photon packets" as they travel through a simulated medium. The path of each photon is modeled as a "random walk," where the key events—the distance traveled between interactions and the angle of scattering at each interaction—are determined by statistically sampling known probability distributions. The step size a photon takes before an interaction is governed by the tissue's absorption coefficient (μ_a) and scattering coefficient (μ_s), while the angular deflection upon scattering is determined by the scattering anisotropy factor (g). By simulating a vast number of these individual photon paths, the net distribution of all trajectories yields an accurate approximation of macroscopic light transport within

the tissue.

For transcranial applications, the simulation is constructed using a realistic, multi-layered anatomical model, often derived from structural imaging data like MRI. This model defines distinct layers for the scalp, skull, CSF, gray matter, and white matter, each assigned its own set of optical properties (μ_s, μ_a, g). The simulation then launches photons from a source position on the surface and tracks their paths through these layers until they are either absorbed or exit the surface, where they may be "collected" by a virtual detector.

The primary output of such simulations for depth sensitivity analysis is the spatial sensitivity profile, which maps the region of tissue to which a given source-detector pair is most sensitive. MC simulations consistently predict that this region forms a characteristic "banana-shaped" probability distribution connecting the source and the detector. This profile represents the volume through which photons that successfully travel from source to detector are most likely to have passed. Critically, these models provide the theoretical justification for using S-D separation as a means of depth selection: as the S-D distance is increased, the "banana" is forced to extend deeper into the tissue, thereby increasing the partial path length of photons within the deeper layers and, consequently, the measurement's relative sensitivity to the cerebral cortex. This theoretical relationship is foundational to the design and interpretation of all transcranial DWS systems.

While MC simulation is an indispensable predictive tool, its accuracy is entirely contingent on the accuracy of the input optical properties used for each tissue layer. These parameters are known to exhibit significant inter- and intra-subject variability due to factors such as age, skin pigmentation, and skull thickness and density. Furthermore, obtaining precise, subject-specific in vivo measurements of these properties is exceptionally difficult. This means that while MC simulations provide a robust qualitative prediction—that sensitivity increases with S-D separation—their quantitative predictions (e.g., "at an S-D of 2.5 cm, 50% of the signal originates from the brain") represent an idealized approximation. This inherent uncertainty creates a crucial gap between theory and practice, a gap that can only be bridged by direct and rigorous experimental validation on living subjects. Such experiments are not merely confirmatory; they are essential for translating the idealized models into reliable, real-world measurement protocols. Two works presented in this chapter further explore this topic through experimental results. The first work utilizes an interferometric technique (iSVS), while the second explores a non-interferometric setup

(SCOS) that introduces a novel method for temporarily suppressing the superficial temporal artery in the scalp.

2.2 Assessing depth sensitivity in iSVS in rabbits and humans

This section is adapted from published work: Mahler S, Huang YX, Liang M, Avalos A, Tyszka JM, Mertz J, Yang C. *Assessing depth sensitivity in laser interferometry speckle visibility spectroscopy (iSVS) through source-to-detector distance variation and cerebral blood flow monitoring in humans and rabbits*. Biomed Opt Express. 2023 Aug 29;14(9):4964-4978.

The previous sections have established the critical importance of monitoring cerebral blood flow (CBF) and introduced various optical methods, particularly speckle-based techniques like Diffusing Wave Spectroscopy (DWS), as promising non-invasive solutions. We detailed the fundamental principles of laser speckle, its temporal and spatial sampling methodologies (DCS and SCOS, respectively), and highlighted the advantages of interferometric Speckle Visibility Spectroscopy (iSVS) in enhancing signal-to-noise ratio for deep-tissue measurements.

A central challenge in transcranial optical measurements, however, remains the accurate isolation of cerebral signals from superficial tissue contamination. While theoretical models and previous experiments suggest that increasing the source-to-detector (S-D) separation distance can enhance depth sensitivity, a rigorous experimental validation of this principle for iSVS on living subjects is essential. Such validation is crucial for establishing the anatomical specificity required for reliable clinical application.

Building upon these foundational insights, this section presents an experimental investigation into the depth sensitivity of laser interferometry speckle visibility spectroscopy (iSVS). The primary objective is to systematically determine the relationship between S-D distance and the depth of optical penetration, specifically identifying the transition point at which cerebral blood flow becomes distinctly detectable in humans and rabbits. By varying the S-D distance, we aim to provide direct, in-vivo experimental proof of iSVS's ability to selectively sample brain tissue, thereby solidifying its potential as a clinically viable tool for cerebrovascular monitoring.

Experimental arrangement

The experimental arrangement for laser interferometry speckle visibility spectroscopy (iSVS) is shown in Fig. 2.1 [1, 2]. It is based on an off-axis Mach-Zehnder interferometer. For this study, we used a single-mode, single-frequency continuous wave 785 nm laser source [Thorlabs FPV785S & CLD1015]. This laser source has a long (>5 m) coherence length, useful for interferometry, is thermally stabilized and can deliver up to 50 mW, useful for laser speckle imaging. The arrangement in Fig. 2.1(a) is set as follow: the input laser beam is divided by a 10:90 (Reflectivity:Transmission) beam splitter [Thorlabs BS044] into two light beams: one light beam for illuminating the sample (sample arm) and one light beam for interfering with the sample laser light beam (reference arm).

In the reference arm, the laser light is coupled into a single mode fiber [Thorlabs SM800-5.6-125]. The use of a single mode fiber allows us to generate a circular Gaussian-beam at the output. It also allows us to match the pathlength of the reference arm with the pathlength of the sample arm by choosing the appropriate fiber length. The other end of the single mode fiber illuminates a second 10:90 (R:T) beam splitter [Thorlabs BS044] and the reference laser light is directed onto a scientific CMOS camera [Excelitas pco.edge 5.5] with a pixel size of 6.5 $\times$ 6.5 μm.

In the sample arm, the laser light is coupled into a 600 μm core diameter multimode fiber [Thorlabs FT600UMT]. The other end of the multimode fiber is set a few millimeters away from the sample (e.g. human or rabbit head), such that the laser light intensity level of the area of illumination is well within the American National Standards Institute (ANSI) laser safety standards of 2.96 mW/mm^2 for maximum permissible exposure for skin exposure to a laser beam at 785 nm [3].

At a separation distance S-D from the illumination fiber, a multimode fiber with a 600 μm core diameter [Thorlabs FT600UMT] collects the laser light that propagated inside the head of the subject, see Fig. 2.1(b). By tuning the S-D distance, one can tune the depth of penetration into the head of the subject, see Fig. 2.1(b) [5, 6, 7]. The collected laser light is imaged onto the camera.

To optimize the interferometric measurement, neutral density (ND) filters [Thorlabs NEXXA-B] and shutters [Picard Industries USB Optical Shutter] can be used to reduce or to block the laser light intensity in the sample or in the reference arm. The optical fibers were taped onto the optical table and securely fastened to prevent any slight movements that could potentially introduce speckle artifacts. At

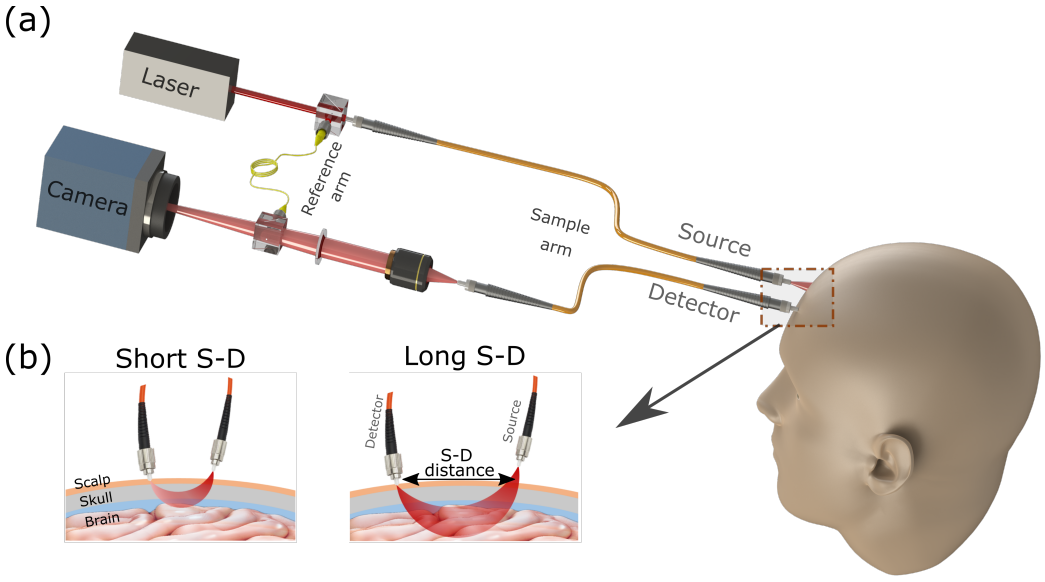


Figure 2.1: (a) Experimental arrangement of laser interferometry Speckle Visibility Spectroscopy (iSVS). In this case, the subject is a human. (b) Example of iSVS depth sensitivity by varying the Source-to-Detector (S-D) distance. As evident, the depth of penetration increases with the S-D distance. [4, 5, 6, 7]

the second beam splitter, the reference and sample arm laser light beams interfere and form an interference pattern recorded by the camera with a speckle to pixel size of about 2×2 pixels.

The camera in Fig. 2.1(a) was recording at a rate of 50-100 frames per second and with an exposure time T of either 0.5 ms (Figs. 2.2, 3 and 4(a)) or 1 ms (Fig. 4(b)). The recorded images by the camera are processed digitally, as shown in Fig. 2.2. For a more accurate measurement, the recorded images (Fig. 2.2(a)) are calibrated by subtracting them with a reference arm only laser light image (Fig. 2.2(b)). To get the reference arm laser light, the sampling laser light beam was blocked (at t=0) and the reference arm laser light was measured from an average over 50 images to reduce shot noise and camera noise effect.

iSVS processing pipeline

In the next chapter, we will delve into a more detailed explanation on iSVS SNR benefits. To summarize, it suppresses the camera noise variance and helps to push the SNR into shot-noise limited regime. The instantaneous intensity at the camera

at pixel j can be expressed as [1, 2]:

$$I_j(t) = I_{Sj}(t) + I_{Rj} + 2\sqrt{I_{Sj}(t)I_{Rj}(t)}\cos(\phi_{Rj} - \phi_{Sj}(t))\exp\left[-\left(\frac{\Delta L}{l_c}\right)^2\right] + n_j(t), \tag{2.1}$$

where in Eq. (2.1), $I_{Sj}(t)$ is the sample arm intensity ($\phi_{Sj}(t)$ the phase) at pixel j, I_{Rj} the reference arm intensity (ϕ_{Rj} the reference phase containing off-axis adjustments), the third term is the interference cross term, and $n_j(t)$ the noise term including shot noise, camera noise and laser noise. The coherence length l_c of the incident laser beam and the path-length difference ΔL between the sample and reference arm of the interferometer were included in the equation by using Eq. 6 of [8] and Eq. 4 of [9]. For the following, we assume $\Delta L \ll l_c$, such that $\exp[-(\Delta L/l_c)^2] \approx 1$.

By subtracting the reference, and assuming $I_{Rj} \gg I_{Sj}$, the signal recorded by the camera for a single frame is given by:

$$N_j = \frac{1}{T}\int_0^T \sqrt{I_{Sj}(t)I_{Rj}}\exp(i\phi_j)dt, \tag{2.2}$$

with ϕ_j the phase difference between the reference laser beam and the sample laser beam light field [1].

The visibility factor F is defined as:

$$F = \frac{\langle|N_j|^2\rangle}{I_S I_R} = \frac{1}{T}\int_0^T 2\left(1 - \frac{t}{T}\right)g_1(t)dt, \tag{2.3}$$

with N_j the iSVS signal, $\langle\cdot\rangle$ the expected value, $I_S I_R$ the normalization factor composed of the averaged reference arm intensity I_R and the averaged sample arm intensity I_S, T is the exposure time of the camera, and g_1 is the field decorrelation function. See Sec. D in the original paper's Supplementary Note of for full derivation. The above derivation assumes well behaved camera and laser noises that can be characterized and corrected. In practical applications, achieving such ideal conditions may pose challenges. If we are interested in measuring the dynamical change in F as a way to gauge blood flow changes, we can compute an unnormalized visibility factor (relative measurement of $\langle|N_j|^2\rangle$ in Eq. (2.3)) by Fourier transforming each recorded image (Fig. 2.2(c)) and integrating the high-frequency interference lobe (Fig. 2.2(d)). By integrating the high-frequency interference lobe (third term of Eq. (2.1)), which carries the reference enhanced blood flow signal information, we can effectively filter out the spatial low-frequency noise.

The temporal dynamics of the blood flow was measured via the computation of an unnormalized visibility factor, Fig. 2.2(e). The time information was retrieved from

the camera time stamps. As shown in Fig. 2.2(e), blood flow can be monitored on the head. The heart rate of the subject can be calculated by Fourier transforming the blood flow signal, Fig. 2.2(f). In Fig. 2.2(f), the Fourier amplitude peak centered around freqHR= 1.0 Hz corresponds to the heart rate amplitude peak of the subject. There are also Fourier peaks centered at 1.8 Hz and 2.8 Hz in Fig. 2.2(f), corresponding to the second and third sub-harmonics of the heart rate pulsations of the subject.

Note that it is also possible to use iSVS for monitoring relative changes in oxygenation levels. However, since iSVS only uses a single wavelength, absolute oxygenation is difficult to obtain. The intensity of the recorded images allows for the possibility of measuring relative fluctuations in oxygenation.

Subject recruiting, MRI/CT sequences, rabbits, and phantom

For this study, we recruited participants from the Caltech and Pasadena community, among healthy adult humans aged 21 to 65 years. The human research protocol for this study received approval from the Caltech Institutional Review Board. Three human subjects were recruited. The first two subjects were comfortable with shaving their heads. To accommodate the third subject, iSVS study was conducted on areas without hair, such as the forehead or frontotemporal area of the head. Two rabbits participated in the experiments and had their heads shaved.

To compare with the iSVS laser results, MRI scans of the head of the human subjects were done at the Caltech Brain Imaging Center, and X-rays of the head of the rabbits were conducted at the Caltech Animal Facility Center.

Structural MRI data were acquired at the Caltech Brain Imaging Center using a 3 Tesla MRI scanner (Prisma Fit model manufactured by Siemens Medical Solutions, Malvern PA) with a 32-channel head receive array. T1-weighted images were acquired with the following parameters: 3D MEMP-RAGE sequence, TR 2550 ms, TE 1.6, 3.5, 5.3, 7.1 ms, TI 1150 ms, 0.9 mm isotropic voxels. T2-weighted images were acquired with the following parameters: 3D T2w SPACE sequence, TR 3200 ms, effective TE 564 ms, 0.9 mm isotropic voxels. Pial surface estimates and skin-to-brain depths were generated using Freesurfer 7.2.

The animal research protocol for the rabbits' study received approval by the Caltech Institutional Animal Care and Use Committee. The two rabbits were 4-month-old male New Zealand White rabbits. Throughout the experiments, the rabbits were kept under anesthesia with the help of a veterinary team to ensure their comfort and

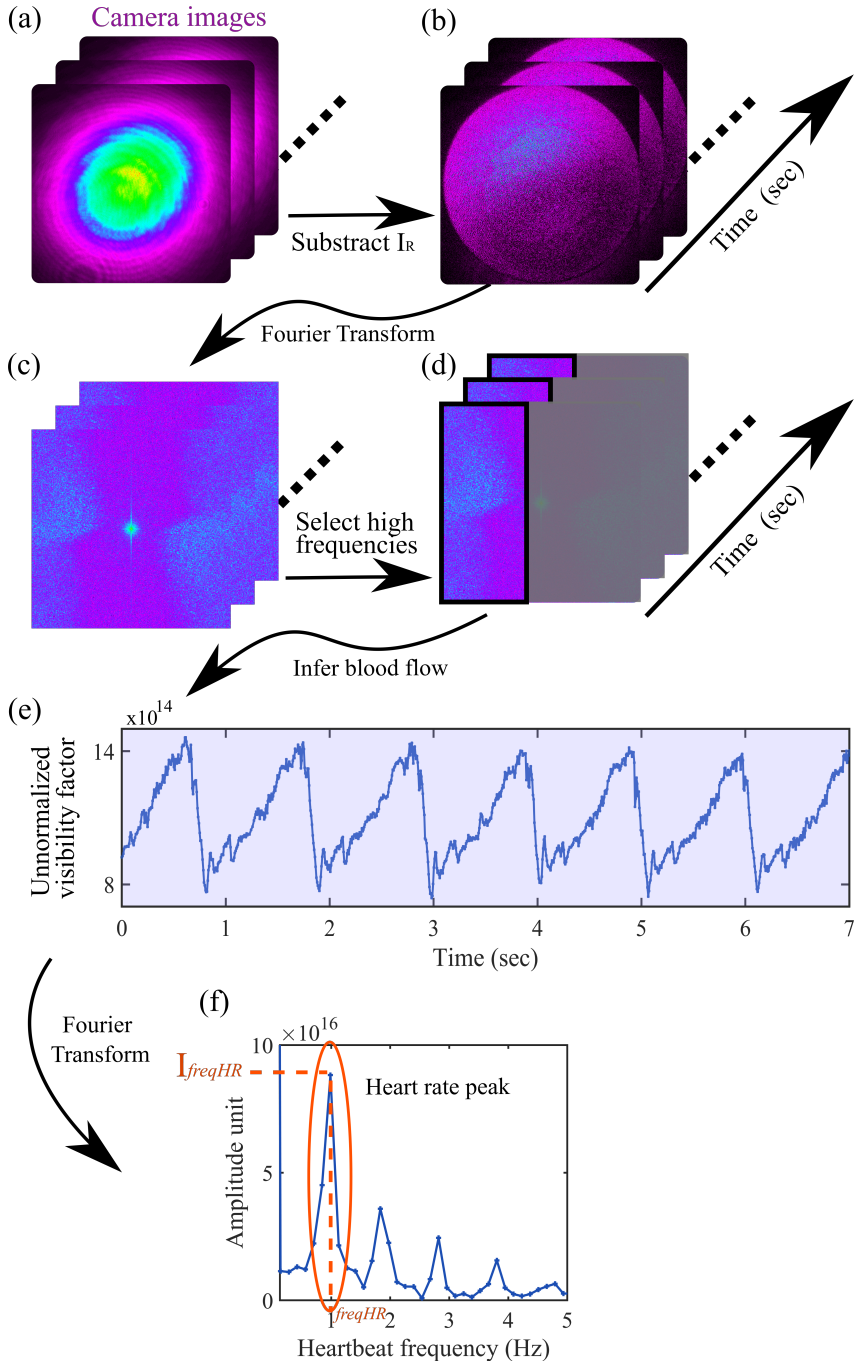


Figure 2.2: Interferometric speckle visibility spectroscopy (iSVS) processing pipeline. (a) A series of interference pattern images are recorded by the camera in Fig. 2.1. (b) The cameras images are calibrated by subtracting the reference intensity. (c) Fourier transform of the calibrated images in (b). (d) The high-frequency interference lobe, which carries blood flow signal information, is selected. (e) The temporal dynamics of the blood flow is inferred by integrating the high-frequency lobe in (d). (f) By Fourier transforming the blood flow dynamics in (e), the heart rate Fourier peak can be identified. The frequency freqHR corresponds to the heart rate (in Hertz) and the amplitude I_{freqHR}indicates the reconstruction quality of the blood flow signal in (e).

safety. Anesthesia induction was achieved using an injectable mixture of ketamine (35 mg/kg) and xylazine (5 mg/kg), administered in a single intramuscular injection in the epaxial muscles, and was maintained with 1.5% to 2% isoflurane gas anesthesia delivered by oxygen and administered via a nose cone. The use of the nose cone for anesthesia delivery may result in occasional short periods of awakening for the rabbit during the experiments.

To compare the human and rabbit results, we designed a phantom. Our phantom comprised a liquid mixture in a plastic cup, placed on an orbital shaker rotating at a 60 rotations per minute speed, see the original paper's appendix for more details. The source and detector fibers were mounted on a separate support above the cup, which was not moving, see sketch in the original paper's appendix. The iSVS system is measuring the difference of angular velocities along the horizontal line of the rotating liquid mixture, producing a liquid flow dynamic similar to the blood flow dynamic for humans, see the original paper's appendix. For the phantom experiments, one phantom was made of 3% fat-milk and another phantom was made with a mixture of 10% 3D printing resin and 90% water.

For this study, iSVS was preferred over SVS/SCOS due to the better depth sensitivity, as shown in Fig. 2.3, but our findings and conclusions are also valid for SVS/SCOS as long as the system can provide adequate proportion of detected light to resolve the cardiac pattern of the blood flow. To conduct the SVS/SCOS measurement, the laser light intensity in the reference arm was blocked, allowing only the laser light emitted from the sample arm [2].

iSVS depth sensitivity results

The peaks observed in the visibility spectrum of Fig. 2.2(f) serve as reliable indicators of the quality of blood flow signal reconstruction. The frequency freqHR, as defined in Fig. 2.2(f), corresponds to the heart rate of the subject, and its amplitude I_{freqHR} indicates the reconstruction accuracy of the blood flow signal. By examining the amplitude of the Fourier peak corresponding to the heart rate I_{freqHR} in the visibility spectrum, variations in reconstruction quality can be detected with greater precision than by observing intensity fluctuations in the reconstructed blood flow or by measuring the amount of light collected, $I_S(t)$. For example, Fig. 2.4 shows the CBF at three different S-D distances of 1.0 cm, 1.5 cm, and 2.0 cm for a human in Fig. 2.4(a) and for a rabbit in Fig. 2.4(b). Note that the heart rate for a human at rest/sleep is typically in the range 0.7-1.5 Hz, while the rabbit heart rate

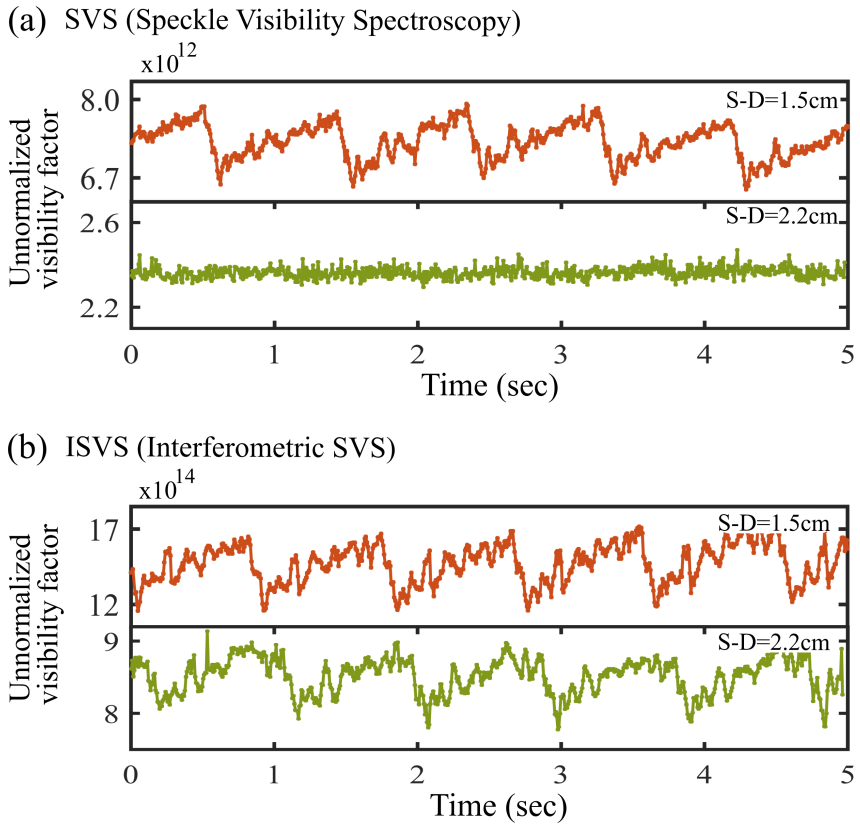


Figure 2.3: Human blood flow measurement comparison between (a) SVS and (b) iSVS detection methods. As evident, iSVS typically produces blood flow with better reconstruction quality than SVS.

at rest/sleep is typically in the range 2.3-3.5 Hz.

In Fig. 2.4, as the S-D distance increases, the accuracy of the reconstruction of the blood flow is diminished. For instance, in Fig. 2.4(a), at S-D = 1.0 cm, the heart rate pulse is easily identified on the left graph. However, at S-D = 2.0 cm, the heart rate pulse becomes less distinct. To quantify this difference in signal quality, we examine the visibility spectrum on the right graph, which is the Fourier transform of the measured blood flow. As the measured blood flow's signal quality diminishes, the amplitude of the heart rate pulse progressively reduces.

As evident in Fig. 2.4 (right column), I_{freqHR} decreases as the S-D distance increases, while the heart rate frequency freqHR remains the same. This can be explained by the fact that when the S-D distance increases, the depth of penetration also increases, as shown in Fig. 2.1(b). As the depth of penetration increases, the laser light travelling distance increases, experiencing a larger scattering process, as shown in Fig. 2.1(b). Then, the number of photons collected back by the detector

decreases, as well as the accuracy of the measurement and the reconstructed blood flow.

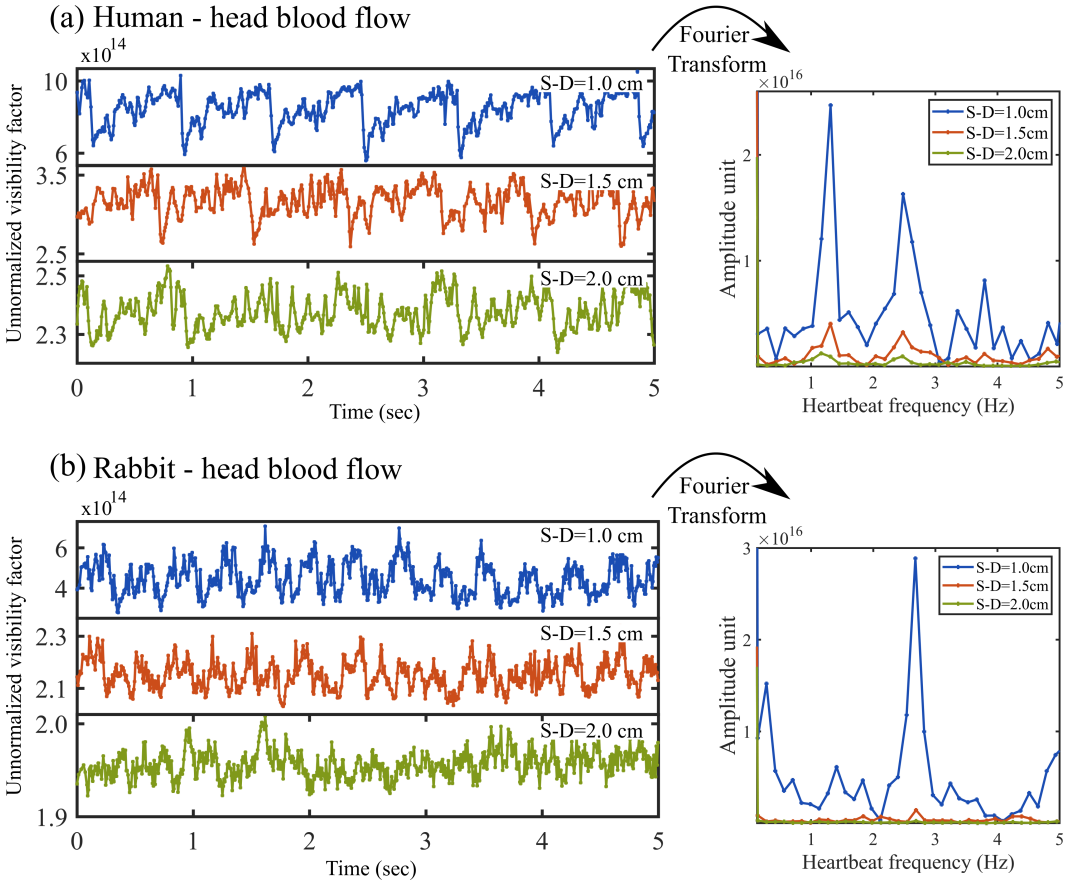


Figure 2.4: Measured blood flow at different source-to-detector (S-D) distances on (a) human head, and (b) rabbit head. As evident, the quality of reconstruction of the blood flow dynamics decreases as the S-D distance increases, both for human and rabbit.

By increasing the S-D distance and measuring the quality of reconstruction of the blood flow, one should observe a double decay curve. This double decay curve arises due to the presence of various head components, namely the scalp+skull layer and the dura mater+brain layer. At short S-D distances, the decay curve corresponds to the absorption and scattering characteristics of the scalp+skull components. Subsequently, as the S-D distance extends further, a different decay curve emerges when the brain component is probed. This differentiation is attributed to the differing optical properties, i.e., absorption and scattering coefficients, between the dura mater+brain and scalp+skull components [10, 2], leading to the observation of a double decay curve.

It is important to note that this phenomenon primarily impacts the quality of blood flow reconstruction I_{freqHR}, and not the frequency freqHR or the pulsation of the blood flow, as both the scalp+skull and dura mater+brain components of the head respond to the same cardiac pulse. Another potential reason for observing the double decay curve lies in the variation of capillary beds between the scalp+skull and dura mater+brain layers of the head.

By measuring the threshold point between the two decay slopes, one can infer the S-D distance at which the iSVS system starts measuring CBF. To verify our hypothesis, we performed experiments on human heads, rabbit heads, and simplistic phantoms composed of a moving liquid, as shown in Fig. 2.5. Both humans and rabbits have a similar head structure that can be modeled as a two-layer phantom with a scalp+skull layer and a dura mater+brain layer. However, the human head is larger than the rabbit head. Thus, the depth of penetration needed to reach the dura mater+brain layer is longer with humans than for rabbits. Our phantom comprised of a liquid mixture in a plastic cup, placed on an orbital shaker rotating at a 60 rotations per minute speed, see the original paper's appendix for more details.

The results are shown in Fig. 2.5 for (a) human head, (b) rabbit head, and (c) liquid mixture phantom. For each subject, the S-D distance was varied in the range 0.5-3.2 cm with a 0.1 cm increment. At each S-D distance, the blood flow of the subject was measured for a period of eight seconds. Then, the amplitude I_{freqHR} and frequency freqHR were calculated. For each S-D distance, the results were averaged over five different realizations. The error-bars in Fig. 2.5 correspond to the standard-deviation of the results from the five different realizations. Approximately, each realization took about 20 sec to be recorded and saved. The recording time for a full scan (e.g., Fig. 2.5(a)) was about 30 min. During this time, the subject was laying down on a massage table and was asked to relax, meditate, and to not move their head. For the rabbit experiments, the rabbit was put under anesthesia.

As shown in Fig. 2.5, left column, I_{freqHR} follows a double decay slope for both human and rabbit, while it follows a single decay slope for the phantom. We define the slope of the first decay curve as a_1 and the slope of the second decay curve as a_2. As evident, both for human and rabbit, the first decay rate is higher than the second decay rate, $a_1 \gg a_2$. This can be interpreted in two ways. One is that the iSVS system experiences more optical loss from the scalp+skull layer than with the dura mater+brain layer as the S-D distance is increasing (fewer photons are captured). Another would be that the brain blood flow is higher, creating more fluctuations in

the blood flow measurements, such that the decay of the amplitude of fluctuation slows down after reaching the brain.

Contrasting these results, the phantom experiment (Fig. 2.5(c)), which involves diluted resin in water, shows a single decay corresponding to the presence of a single liquid layer. In this scenario, there are no complex tissue layers with varying optical properties, and thus, the decay of I_{freqHR} follows a single decay.

The corresponding heart rate frequencies freqHR are shown in the right column of Fig. 2.5. For the human, the frequency fluctuates around 1.2 Hz over the span of the scan (30 min period), corresponding to a normal heart rate for a resting/meditating human. For the rabbit head, due to the anesthesia, the frequency is very stable over the 30 minutes scan, at around 2.7 Hz, except for a few data points when the rabbit temporarily awoke. Due to the limited time window from the anesthesia, the maximal S-D distance for the rabbit study that we were able to measure was 2.8 cm.

For the phantom, the frequency freqHR is 1 Hz for all S-D distances until 2.6 cm. For S-D distances above 2.6 cm, the measured flow suffers from noise to produce good reconstruction results. This indicates that the S-D distance of 2.6 cm for the phantom corresponds to the maximal range of flow measurement for our 785 nm iSVS system. Similarly, we measured the maximal S-D distance at which blood flow can be reconstructed to be 2.8-3.0 cm for human studies and 2.5-2.8 cm for rabbit studies at the 785 nm iSVS system. The difference between human and rabbit is because the rabbit head is smaller than human, so the brain layer is attained at a shorter S-D distance for rabbits.

These results support our hypothesis that by tuning the S-D distance across a scanning line, it is then possible to measure the source-to-detector threshold distance (S-D_{th}) at which a brain signal can be detected. For example, in Fig. 2.5(a) S-D_{th}=1.6 cm and in Fig. 2.5(b) S-D_{th}=1.3 cm. The results in Figs. 2.4 and 2.5 were recorded from subject Human1 and Rabbit1.

Next, we repeated the experiments at N different locations on the heads of subjects Human1, Human2, and Human3, and subjects Rabbit1 and Rabbit2. The skin-to-brain depth varies across different regions of the human head, directly affecting the measured S-D_{th}. For those reasons, we measured the skin-to-brain depth (via MRI/X-ray scans) and S-D_{th} (via iSVS measurements) separately at N different regions of the head for each subject. The statistics were grouped for each subject and presented in Fig. 2.6(a) for the skin-to-brain depth, and in Fig. 2.6(b) for the

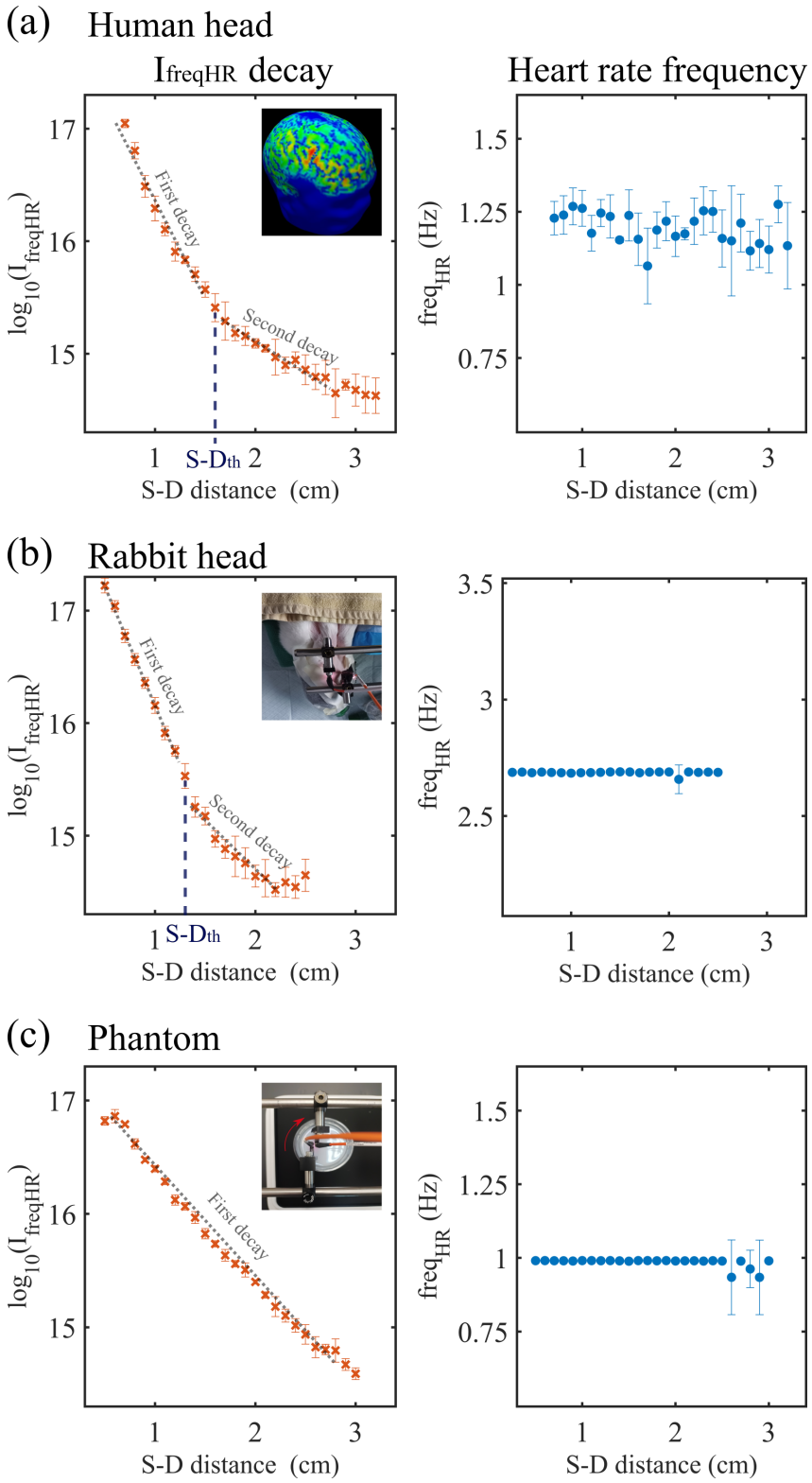


Figure 2.5: Investigating the threshold Source-to-Detector (S-D) distance at which the iSVS system starts to reach the brain component of the subject. (a) Human head, (b) rabbit head, and (c) phantom. In (a) and (b), there is a double decay. The first decay, with slope rate a_1, corresponds to the scalp+skull layer, and the second decay with a slope rate a_2 to the dura mater+brain layer. For the phantom (diluted resin in water) in (c), there is a single decay corresponding to the single liquid layer.

S-D_{th}.

For example, $N = 9$ different measurements were done for Human1, and the results were grouped and presented by showing the mean, the maximum, the minimum, the quartile1, and the quartile3, Fig. 2.6. The grouping of the measurements gives an overall estimation of the skin-to-brain distance of each subject. Such overall estimation helps in comparing the skin-to-brain distances measured from MRI scans for humans (or X-ray scans for rabbits) with the measured S-D_{th}. The MRI scans of the head of the human subjects were done at the Caltech Brain Imaging Center, and the X-rays of the head of the rabbits were done at the Caltech Animal Facility Center. The results are presented in Fig. 2.6.

Figure 2.6(a) shows the averaged skin-to-brain depth z of each subject, measured from the MRI and X-ray scans. Figure 2.6(b) shows the measured threshold S-D_{th} distance from the iSVS blood flow measurements (as in Fig. 2.5). As shown, the skin-to-brain depths estimated from the MRI and X-ray scans agree with the iSVS S-D_{th} distances, where the S-D_{th} distances for humans are larger than for rabbits. In addition, the MRI results show that the skin-to-brain depth of Human3 is slightly larger than Human1 and Human2, Fig. 2.6(a), which was also observed in Fig. 2.6(b).

Figures 2.6(c) and 2.6(d) show the first a_1 and the second a_2 decay coefficients for each subject. As evident, human and rabbit subjects exhibit similar decay coefficients. The absolute value of the first decay coefficient is larger than that of the second, indicating that the iSVS system suffers from more loss from the scalp+skull layer than from the dura mater+brain layer. This can be explained by the fact that increasing the S-D separation distance increases the depth of penetration until the brain component is attained. Then, further increase will not increase the depth of penetration by much but will rather increase the ratio of light attaining the brain component, as predicted by the numerical simulations.

Insights and discussions

The relationship between the threshold distance S-D_{th} and skin-to-brain depth appears to be nonlinear. At short skin-to-brain depths ($z < 1$ cm), as for rabbits, the ratio S-D_{th}/z is around 2, indicating that an S-D_{th} distance of twice the skin-to-brain depth is required to reach the brain component. At longer skin-to-brain depths ($z > 1$ cm), as for humans, the ratio S-D_{th}/z approaches 1.

These results are in line with prior research on depth sensitivity and source-to-

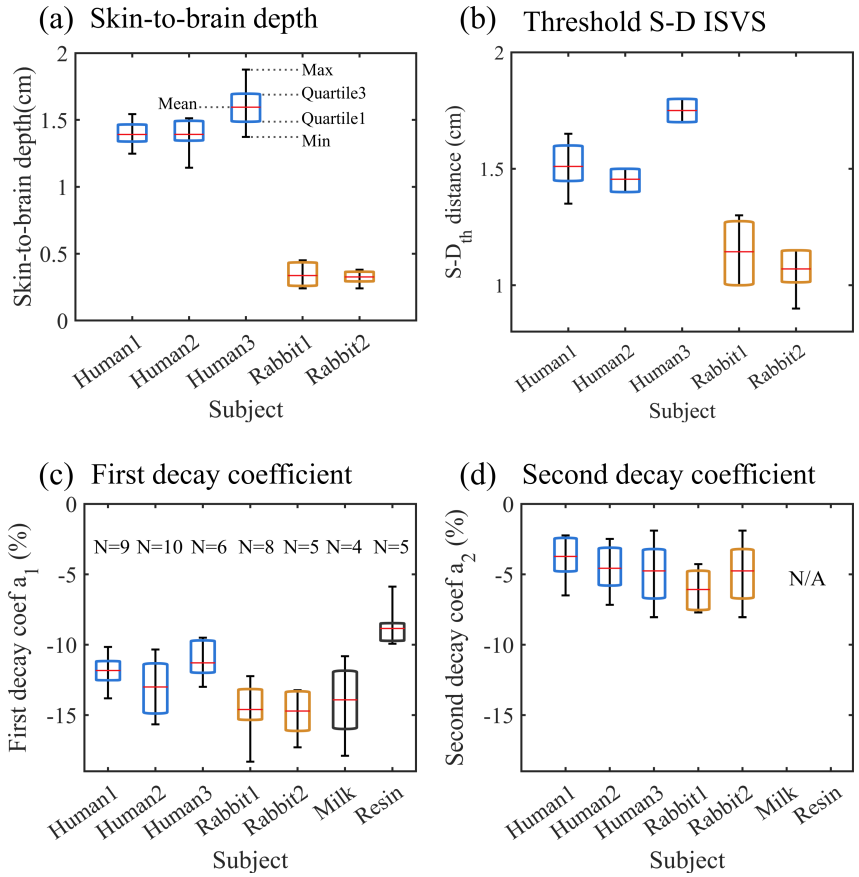


Figure 2.6: (a) and (b) Estimating the threshold S-D distance at which the iSVS system starts to reach the brain aspect of the subjects. (c) and (d) Estimating the two scattering decay slope rates a_1 and a_2, corresponding to the two different components of the head of the subjects, such as the scalp+skull layer and the dura mater+brain layer.

detector separation in near-infrared spectroscopy (NIRS) for humans, where a "banana" spatial sensitivity profile is usually observed. As the S-D distance increases, the "banana" extends deeper into the brain, with deeper brain regions being more challenging to access. The sensitivity was observed to decrease exponentially with the depth of penetration, and there exists a trade-off between greater sensitivity to deeper layers of the brain and signal-to-noise ratio (SNR).

Typically, a substantial gain in brain signal sensitivity can be observed while increasing short source-to-detector distances (S-D < 2.5 cm). However, as the S-D distance extends beyond 2.5 cm, the gains in sensitivity become progressively smaller, ultimately peaking at S-D > 3.5 cm. Beyond this point, further increasing the S-D distance yields diminishing returns in sensitivity to brain function. These findings

underscore the importance of carefully selecting the source-to-detector distance.

As an example, CBF can be modulated through specific brain activation tasks like finger tapping, which induces changes in CBF that can be detected from the motor cortex. Investigating CBF changes during finger tapping using iSVS to measure brain activation tasks holds significant potential, offering new parameters and metrics for functional brain research [11, 12]. It can complement functional MRI, which is often costly and time-consuming, and may help traumatic brain injury detection, diagnosis, and recovery.

However, it is crucial to select the appropriate source-to-detector distance to ensure precise CBF detection. The results presented here offer valuable insights, allowing researchers to make informed decisions regarding the appropriate source-to-detector and to enhance the precision of CBF measurements during brain activation tasks.

Limitations and future work

We investigated the depth-sensitivity of laser interferometry speckle visibility spectroscopy (iSVS) by varying the source-to-detector distance to tune the laser light's penetration depth into the head. This allowed us to identify the transition point at which cerebral blood flow (CBF) in humans and rabbits begins to be detected. A phantom experiment confirmed these findings. We also compared the skin-to-brain depth results measured by the iSVS system with those obtained from MRI and X-ray scans for both humans and rabbits. We observed good agreement, with the skin-to-brain depths estimated from imaging scans aligning with the measured iSVS S-D_{th} distances. A key finding was the nonlinear relationship between S-D_{th} and skin-to-brain depth, differing between short ($z < 1$ cm) and long ($z > 1$ cm) skin-to-brain depths.

By leveraging the depth-sensitivity of iSVS, we can pinpoint the transition point for CBF detectability in humans. This method holds significant promise as an assistive tool for craniotomy surgeries, potentially enhancing their precision and safety through continuous, non-invasive monitoring of CBF dynamics [13, 14]. Such monitoring could be particularly valuable for patients undergoing reconstructive skull surgery, where polymeric skull material acoustic windows are used. Post-craniotomy, iSVS could be employed to scan and compare CBF on the operated side with the intact side, providing medical teams with essential follow-up information to optimize patient outcomes [15].

In this work, we primarily characterized the quality of blood flow signal reconstruc-

tion using the amplitude of the heart rate Fourier peak (I_{freqHR}) in the visibility spectrum, effectively treating it as a proxy for signal-to-noise ratio. We did not explore the more direct Blood Flow Index (BFI) to quantify blood flow. Furthermore, our current experimental setup did not provide the ability to actively modulate blood flow or introduce controlled, observable deltas in blood flow during the measurement process. These inherent limitations in our current approach have motivated the design of a new sensitivity measurement scheme, which will be the subject of the next section and a subsequent follow-up work.

2.3 Superficial temporal artery occlusion: a new approach to SCOS sensitivity

This section is adapted from published work: Huang YX, Mahler S, Dickson M, Abedi A, Lo YT, Lyden PD, Russin J, Liu C, Yang C. Assessing human scalp and brain blood flow sensitivities via superficial temporal artery occlusion using speckle contrast optical spectroscopy. APL Bioengineering. 2025 Oct;9(4):046106.

In the preceding section, our investigation into the depth-sensitivity of iSVS relied primarily on passively observing the strength of the heart rate Fourier peak (I_{freqHR}) as a qualitative indicator of blood flow signal reconstruction quality. While this approach allowed us to identify critical source-to-detector distances and understand the structural influences on light penetration, it inherently limited our ability to precisely quantify blood flow changes or actively perturb the system to directly assess sensitivity. Specifically, we noted that our previous method did not explore the direct Blood Flow Index (BFI) and lacked the ability to modify blood flow or introduce observable deltas during measurement, limiting a comprehensive understanding of absolute sensitivity.

To overcome these limitations and move towards a more robust and quantitative understanding of optical brain sensing, the subsequent work detailed in this section and the attached paper introduces significant advancements aimed at not only quantifying the sensitivity of speckle contrast optical spectroscopy (SCOS) but also validating the differential sensitivity of cerebral blood flow (CBF) versus cerebral blood volume (CBV) measurements experimentally. This is achieved through two key innovations:

1. *Direct measurement of relative CBV and CBF:* Moving beyond pure oscillation signal strength, our new methodology directly extracts both CBV and CBF metrics. This provides a more comprehensive and physiologically relevant

characterization of hemodynamic changes crucial for understanding brain health.

2. *Inducing controlled changes in scalp blood flow with compression:* To experimentally validate and quantify the sensitivity of our measurements, we incorporated a method to actively induce observable changes in superficial (scalp) blood flow through controlled compression of the superficial temporal artery (STA). This allows for a direct assessment of how well our system differentiates between superficial and deeper cerebral signals.

These two innovations collectively enable us to move beyond passive observation, facilitating a more precise quantification of SCOS sensitivity to various tissue layers.

Why STA occlusion?

Monitoring cerebral blood flow dynamics is crucial for understanding brain health, diagnosing neurological conditions such as stroke and structural brain injury, and developing effective treatments [16, 17, 18]. While spatial imaging of the brain has significantly advanced in the last decades with modalities such as magnetic resonance imaging (MRI) [19], computed tomography (CT) [20], and X-rays [21], providing high-resolution images of the brain, temporal imaging—particularly for measuring cerebral blood dynamics—remains challenging with these high spatial resolution modalities [22].

To effectively monitor cerebral blood flow dynamics, a temporal resolution of 20 Hz or higher is desirable. This estimation is based on the typical resting heart rate in adults, which ranges between 50 and 100 beats per minute (bpm) [23]. Considering a nominal heart rate of 60 bpm (1 Hz), the cardiac cycle would include temporal features that we would like to sample at 20 Hz or higher to resolve these temporal fluctuations in blood flow with sufficient fidelity.

For monitoring cerebral blood dynamics, optical transcranial measurement modalities offer compelling advantages: non-ionizing radiation, cost-effective equipment, and ease of use. Speckle contrast optical spectroscopy (SCOS) [24, 25, 26, 27, 28, 29, 30] (also named speckle visibility spectroscopy (SVS) [31, 1, 32]) can measure brain blood characteristics, such as cerebral blood volume (CBV) through optical signal attenuation, and cerebral blood flow (CBF), with high temporal resolution (40-100 Hz). SCOS measures cerebral blood dynamics using affordable consumer cameras [33, 25] by capturing fluctuating speckle patterns, and unlike TCD, it is

sensitive to all blood cell movements, allowing the quantification of microvascular hemodynamics [29].

Despite its significant potential, demonstrating that SCOS and other optical imaging techniques can effectively probe brain signals over confounding scalp and skull layers, and quantifying this sensitivity experimentally, has been an unresolved matter. While numerous numerical studies have assessed the depth sensitivity of optical methods [6, 10, 5], experimental validation of the depth sensitivity, particularly with active manipulation, has been limited.

To address this gap, this work presents experimental investigations to simultaneously monitor blood flows in the scalp, skull/meninges, and brain, with the goal of evaluating the influence of scalp and skull layers on brain blood dynamics measurements for optical techniques. For this purpose, we developed a seven-channel cerebral blood flow and volume monitoring SCOS system. Each detecting channel was strategically positioned at distinct distances relative to the laser source, enabling selective measurement of scalp or brain blood flow. To isolate scalp blood flow from brain blood flow, we performed temporary occlusion on the superficial temporal artery (STA), which supplies blood to the scalp and skull layers but not the brain. Our results demonstrate that channels primarily measuring scalp flow exhibited significant decreases in blood flow during the temporal occlusion, whereas channels with higher brain specificity exhibited minimal decreases. We also compared experimentally the difference in sensitivity between flow and volume measurements.

Importantly, while there has been some recent progress [27, 34, 11, 35], speckle imaging modalities remain limited in their ability to provide accurate absolute CBF quantification, including SCOS systems. Accordingly, this study does not aim to validate absolute CBF values but rather demonstrates relative depth sensitivity under a controlled perturbation of temporal occlusion. Its results serve as a foundational step toward future validation studies where gold-standard techniques such as TCD or MRI perfusion could provide cross-validation.

Several previous studies have investigated the differential sensitivity of optical techniques to scalp and brain hemodynamics using methods such as scalp compression (e.g., with a tourniquet) [36, 37, 38, 39], systemic physiological modulation (e.g., breath-holding, hypercapnia) [36, 39, 40], carotid compression [41], or time-domain approaches (e.g., time gating in DCS or NIRS) [38, 39, 42]. While these works provide valuable insights into scalp and brain sensitivities, they are typically limited by the use of only two or three S-D distances, rely on systemic or less repeatable

manipulations across subjects, or involve techniques that can be uncomfortable and potentially unsafe. In contrast, our study introduces a safe and repeatable method based on temporal artery occlusion, which allows for localized suppression of scalp blood flow without affecting cerebral perfusion. Combined with the simultaneous measurements at seven S-D separations, this approach enables the first quantitative experimental assessment of how scalp and brain signal contributions vary with depth in SCOS-based CBF measurements, and more broadly in optical measurements. This work also provides crucial insights into the optimal device S-D distance configuration for preferentially probing brain signal over scalp signal, with a practical and subject-friendly alternative for evaluating depth sensitivity and complements more advanced, hardware-intensive strategies such as time-domain gating.

Occlusion results

To investigate the effects of superficial temporal artery occlusion on scalp and brain blood flow, we developed a seven-channel SCOS system (Fig. 2.7) to simultaneously monitor blood dynamics in the scalp, skull, and brain, assessing the influence of superficial layers on cerebral measurements. The device features a 3D-printed head mount designed for secure placement over the frontal temporal region, see Fig. 2.7A, targeting the superficial temporal artery. It incorporates a single illumination fiber shining laser light at 830 nm and seven 600 µm core diameter detection fibers positioned at varying source-detector (S–D) distances to capture blood flow dynamics across layers, Fig. 2.7B. The detecting fibers are bundled and imaged onto a scientific CMOS camera for simultaneous signal acquisition. The laser intensity adheres to American National Standards Institute (ANSI) safety limit for skin exposure to an 830 nm laser beam (3.63 mW/mm^2) [3]. The mount's design accommodates head curvature, minimizing movement artifacts. Velcro straps secure the device without restricting scalp blood flow. Temporal artery occlusion was performed by gently applying pressure near the ear bone, isolating scalp blood flow while preserving cerebral circulation, providing a minimally invasive and repeatable method for all subjects.

In this work, cerebral blood flow (CBF) was measured using the blood flow index (BFI) defined in Eqs. (2.6) and (2.7), while cerebral blood volume (CBV) was measured using the blood volume index (BVI) in Eq. (2.8). About 11 out of 20 subjects exhibited detectable pulsatile CBF and CBV signals across all seven S–D channels. The remaining subjects showed reliable signals in up to five channels. A summary of the SNR (in decibels) for each subject and channel is provided in the

original paper's supplemental Fig. S8.

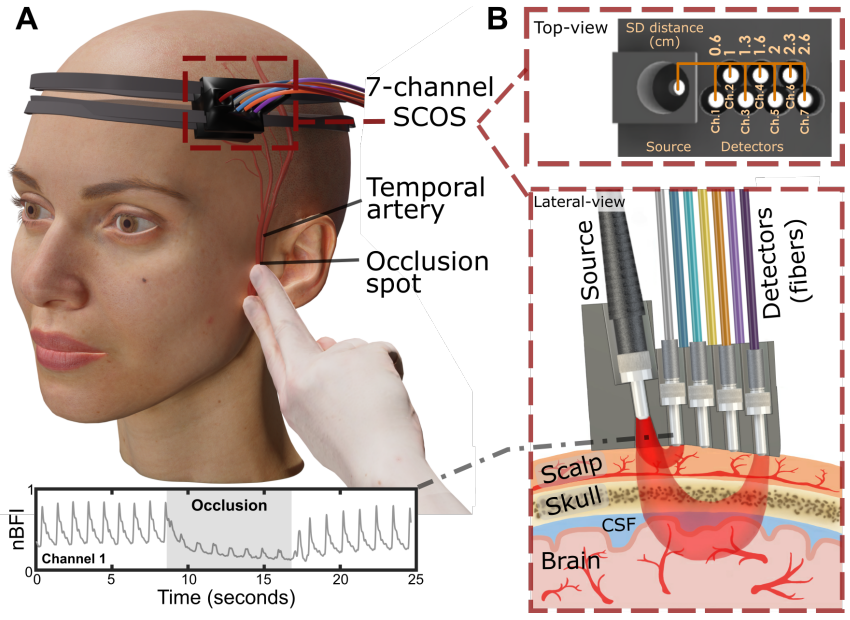


Figure 2.7: Experimental arrangement of the SCOS system for measuring cerebral blood dynamics during superficial temporal artery (STA) occlusion. (A) 3D visualization of the SCOS device positioned over the temple region and the occlusion site near the ear bone. (B) Top and lateral views of the device, illustrating different detecting channels for sensing the scalp, skull, and brain layers.

In Fig. 2.7, we present a typical CBF time trace from Channel 1 (S–DCh1 = 0.6 cm) with the superficial temporal artery occluded between the 8th and 16th seconds. In all our results, the CBF time traces are presented in blood flow index units, and the CBV time traces in blood volume index units, both of which were normalized to display relative changes. As shown in Fig. 2.7A, the significant dip in the CBF signal during the occlusion period indicated a substantial reduction in scalp blood flow.

The different channels in Fig. 2.7B are located at different S–D distance, i.e., at different distances between the illumination point on the head (source) and the detection point (detector) where the scattered light is collected back. As shown in Fig. 2.7B, this dip should become less pronounced with increasing channel numbers and corresponding S–D distances due to decreasing sensitivity to scalp blood flow. The depth of light penetration into the head correlates with the S–D distance, with channels at larger S–D distances probing deeper structures [32, 6]. Based on numerical studies [43, 6, 10, 5] and prior experimental work with interferometric SCOS [44], we anticipate Channel 1 (S–DCh1 = 0.6 cm) to primarily probe scalp

blood flow, Channels 2 (S–DCh2 = 1.0 cm) and 3 (S–DCh3 = 1.3 cm) to primarily probe scalp and skull blood flow, Channel 4 (S–DCh4 = 1.6 cm) to probe scalp, skull, and some brain blood flow, and substantial gains in brain signal sensitivity from Channels 5 to 7 (2.0, 2.3, and 2.6 cm). See the Materials and Methods section for details on the rationale behind selecting seven detection channels and specific S–D distances. We also tested different occlusion durations from 5 to 30 seconds and determined that 8 seconds was the optimal window for scalp blood flow suppression, see the Materials and Methods section for more details.

Figure 2.8 displays the blood flow results from the seven channels, with Channel 1 (0.6 cm) at the top and Channel 7 (2.6 cm) at the bottom of the figure. Figure 2.8A shows the results when a temporal occlusion was applied between the 8th and 16th seconds as in Fig. 2.8A, while Figure 2.8B shows the control results, where a non-occlusive press on the ear was performed during the same time frame. This mimicked the movement induced by the occlusion press, ensuring that the observed results were not attributed to motion artifacts. The recordings of Figs. 2.8A and B were conducted less than 5 minutes apart.

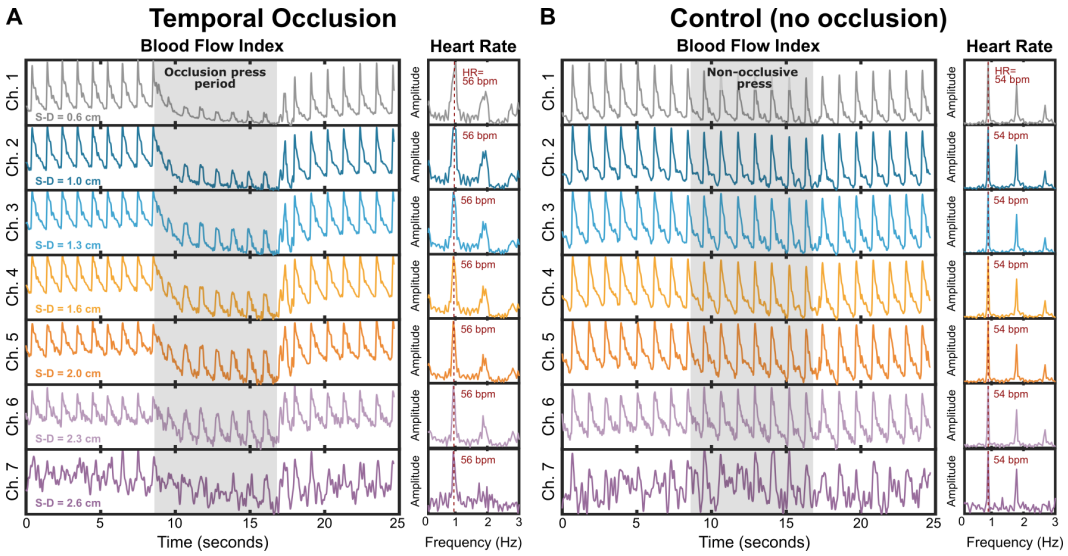


Figure 2.8: Typical cerebral blood flow (CBF) time traces during superficial temporal artery occlusion and non-occlusive pressure. (A) CBF traces from the seven channels during superficial temporal artery occlusion (8th–16th seconds). Channels targeting the scalp show a significant dip in blood flow, while brain-targeting channels exhibit a smaller change. (B) CBF traces under non-occlusive pressure applied to the ear instead of the superficial temporal artery. No significant differences in blood flow dynamics are observed across channels, confirming the specificity of the superficial temporal artery occlusion in blocking scalp blood flow.

As shown, the seven channels were synchronized for both cases, as expected since all channels are detected by the same camera, exhibiting identical oscillation frequencies corresponding to the heart rate and cardiac cycle. The heart rate was determined from the frequency graphs (right panels), obtained by applying a Fourier transform to the CBF time traces [26, 45, 32]. Note that the frequency graphs in Fig. 2.8A exhibit a broader heart rate peak than those in Fig. 2.8B due to the change of blood flow waveforms during temporal occlusion. A significant dip in the blood flow can be observed during the occlusive press, while there was no change in the blood flow time trace during the non-occlusive press. This validates the effectiveness of the occlusive press in reducing blood flow.

As the channel number and corresponding S–D distance increased, the dip in blood flow during the occlusion became progressively smaller, Fig. 2.8A. Additionally, the amplitude of the cardiac waveforms significantly decreased during the occlusion period for Channel 1 (0.6 cm) and increased back to baseline with greater S–D distances. By Channel 7 (2.6 cm), the dip and change in waveform during occlusion were nearly absent. Despite this, the heart rate frequency graph indicates that Channel 7 was still able to capture accurate CBF signals. We quantitatively evaluated signal fidelity across S–D distances by computing the frequency-domain signal-to-noise ratio (SNR) of the BFI time series, assessing the depth-dependent trade-off between signal strength and noise across all subjects, see original paper's supplemental Section S7. See original paper's supplemental Fig. S11 for typical changes of BVI during STA occlusion.

These findings demonstrate that the blood flow time trace of Channel 1 was heavily influenced by the temporal occlusion, with its impact diminished as the S–D distance increased. This aligns with our expectation that the dip becomes less pronounced with increasing channel numbers, reflecting reduced sensitivity to scalp blood flow. In Fig. 2.8B, no changes were observed in the blood flow time traces during the non-occlusive press, and all channels exhibited the same heart rate. These indicate that the motion artifacts induced by the non-occlusive press had no effect on the recorded CBF. This also indicates that blood flow from the scalp and brain layers cannot be directly distinguished without an intervention specifically targeting one of the two layers.

Next, we repeated the measurement of Fig. 2.8 across 20 subjects and quantified the extent of signal reduction during temporal occlusion for each channel (Fig. 2.9). See the Materials and Methods section for details about the subject cohort and study

protocol. First, the blood flow signal was segmented into three periods (a, b, and c), Fig. 2.9A:

- Pre-occlusion: Segment from the start to the 8th second.
- During occlusion: Segment from the 8th to the 16th second.
- Post-occlusion: Segment from the 16th second to the end.

For each segment, we calculated the mean value $\langle \text{nBFI} \rangle$ and the standard deviation σ of the normalized blood flow index (nBFI). See Eq. 2.7 for the definition of nBFI. Figure 2.9B shows the mean ratio of the post-occlusion to pre-occlusion segment $\langle \text{nBFI}_c \rangle / \langle \text{nBFI}_a \rangle$ (amber curve with diamonds) and the mean ratio of the during-occlusion to pre-occlusion segment $\langle \text{nBFI}_b \rangle / \langle \text{nBFI}_a \rangle$ (blue curve with crosses) as a function of the S–D distance for each of the seven channels across the 20 subjects. The dashed lines represent the results from the control case (i.e., non-occlusive press). The gray solid line represents a ratio of one. Error bars indicate the statistical standard deviation across the 20 subjects.

As shown in Fig. 2.9B, the mean ratio for the post-occlusion to pre-occlusion is similar to the ratios observed in the control case, i.e., approximately one, suggesting little to no change in CBF and overall blood flow index before and after the occlusion. However, the mean ratio for the during-occlusion to pre-occlusion segment is significantly lower at an S–D distance of 0.6 cm, around 0.65, and increases back to 1 with increasing S–D distance. At an S–D distance of approximately 2 cm, the mean ratio converges to the control case, indicating that an S–D distance of at least 2.0 cm is necessary to minimize the influence of scalp blood flow. See original paper's supplemental (Fig. S5) for individual mean ratio graphs for each of the 20 subjects. Note that the blood flow data showed in Figs. 2.8A, 2.8, 2.9A, and 2.10A corresponds to Subject #4 in original paper's supplemental Fig. S5.

Figure 2.9C displays the standard deviation ratios. For Channels 6 (2.3 cm) and 7 (2.6 cm), the results are faded out due to insufficient SNR in some subjects, as reflected by the large error bars. The standard deviation ratio for the post-occlusion to pre-occlusion segments remains constant and approaches the control case, similar to the behavior shown in Fig. 2.9B. In contrast, the ratio for the during-occlusion to pre-occlusion segment starts around 0.7 and gradually approaches the control case as the S–D distance increases. The convergence occurs at an S–D distance of approximately 1.3 cm, notably earlier than the S–D distance of 2.0 cm in Fig. 2.9B.

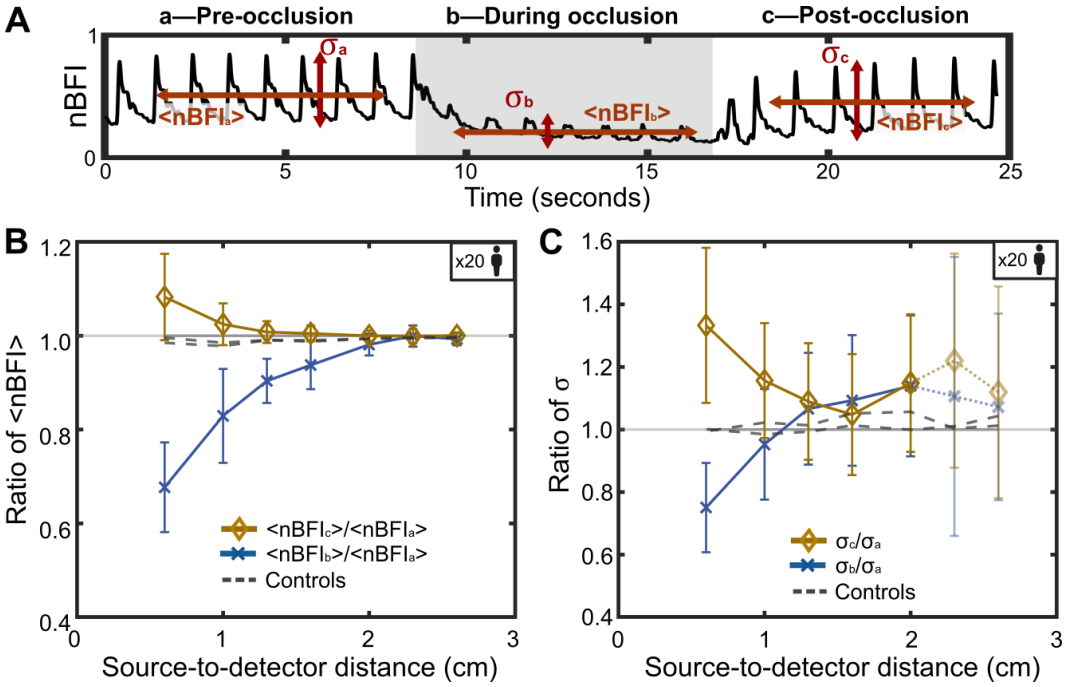


Figure 2.9: Effects of the superficial temporal artery occlusion on the scalp, skull, and brain blood flows measured from 20 subjects. (A) Segmentation of the blood flow time trace into three sections: pre-occlusion, during occlusion, and post-occlusion. Quantification of the normalized blood flow index mean ⟨nBFI⟩ and blood flow standard deviation σ. (B) Average ratio of the blood flow mean among the three sections of A. (C) Average ratio of the blood flow standard deviation among the three sections of A.

We attribute this difference to the fact that Fig. 2.9B and 2.9C quantify different metrics.

Figure 2.9B illustrates the mean value of the nBFI, Eq. 2.7, averaged over the 20 subjects, which quantifies the average blood flow level during each segmented period. This accounts for mean blood circulation over a segmented time period of 8 seconds, encompassing multiple cardiac cycles. During an occlusion, the total amount of flowing blood decreases in the scalp, resulting in a corresponding reduction in the mean nBFI. Channels with shorter S–D distances exhibited a larger decrease in ⟨nBFI⟩ during an occlusion, while channels with longer S–D distances exhibited a smaller decrease due to their lower sensitivity in scalp blood flow. Note that even at very large S–D distances (e.g., greater than 2.6 cm), light would still pass through the scalp and skull layers (Fig. 2.8B). Consequently, a small dip in the CBF signal was expected during an occlusion, showing up as a slightly reduced ⟨nBFI⟩. This explains why the ratio of mean nBFI during to pre-occlusion

($\langle \text{nBFI}_b \rangle / \langle \text{nBFI}_a \rangle$) in Fig. 2.9B remained slightly below one, even at larger S–D distances, as the occlusion always impacts the overall CBF value.

Notably, the ratio of $\langle \text{nBFI} \rangle$ post- to pre-occlusion ($\langle \text{nBFI}_c \rangle / \langle \text{nBFI}_a \rangle$) exceeded one at short S–D distances due to the sharp increase in blood flow after the occlusion is released. This sharp rise occurred because the blockage temporarily restricted blood, and when released, blood flow surged to levels higher than pre-occlusion in some subjects. As the S–D distance increased, the ratio of $\langle \text{nBFI} \rangle$ post- to pre-occlusion gradually converged to one, due to lower sensitivity in scalp blood flow. For control cases (e.g., Fig. 2.8B), the ratio of $\langle \text{nBFI} \rangle$ remained consistently around one, as there was no significant change in the CBF signal during the non-occlusive press. Thus, the ratio of $\langle \text{nBFI} \rangle$ may serve as an effective controlled experimental metric for estimating brain and scalp sensitivity of any optical transcranial devices.

Figure 2.9C illustrates the standard deviation of the nBFI, which was influenced by the amplitude of the cardiac cycle, occurring on a faster timescale—typically within a second or less. The standard deviation of nBFI primarily quantified the variation in blood flow between the peak pressure (systolic phase peak) and the lowest pressure (diastolic phase endpoint) over a series of cardiac cycles. A greater difference in blood flow during a cardiac cycle—corresponding to a higher blood pressure variation between the systolic peak and diastolic endpoint—resulted in a higher standard deviation. During an occlusion, the scalp blood flow waveform was significantly reduced due to the decreased level of blood circulation. Additionally, the repeatability of the waveform (i.e., the cardiac cycle) was markedly diminished because of the blood blockage. As a result, the difference between the systolic phase peak and the diastolic phase endpoint in scalp blood flow was observed to be smaller, leading to a reduced standard deviation of the nBFI. Channels with shorter S–D distances showed a larger decrease in standard deviation during an occlusion, again due to their high sensitivity to scalp blood flow, while channels with longer S–D distances exhibited less or no decrease due to their lower sensitivity to scalp blood flow. In this case, while the difference between the systolic phase peak and diastolic phase endpoint in scalp blood flow remained small, the corresponding difference in brain blood flow remained large, as the occlusion did not affect brain blood flow. Consequently, the cardiac cycle was dominated by brain blood flow, and the standard deviation was unaffected by the occlusion. The larger error bars observed at longer S–D distances (e.g., channels 6 and 7) are attributed to reduced SNR, as a subset of subjects exhibited measurements below the 10 dB threshold

defined in original paper's supplemental Figure S8, leading to increased variability in the group average. This variability influences the amplitude ratios and should be interpreted with caution.

The ratio of post- to pre-occlusion (σ_c/σ_a) exceeded one at short S–D distances due to the sharp increase in blood flow after the occlusion was released, with the blood flow surging at a higher peak pressure than that observed pre-occlusion. As the S–D distance increases, this ratio remained slightly above one. For control cases (Fig. 2.8B), the σ ratio remained consistently around one, as there was no significant change in the CBF signal during the non-occlusive press. Due to the differences between Fig. 2.9B and Fig. 2.9C—where Fig. 2.9B measured more the overall blood levels and Fig. 2.9C captured blood flow differences between systole and diastole—the convergence to the control case varied between the two. Specifically, the results in Fig. 2.9B converged to the control case at a larger S–D distance.

Next, we quantified the reduction in CBF and CBV waveforms during the occlusion. The results are shown in Fig. 2.10. In Fig. 2.10A, we segmented both the CBF and CBV signals into the same three segments (a, b, and c) as in Fig. 2.9A. For each segment, we calculated the average cardiac cycle waveform [25]. The results are presented in Fig. 2.10B for CBF by calculating the blood flow waveform amplitude and Fig. 2.10C for CBV by calculating the blood volume waveform amplitude. Note that Figs. 2.10A to 2.10C show the CBF and CBV data for Channel 1 (0.6 cm) of the subject featured in Fig. 2.8.

We also note that Fig. 2.9C provided an overall view of signal dynamics, while Figs. 2.10B and 2.10D highlighted morphological changes in the pulsatile waveform during occlusion. Since standard deviation is closely related to signal amplitude, similar trends were expected between Figs. 2.9C and 2.10D; however, Fig. 2.10C also captures subtle waveform alterations during occlusion, such as reduced visibility of the dicrotic notch and a slightly elevated secondary peak. To account for this variability, Fig. 2.10D focused solely on amplitude-based trends, allowing for shape-dependent waveform comparisons. A detailed analysis of these morphological changes can be found in original paper's supplemental Section S6, where waveform shapes before, during, and after occlusion were compared.

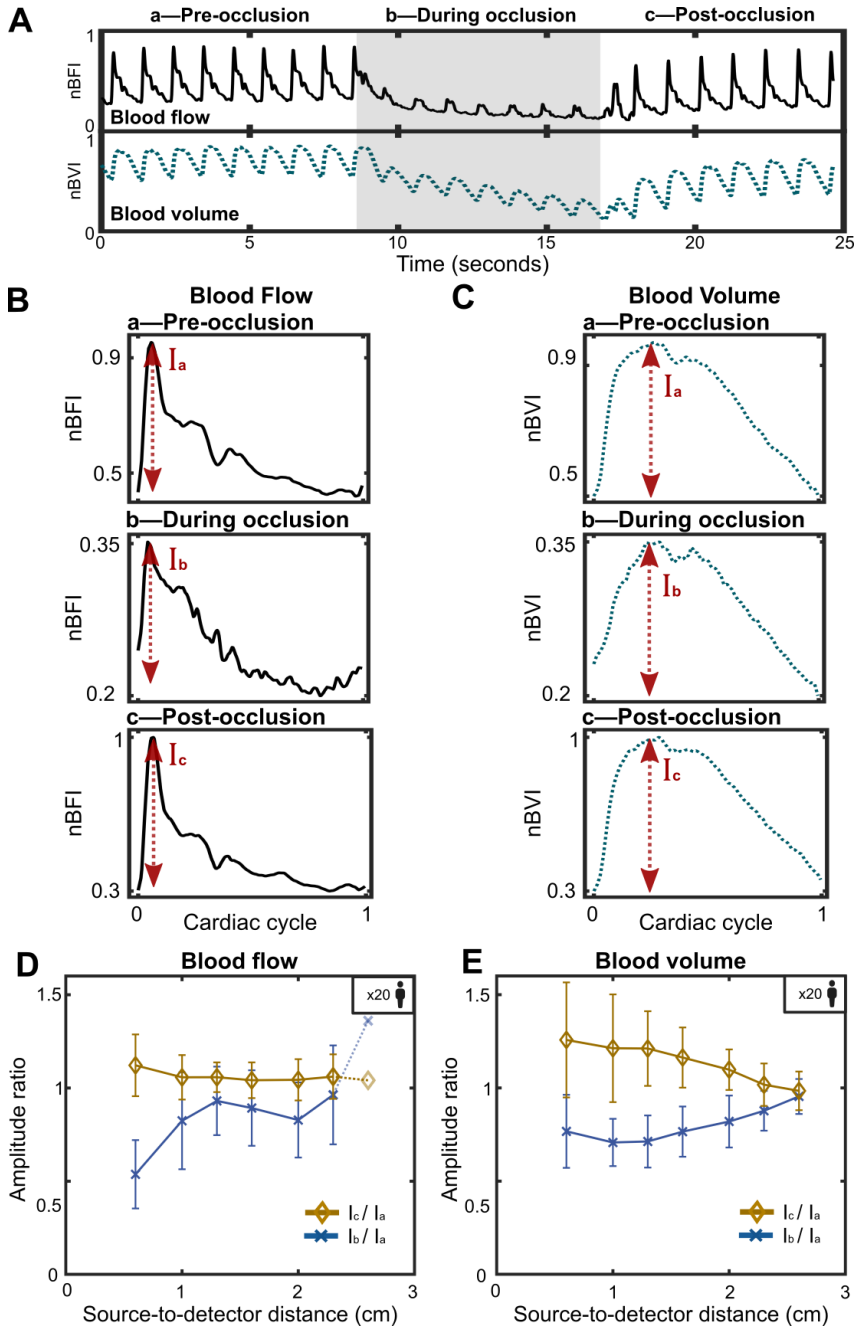


Figure 2.10: Effects of superficial temporal artery occlusion on CBF and CBV. (A) Representative time traces of Channel-1 (S-D=0.6 cm) CBF and CBV time traces during superficial temporal artery occlusion. (B) CBF and (C) CBV cardiac pulse waveforms corresponding to the segment periods defined in A. Amplitude ratio of (D) CBF and (E) CBV as a function of the source-to-detector distance. The results show that with increasing S-D distance, CBF is less influenced by the superficial temporal artery occlusion (i.e. less sensitive to scalp blood flow) compared to CBV.

As shown, the CBF waveform underwent notable changes during the occlusion, particularly in the dicrotic notch and peak pressure, while the CBV waveform remained largely unchanged. However, the overall values of the blood flow index and blood volume index significantly decreased during the occlusion period. To further characterize these changes, we calculated the peak amplitude I for both CBF and CBV in each of the three segments, Figs. 2.10B and 2.10C. The results, shown in Fig. 2.10D for CBF and Fig. 2.10E for CBV, exhibited similar trends but with differing rates of convergence. While the amplitude ratio during to pre-occlusion was less than one at shorter S–D distances, it approached a ratio of one around an S–D distance of 1.3 cm for CBF and an S–D of 2.5 cm for CBV. This disparity highlights the difference in brain sensitivity between CBF and CBV measurements in SCOS and optical systems.

This experimental result aligns with previous numerical simulation results [43, 10]. In Ref. [10], the brain-to-scalp sensitivities of optical BFI and optical absorption (as measured in BVI) were simulated using a double-layer model. Findings shown in Fig. 1 of [10], demonstrated that BFI is intrinsically more brain-specific than absorption (BVI), achieving higher brain-to-scalp sensitivity at a given S–D separation. These findings are consistent with our experimental observations in Figs. 2.10D and 2.10E, where a lower scalp sensitivity during temporal occlusion was observed at an S–D distance of 1.3 cm for CBF and at 2.5 cm for CBV. This can be attributed to the fact that blood flow in gray matter is approximately six times greater than in the scalp, whereas hemoglobin concentration—which relate to blood volume (BVI)—is only two to three times greater in gray matter compared to the scalp [46]. These results highlight the superior brain specificity of CBF measurements obtained using speckle contrast or diffuse correlation systems at similar S–D distances when compared to CBV measurements from absorption-based systems and modalities. We note that the sensitivity simulation in Ref. [10] was conducted using DCS and NIRS. Prior studies have demonstrated that SCOS and DCS differ in their sensitivity to cerebral dynamics, due to fundamental differences in how each technique captures flow information—SCOS through speckle contrast and DCS through autocorrelation decay. The differences have been explored in SCOS-specific simulation studies [43], which show that both sensitivity and contrast-to-noise ratio differ between SCOS and DCS as a function of exposure time and source-detector separation. Accordingly, the comparisons with Fig. 2.10D and 2.10E are intended to be qualitative, highlighting the general trend in how volume and flow signals evolve with increasing S–D separation with the superiority of flow signal's sensitivity at

similar S–D distance, and caution in making direct numerical comparisons between our SCOS data and the DCS-based simulations.

Deviations observed in Fig. 2.10D at 1.6 cm and 2.0 cm may result from subject-specific physiological variability. One likely contributor to these variations is the presence of superficial vasculature directly beneath certain measurement channels, as shown in original paper's supplemental Fig. S4. Nonetheless, these fluctuations remain within the reported error bars and do not affect the overall trend observed across separations.

We further analyzed the periodic curve patterns illustrated in Fig. 2.10B, comparing the autocorrelation of cardiac periods across blood flow data before, during, and after temporal occlusion. Despite thorough examination, no consistent changes in curve shapes were observed. This inconsistency may stem from slight variations in the cardiovascular physiological layout around the temporal region. For additional details, refer to original paper's supplemental Figs. S6 and S7, which includes an example confusion matrix and autocorrelation trends for both CBV and CBF curves.

Experimental arrangement

The experimental setup of our aggregated 7-channel SCOS device is illustrated in Fig. 2.7. Figure 2.7A presents a 3D visualization of the device positioned on a subject's head, typically placed over the frontal temporal region above the superficial temporal artery branches. Occlusion was achieved by gently applying pressure near the ear bone (Fig. 2.7A hand diagram). The lower section of Fig. 2.7A displays a representative CBF time trace from Channel-1 (the closest to the laser source), where a significant dip in the signal during the occlusion period (8 to 17 seconds) confirms a reduction in the scalp blood flow.

Figure 2.7B provides top and lateral views of the 7-channel device, highlighting the detection channels at different S–D distances designed to sense the scalp, skull, and brain layers. The device comprised one multimode optical fiber laser source and seven detection multimode fibers, all housed within a 3D-printed mount. The mount was fabricated using a resin-based printer [Anycubic Photon Mono X 6K] with black resin to enhance light absorption and minimize back reflections and stray light. Post-printing, the components were fully cured under UV light to ensure safe contact.

On one side of the mount, a 600 μm core diameter multimode fiber [Thorlabs M29L01] delivered laser light to the subject's head. The laser was a thermally

stabilized 830 nm laser [Crystalaser DL830-300-SO] with a long coherence length (>5 m), high beam quality factor (M^2<1.3), single-longitudinal mode, and built in optical isolator. Although the laser source could provide up to 300 mW, the output power was limited to 60 mW using a waveplate and a polarized beam splitter before coupling the laser light into the optical fiber (details in original paper's supplemental Fig. S1). The fiber was positioned 8 mm from the skin and was oriented with an angle of 10°from perpendicular illuminance, producing a 5 mm illumination spot diameter, similarly to [25, 26, 32, 47]. This setup ensured the laser intensity remained within the American National Standards Institute (ANSI) safety limit for skin exposure to an 830 nm laser beam (3.63 mW/mm^2) [3].

On the opposite side, seven 600 µm core diameter multimode fibers were positioned at varying S–D distances from the illumination fiber, each representing a separate SCOS channel. These fibers were in direct contact with the skin with perpendicular orientation to maximize light collection efficiency. The seven fibers were combined into a single fiber bundle using a 7-to-1 fan-out bundle fiber [Thorlabs BF76HS01]. The output of the bundled fiber was imaged onto a scientific CMOS camera [Excelitas pco.edge 5.5] featuring a 6.5 ×6.5 µm pixel size and 16-bit pixel depth dynamic range. The large dynamic range is essential for this experiment, as it allows simultaneous recording of signals with vastly different intensities—where short S–D distance channels generate high signal intensities, while long S–D distance channels produce much lower signal intensities, often approaching or falling below the dark noise level. The camera operated with an exposure time of 8 ms and was recording at 65 FPS. This setup resulted in a speckle density of 0.1 speckle per pixel, corresponding to a one-dimensional speckle-to-pixel length ratio of s/p = 3 [26, 28, 48]. The collected light from the seven detecting fibers was therefore imaged onto the camera simultaneously. To prevent cross-channel light leakage in the recorded camera image, a telescope imaging system was meticulously aligned to magnify and focus on the end plane of the fiber bundle, see original paper's supplemental Fig. S1 for details.

The bottom surface of the mount was partially angled to accommodate the curvature of the head, see original paper's supplemental Fig. S2. To minimize noise from fibers' movement, the fibers were secured to the mount using clips and glue. The mount had four slots along the sides to strap the device on the head using Velcro straps tight enough to avoid device sliding but to no restrict scalp blood flow due to the pressure of the mount onto the scalp blood vessels, which can alter our results.

For each subject, the device's location on the head was adjusted to align with the region where the superficial temporal artery spreads, ensuring that the occlusion effects were clearly observed (see original paper's supplemental Fig. S4 for more inputs). Due to the strong light attenuation caused by hair—particularly when longer than a few millimeters—which significantly reduces SCOS signal strength, we conducted imaging in hair-free regions to ensure adequate signal-to-noise ratio. While hair separators may offer partial mitigation, a reliable solution for SCOS measurements through hair has yet to be established. For some subjects, part of the device rested on areas with hair, though efforts were made to minimize this.

The device orientation and location were also adjusted until the signal intensity across of at least five channels largely exceeded the camera dark noise level. Variations in scalp and skull thickness among individuals led to differences in ideal S–D distances [44]. Some subjects displayed CBF and CBV signals across all seven channels, while others exhibited signals across five channels. No subjects exhibited signals for fewer than five channels. Once secured, a 24-second benchmark trial was conducted to confirm CBF and CBV signal quality for Channels 1 to 5 and to ensure no movement artifacts were present. The temporal occlusion and control experiments were conducted only after ensuring proper device positioning and signal quality.

CBF and CBV calculations

In this section, we briefly describe the methods for extracting CBF and CBV from speckle camera images in SCOS. The image processing methodology and related equations can be found in Ref. [26]. While this reference appropriately describes the image analysis pipeline, it does not reflect the optical and hardware setup used in this study, including the camera. Here, we employed a fiber-bundle-based SCOS system with a PCO Edge 5.5 camera, operating at a fixed gain of 1. The camera had a conversion factor (CF) of 0.46 e^-/count for a 16-bit readout mode. Consequently, the gamma unit (γ = gain/CF) remained constant at $\gamma \approx 2.17$. From the collected camera images, we segmented the camera image into seven parts, one for each channel (see original paper's supplemental Figure S3). From each channel, we calculated the raw speckle contrast K as:

$$K^2_{\text{raw}}(t) = K^2_i(I_i(t)) = \frac{\sigma^2(I_i(t))}{\mu^2(I_i(t))} \tag{2.4}$$

Where $\sigma^2(I(t))$ is the variance of the normalized image I of channel i at time t and $\mu(I(t))$ its mean. The various sources of noise were accounted as [26, 27, 49, 50]:

$$K^2_{\text{adjusted}}(t) = K^2_{\text{raw}}(t) - K^2_{\text{shot}}(t) - K^2_{\text{quant}}(t) - K^2_{\text{cam}}(t) \tag{2.5}$$

with K^2_{shot} accounting for variance contributions from the shot noise, K^2_{quant} for the variance inherited from quantization, and K^2_{cam} for the variance contributions of the camera's readout noise and dark noise. See Ref. [26] for more details about the speckle contrast calculations and calibration processes. In implementing the K^2-adjusted correction, all calibration and noise correction steps were performed in analog-to-digital units, i.e., grayscale counts. Camera readout noise was experimentally determined from the variance of dark frames, rather than relying on manufacturer specifications, to address potential CMOS degradation or inter-device variability. Shot noise, originally in electron units, is converted to analog-to-digital units using the γ scaling factor noted above. Quantization noise is minimal in our setup due to the use of 16-bit acquisition and was ignored in our measurements. These steps ensure that all noise sources are consistently expressed in the same units and appropriately scaled.

The blood flow index (BFI) was related to K^2_{adjusted} by:

$$\text{BFI}(t) = \frac{1}{K^2_{\text{adjusted}}(t)}. \tag{2.6}$$

The BFI was normalized (nBFI) from 0 to 1 as follows:

$$\text{nBFI}(t) = \frac{\text{BFI}(t) - \min(\text{BFI}(T))}{\max(\text{BFI}(T)) - \min(\text{BFI}(T))}, \tag{2.7}$$

where $\max(\text{BFI}(T))$ represents the maximal BFI value, and $\min(\text{BFI}(T))$ the minimal BFI value over the measurement period T. The measurement period T corresponds to the entire period of a measured BFI signal, i.e., 24 seconds in our case.

It is important to note that the unit definition of the BFI relies on several key assumptions: (i) the camera's exposure time is much longer than the speckle field's decorrelation time, (ii) blood cell motion from multiple scattering events is random and unordered, and (iii) the scattered light field is ergodic with minimal contribution from static scatterers [51]. Variations in scattering regimes and particle motion types can significantly influence the field correlation function $g_1(\tau)$ [52, 51, 53], complicating the direct conversion of BFI to physical units (e.g., area/time) without

further assumptions or corrections. Additionally, even with careful calibration of noise sources such as readout, shot, or quantization noise, deviations from ground-truth BFI persist, particularly when the photon count approaches the camera noise floor [35]. In this study, we employed a min-max normalized BFI (nBFI) to highlight relative changes in blood flow rather than report absolute values. In future works, we will focus on translating this metric into standard BFI units, which will require addressing challenges such as differences in scattering conditions, exposure time constraints, and partial-volume effects. Notably, we plan to use a recently reported optimization-based algorithm that adaptively refines noise calibration, mitigating CBV-mimicking artifacts by reducing CBF-CBV waveform correlation [35], enabling more accurate and robust CBF measurements, especially at large S–Ds.

The CBV was extracted from the camera images by calculating the change of blood volume index (BVI) over the baseline based on logarithmic definition derived from modified Beer-Lambert law, as defined in Ref. [27]:

$$\mathrm{BVI}(t) = \log_{10}\left(\frac{I_0}{\mu(I(t))}\right), \tag{2.8}$$

where I_0 is the intensity at baseline, calculated as the mean of the average intensity of the entire image acquired during the baseline period (first 7 seconds). The mean $\mu(I(t))$ was calculated as the average spatial intensity of the entire image I acquired at time t, and can be expressed in camera grayscale units. In cases without significant or acute volume change, the logarithmic equation shown in Eq. (2.8) can be linearly approximated, and blood volume index can be evaluated with the equation shown as [54, 25]:

$$\mathrm{BVI}(t) \approx \frac{2I_0 - \mu(I(t))}{I_0}. \tag{2.9}$$

The BVI was also normalized from 0 to 1 similarly to Eq. (2.7).

Source-to-detector distance and brain sensitivity

A main component in transcranial optical measurements of CBF and CBV is the source-to-detector (S–D) distance, defined as the distance between the illumination point on the head (source) and the detection point (detector) where the scattered light is collected back, Fig. 2.7.

As the illuminating light penetrates the scalp layer, it scatters in all directions. A portion of this scattered light penetrates deeper into the skull and brain layers. Some of the light that reaches the brain is scattered backward, traveling back through the brain, skull, and scalp layers. The detector, located at an S–D distance from the

source, collects the scattered light. During this process, only a small fraction of the injected light is collected. When the light is coherent or partially coherent, such as laser light, the multiple scattering events alter the effective optical path lengths, creating a speckle field. As the laser light interacts with dynamic elements, such as blood cells, it scatters with specific dynamics, resulting in a fluctuating speckle field. This fluctuation can be quantified using the speckle contrast metric.

The depth to which light penetrates the head is intrinsically related to the S–D distance, but the exact relationship between penetration depth and S–D distance remains unclear. While extensive numerical simulations have modeled light penetration into the head, experimental investigations in this domain are still limited. Moreover, individual variations in scalp and skull thickness at different locations on the head complicate generalization from numerical studies. These simulations can provide only a reference sensitivity calculation based on the specific physiological shape used in the models. Prior numerical studies in near-infrared spectroscopy (NIRS) revealed a characteristic banana-shaped spatial sensitivity profile [6, 5, 55, 7]. As the S–D distance increases, the 'banana' extends deeper into the head, Fig. 2.7B, although accessing deeper brain regions becomes more challenging [6].

Building on prior numerical studies and due to lower SNR with fiber-based SCOS, we designed our seven-channel SCOS system with S–D distances ranging from 0.6 cm to 2.6 cm. The specific distances for each channel were as follows: Channel 1: 0.6 cm, Channel 2: 1.0 cm, Channel 3: 1.3 cm, Channel 4: 1.6 cm, Channel 5: 2.0 cm, Channel 6: 2.3 cm, and Channel 7: 2.6 cm.

The rationale of these seven S–D distances was constrained by technical and optical limitations. To image all fibers simultaneously on the same camera sensor, we employed a fiber bundle that arranged multiple fibers in a round configuration at one end of the fiber cable. Maximizing photon count and SNR required the largest available fiber core diameter, which was 600 µm in our case for commercially available fiber bundles. We selected the 1-to-7 fiber bundle (Thorlabs BF76HS01), as it provided the best balance for spacing the fibers. To further optimize minimal spacing, we removed the protective plastic sleeve and SMA mounting ring of the fibers, which reduced the outer diameter to approximately 5 mm. As such, at most 7 fibers can be arranged next to each other in a 2 cm distance, covering S–D distances from 0.6 cm to 2.6 cm. Although larger fiber bundles (e.g., 1-to-19) exist, they could not be efficiently arranged within the required spacing constraints. Ideally, a strip camera with a 3 cm length and at least 1,000 pixels per width, to ensure a sufficient

number of independent observables (NIO) [26, 1] while minimizing normalization noise (28), would enable sampling a greater number of S–D distances. The shortest S–D distance (0.6 cm) was dictated by physical constraints, including the source fiber tip diameter (≈8 mm) and the detecting fiber diameter (≈5 mm). This also required a minimum spacing of 0.5 cm in between the detecting fibers (Fig. 2.7B). Additionally, at very short distances, high photon counts could saturate the camera sensor.

Conversely, the longest S–D distance achieved in this study (2.6 cm) was limited by the use of a 600 µm fiber-based SCOS device, where light is coupled through a fiber before being imaged onto the camera, reducing the number of detectable speckles and overall signal strength due to the limited numerical aperture of the fiber. In contrast, as demonstrated in Ref. [26], a compact SCOS configuration—where light is collected directly onto the camera placed atop the skin—offers greater light collection efficiency. This design resulted in a ∼70-fold increase in detected signal compared to the 600 µm fiber-based SCOS, along with improved stability, reproducibility, and SNR, especially at longer S–D separations. Therefore, our proposed 0.5×3 cm strip sensor, intended for use in a compact SCOS configuration, should enable extension of the maximum usable S–D distance from 2.5 cm (in this work) to as much as 5.0 cm [26]. While the exact minimum detectable photon count will depend on the specific camera model selected, the compact geometry itself will provide the optical gain necessary for higher SNR and measurements at longer S–D distances.

Discussion

We present experimental data quantifying the sensitivity of scalp and brain blood flows in SCOS as a function of source-detector (S–D) distance, alongside with a direct comparison of blood flow and blood volume sensitivities. This study employed a brief occlusion of the superficial temporal artery (STA) during CBF and CBV recordings, and showcased it as a robust method to disentangle layers of blood flow dynamics and isolate scalp-specific signals through a safe and non-invasive approach. While our temporal occlusion protocol effectively demonstrates differential scalp flow sensitivity across various S–D distances, we acknowledge the importance of a more direct brain-specific validation experiment. One approach would be to induce a purely brain-originated signal, such as through a well-defined cognitive or functional task. However, designing a robust and reproducible activation task for the temporal region presents challenges, as individuals engage with tasks

differently, leading to inconsistent hemodynamic responses. Addressing this would require refining our system and carefully designing a human study, potentially incorporating fMRI to precisely map the location and intensity of brain activation for each subject. In future work, we aim to integrate a brain-activation paradigm alongside an improved signal-to-noise ratio system, further validating our system's ability to detect cerebral hemodynamics at greater depths.

Our findings represent a significant advancement in non-invasive cerebrovascular monitoring, offering two pivotal contributions. First, we establish an experimental framework for estimating scalp and brain sensitivities in optical systems. Second, we introduce temporal artery occlusion as a simple yet effective intervention for isolating brain-specific signals from disruptive scalp blood flow dynamics. This approach has strong clinical potential, particularly in studying how headaches and migraines influence blood flow at different head layers. Understanding whether these conditions primarily affect scalp or brain circulation remains an open question in the field. Additionally, future studies should investigate the applicability of this method in populations with impaired vascular autoregulation, such as stroke or brain injury patients, where altered physiological responses may impact the reliability of occlusion-based assessments. Our results, derived from a cohort of 20 subjects, demonstrate that CBF exhibits relatively low sensitivity to scalp blood dynamics at S–D distances greater than 1.5 cm, while CBV requires a significantly larger S–D distance of 2.5 cm to achieve the same sensitivity, in agreement with prior numerical studies [10, 46]. This finding underscores the importance of incorporating CBF measurements besides CBV for cerebrovascular monitoring and highlight the utility of SCOS and DCS devices, which are capable of simultaneously detecting both CBF and CBV. Additionally, our results identify an optimal S–D distance of at least 2.0 cm to minimize scalp sensitivity. However, brain sensitivity continues to improve beyond this distance, establishing 2.0 cm as the lower bound for brain blood flow measurements. While the mathematical definition of SCOS has been established for two decades [28, 56], its experimental implementation for cerebral blood flow monitoring is relatively new, with pioneering works in 2018 [57] and 2020 [1]. Since then, several SCOS systems have been developed by independent research groups to effectively measure CBF and CBV. Notable recent SCOS systems include Openwater bedside SCOS system for stroke detection [29, 24], fiber-based SCOS for mental task probing [27] and brain injury in mice [58], compact-SCOS for stroke-risk prediction [25, 26] and brain injury investigation [59], and interferometric SCOS (also named iSVS) for cerebral blood flow measurement on human and animals such as rabbits

or rodents [44, 1].

This variety of systems and applications underscores the reproducibility and effectiveness of SCOS while emphasizing the need for an experimental method to differentiate scalp and brain sensitivities—a gap this work aims to address. Notably, all the SCOS systems referenced utilized a source-to-detector (S–D) distance of 3.0 cm or greater, highlighting the critical importance of carefully selecting the S–D distance in optical systems to optimize sensitivity and accuracy.

Despite the promising results, several limitations must be acknowledged. First, the superficial temporal artery occlusion method, while effective in isolating scalp signals, relies on precise manual placement and consistent pressure application, which may introduce variability. A mechanically designed system with pre-applied, controlled pressure could improve consistency for the same subject but may still face challenges in maintaining uniformity across different individuals. Second, the study's relatively small sample size of 20 subjects may limit the broader generalizability of our findings. Inter-subject variations in scalp thickness, skull density, and vascular anatomy can introduce variability scalp-to-brain distance and, consequently, depth sensitivity. While increasing the cohort size could reduce some statistical variability, it would not eliminate the inherent anatomical variability among subjects. Third, further exploration of waveform dynamics, such as the distinct behaviors of CBF and CBV during occlusion, could yield deeper insights into the physiological responses of cerebral and scalp vasculatures under varying conditions. Fourth, this study does not aim to validate absolute CBF values, but rather to demonstrate relative depth sensitivity using a controlled perturbation via STA occlusion. While comparison with gold-standard techniques such as TCD, DCS, or MRI would enhance the validation of this approach, the current study was designed as a proof of concept to establish the feasibility of using STA occlusion to characterize SCOS sensitivity. Our results serve as a foundational step toward future validation studies where gold-standard techniques such as TCD, DCS, or MRI perfusion could provide cross-validation.

Fifth and last, the low SNR in deeper channels, particularly Channels 6 and 7 (2.3 and 2.6 cm), presents challenges in reliably interpreting brain-specific signals at greater S–D distances. Measuring CBF with relatively high SNR is more challenging than CBV at the same S–D distance. To address this, we plan to combine our previous experience in compact SCOS as in Ref [26] and develop a custom-designed extended camera spanning over 3 cm in one dimension. This setup will enable simultaneous

and continuous measurement of blood dynamics across S–D distances ranging from 0.5 to 3.5 cm, improving spatial resolution and data quality. The fiber-based SCOS system presented in this manuscript was designed as proof of concept to demonstrate how brain specificity and sensitivity vary across different source-detector (S–D) distances. This system served as a benchtop validation platform and is not readily adaptable to a wearable clinical design due to its reliance on bulky and expensive components. Indeed, to measure CBF and CBV at seven S–D distances simultaneously, we used a fiber bundle that arranges the detection fibers together, imaging them on a single large-area camera sensor (>5 million pixels). The longest S–D distance (2.6 cm) was constrained by the use of a 600 µm fiber SCOS device (see Material and Methods), while the spacing between S–D pairs (≈0.35 cm) was limited by the physical size of the detecting fibers, preventing finer resolution. To overcome these limitations, we plan to develop the custom CMOS strip sensor with an integrated graduated neutral-density filter to replace the fiber bundle and allow direct skin contact of the camera sensor as in in Refs. [26, 59]. This design will extend the maximum S–D distance from 2.6 cm to 3.5 cm and enable quasi-continuous sampling across the S–D range. The sensor will measure 3 cm in length and 0.3 cm in width (>6 million pixels) and will be placed directly on the skin. For the laser source, we intend to adopt a compact, portable design similar to those demonstrated in Refs. [26, 59]. With these advancements, we aim to develop a wearable SCOS system with a quasi-continuous S–D range from 0.5 cm to 3.5 cm—enhancing spatial sampling and enabling deeper brain measurements. This crucial step will help transition the system into a compact, wearable form suitable for clinical use.

Our occlusion-based approach can be adapted for real-time monitoring, as demonstrated in our previous work with a six-channel SCOS system achieving 60 frames per second (fps) acquisition on a modern laptop equipped with a consumer-grade GPU (e.g., NVIDIA RTX 4060) [59].

2.4 The imperative for extended S–D and emerging challenges

Through the exploration of the preceding two sections in this chapter, encompassing the work presented, we have established that both SCOS and interferometric SCOS (iSVS) techniques enable a reduction in superficial scalp contamination by increasing source-detector (S–D) distances. Furthermore, we examined the superior performance of diffusion-based modalities in terms of brain specificity compared to absorption-based NIRS, as evidenced by the lower sensitivity of the blood volume

index (BVI).

Now, as we venture into the next chapter, a critical challenge emerges. While increasing the S–D distance enhances brain specificity, we also know that signal intensity exponentially decreases with increasing S–D separation. This presents a fundamental dilemma: how can we reliably achieve S–D distances of 3 cm or more, where brain specificity is sufficiently high, without sacrificing signal quality? What strategies can be employed to overcome this inherent trade-off?

In the following chapter, we will delve deeper into various efforts aimed at improving signal quality and signal-to-noise ratio (SNR) in SCOS and iSVS systems, exploring a range of innovative approaches to enable robust deep brain measurements.

References

[1] Jian Xu et al. "Interferometric speckle visibility spectroscopy (ISVS) for human cerebral blood flow monitoring". en. In: *APL Photonics* 5.12 (Dec. 2020), p. 126102. DOI: 10.1063/5.0021988.

[2] Yu Xi Huang et al. "Interferometric speckle visibility spectroscopy (iSVS) for measuring decorrelation time and dynamics of moving samples with enhanced signal-to-noise ratio and relaxed reference requirements". In: *Opt. Express* 31.19 (Sept. 2023), pp. 31253–31266. DOI: 10.1364/OE.499473.

[3] *ANSI Z136.1-2014 - American National Standard for Safe Use of Lasers*.

[4] Teemu Myllylä et al. "Assessment of the dynamics of human glymphatic system by near-infrared spectroscopy". en. In: *Journal of Biophotonics* 11.8 (2018), e201700123. DOI: 10.1002/jbio.201700123.

[5] Florian B. Haeussinger et al. "Simulation of Near-Infrared Light Absorption Considering Individual Head and Prefrontal Cortex Anatomy: Implications for Optical Neuroimaging". en. In: *PLoS ONE* 6.10 (Oct. 2011). Ed. by Kenji Hashimoto, e26377. DOI: 10.1371/journal.pone.0026377.

[6] Gary E. Strangman, Zhi Li, and Quan Zhang. "Depth Sensitivity and Source-Detector Separations for Near Infrared Spectroscopy Based on the Colin27 Brain Template". en. In: *PLoS ONE* 8.8 (Aug. 2013), e66319. DOI: 10.1371/journal.pone.0066319.

[7] Chemseddine Mansouri et al. "Depth sensitivity analysis of functional near-infrared spectroscopy measurement using three-dimensional Monte Carlo modelling-based magnetic resonance imaging". en. In: *Lasers in Medical Science* 25.3 (May 2010), pp. 431–438. DOI: 10.1007/s10103-010-0754-4.

[8] Alexander Doronin, Callum Macdonald, and Igor V. Meglinski. “Propagation of coherent polarized light in turbid highly scattering medium”. In: *Journal of Biomedical Optics* 19.2 (Feb. 2014). Publisher: SPIE, p. 025005. DOI: 10.1117/1.JBO.19.2.025005.

[9] Alexander Doronin et al. “Backscattering of linearly polarized light from turbid tissue-like scattering medium with rough surface”. In: *Journal of Biomedical Optics* 21.7 (July 2016). Publisher: SPIE, p. 071117. DOI: 10.1117/1.JBO.21.7.071117.

[10] Wenjun Zhou et al. “Functional interferometric diffusing wave spectroscopy of the human brain”. en. In: *Science Advances* 7.20 (May 2021), eabe0150. DOI: 10.1126/sciadv.abe0150.

[11] Sm Shams Kazmi et al. “Expanding Applications, Accuracy, and Interpretation of Laser Speckle Contrast Imaging of Cerebral Blood Flow”. en. In: *Journal of Cerebral Blood Flow & Metabolism* 35.7 (July 2015). Publisher: SAGE Publications, pp. 1076–1084. DOI: 10.1038/jcbfm.2015.84.

[12] Lun-De Liao et al. “Neurovascular coupling: in vivo optical techniques for functional brain imaging”. In: *BioMedical Engineering OnLine* 12.1 (Apr. 2013), p. 38. DOI: 10.1186/1475-925X-12-38.

[13] Anton Konovalov et al. “Laser Speckle Contrast Imaging in Neurosurgery: A Systematic Review”. In: *World Neurosurgery* 171 (Mar. 2023), pp. 35–40. DOI: 10.1016/j.wneu.2022.12.048.

[14] Vyacheslav Kalchenko et al. “Combined laser speckle imaging and fluorescent intravital microscopy for monitoring acute vascular permeability reaction”. In: *Journal of Biomedical Optics* 24.6 (May 2019). Publisher: SPIE, p. 060501. DOI: 10.1117/1.JBO.24.6.060501.

[15] Claire Rabut et al. “A window to the brain: ultrasound imaging of human neural activity through a permanent acoustic window”. eng. In: *bioRxiv: The Preprint Server for Biology* (June 2023), p. 2023.06.14.544094. DOI: 10.1101/2023.06.14.544094.

[16] J. S. Rahul and Gaurav Kakkar. “Cerebral Blood Flow Monitoring”. en. In: *Principles and Practice of Neurocritical Care*. Ed. by Hemanshu Prabhakar et al. Singapore: Springer Nature Singapore, 2024, pp. 75–92. DOI: 10.1007/978-981-99-8059-8_6.

[17] K Yoshida et al. “Dynamics of cerebral blood flow and metabolism in patients with cranioplasty as evaluated by 133Xe CT and 31P magnetic resonance spectroscopy.” en. In: *Journal of Neurology, Neurosurgery & Psychiatry* 61.2 (Aug. 1996), pp. 166–171. DOI: 10.1136/jnnp.61.2.166.

[18] William J. Powers. “Cerebral hemodynamics in ischemic cerebrovascular disease”. en. In: *Annals of Neurology* 29.3 (Mar. 1991), pp. 231–240. DOI: 10.1002/ana.410290302.

[19] Paul M. Thompson et al. “Structural MRI and Brain Development”. en. In: *International Review of Neurobiology*. Vol. 67. Elsevier, 2005, pp. 285–323. DOI: 10.1016/S0074-7742(05)67009-2.

[20] Matthias König. “Brain perfusion CT in acute stroke: current status”. en. In: *European Journal of Radiology* 45 (Mar. 2003), S11–S22. DOI: 10.1016/S0720-048X(02)00359-5.

[21] Paulla Vieira Rodrigues et al. “Illuminating the Brain With X-Rays: Contributions and Future Perspectives of High-Resolution Microtomography to Neuroscience”. In: *Frontiers in Neuroscience* 15 (Mar. 2021), p. 627994. DOI: 10.3389/fnins.2021.627994.

[22] Reidar P. Lystad and Henry Pollard. “Functional neuroimaging: a brief overview and feasibility for use in chiropractic research”. eng. In: *The Journal of the Canadian Chiropractic Association* 53.1 (Mar. 2009), pp. 59–72.

[23] David Nanchen. “Resting heart rate: what is normal?” en. In: *Heart* 104.13 (July 2018), pp. 1048–1049. DOI: 10.1136/heartjnl-2017-312731.

[24] Christopher G. Favilla et al. *Validation of the Openwater wearable optical system: cerebral hemodynamic monitoring during a breath hold maneuver*. en. Pages: 2023.10.11.23296612. Oct. 2023. DOI: 10.1101/2023.10.11.23296612.

[25] Yu Xi Huang et al. “Correlating stroke risk with non-invasive cerebrovascular perfusion dynamics using a portable speckle contrast optical spectroscopy laser device”. In: *Biomed. Opt. Express* 15.10 (Oct. 2024), pp. 6083–6097. DOI: 10.1364/BOE.534796.

[26] Yu Xi Huang et al. “Compact and cost-effective laser-powered speckle contrast optical spectroscopy fiber-free device for measuring cerebral blood flow”. In: *Journal of Biomedical Optics* 29.6 (2024), p. 067001. DOI: 10.1117/1.JBO.29.6.067001.

[27] Byungchan Kim et al. “Measuring human cerebral blood flow and brain function with fiber-based speckle contrast optical spectroscopy system”. en. In: *Communications Biology* 6.1 (Aug. 2023), p. 844. DOI: 10.1038/s42003-023-05211-4.

[28] Claudia P. Valdes et al. “Speckle contrast optical spectroscopy, a non-invasive, diffuse optical method for measuring microvascular blood flow in tissue”. en. In: *Biomedical Optics Express* 5.8 (Aug. 2014), p. 2769. DOI: 10.1364/BOE.5.002769.

[29] Christopher G Favilla et al. “Portable cerebral blood flow monitor to detect large vessel occlusion in patients with suspected stroke”. en. In: *Journal of NeuroInterventional Surgery* (Mar. 2024), jnis–2024–021536. DOI: 10.1136/jnis-2024-021536.

[30] Chen-Hao P. Lin et al. “Multi-mode fiber-based speckle contrast optical spectroscopy: analysis of speckle statistics”. en. In: *Optics Letters* 48.6 (Mar. 2023), p. 1427. DOI: 10.1364/OL.478956.

[31] Yu Xi Huang et al. “Interferometric speckle visibility spectroscopy (iSVS) for measuring decorrelation time and dynamics of moving samples with enhanced signal-to-noise ratio and relaxed reference requirements”. en. In: *Optics Express* 31.19 (Sept. 2023), p. 31253. DOI: 10.1364/OE.499473.

[32] Simon Mahler et al. “Assessing depth sensitivity in laser interferometry speckle visibility spectroscopy (iSVS) through source-to-detector distance variation and cerebral blood flow monitoring in humans and rabbits”. en. In: *Biomedical Optics Express* 14.9 (Sept. 2023), p. 4964. DOI: 10.1364/BOE.498815.

[33] Yu Xi Huang et al. “Compact and cost-effective laser-powered speckle contrast optical spectroscopy fiber-free device for measuring cerebral blood flow”. In: *Journal of Biomedical Optics* 29.06 (May 2024). DOI: 10.1117/1.JBO.29.6.067001.

[34] Jialin Liu et al. “Establishing the quantitative relationship between diffuse speckle contrast analysis signals with absolute blood flow”. en. In: *Biomedical Optics Express* 9.10 (Oct. 2018). Publisher: Optica Publishing Group, p. 4792. DOI: 10.1364/boe.9.004792.

[35] Ninghe Liu et al. “Optimized cerebral blood flow measurement in speckle contrast optical spectroscopy via refinement of noise calibration”. In: *Opt. Lett.* 50.17 (Sept. 2025), pp. 5382–5385. DOI: 10.1364/OL.570951.

[36] Melissa M. Wu et al. “Improved accuracy of cerebral blood flow quantification in the presence of systemic physiology cross-talk using multi-layer Monte Carlo modeling”. In: *Neurophotonics* 8.01 (Jan. 2021). DOI: 10.1117/1.NPh.8.1.015001.

[37] Daniel Milej et al. “Direct assessment of extracerebral signal contamination on optical measurements of cerebral blood flow, oxygenation, and metabolism”. In: *Neurophotonics* 7.04 (Oct. 2020). DOI: 10.1117/1.NPh.7.4.045002.

[38] Mingjun Zhao et al. “Interferometric diffusing wave spectroscopy imaging with an electronically variable time-of-flight filter”. en. In: *Optica* 10.1 (Jan. 2023), p. 42. DOI: 10.1364/OPTICA.472471.

[39] Nisan Ozana et al. “Functional Time Domain Diffuse Correlation Spectroscopy”. In: *Frontiers in Neuroscience* 16 (Aug. 2022), p. 932119. DOI: 10.3389/fnins.2022.932119.

[40] Mitchell B. Robinson et al. “Portable, high speed blood flow measurements enabled by long wavelength, interferometric diffuse correlation spectroscopy (LW-iDCS)”. en. In: *Scientific Reports* 13.1 (May 2023), p. 8803. DOI: 10.1038/s41598-023-36074-8.

[41] Marianne Suwalski et al. “Assessing the Sensitivity of Multi-Distance Hyperspectral NIRS to Changes in the Oxidation State of Cytochrome C Oxidase in the Brain”. en. In: *Metabolites* 12.9 (Aug. 2022), p. 817. DOI: 10.3390/metabo12090817.

[42] Mitchell B. Robinson et al. *Pathlength-selective, interferometric diffuse correlation spectroscopy*. en. June 2024. DOI: 10.1101/2024.06.21.600096.

[43] Mitchell B. Robinson et al. “Comparing the performance potential of speckle contrast optical spectroscopy and diffuse correlation spectroscopy for cerebral blood flow monitoring using Monte Carlo simulations in realistic head geometries”. In: *Neurophotonics* 11.01 (Jan. 2024). DOI: 10.1117/1.NPh.11.1.015004.

[44] Simon Mahler et al. “Assessing depth sensitivity in laser interferometry speckle visibility spectroscopy (iSVS) through source-to-detector distance variation and cerebral blood flow monitoring in humans and rabbits”. In: *Biomed. Opt. Express* 14.9 (Sept. 2023), pp. 4964–4978. DOI: 10.1364/BOE.498815.

[45] Zhenyu Dong et al. “Non-invasive laser speckle contrast imaging (LSCI) of extra-embryonic blood vessels in intact avian eggs at early developmental stages”. en. In: *Biomedical Optics Express* 15.8 (Aug. 2024), p. 4605. DOI: 10.1364/BOE.530366.

[46] Juliette Selb et al. “Sensitivity of near-infrared spectroscopy and diffuse correlation spectroscopy to brain hemodynamics: simulations and experimental findings during hypercapnia”. en. In: *Neurophotonics* 1.1 (Aug. 2014), p. 015005. DOI: 10.1117/1.NPh.1.1.015005.

[47] Simon Mahler et al. “Portable six-channel laser speckle system for simultaneous measurement of cerebral blood flow and volume with potential applications in characterization of brain injury”. en. In: *Neurophotonics* 12.01 (Jan. 2025), p. 2024.10.30.24316429. DOI: 10.1117/1.NPh.12.1.015003.

[48] Sharvari Zilpelwar et al. “Model of dynamic speckle evolution for evaluating laser speckle contrast measurements of tissue dynamics”. en. In: *Biomedical Optics Express* 13.12 (Dec. 2022), p. 6533. DOI: 10.1364/BOE.472263.

[49] W. F. Sheppard. “On the Calculation of the most Probable Values of Frequency-Constants, for Data arranged according to Equidistant Division of a Scale”. en. In: *Proceedings of the London Mathematical Society* s1-29.1 (1897). _eprint: https://onlinelibrary.wiley.com/doi/pdf/10.1112/plms/s1-29.1.353, pp. 353–380. DOI: 10.1112/plms/s1-29.1.353.

[50] Lisa Kobayashi Frisk et al. “Comprehensive workflow and its validation for simulating diffuse speckle statistics for optical blood flow measurements”. en. In: *Biomedical Optics Express* 15.2 (Feb. 2024), p. 875. DOI: 10.1364/BOE.502421.

[51] Chang Liu et al. “Choosing a model for laser speckle contrast imaging”. en. In: *Biomedical Optics Express* 12.6 (June 2021), p. 3571. DOI: 10.1364/BOE.426521.

[52] David A. Boas et al. “Establishing the diffuse correlation spectroscopy signal relationship with blood flow”. eng. In: *Neurophotonics* 3.3 (July 2016), p. 031412. DOI: 10.1117/1.NPh.3.3.031412.

[53] Dmitry D. Postnov et al. “Dynamic light scattering imaging”. en. In: *Science Advances* 6.45 (Nov. 2020), eabc4628. DOI: 10.1126/sciadv.abc4628.

[54] Christopher G. Favilla et al. “Validation of the Openwater wearable optical system: cerebral hemodynamic monitoring during a breath-hold maneuver”. In: *Neurophotonics* 11.01 (Mar. 2024). DOI: 10.1117/1.NPh.11.1.015008.

[55] Teemu Myllylä et al. “Assessment of the dynamics of human glymphatic system by near-infrared spectroscopy”. en. In: *Journal of Biophotonics* 11.8 (2018). _eprint: https://onlinelibrary.wiley.com/doi/pdf/10.1002/jbio.201700123, e201700123. DOI: 10.1002/jbio.201700123.

[56] R. Bandyopadhyay et al. “Speckle-visibility spectroscopy: A tool to study time-varying dynamics”. en. In: *Review of Scientific Instruments* 76.9 (Sept. 2005), p. 093110. DOI: 10.1063/1.2037987.

[57] Tanja Dragojević et al. “Compact, multi-exposure speckle contrast optical spectroscopy (SCOS) device for measuring deep tissue blood flow”. EN. In: *Biomedical Optics Express* 9.1 (Jan. 2018). Publisher: Optica Publishing Group, pp. 322–334. DOI: 10.1364/BOE.9.000322.

[58] Dharminder S. Langri and Ulas Sunar. “Non-Invasive Continuous Optical Monitoring of Cerebral Blood Flow after Traumatic Brain Injury in Mice Using Fiber Camera-Based Speckle Contrast Optical Spectroscopy”. en. In: *Brain Sciences* 13.10 (Sept. 2023), p. 1365. DOI: 10.3390/brainsci13101365.

[59] Simon Mahler et al. “Portable six-channel laser speckle system for simultaneous measurement of cerebral blood flow and volume with potential applications in characterization of brain injury”. In: *Neurophotonics* 12.1 (2025), p. 015003. DOI: 10.1117/1.NPh.12.1.015003.

Chapter 3

SIGNAL IS THE KEY

In the preceding chapter, we rigorously validated the brain specificity of diffuse wave spectroscopy (DWS) techniques—specifically interferometric SVS (iSVS) and standard SCOS—across various metrics. Our findings unequivocally demonstrated a critical principle: the greater the source-detector (S–D) separation, the higher the achieved brain specificity. This insight, while crucial for isolating deep brain signals, simultaneously ushers in a significant new challenge: the inherent trade-off with signal intensity.

The community has rapidly recognized that signal is the key to unlocking the full potential of DWS for deeper brain interrogation. As such, a concerted effort has driven the elongation of S–D distances from typical values of 1.5 cm [1] to currently exceeding 3 cm [2, 3]. This chapter chronicles my endeavors to address this fundamental challenge by significantly increasing the signal-to-noise ratio (SNR) in diffuse correlation systems, thereby enabling robust measurements at these extended S–D separations.

My initial work, detailed in the first part of this chapter, theoretically characterizes the potential benefits of employing interferometry. The core hypothesis was that a well-chosen reference source could effectively mitigate camera noise uncertainty, theoretically pushing the SNR consistently toward the fundamental limit of shot noise under ideal conditions. However, as subsequent experimental validation revealed, achieving such an ideal scenario in practice proved to be remarkably challenging.

This practical hurdle prompted a strategic shift in my research, guiding the second major effort presented herein. Abandoning the complexities associated with fiber usage, this approach embraced a simplified experimental setup designed to maximize photon collection efficiency. This involved substantially increasing both the photon-sensitive area and the numerical aperture (NA) of the detection system. This pivotal transition marked a significant evolution in my PhD work, shifting focus from iSVS toward the more streamlined SCOS methodology, and largely shaped the second half of my research journey.

Finally, towards the end of this chapter, I will present a further optimization of our

brain blood flow index (BFI) signal. This optimization leverages a priori knowledge regarding typical cerebral blood volume (CBV) and cerebral blood flow (CBF) waveforms, demonstrating how physiological insights can further enhance signal quality.

In summary, this chapter is an in-depth exploration of diverse strategies employed to elevate the SNR across various DWS systems. It not only highlights the innovative solutions developed but also candidly discusses the obstacles encountered along this scientific journey and the subsequent methodologies devised to overcome them, ultimately paving the way for more reliable deep brain measurements.

3.1 Interferometry! The solution?

This section is adapted from published work: Huang, Y. X., Mahler, S., Mertz, J., & Yang, C. (2023). *Interferometric speckle visibility spectroscopy (iSVS) for measuring decorrelation time and dynamics of moving samples with enhanced signal-to-noise ratio and relaxed reference requirements*. *Optics Express*, 31(19), 31253-31266.

For DWS, the signal-to-noise ratio (SNR) is determined by the ratio between the measured decorrelation time to the standard error of the measurement. This SNR is often low in certain applications because of high noise variances and low signal intensity, especially in biological applications with restricted exposure and emission levels. To address this photon-limited signal-to-noise ratio problem, in this section we investigated, theoretically and experimentally, the SNR of an interferometric speckle visibility spectroscopy (iSVS) compared to more traditional DWS methods. We found that iSVS can provide excellent SNR performance through its ability to overcome camera noise. We also proved that an iSVS system has more relaxed constraints on the reference beam properties. For an iSVS system to function properly, we only require the reference beam to exhibit local temporal stability, while incident angle, reference phase, and intensity uniformity do not need to be constrained. This flexibility can potentially enable more unconventional iSVS implementation schemes.

Background and context

Temporal sampling-based DWS is also called diffuse correlation spectroscopy (DCS) [4, 5, 6, 7, 8, 9, 10, 11, 12]. In general DCS applications, the laser light propagates through a dynamic scattering medium and the transmission is collected back by using a single-photon avalanche diode (SPAD) or a photodetector. Typically, a

single speckle or a small collection of speckles (constituting a single aggregate speckle) is detected at a sufficiently high frame rate such that the inverse of the frame rate is significantly shorter than the expected decorrelation time of the speckle [13, 2, 14, 15, 16, 17]. The typical DCS algorithm then calculates the signal's time correlation to measure the scattering medium's dynamics. The autocorrelation function derived from the photon's arrival time series can be fitted to multiple scattering models, where models used are determined by the motion type and the scattering regime of the scattering medium [18]. The intensity autocorrelation is fitted to the $g_2(\tau)$ function, and the field autocorrelation function $g_1(\tau)$ is then retrieved via the Siegert relation. In biological applications, DCS generally employs a fast (typically sampled in the MHz range) sensor with high quantum efficiency and low detector noise characteristics, such as an ultrafast SPAD or other forms of fast Time-of-Flight photon detectors, to better detect the typically weak signals.

There are different and more advanced forms of DCS. In interferometric DCS (iDCS) [2, 14, 16, 15, 19, 17, 20, 21], a reference light field is introduced to enable interferometric detection of the optical signal. This provides the ability to reject stray light and enable interferometric suppression of the detector noise when measuring the optical signal. It is also possible to simultaneously detect multiple speckles with multiple high-speed detectors, such as a SPAD array [13, 2, 14, 15]. Recently, a method that combines interferometry and ultrafast cameras for multiple speckle detection has also been reported that sought to combine both advantages to yield a stronger DCS signal [22, 23, 24].

The alternate DWS approach is based on the use of spatial ensemble. This class of method is generally referred to as speckle visibility spectroscopy (SVS) [25, 1, 26, 27] or speckle contrast optical spectroscopy (SCOS) [28, 29, 3]. Other approaches utilizing spatial ensembles of speckles include laser speckle contrast imaging (LSCI) [30, 31, 32, 33, 34, 35, 36, 37]. Here, a high pixel count camera is used to simultaneously detect multiple speckles in the optical transmission. Generally, the camera exposure time is set to be substantially longer than the speckle decorrelation time (typically a magnitude or more). This results in multiple different speckle patterns summing up in a single camera frame within the exposure time and yielding a blurred or washed-out speckle pattern. The speckle decorrelation time can then be calculated from the degree of blurring, or more specifically, the contrast of the speckles over all the detected speckles in the whole frame. By the nature of its operation, SVS does not require high-speed detectors and can work with mature and

commercially available video-rate sCMOS cameras. In addition, SVS can naturally collect more transmitted light as video-rate cameras generally have very high pixel counts – the photon count per pixel may still be low, but a higher aggregate signal is obtained by using more pixels. On the other hand, SVS must contend with the relatively high detector noise characteristics of these cameras. To mitigate this issue, an interferometric SVS (iSVS) system has recently been demonstrated and shown to work well at suppressing detector noise through the interferometric measurement of the optical signal [25].

For clarity within this subsection, we will use "SVS" to refer to what is sometimes termed "SCOS" (Speckle Contrast Optical Spectroscopy) in the broader community. While SVS and SCOS essentially denote the same concept, we chose to use SVS here for direct comparison with iSVS within the scope of this thesis chapter. In subsequent publications, we have reverted to using SCOS to align with established community terminology.

For DWS methods in general (both DCS and SVS), the accuracy of the speckle decorrelation time is a key specification. Mathematically, this accuracy can be quantified as the ratio of the measured decorrelation time to the standard error of the measurement, and it can be interpreted as the signal-to-noise performance specification of DWS methods. While DCS and SVS employ different methods to determine the speckle decorrelation time, their SNR performance can ultimately be tied back to the number of independent observables (NIO) and the detected photon flux [1]. The NIO corresponds to the number of speckle decorrelation events measured for single speckle DCS methods. The NIO then scales proportionately with the speckle count if multiple speckles are simultaneously detected for multi-speckle DCS methods. For SVS methods, the NIO corresponds to the number of speckle grains observed per exposure. Reference [1] details the exact NIO relationships for both DCS and SVS methods. The reference also compared the application of both DCS and SVS methods for biological studies and found that for blood flow measurements, it is generally easier for the SVS method to achieve a higher NIO count and, therefore, better accuracy in decorrelation time measurement. In addition, SVS methods cannot quantify the exact shape of the time decorrelation function, while DCS methods are generally able to do so.

The mathematical treatment of SNR performances in Ref. [1] assumes that the camera/detector is noise-free or that the camera/detector noise variance is low enough to have little impact on the measurements. While such an assumption is reasonable

for a broad range of DWS applications, it will generally fail for low-light situations where the low number of detected signal photons can easily be overwhelmed by the intrinsic camera or detector noise, especially in biological applications where the exposure and emission levels are restricted [38]. We recognize that James et al. have established the analysis and optimization of SNR performance for holographic DCS, but detailed noise analysis has not been published for iSVS type systems yet [39].

This study aims to expand the mathematical model to account for detector noise. We will focus our analysis on an iSVS system, as such a system is specifically designed for low-light application uses, where interferometry is employed to enhance the detection of the signal light in the presence of significant detector noise. This advantage of iSVS over SVS has been experimentally demonstrated in previous studies [25]. It was shown that human cerebral blood flow could be determined with a high sampling rate of 100 Hz, even when the number of collected signal photons per pixel was low (i.e., below the camera noise variance) [25]. That promising result motivates our current analysis.

In this work, extending from the iSVS technique first proposed by Xu et al. in Ref. [25], we mathematically analyze and experimentally verify the signal-to-noise ratio (SNR) gains of iSVS over SVS in the presence of camera noise. We also show that with reasonable prior knowledge of the average signal intensity, the SNR of iSVS will always be higher or on par than SVS with a uniform reference field. Previous work used a uniform plane wave reference beam with a specific angle (off-axis interferometry) to enable cropping in the Fourier domain to select the signal [25]. We show that such requirements can be relaxed, and the results are nearly independent of the reference beam's shape and angle, allowing one to use a non-uniform wave reference, on-axis interferometry setup with no angle between reference and source, or even an entirely spatially speckled reference to achieve a similar result. We also deployed standard calibration methods for iSVS to calibrate noise in experiments, which is necessary for the system to operate in a wider range of intensity. We demonstrated that iSVS has the advantage of retrieving more consistent decorrelation time, especially in signal-limited situations where the number of photons collected are low compared to noise. Finally, we conclude that the properties discovered justify and simplify iSVS application implementation.

iSVS SNR theoretical derivation

In this section, we derive the SNR expressions associated with iSVS, then compare the theoretical performance of iSVS and SVS in the presence of camera noise. The SNR is defined by the ground truth decorrelation time τ and the standard error of the measured τ as:

$$\mathrm{SNR}(\tau) = \frac{\tau}{\mathrm{SE}(\tau)} \tag{3.1}$$

Using a stack of images, one can extract the speckle contrast for each image and determine τ in iSVS experiments. The decorrelation time τ is derived from the autocorrelation function $g(\tau)$, which can be recovered given the presumed form of $g(\tau)$, as well as the measured speckle contrast K. We note that in blood flow measurement setups, the blood flow index (BFI) can also be retrieved directly as $\mathrm{BFI} = 1/K^2$, but the definition of SNR here will be concerning only τ, consistent with the definition in Ref [1]. As such, we will first derive a mathematical expression for the speckle contrast as a function of τ. We begin by assuming that the reference beam's intensity and phase are constant through time locally (i.e., at each pixel). We also assume that each camera pixel is the size of a single speckle grain, so each pixel observes an independent speckle [40]. For details of the full derivation, please see the original paper's Supplemental Document. The iSVS intensity signal for pixel j on the camera sensor, denoted as $I_j(t)$ is given by [25]:

$$I_j(t) = I_{Sj}(t) + I_{Rj}(t) + 2\sqrt{I_{Sj}(t)I_{Rj}(t)}\cos((\phi_{Rj}(t) - \phi_{Sj}(t))) + n_{\text{shot }j}(t) \tag{3.2}$$

which is composed of the sample intensity coming from the moving sample arm $I_{Sj}(t)$, the reference intensity from the reference arm $I_{Rj}(t)$, the interference cross term, and the shot noise $n_S(t)$. For notation, $\phi_{Sj}(t)$ is the phase of the sample beam, $\phi_{Rj}(t)$ is the phase of the reference beam, and any off-axis treatment or other adjustment to the reference is considered in the localized phase term $\phi_{Rj}(t)$. We note that in this derivation, we assume that the reference field can be spatially heterogeneous in both its amplitude, I_{Rj}, and phase, ϕ_{Rj}, but that their values are fixed across all times. In effect, we have a heterogeneous and static reference field.

To obtain a reference-subtracted or reference-calibrated image, we subtract the captured image by the reference image. The reference-calibrated signal readout, in terms of photon counts, on pixel j from the CMOS sensor can be mathematically expressed as:

$$N_j = \alpha \int_0^T I_j(t) - I_{Rj}\, dt = \alpha \int_0^T I_j^*(t)\, dt \tag{3.3}$$

where α is the coefficient encompassing the quantum efficiency, the optical properties, and the other factors dictating the relationship between received photon counts and digitized readout signal. $I_j(t)$ is the intensity received by the pixel j at time t, and T is the exposure time. The speckle contrast K of the entire image sensor is defined as [25, 1]:

$$K = \frac{\sigma_{\text{cam}}}{\langle N_j \rangle} = \frac{\sqrt{\langle (N_j - \langle N_j \rangle)^2 \rangle}}{\langle N_j \rangle} = \frac{K_{\text{up}}}{K_{\text{down}}}. \tag{3.4}$$

As stated before, N_j is the reference-calibrated photon count readout on pixel j, and the speckle contrast is the standard deviation divided by the mean. $\langle \cdot \rangle$ is the expected value of the term representing both an ensemble average and an average across all pixels.

K_{up}^2 can be expressed as:

$$K_{\text{up}}^2 = \langle (N_j - \langle N_j \rangle)^2 \rangle = \langle (\alpha \int_0^T (\tilde{I}_j^*)(t) dt)^2 \rangle, \tag{3.5}$$

Where $(\tilde{I}_j^*)(t)$ is the mean subtracted intensity on pixel j, or $(\tilde{I}_j^*)(t) = I_j^*(t) - \langle I_j^* \rangle$. We can then expand the integral as:

$$\begin{aligned} K_{\text{up}}^2 =& \alpha^2 \langle \iint_0^T \tilde{I}_S(t_1) \tilde{I}_S(t_2) dt_1 dt_2 \rangle \\ &+ 4\alpha^2 \langle I_{Rj} \iint_0^T \sqrt{I_{Sj}(t_1) I_{Sj}(t_2)} \cos(\Delta\phi_j(t_1)) \cos(\Delta\phi_j(t_2)) dt_1 dt_2 \rangle \\ &+ \alpha^2 \langle \iint_0^T n_{\text{shot}_j}(t_1) n_{\text{shot}_j}(t_2) dt_1 dt_2 \rangle. \end{aligned} \tag{3.6}$$

We can extract I_{Rj} out from the second term as reference intensity is constant and independent from the sample intensity. Here as shown in Equation 3.7, we model the scattering dynamics based on Brownian motion, leading to a field intensity autocorrelation function that decays exponentially with a decay constant depending on the decorrelation time τ_{field} [25, 41, 42]. This corresponds to the assumption that the scattering medium is scattered multiple times in ordered fashion, which is likely to occur during blood flow monitoring [18]. In SVS, the intensity decorrelation time τ_s is first measured, and its relationship with the field decorrelation time τ_{field} can be extrapolated from the Siegert relation [18, 43]. In iSVS, there are two decorrelation times influencing the speckle contrast: the first is related to the intensity of the sample arm (τ_s), similar to SVS, and the second is related to the cross term from the interferometry which directly measures field decorrelation (τ_{field}). The difference

is essential here and an important aspect of iSVS, as in the majority of the non-interferometric methods, field autocorrelation function $g_1(t)$ needs to be inferred via Siegert relation, explicitly defined as $g_2(t) = |g_1(t)|^2 + 1$. However, in many situations, Siegert relationship breaks down; for instance, when a strong static field is present. The iSVS technique allows accessing τ_{field} directly, without the necessity of inferring from intensity information $g_2(t)$ first. Assuming the negative exponential decay holds, we approximate the decorrelation function as follows:

$$g_s(t = t_1 - t_2) = \frac{\langle \tilde{I_S}(t_1)\tilde{I_S}(t_2)\rangle}{\langle \tilde{I_S}(t_1)^2\rangle} = e^{-t/\tau_s} = g_2(t) - 1 = |g_1(t)|^2, \tag{3.7}$$

$$g_{\text{cross}}(t = t_1 - t_2) = \frac{\langle \sqrt{I_S(t_1)I_S(t_2)}\cos(\Delta\phi(t_1))\cos(\Delta\phi(t_2))\rangle}{\langle I_s(t_1)\cos^2(\Delta\phi(t_1))\rangle} = e^{-t/\tau_{\text{field}}} = |g_1(t)|. \tag{3.8}$$

$g_1(t)$ and $g_2(t)$ are the field and intensity decorrelation respectively, defined as $g_1(t) = \frac{\langle E(0)E^*(t)\rangle}{\langle I(0)\rangle}$, and $g_2(t) = \frac{\langle I(0)I(t)\rangle}{\langle I(0)\rangle^2} = 1 + |g_1(t)|^2$. Therefore, deriving from Equation 3.7 and Equation 3.8, assuming the Siegert relation holds, $\tau_{\text{field}} = 2\tau_s$. Also, the shot noise is largely determined by reference intensity $\bar{I_R}$, and the Poisson statistics yield variance equal to $\alpha\bar{I_R}T$. By substituting Equation 3.7 and 3.8 into Equation 3.6, we can obtain:

$$\begin{aligned} K_{\text{up}}^2 =& \alpha^2\langle \tilde{I_S}(t)^2\rangle T\int_0^T 2(1 - t/T)g_s(t)dt \\ &+ 4\alpha^2\bar{I_{Rj}}\bar{I_{Sj}}T\langle\cos^2(\Delta\phi(t))\rangle\int_0^T 2(1 - t/T)g_{\text{cross}}(t)dt + \alpha\bar{I_{Rj}}T, \end{aligned} \tag{3.9}$$

and through further simplification, with the assumption that $T \gg \tau_s$ and $T \gg \tau_{\text{field}}$, the integral $(1 - t/T) \approx 1$ before autocorrelation functions drop to 0. We obtain the variance of the calibrated image as:

$$K_{\text{up}}^2 \approx 2c\alpha^2\bar{I_S}^2T\tau_s + 4c\alpha^2\bar{I_S}\bar{I_R}T\tau_{\text{field}} + \alpha\bar{I_R}T, \tag{3.10}$$

where $c = 1$ (derived with the assumption that decorrelation follows exponential decay), but it can be generalized to Gaussian or other forms, depending on the physics and the scattering dynamics. K_{down}^2 can be expressed as the mean of the calibrated image, which only depends on the sample intensity as the reference is subtracted. By combining the denominator and numerator of the term K^2, we obtain its full relationship with τ_s and τ_{field}:

$$K^2 \approx \frac{2\alpha^2\bar{I_S}^2T\tau_s + 4\alpha^2\bar{I_R}\bar{I_S}T\tau_{\text{field}} + \alpha\bar{I_R}T}{\alpha^2\bar{I_S}^2T^2}. \tag{3.11}$$

$\bar{I_R}$ is defined as the average intensity of the reference. $\bar{I_S}$ is defined as the average of the sample intensity. Both $\bar{I_R}$ and $\bar{I_S}$ represent the spatial and time average intensities across the camera. The variance, which is the numerator of K^2, has three main contributors: the variance from sample beam photons alone ($2\alpha^2 \bar{I_S}^2 T\tau_s$), the variance from the interference cross-term signal ($4\alpha^2 \bar{I_R}\bar{I_S} T\tau_{\text{field}}$), and the shot noise from the reference beam ($\alpha \bar{I_R} T$). The above analysis assumes I_{Rj} is much greater than I_{Sj}. For situations where the reference field is uniform, the condition is well satisfied for all pixels if it is well satisfied for any given pixel. When the reference field intensity is spatially heterogeneous, this condition may not be satisfied for all pixels. In this case, the above speckle contrast expression is still valid, except we would need to exclude pixels where I_{Rj} is low compared to I_{Sj} from our count. All averages and expectation values would only take into account the pixels where the condition $I_{Rj} \gg I_{Sj}$ is satisfied. In experiments, it is generally possible to arrange $\bar{I_R}$ to be much higher than $\bar{I_S}$, so that the $I_{Rj} \gg I_{Sj}$ is satisfied for the majority of the pixels. In such a case, the class of pixels to be excluded is so small that including them will only lead to a negligible error. In our later experiments, this is proven to be true since reference can be tuned to an arbitrarily high level, as long as it does not overexpose the camera. Even in situations where reference is a fully developed speckle with negative exponential distributed intensities, we believe the assumption that $I_{Rj} \gg I_{Sj}$ should still hold for the majority of the pixels because iSVS intend to tackle photon-limited scenarios where I_{Sj} is minimal in comparison. However, we do want to emphasize this assumption clearly for future instrument designs. We preserved the first term in the numerator of Equation 3.11 to show the contributions of both τ_s and τ_{field}. In practice, we can further simplify the expression by noting that the first term is much smaller than the second and third numerator terms. If we set $U_I = \bar{I_R}/\bar{I_S}$, and define N_{ST} as the average number of sample beam photons per camera pixel $N_{ST} = \alpha \bar{I_S} T$:

$$\begin{aligned} K^2 &\approx U_I \left(\frac{4\tau_{\text{field}}}{T} + \frac{1}{N_{ST}} \right) \\ &\approx U_I \left(\frac{8\tau_s}{T} + \frac{1}{N_{ST}} \right) \quad \text{(From Siegert Relation)}. \end{aligned} \tag{3.12}$$

The translation from τ_{field} to τ_s assumed Siegert relation holds. It is worth noting that the speckle contrast for SVS has the form of [22]:

$$K^2_{\text{SVS}} = \frac{2\tau_s}{T} + \frac{1}{N_{ST}}. \tag{3.13}$$

The forms are quite similar except for the different decorrelation time constants involved and the scaling term U_I. The speckle contrast can be exactly determined

for an ideal sensor with an infinite number of pixels so that the ensemble averages in the above calculation mirror the spatial averages. However, since only a finite number of pixels is available in a camera, the measured speckle contrast squared ($\hat{K^2}$) will contain an error, as $\hat{K^2}$ will vary from measurement to measurement. The error will depend on the spatial profile of the reference beam and the NIO. We define a metric $R = \frac{\langle I_{Rj}^2 \rangle}{\langle I_{Rj} \rangle^2}$ to evaluate the uniformity of reference distribution. $R = 1$ represents a perfectly uniform reference intensity distribution, and a nonuniform reference pattern will have $R > 1$. As an example, a static speckled reference field where the speckle grain size is comparable or larger than the camera pixel will have an R-value approximately equal to 2. We also assume that the error of K^2 from measurement is only contributed by the numerator K_{up}^2 as $K_{\text{down}}^2 = N_{ST}^2$ can be accurately determined in experiments as a prior. Experimentally, we can determine $K_{\text{down}}^2 = N_{ST}^2$ exactly by blocking the reference beam and averaging arbitrarily many image frames. This leads to a speckle contrast estimate given by:

$$\hat{K^2} = K^2 \left(1 \pm \sqrt{\frac{3R-1}{\text{NIO}}} \right). \tag{3.14}$$

NIO is the number of independent observables as described in Ref [1]. In our current analysis, NIO is equal to the number of camera pixels used in the iSVS and SVS experiment (recall that we are tackling a situation where the average speckle grain is equal to a camera pixel size). We use ± here to denote the standard deviation of the measurement-to-measurement variation.

Equation 3.14 can be rewritten to provide a mathematical expression for determining τ_{field} and its measurement-to-measurement variation from the measured speckle contrast:

$$\hat{\tau}_{\text{field}} = \frac{T}{4U_I} K^2 - \frac{T}{4N_{ST}} \pm \frac{T}{4U_I} K^2 \left(\sqrt{\frac{3R-1}{\text{NIO}}} \right). \tag{3.15}$$

This finally allows us to express the SNR of iSVS with either τ_{field} or τ_s from Siegert relation as (see original paper's Supplemental Document for full derivation):

$$\text{SNR}_{\text{ISVS}} = \frac{1}{\left(1 + \frac{T}{4\tau_{\text{field}} N_{ST}} \right)} \sqrt{\frac{\text{NIO}}{3R-1}}. \tag{3.16}$$

From previous derivations in Ref [1], the SNR of SVS is:

$$\text{SNR}_{\text{SVS}} = \frac{1}{\left(1 + \frac{T}{\tau_s N_{ST}} \right)} \sqrt{\frac{\text{NIO}}{2}}. \tag{3.17}$$

We next consider the situation where camera noise is present in our analysis. We can define the camera noise term as a variable with mean $\langle n_{\text{cam}} \rangle = n_{\text{offset}}$ equal to the offset of the camera and variance $\sigma^2_{n_{\text{cam}}}$ related to the camera readout noise. We assume that the read noise is independent of the input signal strength N_j, independent of the exposure time T of the camera and contains similar distribution on every pixel. The offset component will be eliminated when subtracting with the reference image; therefore, only the fluctuating variance survives. We define $\sigma^2_{n_{\text{cam}}}$ as the variance of the camera noise. Then by adding the variance contributed from the camera noise to K^2_{up}, we can rewrite K^2 for iSVS as:

$$K^2 \approx \frac{4\alpha^2 \bar{I}_R \bar{I}_S T \hat{\tau}_{\text{field}} + \alpha \bar{I}_R T + \sigma^2_{n_{\text{cam}}}}{\alpha^2 {\bar{I}_S}^2 T^2}. \tag{3.18}$$

Then the $\text{SNR}^{\text{cam}}_{\text{ISVS}}$ is:

$$\text{SNR}^{\text{cam}}_{\text{ISVS}}(\tau_{\text{field}}) = \frac{1}{\left(1 + \frac{T}{4\tau_{\text{field}}}\left(\frac{1}{N_{ST}} + \frac{\sigma^2_{n_{\text{cam}}}}{U_I N^2_{ST}}\right)\right)} \sqrt{\frac{\text{NIO}}{3R-1}}. \tag{3.19}$$

$$\begin{aligned} \text{SNR}^{\text{cam}}_{\text{ISVS}}(\tau_S) &= \frac{\tau_s}{\text{SE}(\tau_s)} = \frac{\tau_{\text{field}}/2}{\text{SE}(\tau_{\text{field}})/2} \\ &= \frac{1}{\left(1 + \frac{T}{8\tau_s}\left(\frac{1}{N_{ST}} + \frac{\sigma^2_{n_{\text{cam}}}}{U_I N^2_{ST}}\right)\right)} \sqrt{\frac{\text{NIO}}{3R-1}} \quad \text{(From Siegert Relation)}. \end{aligned} \tag{3.20}$$

Similar to iSVS, for SVS, camera noise can be added to yield:

$$K^2 \approx \frac{2\alpha^2 {\bar{I}_S}^2 T \hat{\tau}_s + \alpha \bar{I}_S T + \sigma^2_{n_{\text{cam}}}}{\alpha^2 {\bar{I}_S}^2 T^2}. \tag{3.21}$$

and:

$$\text{SNR}^{\text{cam}}_{\text{SVS}}(\tau_s) = \frac{1}{\left(1 + \frac{T}{\tau_s}\left(\frac{1}{N_{ST}} + \frac{\sigma^2_{n_{\text{cam}}}}{N^2_{ST}}\right)\right)} \sqrt{\frac{\text{NIO}}{2}}. \tag{3.22}$$

Consequently, in iSVS, when $N_{ST} \leq \sigma_{n_{\text{cam}}}$ (low signal case), the reference laser light field can boost the SNR (Equation 3.19 and 3.20) and substantially decrease the influence of camera noise because $U_I \gg 1$. When $N_{ST} \gg \sigma_{n_{\text{cam}}}$ (high signal case), the camera noise term can be ignored. In this case, the two system's SNR performance converge. Note the decrease of SNR from camera noise is due to the fluctuation of the camera noise variance; in the original paper's Supplemental Document we detailed how such fluctuation is eventually expressed with camera noise variance.

The above analysis indicates that, even though iSVS is an interferometry method, the requirements on the reference field are significantly relaxed. While most interferometry methods require the reference field to be planar and have a spatially invariant phase (or a phase with a linear spatial ramp), iSVS can be performed with a reference field with a spatially varying phase and amplitude. The SNR of iSVS is not penalized by a spatially varying phase and is only mildly penalized by a factor of $\sqrt{2/(3R-1)}$ for spatial heterogeneity. It should be noted that the number of independent observables (NIO) may vary under extreme heterogeneous reference cases, such as when some pixels have a reference intensity lower than the camera noise or the signal intensity, which breaks the assumption overlying the above analysis. In such cases, one should just count those pixels out and modify the NIO appropriately. However, these pixels are generally an overwhelming small class when the average reference intensity is set much higher than the sample intensity. In the following iSVS experiments, the reference intensity is sufficiently high such that less than 0.1% of the pixels had a reference intensity lower than camera noise and corresponding $\bar{I_S}$, and therefore, the effect of scattered reference illumination on NIO was negligible in the experimental data presented in this paper.

Simulation result for iSVS SNR

Figure 3.1 shows the SNR as a function of the decorrelation time for different averaged sample beam intensities ($\bar{I_S}$), plotted with the following parameters: $\sigma^2_{n_{\text{cam}}} = 8$ ph/pxl, $I_R \approx 3000$ ph/(pxl.ms), NIO = 2000, and $T = 200$ μs. Camera noise variance is converted to keep consistency with the measured gray scale value. Note that the decorrelation time on the x-axis is the intensity decorrelation time. Also, the intensity units are in grayscale, but they should be comparable to later sections. Figure 3.1(a) demonstrated the ability of both iSVS systems, uniform reference and non-uniform reference, to achieve significantly better SNR than the typical SVS system as it overcomes the camera noise variance. In Fig. 3.1(b), the performance of SVS and uniform iSVS system overlaps, while non-uniform reference iSVS systems have a lower SNR as an result of larger R value from the speckled reference. From Fig. 3.1(c), a glance of SNR performance over a wide range of sample intensity, one note that iSVS performs better than SVS at low signal intensities ($\bar{I_S}$), but both uniform iSVS and SVS SNRs converge to the same performance as $\bar{I_S}$ is high enough to overwhelm the camera noise variance. The non-uniform reference penalizes the SNR, thus showing a lower SNR, but the advantage at low sample intensity levels still holds. To further validate the theoretical results, we generated

different speckle patterns numerically, and the numerical simulation also agrees with the results shown in Fig. 3.1.

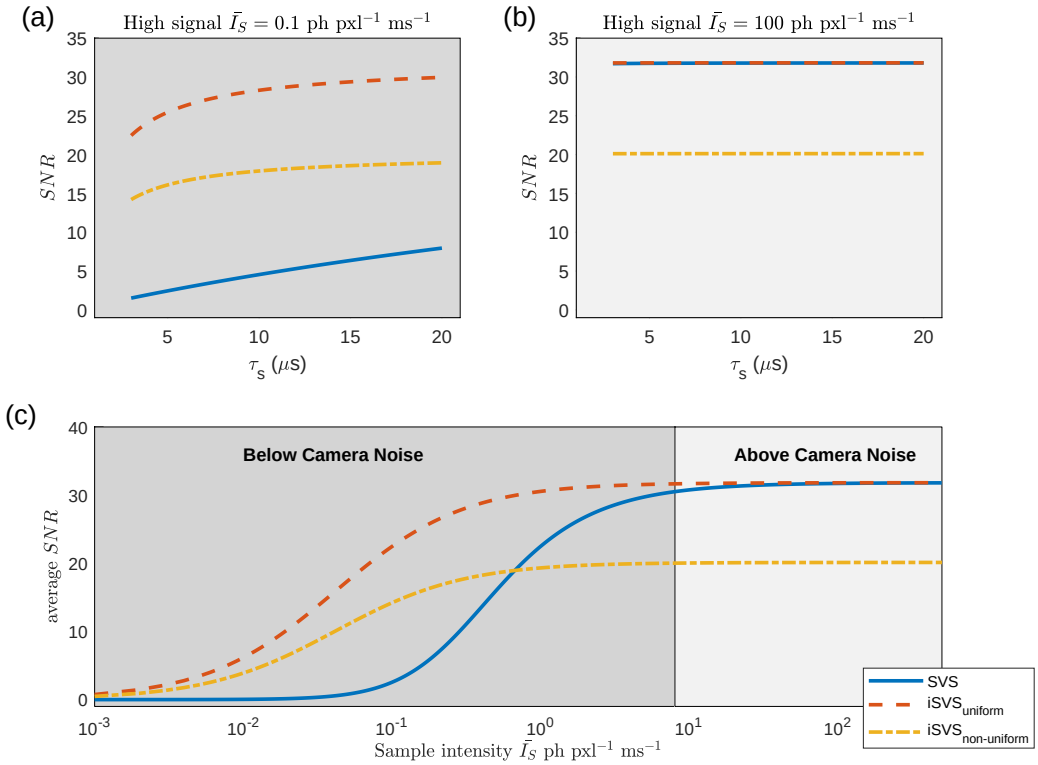


Figure 3.1: Theoretical comparison between iSVS and SVS by using the SNR and the derived speckle contrast equations. (a), (b) SNR as a function of the decorrelation time at different averaged intensities ($\bar{I}_S$) of the sample laser light field. The corresponding sample intensity is labeled in the title. Decorrelation time is the intensity decorrelation time τ_s. (c) average SNR as a function of $\bar{I}_S$ for $\tau_s = [3, 20]$ μs. As evident, iSVS performs better than SVS at low intensities ($\bar{I}_S$), but both converge to same SNR as $\bar{I}_S$ overcome the camera noise variance. Parameters: $\sigma^2_{n_{\text{cam}}} = 8$ ph/pxl, $I_R = 3000$ ph/(pxl.ms), NIO = 2000, and $T = 300$ μs. Reference beam is uniform ($R = 1$) or speckled in iSVS non-uniform ($R = 2$).

Experimental arrangement and results

To validate the theoretical and simulation results shown previously in sections 2 and in numerical simulations, we designed an experiment to measure the SNR utilizing a rotating diffuser and an interferometer. The rotating diffuser is controlled by a DC motor, whose rotation speed is digitally controlled; thus, the decorrelation time of the speckle images is controlled electronically. The experimental arrangement is shown in Fig. 3.2. It is based on a Mach-Zehnder interferometer, whose input

is a highly coherent (single-mode, single-frequency) continuous wave 532 nm collimated laser beam [Spectra-Physics Excelsior-532-200-LDRH]. Note that similar results should be obtained for any wavelength as long as the camera's quantum efficiency is reasonable at the illumination wavelength.

The input laser beam is first divided by a beam splitter ('BS1' in Fig. 3.2) into two light beams; one is the sample laser beam, and the other is the reference laser beam. The sample laser light beam propagates through a rotating diffuser and a static diffuser. The static diffuser counteracts the one-dimensional smearing effects from a single rotating diffuser, generating random speckles at the output. The reference laser light beam propagates in free space onto a second beam splitter ('BS2' in Fig. 3.2). A diffuser can be inserted in the path of the reference beam to generate a speckled reference laser light beam. We use tunable neutral density (ND) filters to control or to block (shut down) the intensities of the sample and the reference laser light beams. At the second beam splitter ('Beam Splitter 2' in Fig. 3.2), the two laser light beams interfere and form an interference pattern that is imaged to and recorded by a scientific CMOS camera sensor [PCO Edge 5.5] with an exposure time T.

To satisfy the prior of measuring $\langle N_j \rangle$ accurately, the reference laser light beam was blocked (at $t = 0$) by closing the reference arm shutter, creating a setup similar to an SVS setup, and $\langle N_j \rangle$ was estimated accurately from an average over 1000 images. This measurement is utilized later in calculating speckle contrast K and K^2 for iSVS. Camera noise and its variance are also measured with both shutters closing, measuring only the camera background fluctuations.

Note that we are using an on-axis Mach–Zehnder interferometer setup, wherein there is no angle between the reference and the sample beams. This approach, as showed in previous works on laser Doppler holography for human blood flow imaging, presents both advantages and limitations [44, 45]. On-axis design simplifies alignment and maximizes field of view, beneficial for working with lower sample beam intensities by leveraging the reference laser beam to mitigate both the camera and laser noise. However, on-axis lacks certain off-axis interferometry advantages like spatial Fourier filtering and frequency-shifted reference beam for selective frequency imaging [44, 45]. Since we are implementing an on-axis setup, there is no need to enforce an angle between the reference and the source; the two beams can be aligned to overlap each other.

A benchmark process is established to compare the performance of iSVS and SVS.

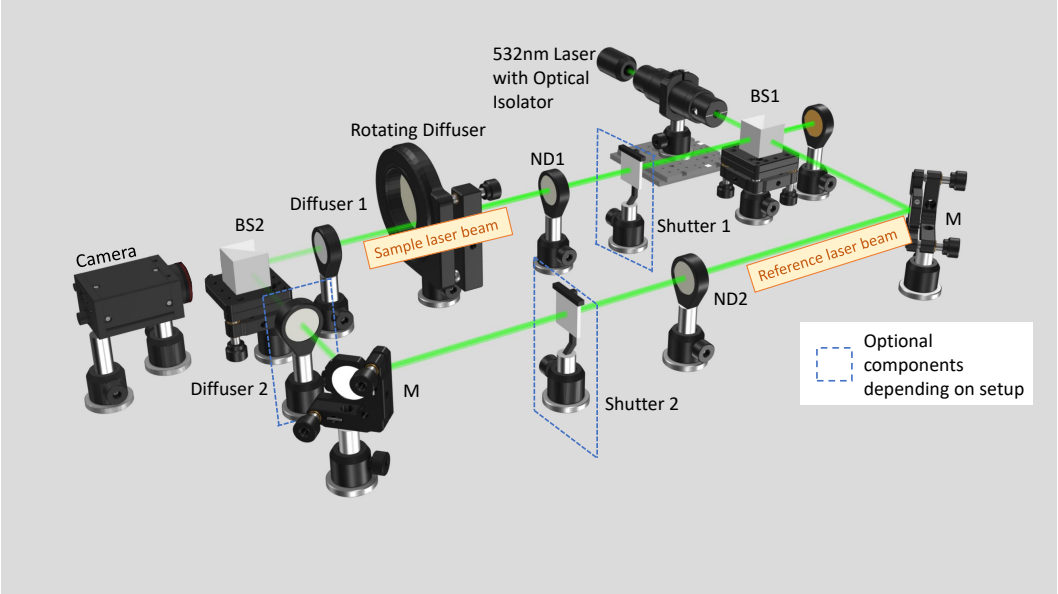


Figure 3.2: Experimental arrangement for measuring the decorrelation time and SNR of a rotating diffuser, acting as moving sample. A diffuser 2 can be inserted to generate a distorted (randomly scattered) reference laser light beam in iSVS. In SVS, the reference laser beam is blocked.

The benchmark includes rotating the diffuser at 16 different rotational velocities. The rotation speed starts at 0 percent, then goes from 25 percent to 95 percent in 5 percent increments. At 100 percent rotation speed, the motor operates at 30 rpm, and is believed to be linear across most of the range except for low rotation speed, which we have intentionally skipped. The speeds are specifically chosen such that $\tau_s \ll T$ holds true. A set of reference τ_s is obtained by DCS experiment operating at a high signal level using an adjustable optical receiver [Newport 2051-FS] sampling at 1.25 MHz. Then, the temporal autocorrelation curves are fitted with a negative exponential function, and decorrelation time is extracted for each rotation speed. Based on this benchmarking DCS reference experiment, the decorrelation time associated with the rotating diffuser was related to the rotational velocity of the DC motor, see the original paper's Supplemental Document.

Furthermore, despite incorporating the framework of shot noise and camera noise in theory, there are other external factors during experiments that would impact the noise profiles. To mitigate this and calibrate noise accurately, noise is measured instead of calculated: by closing both shutters, camera noise can be retrieved by calculating the variance of multiple measurements. Reference noise and sample arm noise can also be measured by keeping the diffuser in the static position and

making multiple measurements. A total of 100 calibration measurements are taken for each trial during experiments, and noise is measured and factored in for both SVS and iSVS. Details of the calibration are presented in the paper's Supplemental Document.

We also observed additional noise terms with low spatial frequency characteristics in the experiment. These terms are likely attributable to the experimental spatial uniformity of the reference field and unaccounted laser mode instability. They introduce systematic errors into the experimental determination of τ_{field} and τ_s. We addressed this by subtracting the empirically determined systematic error from the measured speckle contrast K prior to calculating the SNR. For the details regarding the offset calibration as well as results without calibration, please refer to the paper's Supplemental Document.

We also calculated the R values for the experimental reference beams. The distorted reference field pattern is speckled, but over 99.9% of the pixels are illuminated with a reference intensity larger than the camera noise variance, and therefore the effective NIO of the uniform reference iSVS and speckled reference iSVS can be considered equal. The uniform reference has a Gaussian spatial distribution with $R \approx 1.5$, while the speckled reference has $R \approx 1.9$. Therefore, the theoretical performance difference is about 15 percent—a relatively minor difference. Given the minor impacts of both considerations, we do not expect the two profiles of the reference beams used to significantly impact the SNR.

For each rotational velocity, 200 images are captured with a frame rate of 150 FPS and exposure time $T = 300\ \mu$s. For each of the 200 captured images, speckle contrast is calculated for both iSVS and SVS according to Eq. 4. During SVS experiments, the reference laser beam path is blocked. SNR without noise calibration is demonstrated in the paper's supplementary, but in the main text, we prefer to focus on the calibrated result as it offers better accuracy.

The calibrated SNR results are shown in Fig. 3.3. The ground truth is obtained by using the high sample intensity data. As detailed in the paper's Supplemental Document, a series of noise calibrations is executed to subtract noise measured empirically. As evident in the data, the experimental results shown in Fig. 3.3 coincide with the theoretical results in Fig. 3.2 and numerical results in the original paper's Supplementary. The overall trends in Fig. 3.3 match well with the expectation. Figure 3.3(a) shows iSVS performs better than SVS at low intensities ($\bar{I}_S$), where the SNR of the iSVS signal can still guarantee retrieval of decorrelation time while SVS

signal failed. In this case, the non-uniform, or scattered reference performed slightly worse than uniform iSVS as predicted by the theory. Figure 3.3(b) shows a situation where both iSVS and SVS signals converge to the same SNR as $\bar{I_S}$ overcomes the camera noise variance, indicating no disadvantage present for performing interferometry. We also observed a slight decay in SNR in longer decorrelation times, and this may be due to a larger motor rotation speed discrepancies at these lower percentages. In this case, the scattered reference SNR is in line with the uniform SNR. We attribute the lack of difference in performance to the larger temporal fluctuation that may overwhelm the 15% difference caused by the reference field shape. We note that given the similar NIO and other parameters, the SNR performance is slightly lower than theoretical and simulation values [1]. This can be attributed to instability in the DC rotating motor speed at a high rotation speed. Laser noise in the form of mode hopping, laser intensity fluctuations, and/or environmental noise can also disrupt the coherence condition required for iSVS's interferometry scheme. These factors lead to variations in the measurements [39].

Figure 3.3(c) shows the SNR as a function of the average signal intensities ($\bar{I_S}$) for the three cases: SVS, plane-wave uniform reference iSVS, and non-uniform speckled reference iSVS. Note that plane-wave reference iSVS and speckled reference iSVS exhibit an SNR index gain of at least two to three orders of magnitude higher at low signal situations than SVS. This allows the detection of the dynamics of the sample even if the signal level is below the camera noise. To achieve a similar SNR, iSVS and speckled iSVS both require 100 times fewer photons than SVS. Observe from Fig. 3.3(c) that there is no significant performance difference between the speckled reference iSVS and the uniform reference iSVS in the experiment. In low signal situations, the speckled non-uniform reference iSVS performed slightly worse, as shown in Fig. 3.3(a). However, this discrepancy diminishes as sample's signal strength increases. Again, the reason is likely because laser noise generates temporal fluctuations in reference intensity that equally affected both reference fields, overwhelming the 15% performance difference that may be presented with an ideal stable laser. Note that under the ideal situations, as shown in theory, SNR can reach up to 30, but in experiments the average SNR is constrained to 20 due to the aforementioned instabilities.

Conclusion and remarks on iSVS SNR

In this section, we found that, by the merit of interferometry's ability to suppress camera noise, iSVS can accurately measure field decorrelation time in situations

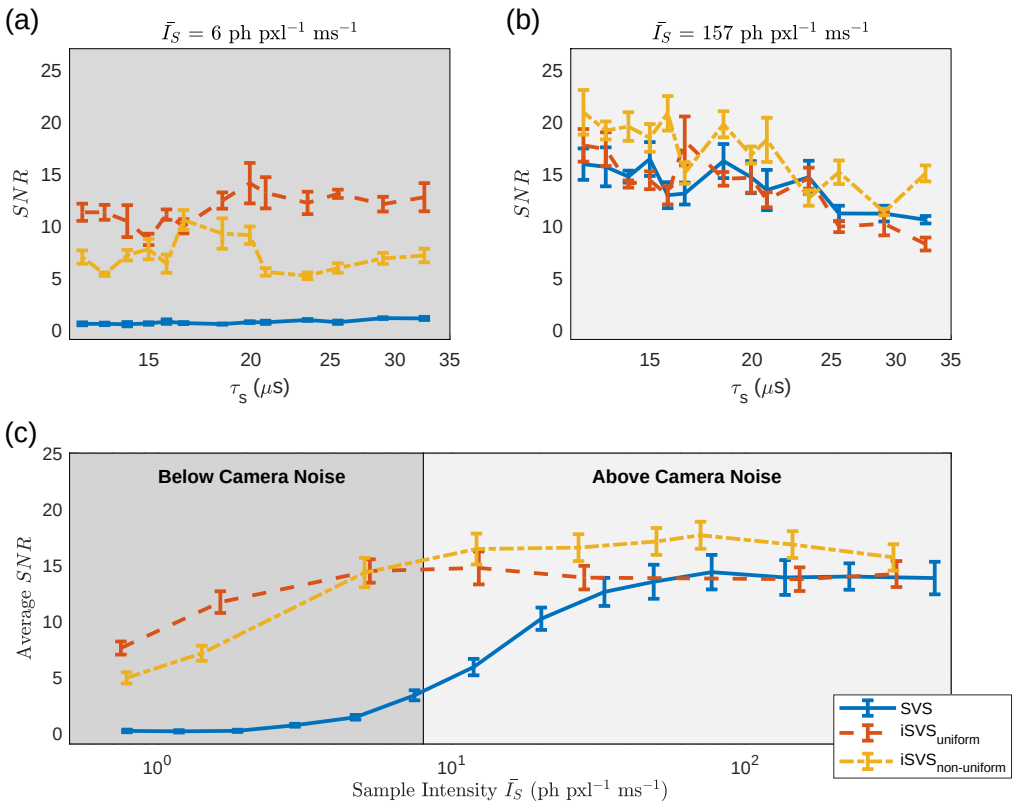


Figure 3.3: The iSVS and SVS experiment results using the measured speckle fields in the controlled experiment. (a), (b) SNR as a function of the decorrelation time at different averaged intensities ($\bar{I}_S$) of the sample laser light beam as specified in the title. X-axis τ_s derived DCS benchmark measurement associated with different rotation speeds. (c) Average SNR at various $\bar{I}_S$. As evident, iSVS performs better than SVS at low intensities ($\bar{I}_S$), but both converge to same SNR as $\bar{I}_S$ overcome the camera noise variance (as in Fig. 3.2). Parameters: $\sigma^2_{n_{\text{cam}}} = 8$ ph/pxl (converted from electron per pixel according to camera QE and conversion factor), $\bar{I}_R \approx 3000$ ph/(pxl.ms), NIO ~ 2000, and $T = 300$ μs.

where the signal would otherwise be overwhelmed by camera noise in an SVS setup. This is particularly important in biomedical applications where the signal intensity tends to be limited and may otherwise require expensive cooled cameras or low-noise detectors to detect DWS signals. We also found that iSVS and SVS performed similarly when the signal intensity is high. This indicates that SVS can be expected to be sufficient in high sample intensity applications. Also, iSVS is more robust to other noises and can be easily calibrated to obtain consistent decorrelation times predictions, while SVS requires a larger signal to overcome the noise. Moreover, the theory shows the potential way to increase SNR, such as utilizing larger sensors with more pixels or to choose exposure time suitable for the particular target's dynamics, but in many cases, the laser instability is the limiting factor that prevents experimental SNR from reaching the theoretical SNR. In this study, we additionally found that the reference field used in iSVS can be spatially heterogeneous (unlike most other interferometry applications), with the heterogeneity only leading to slight performance degradation. This flexibility can potentially open the design space in iSVS system design. For instance, specific interferometer designs of the optical systems can achieve simultaneous direct measurement of both field and intensity properties, as indicated in the theoretical derivation where both direct and cross terms are present in Eq. 3.11.

There is a potential advantage of iSVS that is not explored in this study – the ability to perform path length selection with a short coherence laser, which then can be applied to increase brain-to-scalp sensitivity in cerebral blood flow measurements. This capability can potentially be used in biomedical applications to select a sub-group of photon trajectories for detection. Further investigation can also explore more in depth on different types of decorrelations and how it impacted the results in SVS. There are also potential to apply existing calibrations to further suppress the noise, either by measuring them more accurately or through filtering, increasing accuracy at various signal ranges.

In summary, we have demonstrated a unified approach to characterize the accuracy and SNR of iSVS method compared to SVS. As [1] has made a similar comparison between SVS and DCS methods, albeit without the presence of noise, we now have a unified analytical approach for comparing the major DWS methods.

3.2 Compact speckle contrast optical spectroscopy

This section is adapted from published work: Huang, Y. X., Mahler, S., Dickson, M., Abedi, A., Tyszka, J. M., Lo, Y. T., Russin, J., Liu, C., Yang, C. (2024). *Compact and cost-effective laser-powered speckle contrast optical spectroscopy fiber-free device for measuring cerebral blood flow*. *Journal of Biomedical Optics*, 29(6), 067001.

In the previous section, we theoretically derived the Signal-to-Noise Ratio (SNR) advantage of employing interferometry in spatial sampling Diffusing Wave Spectroscopy (DWS) methods, such as SVS/SCOS and iSVS. We also experimentally demonstrated the signal boost achieved with a reference field. However, our *in vivo* study in Ref [46] revealed that despite using interferometry, we could not achieve the ideal theoretical limit. The maximum source-detector (S-D) separation was limited to approximately 2.3 cm to 2.5 cm. While photon counts remained sufficient at these distances, the signal was significantly corrupted.

This signal degradation stemmed from two primary issues. Firstly, as discussed previously, the subtraction of a reference field is crucial, but maintaining a strong, stable reference field over time proved challenging. Minor intensity fluctuations and mode hopping from the laser introduced residual errors after subtraction calibration. Secondly, the movement of the large-core (600 μm) multimode fiber was a significant culprit. Even slight fiber movements induced mode scrambling and hopping, leading to speckle movement not originating from blood flow dynamics but from subject motion. This artifact is particularly difficult to eliminate in *in vivo* measurements, where natural physiological movements like breathing occur.

These limitations prompted a new direction in our research. Our initial roadmap involved miniaturizing the interferometry approach (iSVS) into a compact module, a solution that would likely necessitate expensive and complex optical designs. However, a simpler alternative emerged, embodying the principle that "sometimes removing is adding."

In this section, I introduce the foundational setup for the second half of my PhD journey: compact SCOS. This innovative approach eliminates the need for optical fibers and long coherence length lasers by integrating the transmitting (Tx) laser diode module and receiving (Rx) CMOS sensor module directly onto the subject's head as an affordable, compact, and modular wearable device.

Introduction and Motivation

This section reports on a novel compact Speckle Contrast Optical Spectroscopy (SCOS) device specifically designed for monitoring relative cerebral blood flow (CBF) at extended source-detector (S-D) distances, exceeding 3 cm. This wearable sensor module offers a significant advancement over traditional approaches by integrating a continuous-wave laser diode and a high-resolution CMOS-based board camera directly onto the subject's head, requiring no external optical elements. The device provides real-time CBF monitoring with an improved sampling rate of 80 Hz, all while maintaining a lightweight and budget-friendly design.

While a similar wearable optical system has recently been employed to measure blood flow changes during breath-hold maneuvers [47], this section delves into the comprehensive design and data processing strategies of our compact SCOS system. Crucially, we present a detailed comparison of its enhanced stability and Signal-to-Noise Ratio (SNR) against conventional single-fiber-based SCOS. The compact SCOS device comprises a laser diode (source unit) controlled by a lightweight, compact driver powered by a 9V battery, all encased within the wearable sensor module. The detection unit consists of a CMOS camera connected to a computer via USB. Although this wired connection currently restricts full portability, we envision future iterations incorporating wireless camera connectivity, making the detector unit both compact and lightweight for truly wearable applications. The total cost of the compact SCOS device, excluding a laptop, is approximately $500, demonstrating its cost-effectiveness.

Our investigations reveal several key advantages of compact SCOS over its single-fiber-based counterpart. First, compact SCOS achieves a superior SNR by collecting a significantly larger number of photons due to an increased detecting area and numerical aperture. Specifically, the compact SCOS captures approximately 70 times more signal compared to a 600 μm single-fiber-based SCOS device, thereby dramatically improving the detectability of CBF at extended S-D distances beyond 3 cm. Second, and equally important, it effectively eliminates the motional artifacts commonly associated with optical fibers connecting the head to the camera, leading to demonstrably superior stability and reproducibility. In conventional setups, where large-diameter multimode fibers are used to guide photons from the head to the camera, even slight movements of the fiber can induce substantial speckle changes, corrupting measurement results [46, 29, 25]. While current mitigation strategies involve extraordinary measures to minimize fiber perturbations, these are often not

ideal for practical, real-world applications.

The remainder of this section is organized as follows. First, we provide a detailed description of the design and experimental arrangement of the proposed compact SCOS system, along with the data processing methodology for calculating blood flow from recorded camera images. Second, we present a comprehensive comparison of the performance of compact SCOS and single-fiber SCOS using both static and moving phantoms. Finally, we experimentally compare the blood flow measurements obtained from compact SCOS and single-fiber SCOS devices at various S-D distances from a cohort of five human subjects. Our results consistently demonstrate significant improvements in blood flow measurement capabilities with the compact SCOS device over the single-fiber SCOS system.

Engineering and construction of the device

The arrangement of our compact SCOS device is shown in Fig. 3.4. The system design is presented in Fig. 3.4(a), with a schematic on the left and a photograph of the 3D-printed device on the right. For size comparison, a dime is included in the photograph. The system fundamentally comprises a laser source for illumination and a board camera for detection.

For this study, we utilized a single-mode continuous-wave 785 nm laser diode [Thorlabs L785H1] as the illumination source, capable of delivering up to 200 mW. To precisely control the illumination spot size and mitigate undesirable laser light reflections or stray light, the laser diode was housed within a custom 3D-printed mount featuring a circular aperture of 5 mm. Similarly, the camera was also secured within its own 3D-printed mount. Both mounts were fabricated using black resin, which effectively absorbs light, thereby minimizing back reflection and stray light artifacts. The laser diode was positioned several millimeters away from the participants' skin, ensuring an illumination spot diameter of 5 mm [46]. The total illumination power was deliberately limited to 45 mW to guarantee that the laser light intensity within the illumination area remained well within the American National Standards Institute (ANSI) laser safety standards for maximum permissible exposure (2.95 mW/mm^2) for skin exposure to a 785 nm laser beam [38]. Further details regarding study participation can be found in the paper's Supplementary Material.

At a predetermined S-D distance from the illumination spot, the detector was carefully positioned on the subject's head to collect the emerging light away from the

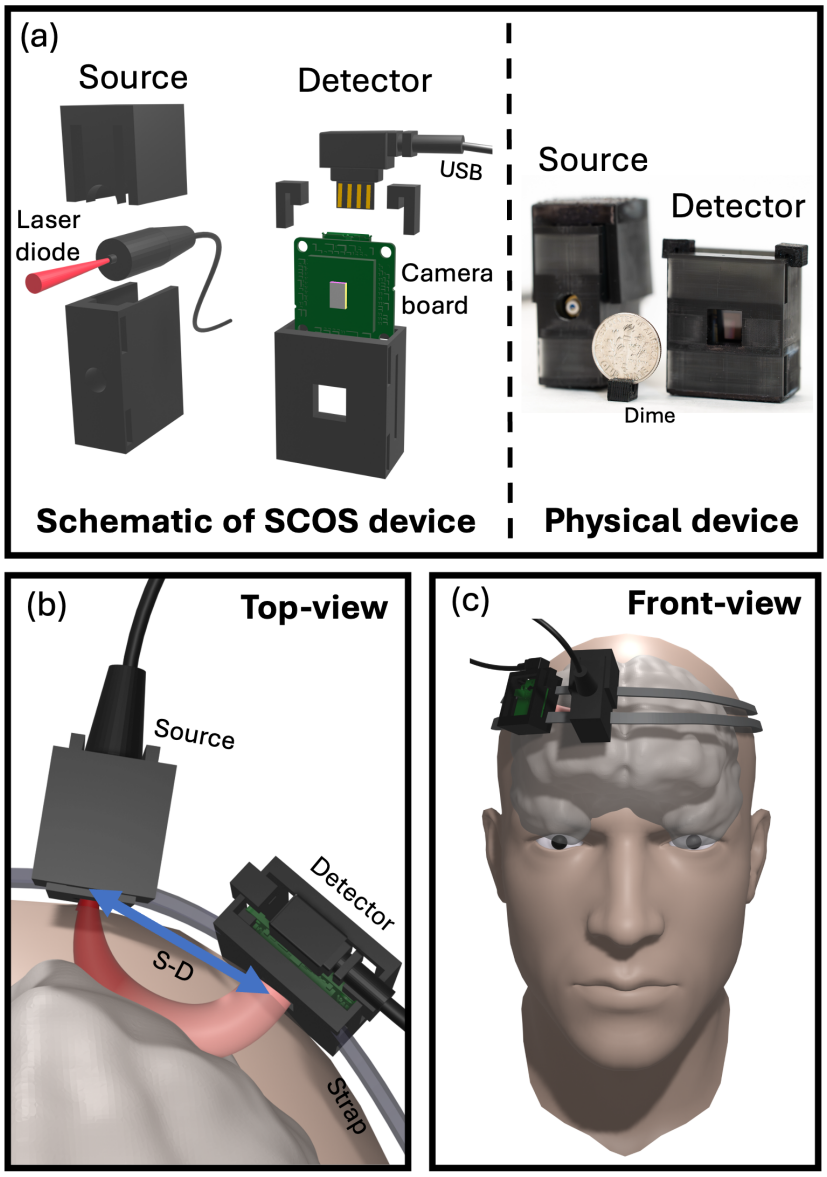


Figure 3.4: Compact speckle contrast optical spectroscopy (SCOS) device. (a) Design of the SCOS device. The system comprises a laser diode (source) and a CMOS-based board camera (detector), both integrated into a custom 3D-printed mount. The left panel shows an exploded 3D schematic breakdown, illustrating component arrangement. The right panel presents a photograph of the assembled SCOS device, with a dime included for scale. (b) Top-view schematic and (c) front-view schematic illustrating the SCOS device positioned on a subject's forehead. When secured at a specific source-detector (S-D) distance, the compact SCOS device is designed to effectively measure cerebral blood flow (CBF).

laser illumination point, as illustrated in Figs. 3.4(b) and 3.4(c). The collected laser light was directed onto a specifically chosen camera featuring a large sensor area and small pixel size, a configuration designed to maximize the number of captured speckles. For this purpose, we employed a USB-board camera [Basler daA1920-160um, equipped with a Sony IMX392 sensor]. For optimal performance and stability during measurements, the camera was typically operated at a framerate of 80 frames-per-second (fps). While the compact SCOS system possesses the capability to achieve a sampling rate of up to 160 fps, it was capped at 80 fps to strike an optimal balance between storage space requirements and desired temporal resolution.

The camera features a pixel pitch of 3.4 μm. This specification offers a deliberate balance between the average intensity per pixel and the number of speckles per pixel, which was estimated to be approximately 10 speckles per pixel. This corresponds to a one-dimensional speckle-to-pixel length ratio (s/p) of 0.3. While a s/p ratio of two or above is typically utilized for conventional speckle imaging, our primary interest here lies in extracting the dynamics of the scattering medium through speckle statistics. For this specific application, it has been previously demonstrated that the maximum Signal-to-Noise Ratio (SNR) can occur at s/p ratios close to or even lower than one [1, 48, 49]. Additional details are provided in the paper's Supplementary Material.

Processing: from images to blood flow

The depth to which photons travel into the head is directly related to the S-D distance [50, 46]. By tuning this distance, one can adjust the penetration depth into the head, where a characteristic banana-shaped spatial sensitivity of the light path is typically observed, as depicted in Fig. 3.4(b) [50, 46]. As the S-D distance increases, this banana-shape extends deeper into the brain, making deeper brain regions progressively more challenging to access. The spatial distribution of the exiting photons collected by a camera exhibits a granular pattern of high and low intensity, known as speckles. Speckles arise from the interference between numerous random scattering events within the coherent light field and constitute a vast area of research. We image these speckles onto a camera with a finite exposure time, as illustrated conceptually in Fig. 3.5(a). The camera must operate at a sufficiently high frame rate to temporally resolve the dynamics, typically above 20 fps for accurate blood flow measurements. Speckles undergo dynamic changes with a specific temporal evolution [51, 52, 53], primarily characterized by the decorrelation time τ_c

of the speckle field [31, 30]. The camera is configured with an exposure time T that is significantly larger than the decorrelation time τ_c. Motions within the light paths, predominantly due to the movement of red blood cells, scatter the light and alter effective optical path lengths, resulting in a fluctuating speckle field that varies over time. As the speckle field fluctuates, the recorded speckled image becomes smeared and washed out: a shorter speckle decorrelation time leads to a more pronounced washout effect. The dynamics of these speckles can be quantitatively assessed by calculating the speckle contrast of the recorded image.

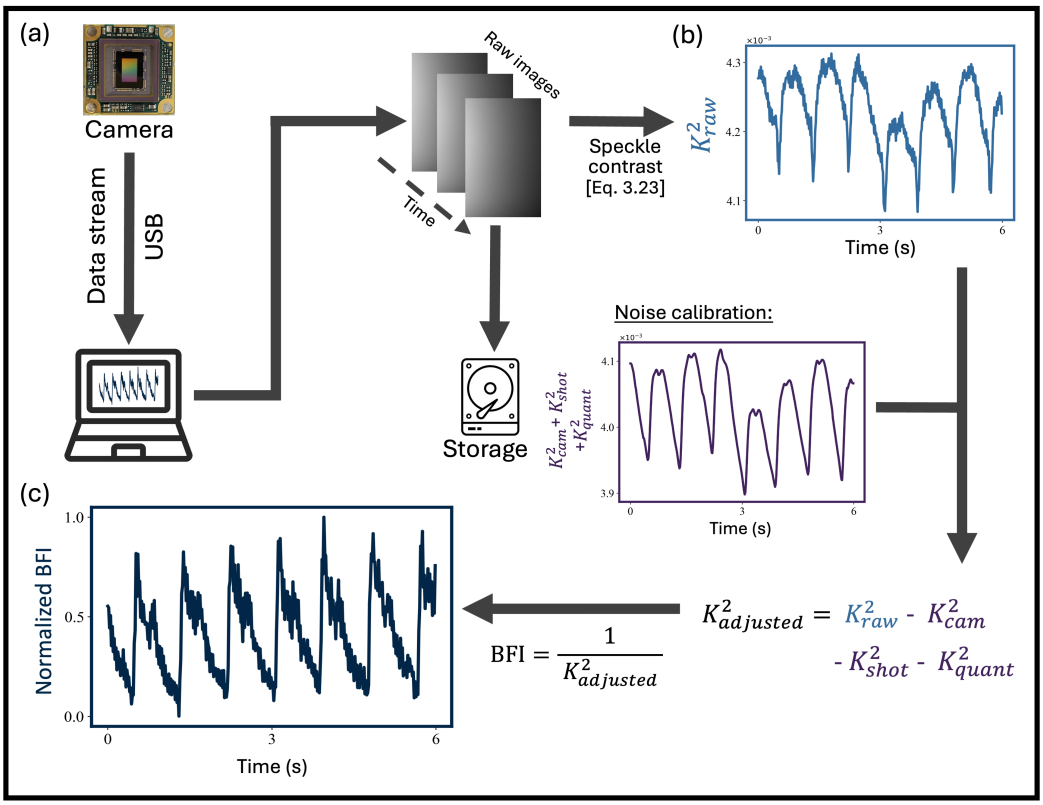


Figure 3.5: Compact SCOS processing analysis flowchart for deriving the blood flow from recorded camera images. (a) Recording and storing of SCOS camera images. (b) Measured raw speckle contrast calculated from the images in (a). (c) Calculated blood flow index (BFI) after calibrating the raw speckle contrast in (b).

The experimental SCOS processing analysis flowchart for deriving blood flow from recorded camera images is detailed in Fig. 3.5. The initial step involves removing the non-uniform intensity distribution from the camera images (normalization). Due to the camera sensor's proximity to the laser source on one side, pixels closer to the source will exhibit a higher recorded intensity readout than those further away. For more specific details regarding the normalization method, please refer

to the original paper's Supplementary Material. Subsequently, the squared speckle contrast $K^2_{raw}(I)$ of the normalized image, conceptually shown in Fig. 3.5(a), is calculated using:

$$K^2_{raw}(I) = \frac{\sigma^2(I)}{\mu^2(I)} \tag{3.23}$$

Here, $\sigma^2(I)$ represents the variance of the normalized image I, and $\mu(I)$ is its mean. This initial calculation, however, does not account for various noise sources that contribute to the image variance. To address these contributions, we employ an adjusted squared speckle contrast, $K^2_{adjusted}$, which is commonly calculated as [29, 54, 55, 56]:

$$K^2_{adjusted} = K^2_{raw} - K^2_{shot} - K^2_{quant} - K^2_{cam} \tag{3.24}$$

In this equation, K^2_{shot} accounts for variance contributions stemming from shot noise, K^2_{quant} for variance inherited from quantization, and K^2_{cam} for variance contributions from the camera's readout noise and dark noise. Refer to Fig. 3.5(b) for examples of raw and noise speckle contrast measurements. For each image $\tilde{I}$, these noise terms can be calculated as follows [29, 54, 55, 56]:

$$K^2_{shot}(I) = \frac{\gamma}{\mu(I)}, \tag{3.25}$$

$$K^2_{quant}(I) = \frac{1}{12\mu(I)^2}, \tag{3.26}$$

$$K^2_{cam}(I) = \frac{\sigma^2_{cam}}{\mu(I)^2}. \tag{3.27}$$

In Eq. (3.25), γ represents the analog-to-digital conversion ratio associated with the camera. This ratio depends on the gain setting and the conversion factor (CF) of the camera, expressed as γ = gain/CF. In our investigations, the gain was set within a range of 1 to 72, corresponding to a 0 to 37 dB setting. The gain was dynamically tuned based on the signal intensity. When operating in 8-bit mode, the Basler camera utilized in this study had a conversion factor of CF=40.7. To minimize quantization noise, the camera's gain was adjusted such that the readout grayscale values typically fell within the range of 40 to 255 during 8-bit recording, unless the signal intensity was too low. The camera noise σ^2_{cam} was estimated by

calculating the variance of a series of 500 camera images recorded in the complete absence of any illumination sources.

The blood flow index (BFI) can be related to $K^2_{adjusted}$ through the following empirical relationship [33, 57]:

$$\text{BFI} = \frac{1}{K^2_{adjusted}}. \tag{3.28}$$

In all results presented in this section, we utilize the normalized blood flow index (normalized BFI) metric to provide normalized blood flow information, enhancing comparability across various measurements. For further details on absolute blood flow measurement, please consult the original paper's Supplementary Material. Figure 3.5(c) illustrates a representative example of blood flow dynamics measured with our SCOS device positioned on the forehead. The BFI metric effectively accounts for the total volume of blood moved within a given time period. According to classical fluid mechanics and Poiseuille's law, blood flow (BF) can be expressed as $\text{BF} = (\delta P \pi r^4)/(8\eta L)$, where δP represents the difference in blood pressure, r denotes the radius of the blood vessel, η is the dynamic viscosity of the blood, and L signifies the length of the blood vessel [58]. Thus, any alteration in the BFI implies a change in either the blood pressure or the diameter of the blood vessel. It is particularly noteworthy that even a slight adjustment in the blood vessel's radius can have a profound impact on blood flow due to its fourth-power relationship with r. Such variations are especially significant as they accompany the modulation and regulation of blood flow [59].

It is important to note that the computational requirements for calculating the speckle contrast in Eqs. (3.23)–(3.28) from the recorded camera images are manageable by a standard consumer-grade computer [e.g., AMD 7950X CPU]. The most resource-demanding steps are the normalization of the images and the initial calculation of K^2_{raw} in Eq. (3.23), as the noise terms in Eq. (3.25)–(3.27) typically only need to be calculated once (during pre-calibration) or are already partially derived in the process of calculating K^2_{raw}. Therefore, the data recorded from our compact SCOS device can be processed and stored in real-time by utilizing a dedicated Basler USB-PCIE card and a Solid State Drive (SSD). Furthermore, the device design also allows for potential expansion to multiple channels.

Compact SCOS results: signal and stability improvements

The experimental configuration for this comparison is depicted in Fig. 3.6(a). This setup features a continuous-wave 785 nm laser diode, serving as a common light source, with two SCOS detection modules symmetrically placed on each side of the laser source at identical source-detector (S-D) separation distances. On one detection side, the compact SCOS module was composed of a board camera [Basler daA1920-160um], directly positioned on the sample. On the opposing detection side, the fiber SCOS module utilized a 600-μm core diameter multimode optical fiber [Thorlabs FT600UMT], also positioned on the sample. The distal end of this fiber was coupled onto an identical camera to the one used in the compact version [46]. It is important to note that for our comparisons, we employed a single fiber with a 600-μm core diameter, although systems exist with larger core multimode fibers (up to 1.5 mm) or with fiber bundles that offer improved signal collection capabilities [60, 61].

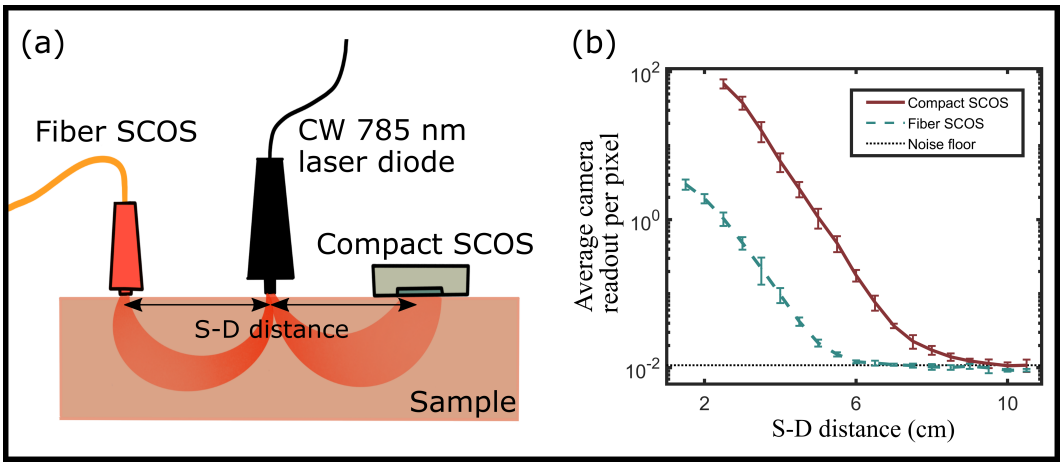


Figure 3.6: Experimental comparison between fiber SCOS and compact SCOS: (a) Overview of the experimental setup. (b) Average camera readout per pixel in analog-to-digital unit for fiber and compact SCOS measured at various S-D distances on a static sample. Notably, the compact SCOS demonstrates a significantly higher readout signal, averaging approximately 70 times more than its fiber counterpart. The fiber SCOS reaches the noise floor level at an S-D distance of approximately 5.5 cm, whereas the compact SCOS maintains a robust signal up to S-D distance of 8.5 cm.

Theoretically, we anticipate the compact SCOS version to yield a signal gain of approximately 70 times compared to the fiber SCOS, primarily as a result of its substantially increased collection area. The camera sensor's dimensions are 6.6 mm by 4.1 mm, resulting in an approximate sensor area of 27 mm^2. This contrasts

with the 0.28 mm^2 area of the 600-μm diameter multimode optical fiber, leading to an approximate 95-fold gain in detecting area. However, the camera sensor in the compact SCOS is positioned with a 5 to 7 mm gap from the sample, whereas the fiber is typically placed in direct contact with the sample. In this specific configuration, we calculated the numerical aperture (NA) of the camera using the formula $\text{NA} = n\sin(\theta) = n(d/2)/\sqrt{((d/2)^2 + z^2)}$, where n is the refractive index of air (assumed $n = 1.00$), θ is the half-angle of the cone of light entering the camera, d represents the dimension (either in x or y) of the camera sensor ($d_x = 4.1$ mm and $d_y = 6.6$ mm), and z is the distance between the skin/sample and the camera ($z = 7$ mm). Given the differing sensor dimensions, the NAs of the camera were calculated independently for the x and y directions. Based on these figures, we found $\text{NA}_x = 0.28$ and $\text{NA}_y = 0.42$. For comparison, the fiber utilized has a numerical aperture of $\text{NA}_{fiber} = 0.39$. By accounting for the NA difference between the camera and the fiber, we theoretically expect the collected signal gain between the compact SCOS over single-fiber SCOS to be approximately $(\text{NA}_x \cdot \text{NA}_y)/(\text{NA}_{fiber})^2 \cdot (\text{Area}_{CMOS})/(\text{Area}_{fiber}) \approx 75$ times.

To experimentally validate this predicted gain, we utilized a static sample (a block of meat) and measured the average camera readout per pixel at different S-D distances for both detection systems. The camera readout per pixel was defined in analog-to-digital units, representing the average grayscale readout of the camera per pixel. While this can be converted to physical measurements such as flux or number of electrons, direct comparison of analog-to-digital units is fair given that both cameras are identical models and the experiment was conducted with consistent camera settings. The S-D distances ranged from 1.5 cm (for the fiber SCOS) to 10.5 cm, and from 2.5 cm (for the compact SCOS) to 10.5 cm. The physical size of the encasing blocks prevented the use of smaller S-D distances. The results are presented in Fig. 3.6(b) and represent averages over six different realizations conducted at various locations. Error bars were estimated by calculating the standard deviation across these six realizations. As demonstrated, the compact SCOS consistently captured a greater number of photons compared to the fiber SCOS system across all tested S-D distances. By calculating the signal ratio between the two systems, we determined that the compact version captures approximately 70 times more signal than its fiber-based SCOS counterpart. This significant improvement leads to enhanced detectability at extended S-D distances, effectively extending the measurable range by approximately 2.5 cm for the same signal readout in this specific case. It is important to note that both devices eventually reach the camera's noise floor, albeit

at different S-D distances. The fiber SCOS reached the noise floor level at an S-D distance of approximately 5.5 cm, whereas the compact SCOS maintained a robust signal even at an S-D distance of 8.0 cm on a static sample. These results unequivocally showcase the superiority of compact SCOS over fiber SCOS in its ability to collect more signal, thereby enabling the detectability of blood flow at significantly extended S-D distances. This increase in signal collection has not yet considered the additional increase in stability achieved by eliminating potential fiber movement during the camera exposure time.

Next, we characterized the stability of the compact SCOS relative to the fiber SCOS. To achieve this, we designed two distinct experiments where relative flow index values were calculated as described in Eqs. (3.23)–(3.28) and as conceptually depicted in Fig. 3.4.

In the first experiment, illustrated in Fig. 3.7(a), both the compact and fiber SCOS systems were affixed on top of a single-layer phantom. This phantom consisted of a sealed container filled with a liquid mixture [3D printing resin] [46]. The liquid mixture within the phantom was agitated on an orbital shaker (ONiLAB) set at a rotating speed of 90 rotations per minute [46]. The laser source, compact SCOS, and single-fiber SCOS systems were securely fastened to the phantom using the strap slots of their respective 3D-printed mounts (refer to Fig. 3.4 schematics). The phantom itself was affixed to the orbital shaker using straps that engaged with the shaker's dedicated strap slots. A non-slip rubber mat was utilized to ensure optimal adhesion and stability of the entire setup. Both the compact SCOS and fiber SCOS systems rotated synchronously with the liquid mixture. During each rotation, the SCOS systems measured the change in decorrelation time within the liquid mixture [46]. In this context, the SCOS systems effectively measured a liquid flow dynamic analogous to human blood flow dynamics (see Appendix A of Ref [46]).

The compact SCOS and fiber SCOS were deliberately set at S-D distances that yielded an equivalent photon count. In this configuration, the light power collected by both the compact SCOS and fiber SCOS detection systems was equivalent. Consequently, we were able to assess the inherent stability of the compact SCOS and fiber SCOS by comparing the recorded liquid flow from the rotating phantom. The results of this experiment are shown in Fig. 3.7(b). As anticipated, the liquid flow measured by the compact SCOS exhibits superior signal quality compared to that obtained by the fiber SCOS. This observation is further validated when examining the frequencies present in the Fourier spectrum of the flow index signal, I, presented

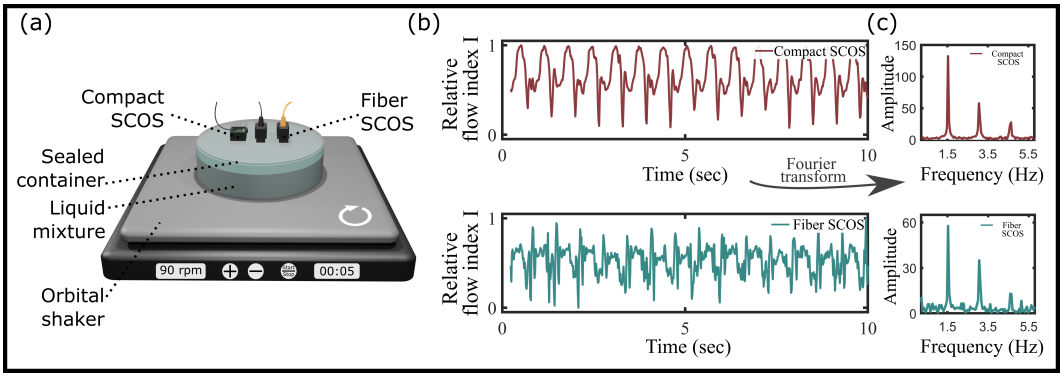


Figure 3.7: Experimental comparison of flow reproducibility between fiber SCOS and compact SCOS by using a one-layer phantom rotating on an orbital shaker. (a) Experimental arrangement. (b) Measured flow index. (c) Rotating frequencies obtained by Fourier transforming the flow signal in (b).

in Fig. 3.7(c). The prominent Fourier amplitude peak, centered around 1.5 Hz, precisely corresponds to the rotational frequency of the orbital shaker (90 rotations per minute, which translates to 1.5 rotations per second). However, a discernibly higher noise level is evident in the fiber SCOS Fourier spectrum, indicating that the measured flow index from the fiber SCOS is less reproducible than that from the compact SCOS. To quantitatively evaluate the reproducibility of the measured liquid flow signal, we computed the Pearson correlation factor for each SCOS system as:

$$\rho(I(t), I(t+dt)) = \frac{\sum_{t=1}^{T}(I(t)-\bar{I})(I(t+dt)-\bar{I})}{\sqrt{\sum_{t=1}^{T}(I(t)-\bar{I})^2 \sum_{t=1}^{T}(I(t+dt)-\bar{I})^2}} \tag{3.29}$$

where $I(t)$ is the measured flow signal shown in Fig. 3.7(b), $\bar{I}$ is the mean flow index, and $I(t+dt)$ is the signal shifted by one period, $dt = 1/(1.5\text{ Hz}) = 0.66\text{ s}$. The computed Pearson correlation factor for the compact SCOS was $\rho_{compact} = 0.94$, while for the fiber SCOS it was $\rho_{fiber} = 0.67$. This stark difference conclusively demonstrates that the measured periodic signal from the compact SCOS is significantly more stable and reproducible than that from its fiber-based counterpart.

Next, we further investigated the robustness of both systems against human head movements, as conceptually presented in Fig. 3.8(a). To conduct this assessment, both SCOS systems were positioned on the forehead of a subject, with a static scattering block carefully interposed between the SCOS setups and the subject's forehead. This static scattering block comprised a rigid block of packaging foam, which was complemented by a thick layer of black tape on its backside to prevent

any laser light from entering the subject's head. Consequently, the SCOS systems exclusively detected light interacting with the static scattering block itself. The source-detector (S-D) distances for both the compact SCOS and fiber SCOS were set to be equivalent, in order to accurately replicate cerebral blood flow (CBF) data acquisition scenarios. As a direct consequence of this setup, the signal intensity observed on the fiber SCOS was approximately 70 times lower than that of the compact SCOS, consistent with our previous findings regarding signal collection efficiency.

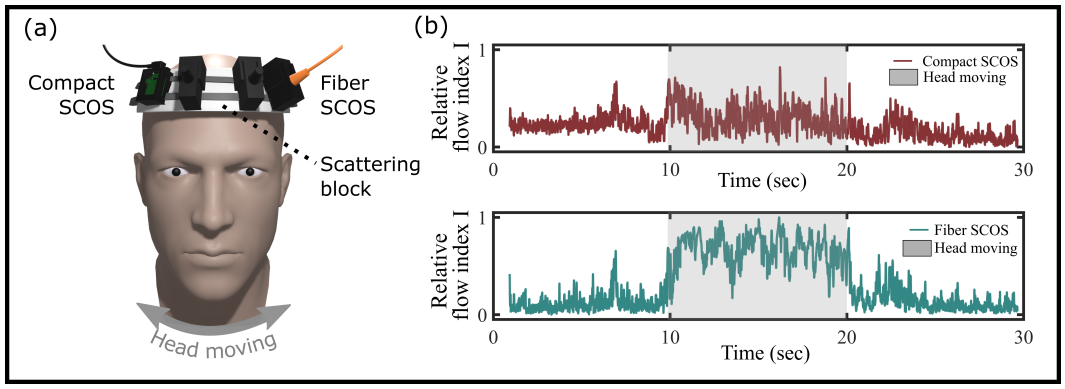


Figure 3.8: Experimental comparison of stability between fiber SCOS and compact SCOS by using a static scattering block on the forehead of a subject. (a) Experimental arrangement. (b) Measured flow index where the head is moving from 10 to 20 sec.

The measurement was performed over a 30-second interval, strictly adhering to a specific protocol: from 0 to 10 seconds, the subject maintained a still position; at the 10-second mark, the subject was instructed to laterally move their head (left to right and right to left) for the subsequent 10 seconds; and finally, the subject resumed a stationary position for the remaining 10 seconds. The results of this experiment are presented in Fig. 3.8(b). As shown, the flow measured by the compact SCOS exhibits significantly less noise and movement-induced artifacts compared to the fiber SCOS during periods of head movement. Furthermore, the overall flow index notably rises during head motion, a phenomenon attributable to the SCOS systems' movements accompanying the subject's head motions. As evident in Fig. 3.8(b), this increase in flow is more pronounced for the fiber SCOS than for the compact SCOS, indicating that the compact SCOS experiences less movement-induced vibrations and decorrelation than the fiber SCOS during head motions. The more prominent shift observed in the fiber SCOS is primarily due to additional decorrelation resulting from fiber movement, which leads to lower contrast and consequently, a higher calculated flow index. By eliminating the fiber

altogether, this significant source of instability is largely removed, resulting in the compact SCOS consistently displaying more stable and reliable flow measurements even in the presence of subject movements.

The results presented in Figs. 3.7 and 3.8 conclusively demonstrate that despite both systems being susceptible to noise induced by head motion, compact SCOS exhibits superior stability compared to fiber SCOS. In traditional fiber-based SVS, two primary factors contribute to noise during head motion: the subtle movements of the fiber tip in direct contact with the sample, and the amplified mode mixing of laser light within the vibrating optical fiber itself. Compact SCOS, however, is inherently more resilient to sensor movement at the sample interface due to its larger surface contact area and increased sensor size. Crucially, compact SCOS completely eliminates the issue of mode mixing, as it does not rely on an optical fiber for light delivery or collection. It is important to acknowledge that other sources of noise during head movement are common to both systems; for instance, any movement of the laser source will alter the trajectories of the laser light within the sample, thereby resulting in shifts and movements in the transmitted speckle pattern.

Compact SCOS results on human forehead

To comprehensively determine the capability of the compact SCOS system to detect cerebral blood flow (CBF) at large source-detector (S-D) distances, we further tested both SCOS systems by measuring blood flow on the forehead of a human subject. These measurements were conducted at S-D distances ranging from 3 cm to 5.5 cm. To specifically assess deep cerebral blood flow dynamics, it is crucial to configure the system such that it detects a larger proportion of the signal originating from the brain compared to the superficial scalp and skull layers. Previous studies have demonstrated that laser light propagating inside the human head follows a "banana" spatial sensitivity profile, which extends deeper into the head as the S-D distance increases [2, 50, 46, 62, 63, 64]. The brain sensitivity has been reported to significantly increase with depth of penetration, particularly with S-D distances greater than 3 cm. It is important to note, however, that even at such large S-D distances, the collected signal would still be influenced by blood flow within the scalp. Techniques such as time-gating [19] or calibration via short S-D measurements [65] have been previously proposed to filter out extraneous signals originating from the scalp and skull layers.

The results of these human forehead measurements are presented in Fig. 3.9.

Figure 3.9(a) displays the measured blood flow obtained by both the compact and fiber SCOS systems at S-D distances of 3 cm, 4 cm, and 5 cm. Figure 3.9(b) shows the normalized Fourier transform of the blood flow signals presented in Fig. 3.9(a). The prominent Fourier amplitude peak, centered around HR = 1 Hz, corresponds to the subject's heart rate amplitude peak [46]. We rigorously verified that the heart rate measured by our systems matched that obtained from a standard pulse oximeter.

The quality of the measured blood flow signal can be quantitatively assessed by examining the amplitude of this heart rate Fourier peak [46]. Figure 3.9(c) illustrates the amplitude of the heart rate Fourier peak at various S-D distances, ranging from 3 cm to 5.5 cm, for both the compact and fiber SCOS. These results were averaged over three independent realizations. As clearly shown, the compact SCOS consistently exhibits a significant gain in heart rate peak amplitude over the fiber SCOS system across all tested S-D distances. Finally, the heartbeat frequency of the subject can be determined by measuring the frequency of the heart rate freq_{HR} Fourier peak [46]. The measured SCOS heart rate, freq_{HR}^{SVS}, can then be compared with the heart rate obtained from a standard pulse oximeter, $\text{freq}_{HR}^{oxymeter}$, by calculating the relative percentage error as:

$$\Delta\text{freq}_{HR} = \frac{|\text{freq}_{HR}^{oxymeter} - \text{freq}_{HR}^{SVS}|}{\text{freq}_{HR}^{oxymeter}} \times 100\% \tag{3.30}$$

Figure 3.9(d) presents the heart rate relative percentage error across the S-D distances for both the compact and fiber SCOS systems. As evident, the compact SCOS consistently demonstrates a lower error than the fiber SCOS system within S-D distances ranging from 3 cm to 5 cm.

Finally, the measurements detailed in Fig. 3.9 were subsequently repeated on a cohort of five human subjects. The aggregate results from this cohort study are presented in Fig. 3.10, showcasing both the amplitude of the heart rate Fourier peak and the heart rate relative error at different S-D distances for both SCOS systems. For each subject, three independent realizations were recorded. The overall results were then averaged across the five different subjects, with the error bars determined by calculating the standard deviation. Across all five subjects, compact SCOS consistently demonstrated a significant gain in signal quality over the fiber SCOS, successfully measuring CBF up to an S-D distance of 5 cm. Based on Fig. 3.10(a), the heart rate peak amplitude (I_{freqHR}) for the compact SCOS at an S-D distance of 5 cm is comparable to that obtained at an S-D distance of only 3 cm for the fiber

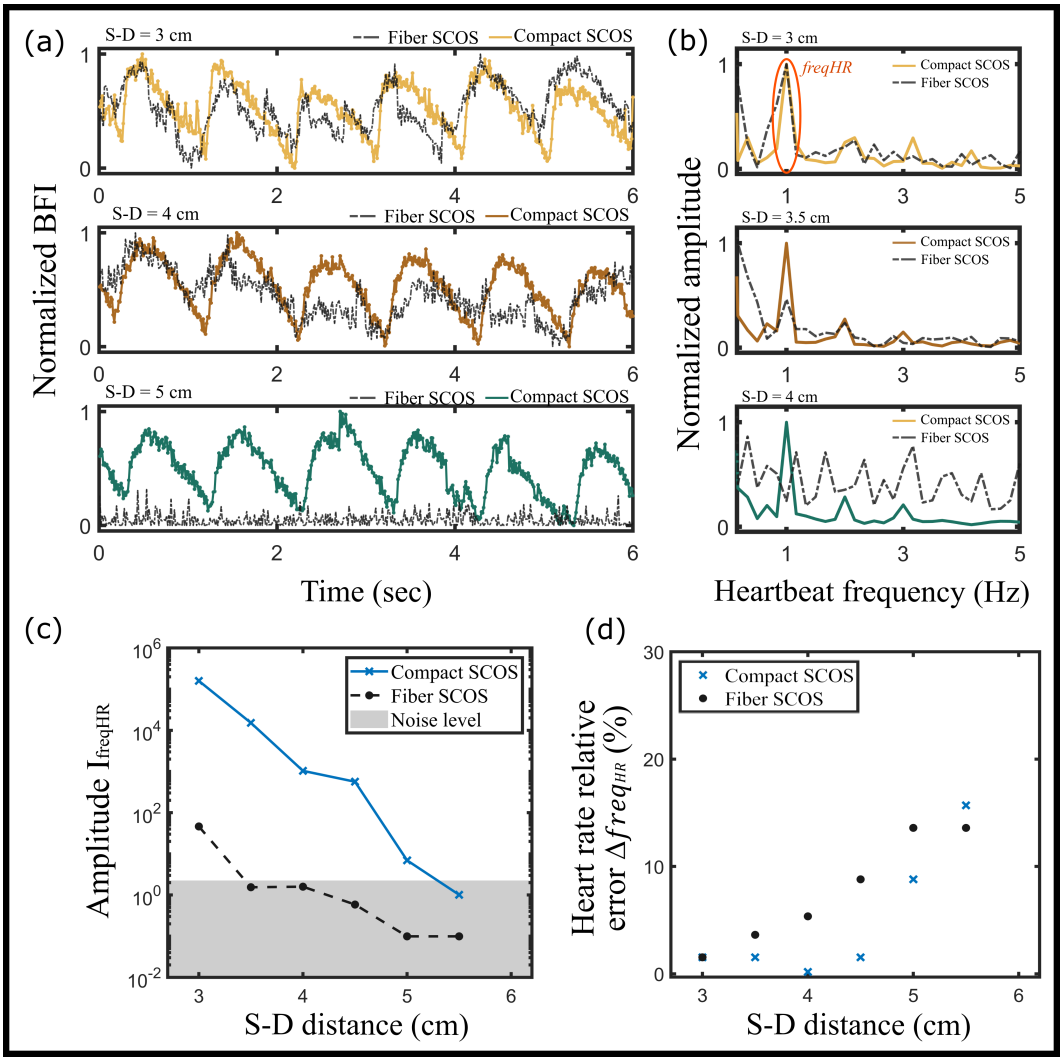


Figure 3.9: Experimental comparison between fiber SCOS and compact SCOS for cerebral blood flow measurement on a human forehead. (a) Representative measured blood flow signals obtained at different source-detector (S-D) distances on the forehead of a human subject. (b) Normalized Fourier transform of the blood flow signals shown in panel (a), illustrating the presence of the heart rate frequency peak. (c) Amplitude of the heartbeat frequency peak (I_{freqHR}) as a function of the S-D distance for both SCOS systems. (d) Heart rate relative percentage error between the SCOS measurements and a standard pulse oximeter. For panels (c) and (d), the results were averaged over three independent realizations, demonstrating consistency.

SCOS. This enhanced performance is further validated by the correct prediction of the heart rate frequency at larger S-D distances, as illustrated in Fig. 3.10(b). The more pronounced error bars observed at larger S-D distances for the fiber SCOS result from the signal being heavily masked by noise, leading to inconsistent and unreliable heart rate predictions across different realizations and subjects. Typical measured blood flow signals across the five subjects are shown in the original paper's Supplementary Material.

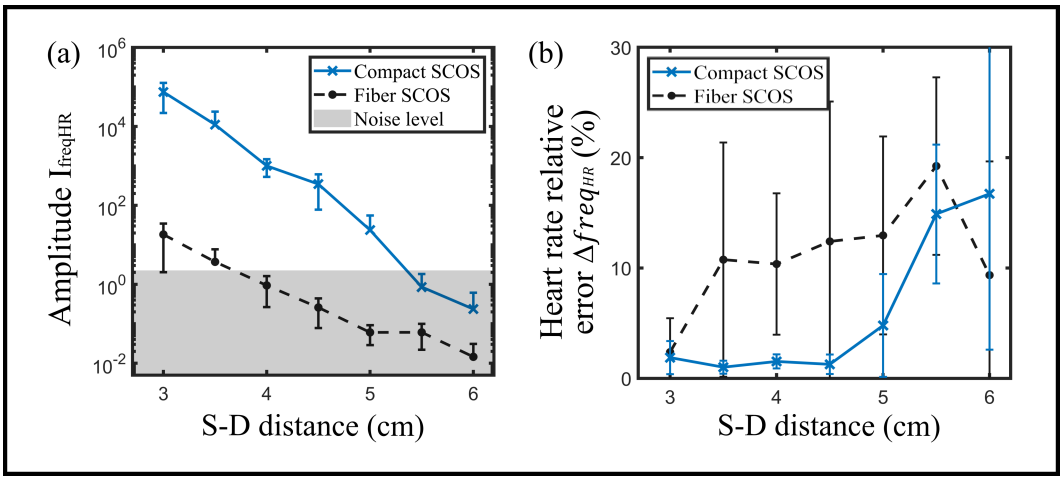


Figure 3.10: Experimental comparison between fiber and compact SCOS in blood flow measurement on a cohort of five subjects. (a) Averaged amplitude of the heartbeat frequency peak and (b) heart rate relative error as a function of the S-D distance.

Concluding the compact SCOS, and the next step forward

In this section, we have presented and characterized a compact and cost-effective laser-powered device specifically designed for assessing cerebral blood flow (CBF) at extended source-detector (S-D) distances, up to 5 cm. This device leverages speckle contrast optical spectroscopy (SCOS) technology, a method derived from laser speckle contrast imaging (LSCI). Its minimalist hardware comprises only two essential components: a continuous-wave laser diode for illumination and a high-resolution CMOS-based board camera for detection. The system offers real-time blood flow monitoring at an impressive 80 Hz sampling rate, all while maintaining a lightweight, modular, and budget-friendly design. A key finding of our work is the approximately 70-fold improvement in collected signal over traditional single-fiber-based SCOS, which directly contributes to its enhanced performance. We rigorously demonstrated the device's capability to measure cerebral blood flow up

to a source-to-detector distance of 5 cm across a cohort of five human subjects.

Furthermore, we observed clear periodic and pulsatile signals even at S-D separations greater than 3 cm, as distinctly shown in Fig. 3.9, with these signals persisting in some cases up to an S-D separation of 5 cm. However, it is noteworthy that the shape of these pulsatile signals appears to differ slightly from conventional observations. In the subsequent section, we will delve deeper into this phenomenon, exploring scenarios where the signal strength may be weaker, and where cerebral blood volume (CBV) and CBF signals could potentially intermingle. This intermingling can make it challenging to reliably observe certain characteristic peaks and dicrotic notches typically present in CBF waveforms.

3.3 Separating CBV and CBF waveforms

This section is adapted from published work: Liu, N., Huang, Y. X., Mahler, S., Yang, C. (2025). *Optimized cerebral blood flow measurement in speckle contrast optical spectroscopy via refinement of noise calibration*. *Optics Letters*, 50(23), 5382-5385.

CBV or CBF, which metric are we observing?

To achieve high brain specificity in cerebral blood flow (CBF) assessment, speckle contrast optical spectroscopy (SCOS) commonly employs a large source-to-detector (S-D) distance [46, 66]. This configuration allows light to predominantly probe deeper cerebral tissue rather than superficial scalp and skull layers [50, 2, 49], as schematically illustrated in Fig. 3.11(a). By leveraging cost-effective CMOS sensors to simultaneously collect millions of speckles over a large detection area, SCOS inherently achieves a high signal-to-noise ratio (SNR) [49, 1]. This enhanced SNR makes SCOS particularly well-suited to overcome the significant signal loss experienced at large S-D distances, thereby enabling effective CBF measurements from deeper cerebral tissue [67, 2, 64, 68, 69, 70, 71].

Despite the inherent SNR advantages of SCOS's spatial sampling approach, the accuracy of its derived CBF values critically depends on robust noise calibration [3, 29]. Fundamentally, the squared speckle contrast (K^2) is defined as the ratio of the spatial variance of pixel intensities (σ_I^2) to the square of their mean intensity ($\langle I \rangle^2$):

$$K^2 = \frac{\sigma_I^2}{\langle I \rangle^2} \tag{3.31}$$

However, the initially measured K^2 is a composite value. It includes not only the desired flow-induced signal but also contributions from multiple noise-related terms. Prominent among these are photon shot noise, speckle inhomogeneity, and various forms of detector noise such as read noise and dark current, all of which influence the K^2 calculated via Eq. (3.31). A common SCOS processing scheme, as illustrated in Fig. 3.11(a), first involves signal averaging to mitigate speckle inhomogeneity arising from non-uniform intensity profiles [3], yielding the normalized speckle contrast squared (K^2_{raw}). Subsequently, speckle contrast contributions from photon shot noise and specific camera-related detector noises are addressed by subtraction of the corresponding terms to isolate the true flow-induced speckle contrast squared (K^2_f). This crucial subtraction step, however, requires precise, often context-specific, knowledge of parameters such as camera gain factors and dark noise characteristics. Obtaining and consistently maintaining such precise parameter values is a persistent challenge due to their sensitivity to dynamic operational conditions, including ambient temperature fluctuations, inherent inter-camera variability, and camera gain drifts over time. As depicted in Fig. 3.11(b), speckle contrast associated with shot noise and camera noise from raw speckle images can constitute a substantial portion of K^2_{raw}. Imperfect noise subtraction can therefore leave residual noise components comparable in magnitude to the actual blood flow-induced signal, thereby significantly compromising CBF fidelity. The impact of effective noise calibration is visually underscored by the distinct differences between the cardiac cycle waveforms observed pre- and post-calibration (Fig. 3.11(b), insets). This vulnerability to residual noise becomes particularly acute when targeting deeper cerebral tissue, a process that inherently requires larger S-D separations and is thus challenged by inherently low signal levels.

To overcome these identified limitations, we introduce an optimization-based framework that performs a refinement of noise calibration, thereby significantly improving the robustness of CBF measurements in SCOS. A central insight underpinning our approach is the recognition that speckle contrast associated with residual noise from imperfect calibrations, notably camera and shot noise, leads to temporal fluctuations in the derived speckle contrast that inadvertently mimic cerebral blood volume (CBV) signals. These artifacts increase the similarity between CBF and CBV signals, which we quantify using the Volume-Flow Similarity Index (VFSI): the Pearson correlation of their respective signal waveforms (see Algorithm 1). The algorithm adaptively refines the coefficients of different noise terms to effectively decorrelate the CBF and CBV signals. In this Letter, we first validate our method

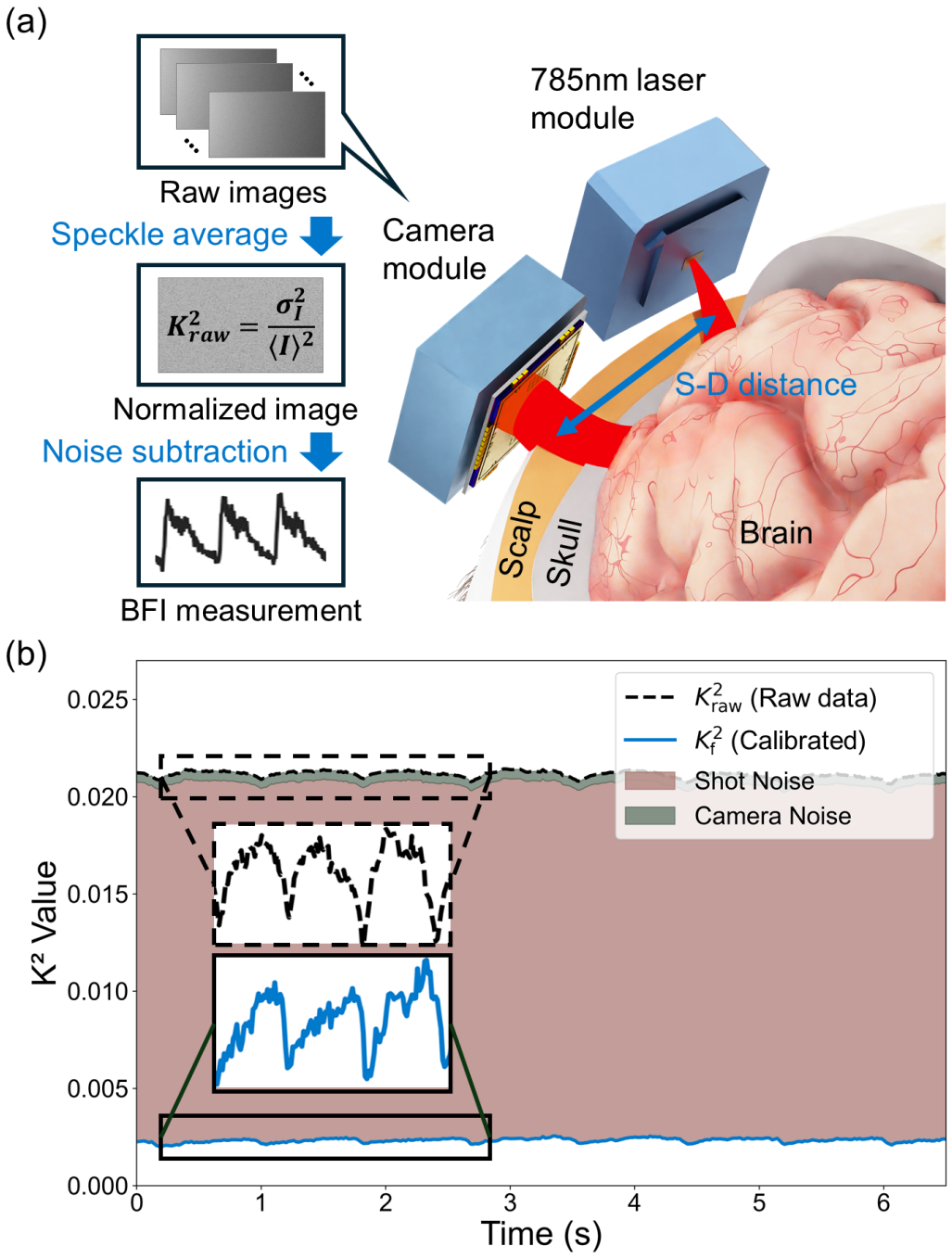


Figure 3.11: (a) Compact SCOS device configuration and schematic of standard BFI processing pipeline. (b) Comparison of speckle contrast signal before (K^2_{raw}) and after (K^2_f) noise subtraction.

across various signal regimes and demonstrate that it effectively suppresses the CBV-mimicking noise in the processed CBF waveforms. We then present results from 10 human subjects, showcasing marked improvements that enable reliable CBF measurements at larger S-D distances and significantly lower signal levels. This advancement contributes to more accurate and robust CBF measurements in SCOS with computationally efficient post-processing, ultimately lowering barriers for its broader adoption in clinical neuromonitoring applications.

In the noise subtraction step, conceptually illustrated in Fig. 3.11(b), we apply the established noise model for speckle contrast to isolate the desired flow-induced signal (K_f^2) from the raw speckle contrast (K_{raw}^2) [3, 29] as:

$$K_f^2 = K_{raw}^2 - K_{shot}^2 - K_{cam}^2. \tag{3.32}$$

Here, K_{shot}^2 and K_{cam}^2 represent the shot noise and camera noise-related speckle contrast terms, respectively, which can be formulated as:

$$K_{shot}^2 = \frac{g}{\langle I \rangle}, \tag{3.33}$$

$$K_{cam}^2 = \frac{\sigma_{cam}^2}{\langle I \rangle^2}. \tag{3.34}$$

where g denotes the camera gain and σ_{cam}^2 is the pre-characterized camera noise variance. Both K_{shot}^2 and K_{cam}^2 are critically dependent on the mean detected light intensity $\langle I \rangle$ [3, 29], which itself fluctuates over time, reflecting physiological dynamics such as the heart rate cardiac cycle. Cerebral blood volume (CBV) fluctuations can also be estimated via the Beer-Lambert Law [72, 73] by computing the mean intensity $\langle I \rangle$ of the recorded camera images:

$$\text{CBV} = 1 + \ln\left(\frac{I_0}{\langle I \rangle}\right), \tag{3.35}$$

where I_0 is the baseline intensity, and the logarithmic term represents the change in optical density due to blood absorption. This shared dependence on $\langle I \rangle$ is a key insight: if the pre-calibrated values for camera gain and noise variance contain residual errors Δg and $\Delta\sigma_{cam}^2$ respectively, the inaccuracies in the subtracted noise-related terms, ΔK_{shot}^2 and ΔK_{cam}^2, are given by:

$$\Delta K^2_{shot} = \frac{\Delta g}{\langle I \rangle}, \tag{3.36}$$

$$\Delta K^2_{cam} = \frac{\Delta \sigma^2_{cam}}{\langle I \rangle^2}. \tag{3.37}$$

The intensity-dependence of these error terms, explicitly shown in Eqs. (3.36)–(3.37), means that as $\langle I \rangle$ fluctuates with CBV, the errors also fluctuate in a similar manner. This systematically imprints a CBV-like temporal pattern onto the calculated K^2_f and creates artifacts in the derived CBF. As $\langle I \rangle$ decreases towards lower signal levels, these structured noise-related terms become increasingly visible in the derived CBF waveform, as shown in Fig. 3.12.

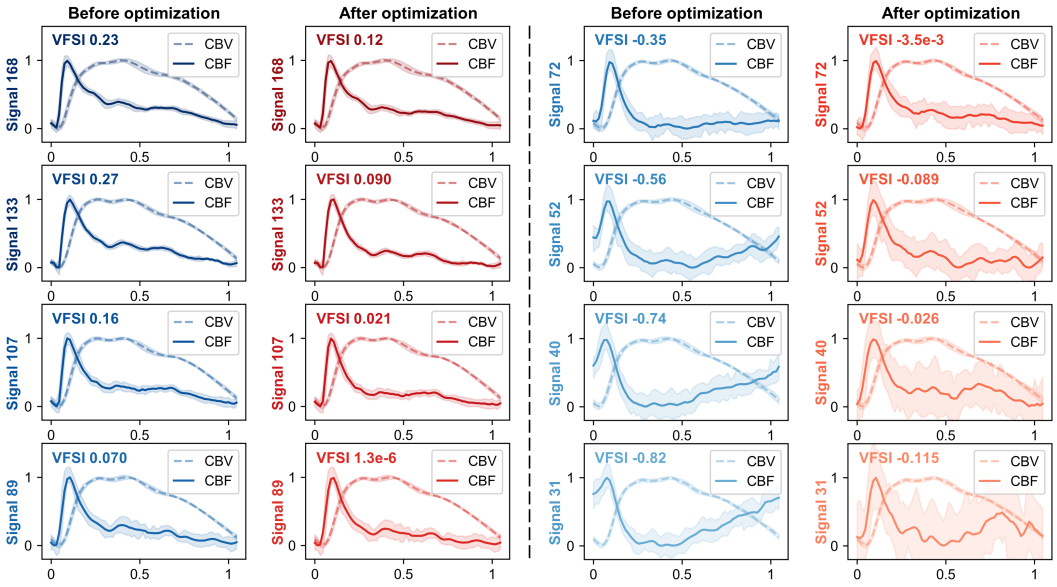


Figure 3.12: Detailed CBF and CBV waveforms measured with our SCOS system before and after optimization across eight signal strengths. Signal levels are arranged in decreasing order, ranging from 168 to 31 electrons per pixel. Blue traces represent waveforms before optimization; red traces represent waveforms after optimization. CBF is shown as a solid line with shaded standard deviation, while CBV is shown as a dashed line.

Consistent with our primary findings, CBF waveforms before optimization increasingly exhibit miscalibration as signal strength diminishes. This signal degradation is accompanied by an artifactual similarity between the CBF and CBV waveforms, as indicated by the VFSI values. In contrast, the CBF waveforms after optimization consistently demonstrate markedly reduced similarity to CBV signals and restored CBF physiological morphology at higher signal levels. While the optimized CBF

waveforms at low signal strengths exhibit more random fluctuations and wider standard deviations due to their low SNR, their essential physiological features are substantially clearer and more reliably recovered compared to the unoptimized data.

To address such CBV-mimicking artifacts arising from imperfect noise parameter pre-calibration, we developed an optimization framework detailed in Algorithm 1. This algorithm adaptively refines the estimates for g and σ^2_{cam} by iteratively working to reduce the squared value of the Volume-Flow Similarity Index (VFSI^2). Such an optimization algorithm effectively decreases the artifactual similarity between the optimized CBF waveform and the concurrently measured CBV waveform, thus selectively mitigating the mis-calibrated noise components. The validity of using VFSI^2 as an optimization metric is predicated on the assumption that the inherent correlation between the high-pass filtered CBF and CBV pulsatile waveforms is weak [74, 75, 76, 77].

Discussion on the inherent weak correlation between CBF and CBV pulsatile waveforms

In the main manuscript, we systematically analyzed and experimentally demonstrated that the artificial noise-related speckle contrast terms will markedly increase the magnitude of the measured correlation (whether positive or negative) between the derived CBF and CBV waveforms. Our proposed optimization framework mitigates these artifacts by iteratively refining noise calibration parameters to reduce the VFSI^2. The validity of using VFSI^2 as a loss function is predicated on the assumption that the inherent correlation between the high-pass filtered CBF and CBV pulsatile waveforms is weak. In this note, we provide a more comprehensive discussion of this relationship between CBF and CBV pulsatile dynamics. This analysis helps justify the use of VFSI as an effective indicator for optimizing away CBV-mimicking artifacts and provides a basis for determining the extent to which the corrected CBF signal can be considered free from such noise-related influences.

Due to the biomechanical properties of blood vessels, there is an effective phase lag between the peak blood flow and the peak blood volume pulsation within each cardiac cycle. In the simplest approximation, this phase lag is 90 degrees, which allows previous works to reasonably approximate CBF signal by taking the temporal derivative of a volume signal, such as those obtained from near-infrared spectroscopy (NIRS) or pulse oximetry [74, 75]. A 90-degree phase shift between two periodic signals mathematically results in zero correlation over a full cycle, providing a

first-order justification for the weak correlation premise.

From a more detailed physiological viewpoint, changes in cerebral blood volume (ΔCBV) can be modeled as the net difference between arterial inflow (CBF_{in}) and venous outflow (CBF_{out}):

$$\Delta\mathrm{CBV}(t) = \int_{t_0}^{t} [\mathrm{CBF}_{in}(t') - \mathrm{CBF}_{out}(t')]dt' \tag{3.38}$$

Using the continuous-flow forward (CFF) model [76, 77], the venous outflow can be approximated as the time-averaged arterial inflow, i.e., $\mathrm{CBF}_{out} \approx \mathrm{mean}(\mathrm{CBF}_{in})$. Meanwhile, the total CBF signal measured by SCOS, CBF_{tot}, is the sum of the inflow and outflow components, $\mathrm{CBF}_{tot} \approx \mathrm{CBF}_{in} + \mathrm{CBF}_{out}$ [68]. By substituting these relationships, Eq. (3.38) can be reformulated as:

$$\Delta\mathrm{CBV}(t) = \int_{t_0}^{t} \{\mathrm{CBF}_{tot}(t') - 2\mathrm{CBF}_{out}(t')\}dt' = \int_{t_0}^{t} \{\mathrm{CBF}_{tot}(t') - \mathrm{mean}[\mathrm{CBF}_{tot}(t')]\}dt' \tag{3.39}$$

Taking the temporal derivative of Eq. (3.39) yields:

$$\frac{d}{dt}\Delta\mathrm{CBV}(t) \approx \mathrm{CBF}_{tot}(t) - \mathrm{mean}[\mathrm{CBF}_{tot}(t)] = \tilde{\mathrm{CBF}}_{tot}(t) \tag{3.40}$$

where $\tilde{\mathrm{CBF}}_{tot}$ denotes the high-frequency oscillatory component (i.e., the high-pass filtered signal) of the measured CBF. In practice, average filtering is applied to the whole cardiac cycle (61 data points for our 60 fps camera setup in the 10-subject experiment) to calculate the mean in Eq. (3.40). The correlation between the zero-mean variables ΔCBV and $\tilde{\mathrm{CBF}}_{tot}$ over a cardiac cycle can be expressed as:

$$\mathrm{VFSI} = \int_{t_0}^{t_0+T} \Delta\mathrm{CBV}(t)\tilde{\mathrm{CBF}}_{tot}(t)dt = \int_{t_0}^{t_0+T} \Delta\mathrm{CBV}(t)d(\Delta\mathrm{CBV}(t)) \approx 0 \tag{3.41}$$

In Eq. (3.41), the integral evaluates to $1/2[\Delta\mathrm{CBV}(t_0+T)^2 - \Delta\mathrm{CBV}(t_0)^2]$. Because the CBV fluctuation is periodic, VFSI can be approximated as zero. It is important to note, however, that this outcome relies on several priors, such as those in the CFF model and the assumption of strict periodicity. These idealizations cannot be perfectly met in practice, which could lead to small, non-zero physiological correlations in human subjects, potentially varying with their health states.

Optimization algorithm and results

Algorithm 1 CBF Optimization Framework

Input: Time-sequence speckle contrast signal K^2_{raw}, average intensity $\langle I \rangle$, pre-calibrated camera gain g_0 and noise variance σ^2_0.
Output: Optimized CBF signal CBF_{opt}.

Initialization:
Initialize Adam optimizer.
Initialize noise coefficients: $g \leftarrow g_0$, $\sigma^2_{cam} \leftarrow \sigma^2_0$.

Main Algorithm:
Extract high-pass filtered CBV waveform: $\mathrm{CBV}_{hp} \leftarrow \mathrm{Highpass}(\mathrm{CBV})$.
for each iteration $i = 1, 2, \ldots, n$ **do**
    Adjust flow-induced speckle contrast: $K^2_{af} \leftarrow K^2_{raw} - g/\langle I \rangle - \sigma^2_{cam}/\langle I \rangle^2$.
    Calculate high-pass filtered CBF waveform: $\mathrm{CBF}_{hp} \leftarrow \mathrm{Highpass}(1/K^2_{af})$.
    Calculate Volume-Flow Similarity Index: $\mathrm{VFSI} \leftarrow \mathrm{corr}(\mathrm{CBF}_{hp}, \mathrm{CBV}_{hp})$.
    Define loss function: $\mathcal{L} \leftarrow \mathrm{VFSI}^2$.
    Update g and σ^2_{cam} using Adam optimizer to minimize $\mathcal{L}$.
end for

Termination:
return Optimized $\mathrm{CBF}_{opt} \leftarrow 1/K^2_{af}$.

To investigate SCOS performance across varying signal levels under controlled conditions, we acquired 20-second data traces from a subject's forehead using our previously developed compact SCOS device [3]. The detected signal level was precisely adjusted by varying the laser source current from 100mA to 65mA in 5mA increments. This setup allowed for precise modulation of the signal level (quantified as average electrons per pixel) by adjusting illumination laser power to eight distinct levels, while keeping the fixed 3 cm S-D distance and probing position constant. In the ideal situation with perfect noise calibration, decreasing signal levels should cause the CBF waveform to primarily exhibit increased random fluctuations without fundamentally altering its physiological morphology, given the unchanged measurement geometry. However, as shown in Fig. 3.13(a), because standard pre-calibration typically leaves residual errors, the derived CBF waveforms increasingly mirror an inverted CBV waveform as the signal levels decrease, leading to larger VFSI^2. To quantitatively assess this CBF fidelity degradation, we correlated the CBF signal at each illumination level with that obtained at the highest signal level, as illustrated in Fig. 3.13(c). We also present the VFSI^2 values across different signal levels in Fig.

3.13(d). For standard processing (blue dots in Figs. 3.13(c) and 3.13(d)), a sharp decline in fidelity and a rapid increase in $VFSI^2$ are observed below a signal threshold of approximately 90 electrons per pixel. In contrast, CBF waveforms derived using our proposed method (Fig. 3.13(b)) consistently exhibit clear pulsatile traits with robust physiological features. Correspondingly, as shown by the red stars in Figs. 3.13(c) and 3.13(d), our method maintains high CBF fidelity and low $VFSI^2$ across all tested signal levels. While the standard deviation of the optimized CBF waveform naturally increases at lower signal levels, its crucial physiological morphology—including the systolic peak and dicrotic notch—is accurately recovered. Such SNR decrease at lower signal is a natural and expected behavior, consistent with our detailed analysis in original paper's Supplemental Note 3. This analysis also demonstrates the intrinsically higher SNR of the CBV signal in our SCOS setup, justifying its use as a reliable reference for our optimization framework.

To further evaluate the efficacy and robustness of our optimization framework across a practical range of measurement conditions, we analyzed SCOS data acquired from 10 human subjects. These recordings were taken at varying S-D distances on the forehead. For each subject, three independent 20-second recordings were acquired at each S-D distance, while keeping the laser illumination power constant. The S-D distance was progressively increased from 3.0 cm until the detected signal level dropped below a threshold of 10 electrons per pixel. As shown in Fig. 3.14(a), the detected signal strength reliably diminishes with increasing S-D distance, following an exponential decay pattern, which is linearly fitted when plotted on a logarithmic signal axis.

We then comprehensively assessed the data quality using $VFSI^2$ as an indicator of CBV-mimicking artifact levels relative to signal strength. For data processed with standard methods (Fig. 3.14(b)), a piece-wise linear fit applied to the $VFSI^2$ versus signal strength data indicates a critical signal threshold of approximately 97 electrons per pixel; below this threshold, $VFSI^2$ values rapidly increase, signifying severely compromised data quality due to amplified CBV-mimicking noise. This observed signal threshold and the trend of escalating $VFSI^2$ at lower signal strengths are consistent with the performance limitations of standard SCOS processing previously shown in Fig. 3.13. In stark contrast, applying our optimization framework (Fig. 3.14(d)) yields a significantly reduced effective signal threshold of approximately 26 electrons per pixel. This substantial reduction demonstrates the robust performance of our method even at significantly lower signal levels, which

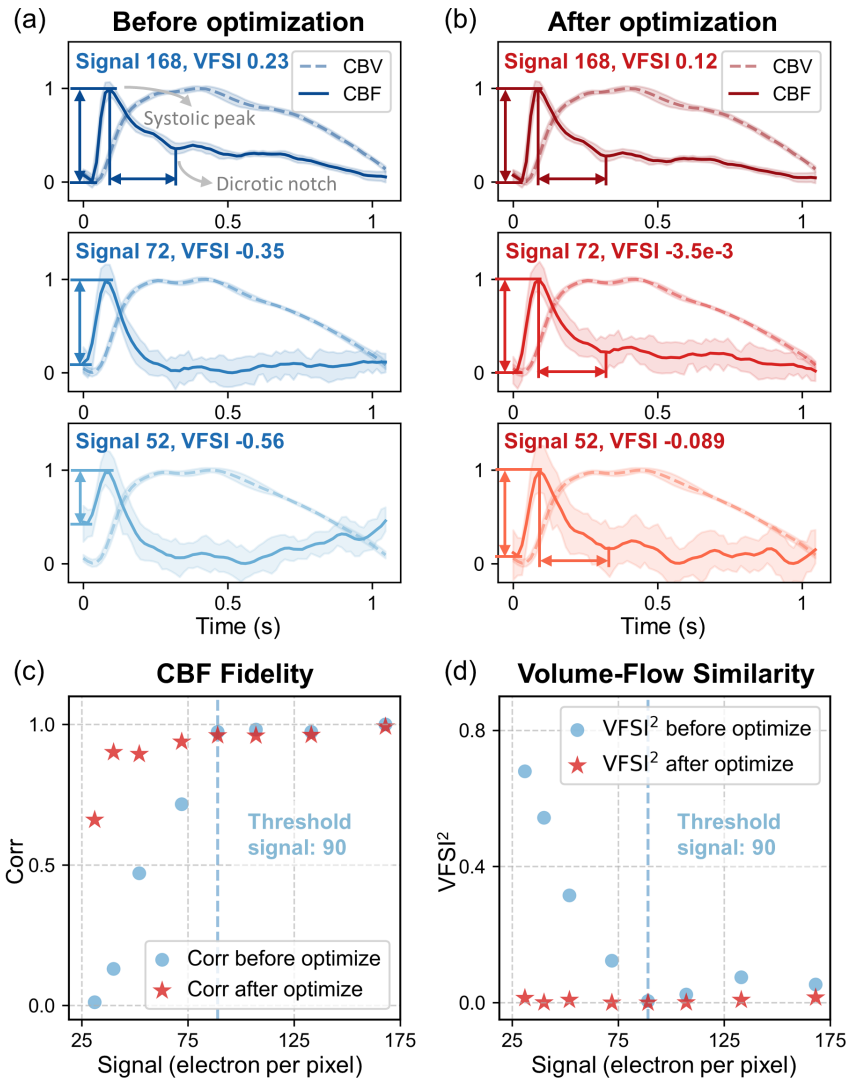


Figure 3.13: Comparison of CBF measurements in SCOS using standard pre-calibration and the proposed optimization framework at varying signal strengths. (a) Representative cerebral blood flow (CBF) and cerebral blood volume (CBV) waveforms obtained using standard pre-calibration processing. (b) Representative CBF and CBV waveforms obtained using our proposed optimization scheme. In both (a) and (b), central lines denote the mean waveforms over the 20-second recordings, with shaded areas representing ±1 standard deviation. (c) Plot showing CBF fidelity as a function of varying signal strengths. (d) Plot showing the Volume-Flow Similarity Index ($VFSI^2$) across varying signal strengths. Blue data points represent standard processing, while red data points (stars) represent results from the optimized framework.

are typically challenging for conventional processing.

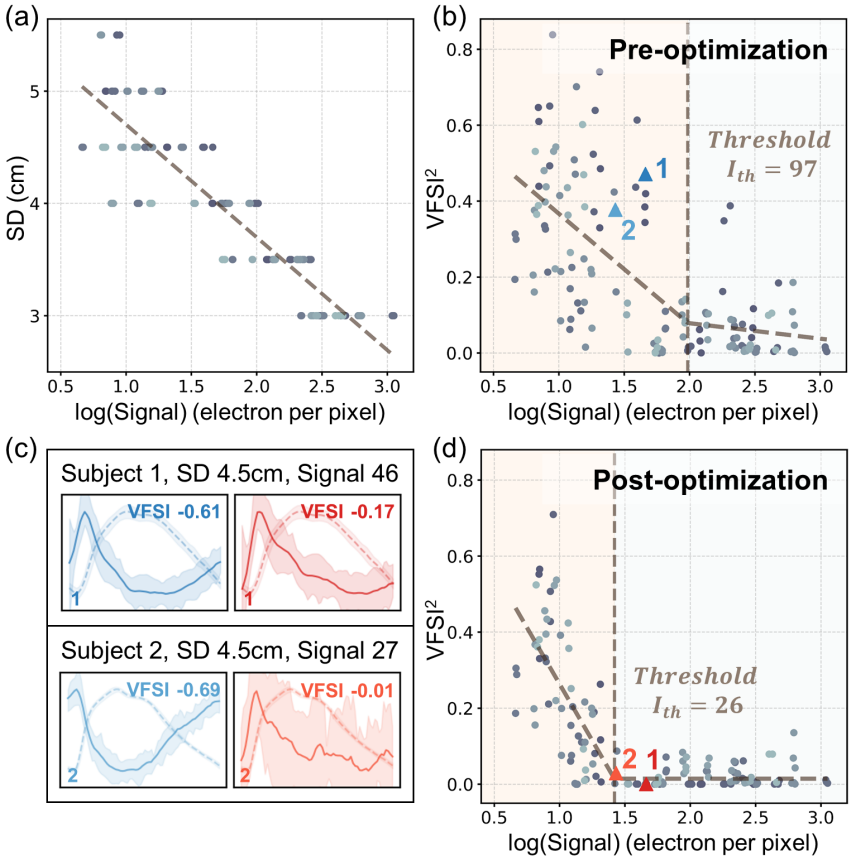


Figure 3.14: Enhanced SCOS performance using the proposed algorithm across varying S-D separations and signal strengths in 10 human subjects. (a) Detected signal strength as a function of source-detector (S-D) separation, demonstrating exponential decay. (b, d) Volume-Flow Similarity Index ($VFSI^2$) plotted against signal strength before (b) and after (d) optimization. The signal threshold, determined by piece-wise linear fitting, is significantly reduced from 97 to 26 electrons per pixel post-optimization. (c) Representative CBF and CBV waveforms for two highlighted subjects (points 1 and 2) at a challenging 4.5 cm S-D separation, shown before and after optimization to illustrate the recovery of physiological features.

Figure 3.14(c) presents illustrative examples of this improvement for two representative subjects, corresponding to data points 1 and 2 highlighted in Figs. 3.14(b) and 3.14(d). These particular measurements were conducted at a 4.5 cm S-D distance, resulting in challenging low signal levels of 46 and 27 electrons per pixel, respectively. Before optimization, the derived CBF waveforms are heavily distorted and exhibit high absolute VFSI values (-0.61 and -0.69), indicative of strong CBV-mimicking artifacts. After optimization, the CBF waveforms clearly display distinct physiological features, such as prominent systolic peaks and dicrotic notches, with

substantially reduced absolute VFSI values (-0.17 and -0.01), visually confirming the enhanced CBF signal fidelity and suppression of artifacts. These compelling results collectively demonstrate that our proposed method significantly expands the operational range of SCOS, enabling more reliable and consistent CBF measurements at larger S-D distances that are critical for achieving deep brain tissue detection and analysis.

Framework Robustness and Conclusion

We also showcase the robustness of the proposed optimization framework by applying it to cases where *a priori* estimation of noise parameters is entirely absent, as detailed in the original paper's Supplement 1, Note 4. The adaptive nature of the algorithm allows it to effectively auto-calibrate the camera gain and noise variance by directly constraining the similarity between the derived CBF and concurrently measured CBV waveforms. As demonstrated with SCOS data acquired at a challenging low signal strength (4 cm S-D separation, 55 electrons per pixel), our method successfully retrieved reliable CBF signals even when the initial pre-calibrated values, g_0 and σ_0^2, were set to zero. Beyond its robustness to unknown priors, the framework is computationally efficient: processing a 20-second SCOS time trace through 500 iterations of our Algorithm 1 took approximately 0.5 seconds on a commercial GPU (NVIDIA GTX 1080 Ti).

In conclusion, this section has presented and validated an optimization-based framework for the adaptive refinement of noise calibration in SCOS. This approach effectively mitigates the CBV-mimicking artifacts that stem from noise mis-calibration, thereby enhancing the fidelity and robustness of derived CBF signals at large S-D distances (i.e., low signal levels). We have demonstrated its capability to extend the reliable operational range of SCOS, particularly for challenging low-light conditions critical for deeper brain detection, and to perform robustly even with minimal or absent *a priori* knowledge of underlying noise parameters. This computationally efficient method significantly reduces the dependence on meticulous and often difficult-to-maintain noise pre-calibrations, thereby broadening its applicability across diverse SCOS instrumentations in both clinical research and potentially commercial applications.

3.4 Concluding Remarks and Future Directions

This chapter has detailed three distinct approaches developed to advance CBF monitoring: an interferometric method to boost signal, a compact SCOS device to

increase photon collection and stability, and an optimization framework to refine noise calibration. Each innovation shares the common goal of enhancing signal quality, which is paramount for extending S-D separation and improving the specificity of brain measurements. The optimization framework, in particular, proved effective at isolating CBF from CBV-mimicking artifacts.

While powerful, this optimization framework relies on a critical prior: the assumption of a near-zero correlation between the pulsatile CBF and CBV waveforms. This premise is rooted in physiological models of arterial and venous response, which posit that these signals are largely out of phase. However, this assumption may not be universally valid and could become a significant limitation. It may no longer hold true in clinical scenarios involving neurovascular anomalies where the inherent synchronization between CBF and CBV might be disrupted, making it a critical area for future investigation.

This limitation highlights two primary avenues for future research aimed at further advancing deep-tissue blood flow monitoring. The first avenue is advanced sensor characterization and auto-calibration. As demonstrated in our work [78], improper calibration of sensor parameters like gain—which can drift with temperature or vary between units—introduces significant artifacts that mimic physiological signals. A key future direction is the development of a rapid, on-demand auto-calibration routine (e.g., 5-10 seconds) that could be executed before each measurement. Such a system would establish the sensor's precise operational state in real-time, providing a more robust foundation for separating true flow dynamics from measurement noise without relying on physiological priors.

The second avenue involves developing novel methods for signal enhancement. This includes strategies already being explored by various research groups, such as pulsed laser illumination to manage power deposition while increasing peak photon flux. It also encompasses further innovations in sensor design and light collection optics, following the precedent set by the compact SCOS device. Synergistic progress in both sensor characterization and signal enhancement will be crucial for extending measurable S-D distances and improving the signal-to-noise ratio (SNR), thereby unlocking new applications and enabling measurements at more diverse locations on the head.

With the foundational and methodological advancements of iSVS/SCOS established, this thesis now shifts focus from signal acquisition to practical application. This transition naturally raises two pivotal questions: First, how can these modular

compact SCOS systems be scaled for broader coverage and deployment? Second, what new physiological and clinical insights can be derived from the high-fidelity CBF and CBV signals these systems provide? These questions form the central themes of the subsequent two chapters.

References

[1] Jian Xu, Ali K Jahromi, and Changhuei Yang. "Diffusing wave spectroscopy: A unified treatment on temporal sampling and speckle ensemble methods". en. In: *APL Photonics* 6.1 (Jan. 2021). Publisher: AIP Publishing, p. 016105. DOI: 10.1063/5.0034576.

[2] Wenjun Zhou et al. "Functional interferometric diffusing wave spectroscopy of the human brain". en. In: *Science Advances* 7.20 (May 2021), eabe0150. DOI: 10.1126/sciadv.abe0150.

[3] Yu Xi Huang et al. "Compact and cost-effective laser-powered speckle contrast optical spectroscopy fiber-free device for measuring cerebral blood flow". In: *Journal of Biomedical Optics* 29.6 (2024), p. 067001. DOI: 10.1117/1.JBO.29.6.067001.

[4] Mamadou Diop et al. "Calibration of diffuse correlation spectroscopy with a time-resolved near-infrared technique to yield absolute cerebral blood flow measurements". en. In: *Biomedical Optics Express* 2.7 (July 2011), p. 2068. DOI: 10.1364/BOE.2.002068.

[5] Jun Li et al. "Noninvasive detection of functional brain activity with near-infrared diffusing-wave spectroscopy". In: *Journal of Biomedical Optics* 10.4 (July 2005). Publisher: SPIE, p. 044002. DOI: 10.1117/1.2007987.

[6] Erin M. Buckley et al. "Diffuse correlation spectroscopy for measurement of cerebral blood flow: future prospects". en. In: *Neurophotonics* 1.1 (June 2014), p. 011009. DOI: 10.1117/1.NPh.1.1.011009.

[7] Joshua Brake, Mooseok Jang, and Changhuei Yang. "Analyzing the relationship between decorrelation time and tissue thickness in acute rat brain slices using multispeckle diffusing wave spectroscopy". EN. In: *JOSA A* 33.2 (Feb. 2016). Publisher: Optica Publishing Group, pp. 270–275. DOI: 10.1364/JOSAA.33.000270.

[8] Turgut Durduran and Arjun G. Yodh. "Diffuse correlation spectroscopy for non-invasive, micro-vascular cerebral blood flow measurement". en. In: *NeuroImage* 85 (Jan. 2014), pp. 51–63. DOI: 10.1016/j.neuroimage.2013.06.017.

[9] T Durduran et al. "Diffuse optics for tissue monitoring and tomography". In: *Reports on Progress in Physics* 73.7 (July 2010), p. 076701. DOI: 10.1088/0034-4885/73/7/076701.

[10] Stefan A. Carp et al. “Diffuse correlation spectroscopy measurements of blood flow using 1064 nm light”. In: *Journal of Biomedical Optics* 25.9 (Sept. 2020). Publisher: SPIE, p. 097003. DOI: 10.1117/1.JBO.25.9.097003.

[11] Meeri N. Kim et al. “Noninvasive Measurement of Cerebral Blood Flow and Blood Oxygenation Using Near-Infrared and Diffuse Correlation Spectroscopies in Critically Brain-Injured Adults”. en. In: *Neurocritical Care* 12.2 (Apr. 2010), pp. 173–180. DOI: 10.1007/s12028-009-9305-x.

[12] Saeed Samaei et al. “Time-domain diffuse correlation spectroscopy (TD-DCS) for noninvasive, depth-dependent blood flow quantification in human tissue in vivo”. en. In: *Scientific Reports* 11.1 (Jan. 2021). Number: 1 Publisher: Nature Publishing Group, p. 1817. DOI: 10.1038/s41598-021-81448-5.

[13] Michael A. Wayne et al. “Massively parallel, real-time multispeckle diffuse correlation spectroscopy using a 500 x 500 SPAD camera”. EN. In: *Biomedical Optics Express* 14.2 (Feb. 2023). Publisher: Optica Publishing Group, pp. 703–713. DOI: 10.1364/BOE.473992.

[14] Wenjun Zhou et al. “Highly parallel, interferometric diffusing wave spectroscopy for monitoring cerebral blood flow dynamics”. EN. In: *Optica* 5.5 (May 2018). Publisher: Optica Publishing Group, pp. 518–527. DOI: 10.1364/OPTICA.5.000518.

[15] Oybek Kholiqov et al. “Scanning interferometric near-infrared spectroscopy”. EN. In: *Optics Letters* 47.1 (Jan. 2022). Publisher: Optica Publishing Group, pp. 110–113. DOI: 10.1364/OL.443533.

[16] Oybek Kholiqov, Dawid Borycki, and Vivek J. Srinivasan. “Interferometric near-infrared spectroscopy (iNIRS): performance tradeoffs and optimization”. EN. In: *Optics Express* 25.23 (Nov. 2017). Publisher: Optica Publishing Group, pp. 28567–28589. DOI: 10.1364/OE.25.028567.

[17] Dawid Borycki, Oybek Kholiqov, and Vivek J. Srinivasan. “Interferometric near-infrared spectroscopy directly quantifies optical field dynamics in turbid media”. en. In: *Optica* 3.12 (Dec. 2016), p. 1471. DOI: 10.1364/OPTICA.3.001471.

[18] Dmitry D. Postnov et al. “Dynamic light scattering imaging”. en. In: *Science Advances* 6.45 (Nov. 2020), eabc4628. DOI: 10.1126/sciadv.abc4628.

[19] Wenjun Zhou et al. “Multi-exposure interferometric diffusing wave spectroscopy”. EN. In: *Optics Letters* 46.18 (Sept. 2021). Publisher: Optica Publishing Group, pp. 4498–4501. DOI: 10.1364/OL.427746.

[20] Edward James and Samuel Powell. “Fourier domain diffuse correlation spectroscopy with heterodyne holographic detection”. EN. In: *Biomedical Optics Express* 11.11 (Nov. 2020). Publisher: Optica Publishing Group, pp. 6755–6779. DOI: 10.1364/BOE.400525.

[21] Mitchell Robinson et al. “Interferometric diffuse correlation spectroscopy improves measurements at long source-detector separation and low photon count rate”. eng. In: *Journal of Biomedical Optics* 25.9 (Sept. 2020), p. 097004. DOI: 10.1117/1.JBO.25.9.097004.

[22] Saeed Samaei et al. “Continuous-wave parallel interferometric near-infrared spectroscopy (CW NIRS) with a fast two-dimensional camera”. EN. In: *Biomedical Optics Express* 13.11 (Nov. 2022). Publisher: Optica Publishing Group, pp. 5753–5774. DOI: 10.1364/BOE.472643.

[23] Mitchell B. Robinson et al. “Portable, high speed blood flow measurements enabled by long wavelength, interferometric diffuse correlation spectroscopy (LW-iDCS)”. en. In: *Scientific Reports* 13.1 (May 2023), p. 8803. DOI: 10.1038/s41598-023-36074-8.

[24] Mingjun Zhao et al. “Interferometric diffusing wave spectroscopy imaging with an electronically variable time-of-flight filter”. en. In: *Optica* 10.1 (Jan. 2023), p. 42. DOI: 10.1364/OPTICA.472471.

[25] Jian Xu et al. “Interferometric speckle visibility spectroscopy (ISVS) for human cerebral blood flow monitoring”. en. In: *APL Photonics* 5.12 (Dec. 2020), p. 126102. DOI: 10.1063/5.0021988.

[26] R. Bandyopadhyay et al. “Speckle-visibility spectroscopy: A tool to study time-varying dynamics”. en. In: *Review of Scientific Instruments* 76.9 (Sept. 2005), p. 093110. DOI: 10.1063/1.2037987.

[27] K. Murali and Hari M. Varma. “Multi-speckle diffuse correlation spectroscopy to measure cerebral blood flow”. EN. In: *Biomedical Optics Express* 11.11 (Nov. 2020). Publisher: Optica Publishing Group, pp. 6699–6709. DOI: 10.1364/BOE.401702.

[28] Claudia P. Valdes et al. “Speckle contrast optical spectroscopy, a non-invasive, diffuse optical method for measuring microvascular blood flow in tissue”. en. In: *Biomedical Optics Express* 5.8 (Aug. 2014), p. 2769. DOI: 10.1364/BOE.5.002769.

[29] Byungchan Kim et al. “Measuring human cerebral blood flow and brain function with fiber-based speckle contrast optical spectroscopy system”. en. In: *Communications Biology* 6.1 (Aug. 2023), p. 844. DOI: 10.1038/s42003-023-05211-4.

[30] David Briers et al. “Laser speckle contrast imaging: theoretical and practical limitations”. In: *Journal of Biomedical Optics* 18.6 (June 2013). Publisher: SPIE, p. 066018. DOI: 10.1117/1.JBO.18.6.066018.

[31] David A. Boas and Andrew K. Dunn. “Laser speckle contrast imaging in biomedical optics”. en. In: *Journal of Biomedical Optics* 15.1 (2010), p. 011109. DOI: 10.1117/1.3285504.

[32] Andrew K. Dunn. “Laser Speckle Contrast Imaging of Cerebral Blood Flow”. en. In: *Annals of Biomedical Engineering* 40.2 (Feb. 2012), pp. 367–377. DOI: 10.1007/s10439-011-0469-0.

[33] Janaka Senarathna et al. “Laser Speckle Contrast Imaging: theory, instrumentation and applications”. eng. In: *IEEE reviews in biomedical engineering* 6 (2013), pp. 99–110. DOI: 10.1109/RBME.2013.2243140.

[34] Amaan Mazhar et al. “Laser speckle imaging in the spatial frequency domain”. EN. In: *Biomedical Optics Express* 2.6 (June 2011). Publisher: Optica Publishing Group, pp. 1553–1563. DOI: 10.1364/BOE.2.001553.

[35] Andrew K. Dunn et al. “Dynamic Imaging of Cerebral Blood Flow Using Laser Speckle”. en. In: *Journal of Cerebral Blood Flow & Metabolism* 21.3 (Mar. 2001). Publisher: SAGE Publications Ltd STM, pp. 195–201. DOI: 10.1097/00004647-200103000-00002.

[36] Shuqi Zheng and Jerome Mertz. “Direct characterization of tissue dynamics with laser speckle contrast imaging”. en. In: *Biomedical Optics Express* 13.8 (Aug. 2022), p. 4118. DOI: 10.1364/BOE.462913.

[37] Shuqi Zheng and Jerome Mertz. “Correcting sampling bias in speckle contrast imaging”. EN. In: *Optics Letters* 47.24 (Dec. 2022). Publisher: Optica Publishing Group, pp. 6333–6336. DOI: 10.1364/OL.474604.

[38] *ANSI Z136.1-2014 - American National Standard for Safe Use of Lasers*.

[39] Edward James, Samuel Powell, and Peter Munro. “Performance optimisation of a holographic Fourier domain diffuse correlation spectroscopy instrument”. EN. In: *Biomedical Optics Express* 13.7 (July 2022). Publisher: Optica Publishing Group, pp. 3836–3853. DOI: 10.1364/BOE.454346.

[40] Sean J. Kirkpatrick, Donald D. Duncan, and Elaine M. Wells-Gray. “Detrimental effects of speckle-pixel size matching in laser speckle contrast imaging”. EN. In: *Optics Letters* 33.24 (Dec. 2008). Publisher: Optica Publishing Group, pp. 2886–2888. DOI: 10.1364/OL.33.002886.

[41] D. A. Boas and A. G. Yodh. “Spatially varying dynamical properties of turbid media probed with diffusing temporal light correlation”. EN. In: *JOSA A* 14.1 (Jan. 1997). Publisher: Optica Publishing Group, pp. 192–215. DOI: 10.1364/JOSAA.14.000192.

[42] Pedro G. Vaz et al. “Laser Speckle Imaging to Monitor Microvascular Blood Flow: A Review”. In: *IEEE Reviews in Biomedical Engineering* 9 (2016). Conference Name: IEEE Reviews in Biomedical Engineering, pp. 106–120. DOI: 10.1109/RBME.2016.2532598.

[43] Dilleys Ferreira et al. “Connecting field and intensity correlations: The Siegert relation and how to test it”. en. In: *American Journal of Physics* 88.10 (Oct. 2020), pp. 831–837. DOI: 10.1119/10.0001630.

[44] C. Magnain et al. “Holographic laser Doppler imaging of microvascular blood flow”. EN. In: *JOSA A* 31.12 (Dec. 2014). Publisher: Optica Publishing Group, pp. 2723–2735. DOI: 10.1364/JOSAA.31.002723.

[45] L. Puyo et al. “In vivo laser Doppler holography of the human retina”. EN. In: *Biomedical Optics Express* 9.9 (Sept. 2018). Publisher: Optica Publishing Group, pp. 4113–4129. DOI: 10.1364/BOE.9.004113.

[46] Simon Mahler et al. “Assessing depth sensitivity in laser interferometry speckle visibility spectroscopy (iSVS) through source-to-detector distance variation and cerebral blood flow monitoring in humans and rabbits”. In: *Biomed. Opt. Express* 14.9 (Sept. 2023), pp. 4964–4978. DOI: 10.1364/BOE.498815.

[47] Christopher G. Favilla et al. “Validation of the Openwater wearable optical system: cerebral hemodynamic monitoring during a breath-hold maneuver”. In: *Neurophotonics* 11.01 (Mar. 2024). DOI: 10.1117/1.NPh.11.1.015008.

[48] Sharvari Zilpelwar et al. “Model of dynamic speckle evolution for evaluating laser speckle contrast measurements of tissue dynamics”. en. In: *Biomedical Optics Express* 13.12 (Dec. 2022), p. 6533. DOI: 10.1364/BOE.472263.

[49] Mitchell B. Robinson et al. “Comparing the performance potential of speckle contrast optical spectroscopy and diffuse correlation spectroscopy for cerebral blood flow monitoring using Monte Carlo simulations in realistic head geometries”. In: *Neurophotonics* 11.01 (Jan. 2024). DOI: 10.1117/1.NPh.11.1.015004.

[50] Gary E. Strangman, Zhi Li, and Quan Zhang. “Depth Sensitivity and Source-Detector Separations for Near Infrared Spectroscopy Based on the Colin27 Brain Template”. en. In: *PLoS ONE* 8.8 (Aug. 2013), e66319. DOI: 10.1371/journal.pone.0066319.

[51] Ronen Chriki. “Spatiotemporal supermodes: Rapid reduction of spatial coherence in highly multimode lasers”. In: *Physical Review A* 98.2 (2018). DOI: 10.1103/PhysRevA.98.023812.

[52] Simon Mahler et al. “Fast laser speckle suppression with an intracavity diffuser”. en. In: *Nanophotonics* 10.1 (Jan. 2021). Publisher: De Gruyter, pp. 129–136. DOI: 10.1515/nanoph-2020-0390.

[53] Yaniv Eliezer. “Controlling Nonlinear Interaction in a Many-Mode Laser by Tuning Disorder”. In: *Physical Review Letters* 128.14 (2022). DOI: 10.1103/PhysRevLett.128.143901.

[54] W. F. Sheppard. “On the Calculation of the most Probable Values of Frequency-Constants, for Data arranged according to Equidistant Division of a Scale”. en. In: *Proceedings of the London Mathematical Society* s1-29.1 (1897). _eprint: https://onlinelibrary.wiley.com/doi/pdf/10.1112/plms/s1-29.1.353, pp. 353–380. DOI: 10.1112/plms/s1-29.1.353.

[55] Bernd Jähne. “EMVA 1288 Standard for Machine Vision”. en. In: *Optik & Photonik* 5.1 (2010). _eprint: https://onlinelibrary.wiley.com/doi/pdf/10.1002/opph.201190082, pp. 53–54. DOI: 10.1002/opph.201190082.

[56] Lisa Kobayashi Frisk et al. “Comprehensive workflow and its validation for simulating diffuse speckle statistics for optical blood flow measurements”. en. In: *Biomedical Optics Express* 15.2 (Feb. 2024), p. 875. DOI: 10.1364/BOE.502421.

[57] David A. Boas et al. “Establishing the diffuse correlation spectroscopy signal relationship with blood flow”. eng. In: *Neurophotonics* 3.3 (July 2016), p. 031412. DOI: 10.1117/1.NPh.3.3.031412.

[58] Sergio Fantini et al. “Cerebral blood flow and autoregulation: current measurement techniques and prospects for noninvasive optical methods”. en. In: *Neurophotonics* 3.3 (June 2016), p. 031411. DOI: 10.1117/1.NPh.3.3.031411.

[59] Jurgen A. H. R. Claassen et al. “Regulation of cerebral blood flow in humans: physiology and clinical implications of autoregulation”. en. In: *Physiological Reviews* 101.4 (Oct. 2021), pp. 1487–1559. DOI: 10.1152/physrev.00022.2020.

[60] Chong Huang et al. “A Wearable Fiberless Optical Sensor for Continuous Monitoring of Cerebral Blood Flow in Mice”. In: *IEEE Journal of Selected Topics in Quantum Electronics* 25.1 (Jan. 2019), pp. 1–8. DOI: 10.1109/JSTQE.2018.2854597.

[61] Chen-Hao P. Lin et al. “Multi-mode fiber-based speckle contrast optical spectroscopy: analysis of speckle statistics”. en. In: *Optics Letters* 48.6 (Mar. 2023), p. 1427. DOI: 10.1364/OL.478956.

[62] Florian B. Haeussinger et al. “Simulation of Near-Infrared Light Absorption Considering Individual Head and Prefrontal Cortex Anatomy: Implications for Optical Neuroimaging”. en. In: *PLoS ONE* 6.10 (Oct. 2011). Ed. by Kenji Hashimoto, e26377. DOI: 10.1371/journal.pone.0026377.

[63] Chemseddine Mansouri et al. “Depth sensitivity analysis of functional near-infrared spectroscopy measurement using three-dimensional Monte Carlo modelling-based magnetic resonance imaging”. en. In: *Lasers in Medical Science* 25.3 (May 2010), pp. 431–438. DOI: 10.1007/s10103-010-0754-4.

[64] Stefan A. Carp, Mitchell B. Robinson, and Maria A. Franceschini. “Diffuse correlation spectroscopy: current status and future outlook”. In: *Neurophotonics* 10.01 (Jan. 2023). DOI: 10.1117/1.NPh.10.1.013509.

[65] J. Adam Noah et al. “Comparison of short-channel separation and spatial domain filtering for removal of non-neural components in functional near-infrared spectroscopy signals”. In: *Neurophotonics* 8.01 (Feb. 2021). DOI: 10.1117/1.NPh.8.1.015004.

[66] Yu Xi Huang et al. “Assessing human scalp and brain blood flow sensitivities via superficial temporal artery occlusion using speckle contrast optical spectroscopy”. In: *APL Bioengineering* 9.4 (Oct. 2025), p. 046106. DOI: 10.1063/5.0263953.

[67] Simon Mahler et al. “Portable six-channel laser speckle system for simultaneous measurement of cerebral blood flow and volume with potential applications in characterization of brain injury”. In: *Neurophotonics* 12.1 (2025), p. 015003. DOI: 10.1117/1.NPh.12.1.015003.

[68] Kuan Cheng Wu et al. “Enhancing diffuse correlation spectroscopy pulsatile cerebral blood flow signal with near-infrared spectroscopy photoplethysmography”. In: *Neurophotonics* 10.03 (Sept. 2023). DOI: 10.1117/1.NPh.10.3.035008.

[69] Christopher G Favilla et al. “Portable cerebral blood flow monitor to detect large vessel occlusion in patients with suspected stroke”. en. In: *Journal of NeuroInterventional Surgery* (Mar. 2024), jnis–2024–021536. DOI: 10.1136/jnis-2024-021536.

[70] Byungchan (Kenny) Kim et al. *Mapping human cerebral blood flow with high-density, multi-channel speckle contrast optical spectroscopy*. en. Mar. 2025. DOI: 10.1101/2025.03.03.638332.

[71] Yu Xi Huang et al. “Correlating stroke risk with non-invasive cerebrovascular perfusion dynamics using a portable speckle contrast optical spectroscopy laser device”. In: *Biomed. Opt. Express* 15.10 (Oct. 2024), pp. 6083–6097. DOI: 10.1364/BOE.534796.

[72] Wesley B. Baker et al. “Modified Beer-Lambert law for blood flow”. en. In: *Biomedical Optics Express* 5.11 (Nov. 2014). Publisher: Optica Publishing Group, p. 4053. DOI: 10.1364/boe.5.004053.

[73] Ilze Oshina and Janis Spigulis. “Beer–Lambert law for optical tissue diagnostics: current state of the art and the main limitations”. In: *Journal of Biomedical Optics* 26.10 (Oct. 2021). Publisher: SPIE-Intl Soc Optical Eng. DOI: 10.1117/1.jbo.26.10.100901.

[74] George Themelis et al. “Near-infrared spectroscopy measurement of the pulsatile component of cerebral blood flow and volume from arterial oscillations”. en. In: *Journal of Biomedical Optics* 12.1 (2007). Publisher: SPIE-Intl Soc Optical Eng, p. 014033. DOI: 10.1117/1.2710250.

[75] N. A. Wisely and L. B. Cook. “Arterial flow waveforms from pulse oximetry compared with measured Doppler flow waveforms: apparatus”. en. In: *Anaesthesia* 56.6 (June 2001). Publisher: Wiley, pp. 556–561. DOI: 10.1046/j.1365-2044.2001.01987.x.

[76] Dong-Joo Kim et al. “The monitoring of relative changes in compartmental compliances of brain”. In: *Physiological Measurement* 30.7 (July 2009). Publisher: IOP Publishing, pp. 647–659. DOI: 10.1088/0967-3334/30/7/009.

[77] Agnieszka Uryga et al. “Assessment of cerebral hemodynamic parameters using pulsatile versus non-pulsatile cerebral blood outflow models”. en. In: *Journal of Clinical Monitoring and Computing* 33.1 (Feb. 2019). Publisher: Springer Science and Business Media LLC, pp. 85–94. DOI: 10.1007/s10877-018-0136-1.

[78] Ninghe Liu et al. “Optimized cerebral blood flow measurement in speckle contrast optical spectroscopy via refinement of noise calibration”. In: *Opt. Lett.* 50.17 (Sept. 2025), pp. 5382–5385. DOI: 10.1364/OL.570951.

Chapter 4

FROM SINGLE-CHANNEL SENSOR TO MULTI-CHANNEL SYSTEM

This chapter is adapted from published work: Mahler, S., Huang, Y. X., Ismagilov, M., Álvarez-Chou, D., Abedi, A., Tyszka, J. M., Lo, Y. T., Russin, J., Pantera, R. L., Liu, C., Yang, C. (2025). *Portable six-channel laser speckle system for simultaneous measurement of cerebral blood flow and volume with potential applications in characterization of brain injury*. *Neurophotonics*, 12(1), 015003.

The preceding chapters have systematically addressed and resolved the core challenges of acquiring a high-fidelity, brain-specific optical signal from a single cranial location. Chapter 2 experimentally validated the foundational principle of depth sensitivity, demonstrating that by extending the source-detector (S-D) distance, we can indeed measure hemodynamics within the brain. Chapter 3 confronted the practical consequences of this principle—the inherent trade-off between brain specificity and signal intensity. Through a rigorous investigation of interferometric techniques, the development of a novel compact device, and the creation of an advanced noise-calibration algorithm, we established a robust solution: the compact, fiber-free Speckle Contrast Optical Spectroscopy (SCOS) architecture. This approach emerged as the superior methodology, offering an optimal balance of signal-to-noise ratio, stability, and cost-effectiveness essential for clinical translation.

However, the diagnostic power of a single-point measurement, no matter how precise, is inherently limited. Neurological conditions, from traumatic brain injury to stroke, manifest with complex spatial and temporal dynamics that demand a multi-regional perspective. A single data stream cannot, for instance, compare the vascular response in an injured hemisphere against a healthy one or map the hemodynamic consequences of a localized event. Therefore, the logical and critical next step in this research is to evolve the validated single-channel sensor into a multi-channel neuro-monitoring system. This chapter details the scientific and engineering efforts required to achieve this crucial scaling.

The transition from a single prototype to a deployable multi-channel array introduces a distinct set of challenges that extend beyond the signal acquisition principles

already established. These challenges are addressed here in two primary sections:

First, this chapter details the hardware and engineering refinements necessary for practical, long-term wearability. As the number of modules on the head increases, considerations of subject comfort, thermal management, and ergonomic stability become paramount. We present the design solutions developed to ensure the system can be worn comfortably and safely for extended clinical monitoring sessions. We will also focus on the creation of a cohesive and scalable software ecosystem. This encompasses the complex requirements of multi-sensor calibration, synchronized data acquisition, and real-time processing. We discuss the key system architecture choices and culminate with the development of an intuitive Graphical User Interface (GUI). This final piece is designed to abstract the system's underlying complexity, with the ultimate aim of empowering trained clinical personnel to operate the device effectively, thereby paving the way for its broader adoption in settings such as the emergency room.

Next, we will present a use case of using the multi-channel system in clinical settings. More specifically, we compared measurements from normal healthy subjects with subjects that have or had severe traumatic brain injury, and a difference is observed between the channels and the subjects. This showcases the potential use case of the multi-channel system.

4.1 Scaling up, from single to multi-channel

Building upon the success of the single-channel compact SCOS prototype, we developed a six-channel portable system capable of simultaneously measuring CBF and CBV at six different brain locations, as depicted in Fig. 4.1. The system integrates three laser diode modules and six USB board camera sensor modules into a wearable headband, allowing them to be conveniently positioned at distinct locations around the subject's head. With the exception of the USB cables connecting the cameras to a laptop, the entire system is self-contained and powered by embedded, rechargeable 9V batteries.

Addressing the critical hardware challenges of wearability and long-term use, the camera modules were specifically designed to dissipate heat effectively, ensuring a comfortable contact temperature during extended recordings. On the software front, a custom Graphical User Interface (GUI) was developed, enabling non-expert users to operate the system with ease while data is transmitted for real-time processing.

The complete system was characterized and tested on a cohort of five healthy human

subjects. Performance validation demonstrated synchronized and highly correlated dynamics of blood flow and blood volume across all six channels. Furthermore, dedicated comfort evaluation tests confirmed the wearable system's practicality for clinical use and established its maximum operational duration. The following subsections provide a detailed breakdown of the system's hardware design, software architecture, and performance validation.

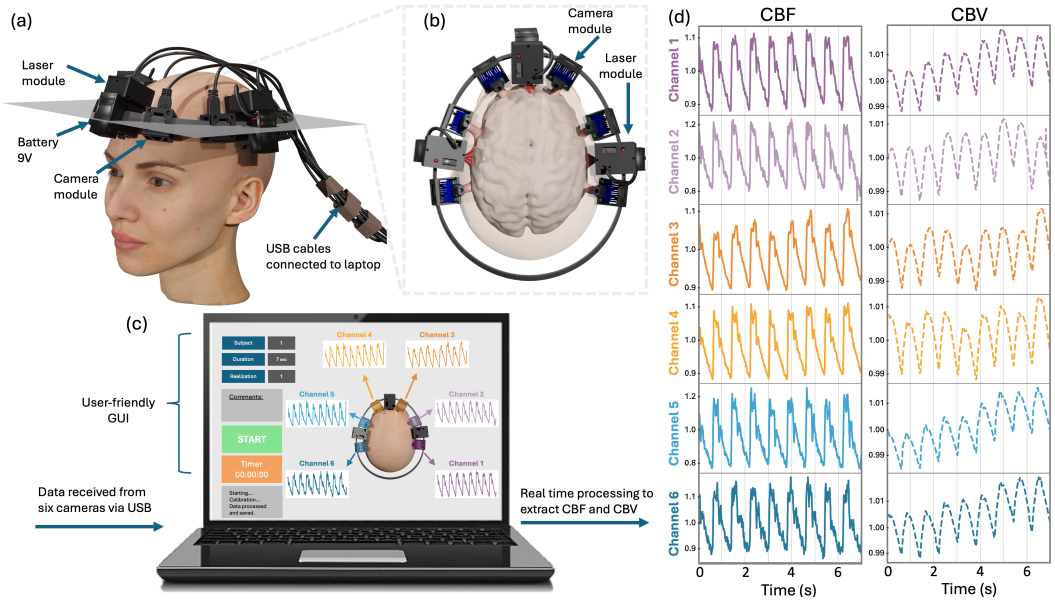


Figure 4.1: Experimental arrangement of the six-channel SCOS system. (a) 3D visualization of the six-channel system positioned on the head. (b) Schematic of the light penetrating the brain. (c) Graphical User Interface for operating the system and for real time visualization of the cerebral blood flow (CBF) and cerebral blood volume (CBV). (d) Typical CBF and CBV blood dynamics measured at six different locations of the head from our compact SCOS system.

Six-channel SCOS system

The arrangement of our compact six-channel SCOS system is shown in Fig. 4.1. The wearable headband and location of each channel on the head are shown in Fig. 4.1(a). The system contains three laser sources for illumination and six board-cameras for detection. The cameras are distributed on the head as follows: two on each side of the forehead, one on the front and one on the back of the left hemisphere, and one on the front and one on the back of the right hemisphere. Each camera is placed at a source-to-detector (S-D) distance from the laser source around 3.2 ± 0.2 cm, see Fig. 4.1(b). It was previously reported that a S-D distance between 3.0 to 3.5 cm corresponds to an optimal brain sensitivity over signal-to-noise ratio [1, 2, 3, 4, 5, 6,

7]. We note that, even at such a large S-D distance, the collected signal would still be influenced by blood flow in the scalp. Each laser source is a single-mode continuous wave laser diode of 808 nm [Thorlabs M9-808-0150]. To ensure control over the illumination spot size and prevent undesirable laser light reflections or stray light, the laser diode is housed in a 3D-printed mount with a circular aperture of 5.5 mm diameter. A sliding block switch at the end of the laser mount can block laser light when the system is not in use. The camera is also housed in a 3D-printed mount. All the mounts were printed using an Anycubic 3D printer in black resin which absorbs light and minimizes back reflection and stray light disturbances. The laser diode is positioned 6 mm away from the skin of participants such that the illumination spot diameter was 5.5 mm [8, 9]. The total illumination power is limited to 67 mW to ensure that the laser light intensity level of the area of illumination is well within the American National Standards Institute (ANSI) laser safety standards for maximum permissible exposure (3.28 mW/mm^2) for skin exposure to a 808 nm laser beam [10]. Each laser is operated by a custom-made printed circuit board combined with a laser diode driver [Thorlabs LD1100], both encased atop the laser diode, see Fig. 4.1(a). Three 9V batteries (located on the top area of the head) provide electrical energy for switching the three laser sources with battery life lasting greater than 3 hours of usage (Figs. 4.2(a) and 4.2(b)).

The camera used is a rolling shutter camera [Basler daA3840-45um (Sony IMX334 sensor)] operating at a framerate of 40 frames-per-second, with a pixel pitch of 2×2 μm, a pixel resolution of 3840×2160 pixels, a pixel depth of 8 bits, and operated at an exposure time $T = 6$ ms. A heat management system ensures that the contact temperature of the camera mount remains below the safety threshold. The passive heat management system comprises of the following materials: a 0.040" laser-cut copper sheet, a 1 mm neoprene sheet [McMaster 93375K608] and an anodized aluminum heat sink of $30 \times 20 \times 10$ mm placed on the back of the copper sheet, a 1 mm thickness cork sheet, and a 1 mm thickness black silicone sheet. The design and dimensions of the camera module system are illustrated in Fig. 4.2(c).

Recap of CBF and CBV Index Calculation

As established in the previous chapters, the core metrics for our system are the Cerebral Blood Flow Index (CBFI) and the Cerebral Blood Volume Index (CBVI). This section briefly recaps the methodology for their calculation from the raw camera data.

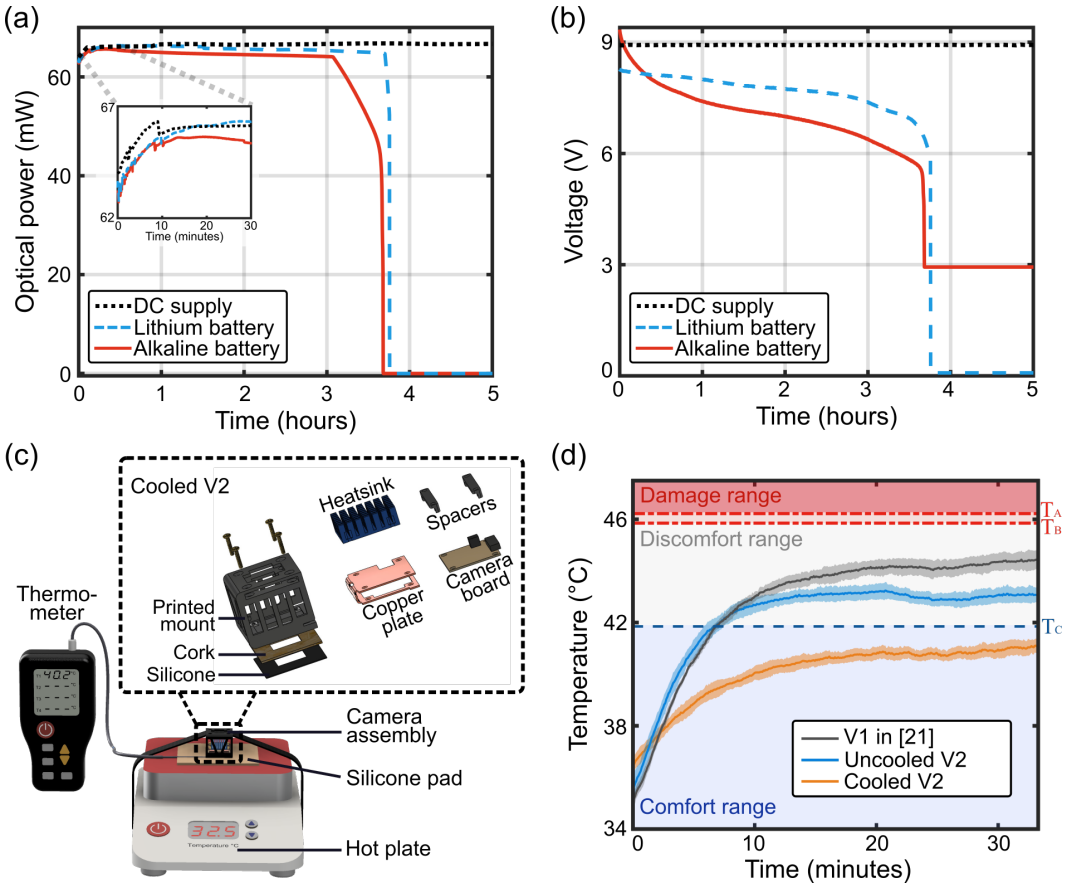


Figure 4.2: Optical lasing power and camera heating temperature characterization of the system. (a) Optical power and (b) power supply voltage plotted as functions of laser operating time. (c) Diagram of the camera module, including an exploded view of the heat management system (inset). (d) Contact temperature measured as a function of the camera's operating time.

The estimated number of speckles per pixel collected by the camera is approximately 4, corresponding to a one-dimensional speckle-to-pixel length ratio (s/p) of 0.5 [11, 12, 13]. The raw squared speckle contrast, K^2_{raw}, is calculated from the recorded speckle images as:

$$K^2_{raw}(I(t)) = \frac{\sigma^2(I(t))}{\mu^2(I(t))}. \tag{4.1}$$

where $\sigma^2(I(t))$ is the variance of the normalized image I at time t and $\mu(I(t))$ is its mean. The various sources of noise are then accounted for to find the adjusted speckle contrast [9, 14, 15, 16]:

$$K^2_{adjusted}(t) = K^2_{raw}(t) - K^2_{shot}(t) - K^2_{quant}(t) - K^2_{cam}(t), \tag{4.2}$$

with K^2_{shot} accounting for variance contributions from shot noise, K^2_{quant} for vari-

ance inherited from quantization, and K^2_{cam} for the variance contributions from the camera's readout and dark noise. A detailed description of these calculations can be found in Ref. [9]. The Cerebral Blood Flow Index (CBFI) is then related to $K^2_{adjusted}$ as [9]:

$$\mathrm{CBFI}(t) = \frac{1}{K^2_{adjusted}(t)}. \tag{4.3}$$

The blood volume is extracted from the camera images by calculating the Cerebral Blood Volume Index (CBVI) from the recorded images as [17, 2]:

$$\mathrm{CBVI}(t) = \frac{2I_0 - \langle I(t) \rangle}{I_0}, \tag{4.4}$$

where I_0 is the intensity at baseline. In the results presented in this chapter, we utilize the normalized CBFI and CBVI metrics to provide normalized blood dynamics information for enhanced comparability across measurements.

Graphical User Interface and System Cost

A key component for clinical translation is a user-friendly software interface. The Graphical User Interface, illustrated in Fig. 4.1(c), controls the system and displays the CBF and CBV results at the end of each recording. The Python-based GUI prompts users to input details such as subject information, trial number, and the duration of the recording, which is capped at 180 seconds. Users can also add comments regarding the quality of the recording, potential movements, and other subject information. Furthermore, the GUI ensures safety by requiring users to confirm adherence to all laser safety protocols before initiating any measurements. Upon completion, the GUI immediately presents the processed results, including CBF and CBV waveforms for each channel (Fig. 4.1(c)). The real-time processing of data negates the need to save raw images, thereby optimizing disk space usage.

The total hardware cost of the six-channel SCOS system is approximately $3,000. Data collection and processing are performed by a laptop equipped with a modern GPU (e.g., Nvidia RTX 4070), costing approximately $1,500.

Figure 4.1(d) shows typical CBF and CBV time traces measured over 5 seconds by the six-channel SCOS system on a human subject. As shown, all CBF and CBV time traces exhibit the same frequency of oscillation and are temporally synchronized. Note that the CBF time traces contain more high-frequency information than the CBV time traces, including variations such as the peak systole or dicrotic notch of the cardiac pulse [2]. Additionally, the CBF time traces show greater temporal stability compared to CBV, as minor fluctuations in blood oxygen concentration

and other instabilities do not significantly impact the normalized speckle contrast calculations (Eq. 4.1).

4.2 System Stability: Power and Thermal Management

Next, we evaluated the stability and longevity of the laser source when powered by a DC power supply versus a 9V battery (Figs. 4.2(a) and 4.2(b)) and examined the contact temperature of the camera module (Figs. 4.2(c) and 4.2(d)). These characterizations are critical for using the system in a clinical setting, as patients in such environments may not be able to respond to pain or discomfort, or they may be unconscious. Therefore, it is essential to first ensure that powering the system with a low-voltage battery guarantees electrical safety for the patients being scanned, and that the system's temperature is carefully constrained to prevent any risk of heat-induced damage.

Figure 4.2(a) shows the laser output power, measured with an optical power meter positioned on the mounted laser diode, for three different power sources: a 9V DC bench power supply, a 9V alkaline battery, and a rechargeable 9V lithium-ion battery. As shown, all three power sources provided the laser with an optical power of approximately 66 mW over time. The DC power supply maintained a constant output, while the alkaline and rechargeable lithium-ion batteries' power decreased to zero after a few hours due to discharge. Overall, the lithium-ion battery outperformed the others, lasting the longest (approximately 3.7 hours), demonstrating the highest stability in optical power output, and being the most lightweight. Detailed performance comparisons of the batteries can be found in Appendix A. Additionally, the system optical power with the rechargeable lithium-ion battery sharply dropped to zero within 3 minutes, due to an internal electrical switch that automatically disables the battery when the voltage falls below a certain threshold. In our case, this feature is beneficial as it prevents noisy data collection during the battery's discharge phase. With an average measurement time of 15 minutes per subject, the lithium battery can support up to 12 recordings or more on a single charge. This is practical, as the battery can be recharged between sessions.

Next, we tested the effectiveness of the passive heat management system for the camera modules by measuring the contact temperature after placing the system on silicone skin pads [Stylia] positioned on a hot plate [VWR] set at 32.5 °C to simulate human skin contact (Fig. 4.2(c)). Our goal was to ensure compliance with thermal guidelines for skin contact (ASTM C1055 [18]) and to provide user comfort dur-

ing extended system operation. From the ASTM guidelines, we established three temperature thresholds for one hour of operation of the system: 1) a comfort temperature threshold T_A = 41.85 °C, 2) a reversible skin damage threshold temperature T_B = 45.85 °C, and 3) a severe skin damage threshold temperature T_C = 46.22 °C. Our aim was to not overcome the comfort temperature T_A. We tested three camera module configurations. The first (V1) was the camera module [Basler daA1920-160um] used in Refs. [9, 2], running at 80 FPS with 2.3 million pixels. The second (uncooled V2) was a Basler daA3840-45um board camera running at 30 FPS and 8.3 million pixels. The third (cooled V2) was the camera module used in the rest of this paper, which consists of a Basler daA3840-45um board camera running at 40 FPS and 8.3 million pixels encased in the heat management system shown in Fig. 4.2(c). The averaged temperature results for each module are presented in Fig. 4.2(d). As shown, all the cameras' temperatures remained below both the reversible (T_B) and irreversible (T_C) damage thresholds, in accordance with ASTM guidelines. However, only the cooled V2 module stayed within the targeted comfort temperature range (T_A).

4.3 Can we detect brain injury?

In this section, we put the device on a handful of human subjects to evaluate feedback on comfort as well as investigate the potential of the multi-channel device in discovering discrepancies in blood flow signals across channels.

Human Research Study Protocol

Participants for this study were recruited from the greater Los Angeles area, selected from adult volunteers aged 18 to 70 years. Before the experiments, each participant completed a health questionnaire, and their blood pressure was recorded. Informed consent was obtained from all participants beforehand. The human research protocol was approved by the Caltech Committee for the Protection of Human Subjects and the Institutional Review Board (IRB), under Caltech IRB Protocol IR21-1074. To simplify the experimental setup and system implementation, all measurements were taken on hairless areas or areas with minimal hair. The total illumination power adhered to the American National-Standards-Institute (ANSI) laser safety standards for maximum permissible skin exposure to an 808 nm laser beam.

A total of seven subjects were enrolled in the study, comprising five "healthy" control subjects with no history of brain injury. In addition, two subjects with a history of severe brain injury were recruited to provide a preliminary clinical comparison. The

first, designated as the "TBI" subject, had a history of severe traumatic brain injury requiring decompressive hemicraniectomy and subsequent cranioplasty with a skull implant (SI). The second, designated as the "NTBI" subject, had suffered a non-traumatic brain injury from a large brain hemorrhage due to a ruptured arteriovenous malformation. The NTBI patient also underwent decompressive hemicraniectomy and subsequent cranioplasty. At the time of the study, the NTBI patient had more evidence of structural brain damage and was still in post-discharge care due to behavioral issues. In contrast, the TBI patient had relatively less structural brain damage and was living independently. Neither of the brain-injured subjects presented with focal neurological deficits.

Thermal performance and user comfort

For blood flow measuring systems, characterizing the contact temperature during operation is critical to ensuring participant safety. This is particularly important for systems intended for clinical use, where patients may be unable to respond to pain or discomfort, or may be unconscious [19]. While the laser source of our system adheres to ANSI standards, limiting the optical power level to prevent heat induction, the detection module generates heat during high-speed operation [20, 21]. In systems where modules are in direct contact with the participants' skin, this heat becomes a significant concern, especially since these units typically operate at high speeds [19, 20, 21]. Common mitigation strategies, such as operating for only short periods or cycling the power, are not practical for non-expert users and still pose safety risks. To address these challenges, we designed the passive heat modulation system previously illustrated in Fig. 4.2, enabling our system to operate for more than half an hour while maintaining a comfortable temperature range. Passive cooling offers the advantage of regulating temperature without complex or vibrating equipment that requires external energy sources, making it more user-friendly and practical for long-term use [21, 22].

To validate this performance in a realistic setting, we measured the contact temperature of our detecting modules on the foreheads of five human subjects. The cameras were run for 35 minutes with repeated 3-minute image acquisition sessions followed by 30-second breaks, simulating an extreme usage scenario that might occur during hospital scanning. The ambient room temperature was maintained at approximately 23°C to mimic typical hospital conditions (usually 20°C to 24°C). The temperature was recorded using a commercial thermocouple [Risepro 4 channels] positioned between the camera module and the participants' foreheads. The results are presented

in Fig. 4.3.

Across all five subjects, the contact temperature stabilized after approximately 20 minutes and never exceeded 41°C, remaining within the established comfort temperature range (T_A). These results are consistent with those obtained from the silicone hotplate tests shown previously in Fig. 4.2(d). Concurrently, participants were asked to provide subjective comfort ratings on a scale of 'Comfortable', 'Mild', 'Tolerable', 'Painful', or 'Severe' throughout the 35-minute experiment (Fig. 4.3). None of the subjects reported intolerable discomfort during the entire duration of the study. Only one participant indicated a comfort level worse than 'Mild,' which was attributed not to heat but to the pressure from the tightening of the headband. These experiments collectively demonstrate that the multi-channel compact SCOS system can operate for extended durations without the risk of heat-induced skin damage while maintaining an adequate level of user comfort.

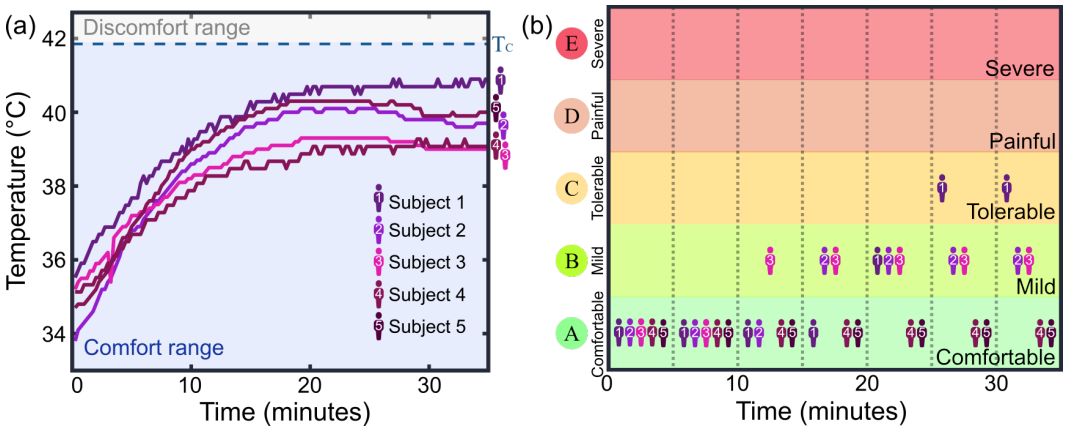


Figure 4.3: In-vivo thermal performance and comfort ratings. (a) Temperature measurements taken at the contact surface of the camera module on the foreheads of five human subjects. The measured temperature saturated after twenty minutes of continuous operation and always remained within the comfort range (i.e., below the comfort threshold T_A = 41.85 °C).(b) Comfort ratings provided by participants during the 35 minutes of continuous recording. The experiment was conducted at a room temperature of 23 °C.

4.4 Multi-Channel System Results: Human Subject Studies

Using the six-channel portable system, we measured CBF and CBV on a cohort of seven subjects. The cohort consisted of five subjects with no history of brain injury (healthy), one subject with a cranioplasty skull implant following a TBI but with no major structural brain damage at the time of the study (TBI), and one subject with

a non-traumatic brain injury who had also undergone a cranioplasty skull implant and was in post-discharge care at the time of the study (NTBI).

Figure 4.4 shows typical CBF time traces measured on a healthy subject (Fig. 4.4(a)), the TBI subject (Fig. 4.4(b)), and the NTBI subject (Fig. 4.4(c)). As shown, the CBF data for the healthy subject displays synchronized and highly correlated blood flow dynamics across all six channels. A similar pattern is observed in the TBI subject. MRI scans confirmed that neither the healthy control subjects nor the TBI subject had significant structural brain damage. In contrast, the CBF data for the NTBI subject exhibited synchronized and correlated blood flow dynamics across all channels *except* for the two channels positioned over the area of brain injury, as revealed by the corresponding MRI scan.

To further characterize the differences across channels and subjects, we calculated the mean intensity of each of the six channels from the CBV recordings (Fig. 4.5(a)) and the two-channel correlation factor from each subject's CBF recordings (Fig. 4.5(b)). The two-channel correlation factor was calculated using the Pearson correlation formula as:

$$\rho(i,j) = \frac{\sum_{t=1}^{T}(\mathrm{CBFI}(i,t) - \overline{\mathrm{CBFI}}(i))(\mathrm{CBFI}(j,t) - \overline{\mathrm{CBFI}}(j))}{\sqrt{\sum_{t=1}^{T}(\mathrm{CBFI}(i,t) - \overline{\mathrm{CBFI}}(i))^2 \sum_{t=1}^{T}(\mathrm{CBFI}(j,t) - \overline{\mathrm{CBFI}}(j))^2}}, \quad (4.5)$$

where $\mathrm{CBFI}(i,t)$ and $\mathrm{CBFI}(j,t)$ are the cerebral blood flow indices at channels i and j respectively, $\overline{\mathrm{CBFI}}(i)$ and $\overline{\mathrm{CBFI}}(j)$ are the average CBFI over time, and T is the total number of data points in a time trace. Note that the number of possible combinations to calculate the correlation factor is 15, since we correlate pairs of channels out of six total channels ($\binom{6}{2}$).

An analysis of the results, presented in Figs. 4.5(a) and 4.5(b), reveals distinct patterns across the subject cohorts. For the five healthy subjects, both the mean channel intensity and the inter-channel correlation factors were consistently high. The TBI subject exhibited comparable mean channel intensities but a noticeably lower and wider distribution of correlation factors. In stark contrast, the NTBI subject demonstrated significantly lower mean intensities and correlation factors, particularly in the four channels positioned over the posterior-right side of the head, which was the known injury location.

This decorrelation is further visualized in the channel-to-channel correlation matrices shown in Fig. 4.5(c). For the representative healthy subject (Subject 5,

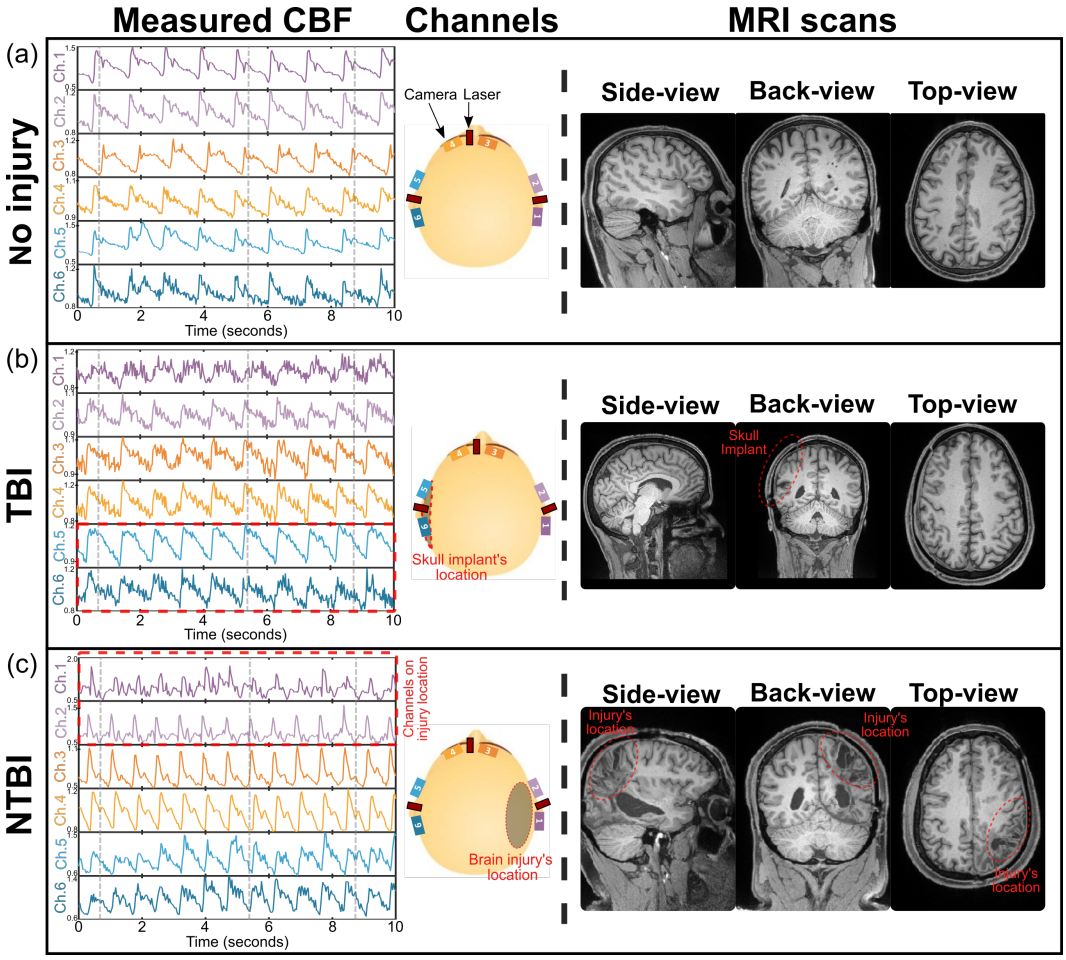


Figure 4.4: Measured CBF at six different locations and MRI scans of the heads of (a) healthy, (b) TBI, and (c) NTBI subjects. Note that the MRI images are not mirrored; the right side of the image corresponds to the subject's right side.

corresponding to the waveforms in Fig. 4.4(a)), the correlation coefficients are uniformly high (> 0.75). In contrast, the matrix for the NTBI subject (corresponding to Fig. 4.4(c)) reveals two distinct clusters. Channels 1 and 2 are correlated with each other, while Channels 3 through 6 form a separate, internally correlated group. This quantitative result confirms the visual observation that the channels positioned over the injury site exhibit distinct CBF dynamics compared to those over healthier tissue.

Figure 4.5(d) synthesizes these findings by plotting the inter-channel correlation factor (from Eq. 4.5) as a function of the two-channel mean intensity. The two-channel mean intensity was calculated by averaging the mean intensity of the two channels used to compute the correlation factor. As shown, the data points for all

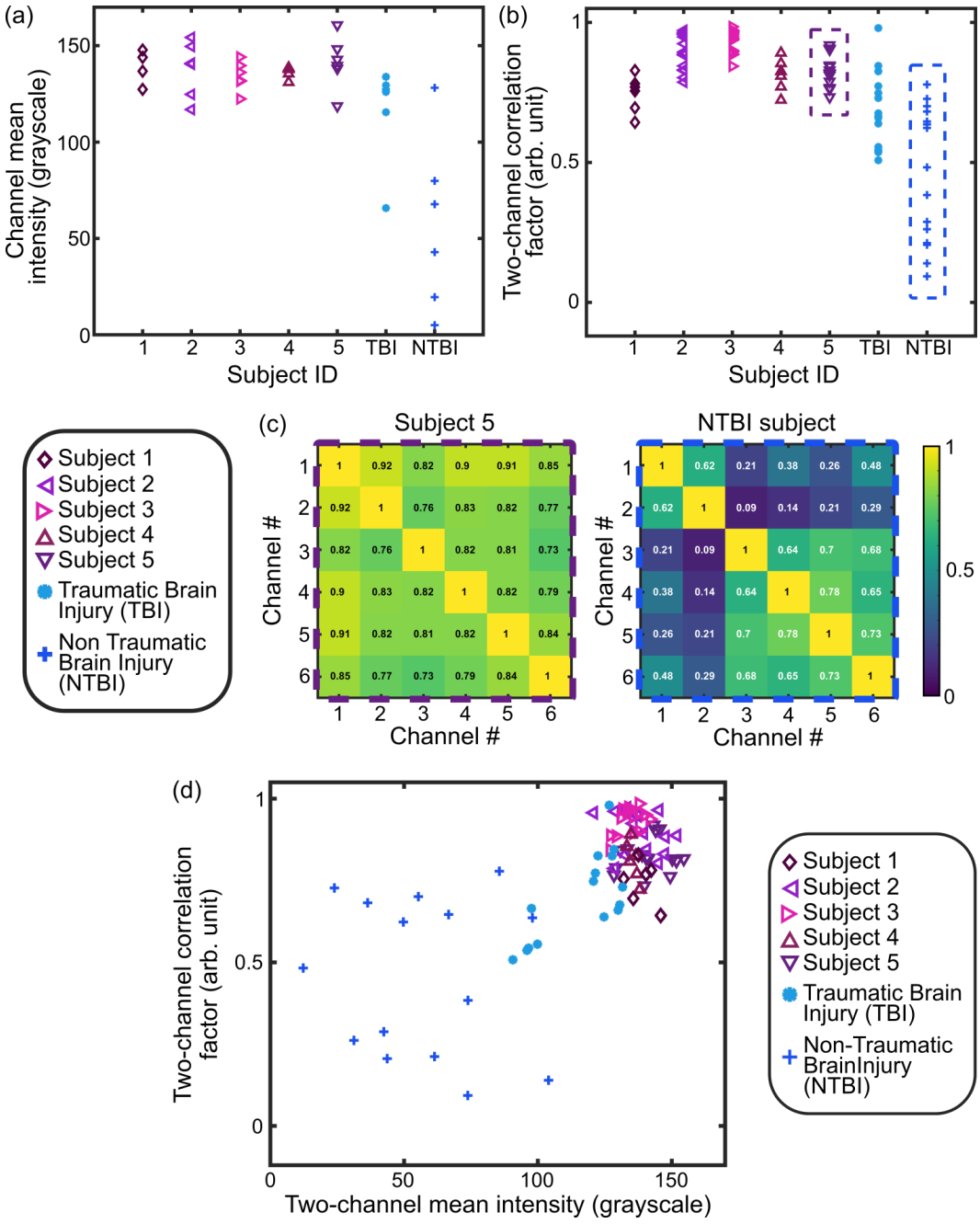


Figure 4.5: Quantitative results from multi-channel CBF data between subjects. (a) Channel mean intensity and (b) two-channel correlation factor for each of the seven subjects. (c) Correlation matrix of all channels of Subject 5 (also shown in Fig. 4(a)) and NTBI Subject (also shown in Fig. 4(c)). (d) Two-channel correlation factor as a function of the two-channel mean intensity for all the subjects.

healthy subjects and the TBI subject cluster in the upper-right quadrant, indicating both high signal intensity and strong inter-channel synchronization across all six channels. In contrast, the data points for the NTBI subject are scattered, with many exhibiting lower mean intensity and significantly reduced correlation. This suggests that regional differences in CBF and CBV dynamics, likely due to the injury, are being captured by the system.

It is critical to emphasize that these observations are preliminary, given the small sample size of only one subject for each brain injury case (TBI and NTBI). A larger study with more subjects is necessary to draw definitive conclusions regarding the diagnostic efficacy of this multi-channel approach for characterizing traumatic and non-traumatic brain injury. Nonetheless, these initial results serve as a compelling proof-of-concept. They demonstrate the potential of a multi-channel SCOS system to leverage its high throughput, multi-location, and parallel processing capabilities to identify and compare regional hemodynamic discrepancies that may be of clinical significance.

4.5 Concluding Remarks on the Multi-Channel System

This chapter has chronicled the critical evolution from the validated single-channel sensor, developed in Chapter 3, into a fully functional, deployable, six-channel neuro-monitoring system. We successfully addressed the key engineering challenges—both hardware and software—required to achieve this crucial scaling. The resulting system effectively demonstrates that the modular, compact SCOS architecture can be expanded for continuous, multi-regional monitoring of cerebral blood flow and volume over extended periods.

The final hardware integrates three battery-powered laser modules and six camera sensors into a single wearable headband, offering portability and flexible positioning for targeting specific areas of interest. Crucially, through dedicated hardware characterization and design, we validated the system's long-term operational stability. The optimized passive thermal management enables continuous operation for over 30 minutes while keeping the sensor contact temperature within a safe and comfortable range for human subjects. On the software front, the development of a user-friendly GUI and a near real-time processing pipeline on a standard commercial laptop makes the system accessible and practical for deployment in diverse environments, from research labs to clinics.

The system's potential was preliminarily explored in a human study that included

five healthy subjects and two subjects with a history of severe brain injury (TBI and NTBI). We observed noticeable differences in CBF and CBV dynamics, with significant signal decorrelation found specifically at the channels overlying the site of structural brain damage in the NTBI subject, as confirmed by MRI.

It is critical to emphasize that with a sample size of one for each brain injury case, these observations serve only as an initial case study and are not sufficient to draw any clinical conclusions. The primary purpose of this demonstration was not to characterize brain injury, but to showcase the unique capabilities of a multi-channel SCOS system. Specifically, this experiment highlights the system's ability to:

1. **Measure hemodynamics from multiple distinct brain regions simultaneously**, a fundamental requirement for assessing spatially heterogeneous conditions.

2. **Quantify the degree of synchronization** between these regions by calculating inter-channel correlations.

3. **Extract potentially useful information** by identifying regional discrepancies that would be entirely missed by a single-point measurement.

These results, while not generalizable, serve as a compelling proof-of-concept for the methodology itself. They demonstrate that a multi-channel SCOS system can leverage its high throughput and multi-location architecture to identify and compare regional hemodynamic patterns.

Having now established and validated a robust multi-channel platform capable of detecting such regional differences, the logical next step is to deploy this system to investigate a specific and pressing clinical question with a larger cohort. The following chapter, therefore, moves beyond system characterization to a targeted application: assessing cerebrovascular health and stroke risk by subjecting the brain to a physiological "stress test."

References

[1] Simon Mahler et al. "Assessing depth sensitivity in laser interferometry speckle visibility spectroscopy (iSVS) through source-to-detector distance variation and cerebral blood flow monitoring in humans and rabbits". en. In: *Biomedical Optics Express* 14.9 (Sept. 2023), p. 4964. DOI: 10.1364/BOE.498815.

[2] Yu Xi Huang et al. “Correlating stroke risk with non-invasive cerebrovascular perfusion dynamics using a portable speckle contrast optical spectroscopy laser device”. In: *Biomed. Opt. Express* 15.10 (Oct. 2024), pp. 6083–6097. DOI: 10.1364/BOE.534796.

[3] Gary E. Strangman, Zhi Li, and Quan Zhang. “Depth Sensitivity and Source-Detector Separations for Near Infrared Spectroscopy Based on the Colin27 Brain Template”. en. In: *PLoS ONE* 8.8 (Aug. 2013), e66319. DOI: 10.1371/journal.pone.0066319.

[4] Florian B. Haeussinger et al. “Simulation of Near-Infrared Light Absorption Considering Individual Head and Prefrontal Cortex Anatomy: Implications for Optical Neuroimaging”. en. In: *PLoS ONE* 6.10 (Oct. 2011). Ed. by Kenji Hashimoto, e26377. DOI: 10.1371/journal.pone.0026377.

[5] Chemseddine Mansouri et al. “Depth sensitivity analysis of functional near-infrared spectroscopy measurement using three-dimensional Monte Carlo modelling-based magnetic resonance imaging”. en. In: *Lasers in Medical Science* 25.3 (May 2010), pp. 431–438. DOI: 10.1007/s10103-010-0754-4.

[6] Stefan A. Carp, Mitchell B. Robinson, and Maria A. Franceschini. “Diffuse correlation spectroscopy: current status and future outlook”. In: *Neurophotonics* 10.01 (Jan. 2023). DOI: 10.1117/1.NPh.10.1.013509.

[7] Wenjun Zhou et al. “Functional interferometric diffusing wave spectroscopy of the human brain”. en. In: *Science Advances* 7.20 (May 2021), eabe0150. DOI: 10.1126/sciadv.abe0150.

[8] Simon Mahler et al. “Assessing depth sensitivity in laser interferometry speckle visibility spectroscopy (iSVS) through source-to-detector distance variation and cerebral blood flow monitoring in humans and rabbits”. In: *Biomed. Opt. Express* 14.9 (Sept. 2023), pp. 4964–4978. DOI: 10.1364/BOE.498815.

[9] Yu Xi Huang et al. “Compact and cost-effective laser-powered speckle contrast optical spectroscopy fiber-free device for measuring cerebral blood flow”. In: *Journal of Biomedical Optics* 29.6 (2024), p. 067001. DOI: 10.1117/1.JBO.29.6.067001.

[10] *ANSI Z136.1-2014 - American National Standard for Safe Use of Lasers*.

[11] Jian Xu, Ali K Jahromi, and Changhuei Yang. “Diffusing wave spectroscopy: A unified treatment on temporal sampling and speckle ensemble methods”. en. In: *APL Photonics* 6.1 (Jan. 2021). Publisher: AIP Publishing, p. 016105. DOI: 10.1063/5.0034576.

[12] Sharvari Zilpelwar et al. “Model of dynamic speckle evolution for evaluating laser speckle contrast measurements of tissue dynamics”. en. In: *Biomedical Optics Express* 13.12 (Dec. 2022), p. 6533. DOI: 10.1364/BOE.472263.

[13] Mitchell B. Robinson et al. “Comparing the performance potential of speckle contrast optical spectroscopy and diffuse correlation spectroscopy for cerebral blood flow monitoring using Monte Carlo simulations in realistic head geometries”. In: *Neurophotonics* 11.01 (Jan. 2024). DOI: 10.1117/1.NPh.11.1.015004.

[14] Byungchan Kim et al. “Measuring human cerebral blood flow and brain function with fiber-based speckle contrast optical spectroscopy system”. en. In: *Communications Biology* 6.1 (Aug. 2023), p. 844. DOI: 10.1038/s42003-023-05211-4.

[15] W. F. Sheppard. “On the Calculation of the most Probable Values of Frequency-Constants, for Data arranged according to Equidistant Division of a Scale”. en. In: *Proceedings of the London Mathematical Society* s1-29.1 (1897). _eprint: https://onlinelibrary.wiley.com/doi/pdf/10.1112/plms/s1-29.1.353, pp. 353–380. DOI: 10.1112/plms/s1-29.1.353.

[16] Lisa Kobayashi Frisk et al. “Comprehensive workflow and its validation for simulating diffuse speckle statistics for optical blood flow measurements”. en. In: *Biomedical Optics Express* 15.2 (Feb. 2024), p. 875. DOI: 10.1364/BOE.502421.

[17] Christopher G. Favilla et al. “Validation of the Openwater wearable optical system: cerebral hemodynamic monitoring during a breath-hold maneuver”. In: *Neurophotonics* 11.01 (Mar. 2024). DOI: 10.1117/1.NPh.11.1.015008.

[18] C16 Committee. *Guide for Heated System Surface Conditions that Produce Contact Burn Injuries*. en. DOI: 10.1520/C1055-20.

[19] R. Defrin et al. “Sensory determinants of thermal pain”. en. In: *Brain* 125.3 (Mar. 2002), pp. 501–510. DOI: 10.1093/brain/awf055.

[20] Seonggwang Yoo et al. “Responsive materials and mechanisms as thermal safety systems for skin-interfaced electronic devices”. en. In: *Nature Communications* 14.1 (Feb. 2023), p. 1024. DOI: 10.1038/s41467-023-36690-y.

[21] Hyoyoung Jeong et al. “Differential cardiopulmonary monitoring system for artifact-canceled physiological tracking of athletes, workers, and COVID-19 patients”. en. In: *Science Advances* 7.20 (May 2021), eabg3092. DOI: 10.1126/sciadv.abg3092.

[22] Jing Liu et al. “Enhancing wearable electronics through thermal management innovations”. en. In: *Wearable Electronics* 1 (Dec. 2024), pp. 160–179. DOI: 10.1016/j.wees.2024.07.005.

Chapter 5

STROKE RISK? A STRESS TEST FOR YOUR BRAIN

This chapter is adapted from published work: Huang YX, Mahler S, Abedi A, Tyszka JM, Lo YT, Lyden PD, Russin J, Liu C, Yang C. Correlating stroke risk with non-invasive cerebrovascular perfusion dynamics using a portable speckle contrast optical spectroscopy laser device. Biomed Opt Express. 2024 Oct;15(10):6083-6097.

5.1 Introduction to stroke risk and our approaches

Stroke is a global health concern, with a distressingly high incidence and substantial morbidity and mortality [1]. Annually, more than ten million people worldwide are impacted by strokes, imposing a heavy toll on affected individuals and their families, with significant health, financial, and quality of life burdens [2]. From the age of 25, the lifetime risk of stroke is around 25% [3]. In the US, stroke affects nearly 800,000 individuals each year, contributing to significant healthcare challenges [4]. Early detection of stroke risk is pivotal in reducing its incidence and severity and improving outcomes. A variety of interventions, such as lifestyle modifications (including diet, exercise, and smoking cessation) and medical management strategies (such as blood pressure control), exist to mitigate stroke risk [4, 5, 6, 7].

Traditionally, stroke risk estimation relies on indirect markers such as demographics and comorbidities. As such, the most widely used questionnaires for stroke risk estimation capture factors such as diabetes and hypertension, along with lifestyle-related factors such as smoking and low physical activity [2, 8, 9, 10, 11, 12, 13]. These risk profiles are based on population data and are useful for general assessments. However, they are not definitive for determining the need for invasive or non-invasive evaluations, nor for guiding surgical or pharmacological interventions in individual patients to prevent future strokes. The community has pushed forward exploration in using non-invasive models to detect and characterize after the onset of stroke, but not for the quantification of stroke risk [14, 15]. Limited non-invasive, scalable, and cost-effective measures based on direct neuroimaging currently exist to stratify stroke risk in the general population. This gap highlights the pressing need for objective and cost-effective measures of cerebral perfusion reserve. This need is particularly evident when compared to the management of

myocardial ischemia through stress testing. Stress tests serve as a pivotal, objective method to evaluate cardiac health, functional capacity, and myocardial ischemia risk. An equivalent direct and objective measure for assessing neurovascular health that is low-cost enough to deploy broadly in the community—akin to but potentially more available than cardiac stress testing—is conspicuously absent. We believe that this study introduces a simple, cost-effective solution that does not require ionizing radiation or radioactive isotopes that has the potential to lead to better development of personalized strategies for reducing stroke risk.

Efforts to characterize cerebral perfusion capacity have been underway for the past four decades. Neuroimaging modalities such as PET, SPECT, xenon-enhanced CT, and perfusion CT can be coupled with acetazolamide administration to augment brain perfusion and reveal areas of diminished reserve [16, 17, 18]. However, all existing imaging modalities share several common limitations: they cannot be performed under exercise stimuli such as a treadmill stress test; they all require expensive equipment; and their lack of scalability and logistic limitations do not permit implementation at bedside, in the clinic, or widespread use for screening in the community settings. Each method also has its specific limitations. For instance, the acetazolamide challenge has various side effects and contraindications in the presence of certain comorbidities, while the reference measurements used in CT perfusion assessment are derived from a single unaffected major cerebral vessel in each individual, which in many cases may lead to the underestimation of cerebral blood flow (CBF) in affected regions [17]. The Framingham Stroke Risk Profile has recently been augmented with multimodal magnetic resonance imaging (MRI) to quantify the risk of acute stroke in patients with symptomatic ischemia [19, 20]. This approach requires access to contrast-enhanced MRI, rendering it impractical for routine stroke risk screening. Further, with the advent of ischemic symptoms, primary prevention likely becomes moot, as the presence of symptoms suggests the progression of vascular disease to a clinically significant stage. There have been efforts using transcranial Doppler (TCD) ultrasonography to evaluate brain blood flow [21, 22, 23] with technician-dependent results. In addition, TCD only targets larger arteries and can only be used on limited areas of the skull, most commonly the temporal acoustic window [24]. A cost-effective and scalable stroke risk assessment system does not exist currently. This complicates the effective long-term prevention of stroke. Having established through a questionnaire that a patient is at high risk for stroke, a physician has no good way to know whether a patient's risk is increasing or stable, and whether or when a patient needs intervention.

Physiologically, a stroke occurs when the brain's vascular system is compromised, either through the blocking of blood flow (ischemic stroke) or a rupture of a blood vessel (hemorrhagic stroke). Both events lead to reduced blood flow and consequently oxygen supply to brain tissues. Risk factors of stroke include age, cardiovascular diseases, high blood pressure, high blood sugar, smoking, and elevated cholesterol [9]. These same factors also impact how the brain reacts to oxygen deprivation or carbon dioxide buildup during events like breath-holding. During breath-holding, both cerebral blood volume and cerebral blood flow increase in response to higher carbon dioxide and lower oxygen levels. To mitigate the increased shear pressure of the blood caused by the rising blood flow, the cerebral autoregulation system prompts blood vessel dilation. Such cerebral autoregulation is impaired in diseased atherosclerotic vessels, including in response to other hemodynamic perturbations such as hypotension and upstream stenosis (e.g., carotid stenosis).

The skull blocks most means for direct, non-invasive measurements of the brain's blood dynamics. Fortunately, infrared light can transmit relatively well through the skull and brain [25, 26, 27, 28]. By transmitting infrared light through one location on the skull and collecting its transmission from another location, it is possible to track the relative blood volume by measuring the light attenuation rate [24, 29, 30]. If the light used is coherent, such as a laser, mutual interference of light following different trajectories causes speckle patterns, which depend on the coherence of the laser source [31, 32, 33, 34]. By observing how fast the transmitted laser speckle field fluctuates, it is possible to also determine relative blood flow by using a camera [24, 35, 30, 36, 37]. This technique is commonly called speckle contrast optical spectroscopy (SCOS) [24, 35, 30, 38] or speckle visibility spectroscopy (SVS) [27, 35, 36, 39]. The movement of blood within the brain causes this speckle field to fluctuate – the faster the blood flow, the faster the fluctuation. Compared to diffuse wave spectroscopy, also known as diffuse correlation spectroscopy, which utilizes a photodetector and requires a sampling frequency in the MHz range, SCOS, which utilizes a CMOS sensor is not only more cost-effective to implement but also enhances signal sensitivity by leveraging the large pixel count of the camera [36, 39, 40]. We previously demonstrated the use of a compact SCOS device on the frontal area of the head to non-invasively measure brain blood flow, by using a large source-to-detector (S-D) distance, greater than 3 cm [36].

In this chapter, we combine a compact and comprehensive brain blood flow and blood volume SCOS system with a breath-holding exercise to provide a direct

physiology-based measurement of the brain blood vessel condition. Such a system consists solely of a laser diode and a CMOS-based board camera that can be placed on the head with no external optical elements, providing a lightweight, portable, and budget-friendly design [36]. Monitoring of local cerebral blood flow and blood volume rate changes during breath-holding was performed on a cohort of 50 subjects, divided into two groups of 25 each. Subjects were evaluated using the Cleveland Clinic Stroke Risk Calculator where the lower the score, the lower the risk [8]. One group was at low risk for stroke (low-risk group, score 1), and the other was at higher risk for stroke (higher-risk group, score 4). By comparing the ratio of blood flow changes over blood volume changes—a proxy to blood pressure changes—we aim to observe a highly significant difference between the groups [24, 41]. These findings would align with our expectations: during breath-holding among those at elevated stroke risk, less flexible blood vessels impede dilation (lack of compliance), prompting accelerated blood flow in response to the brain's heightened demand for oxygen caused by carbon dioxide buildup (hypercapnia). We further stratified the higher-risk cohort into smaller sub-groups according to the Cleveland Clinic Stroke Risk Calculator. Our analysis revealed significant correlations between stroke risk scores and flow to volume ratio during breath-holding. This study offers preliminary physiological insights into stroke risk assessment by establishing correlations between these two methods.

5.2 Methods to evaluate stroke risk

Participants Participants for this study were recruited from the Caltech, Pasadena, and greater Los Angeles local communities, selected among adult humans aged from 18 to 65 years. Subjects uncomfortable with holding their breath or with major respiratory diseases were excluded from this study. Before the experiments, each participant completed a health questionnaire (showed in Supplementary Material), and their blood pressure was recorded. Informed consent was obtained from the participants beforehand. The human research protocol for this study received approval from the Caltech Committee for the Protection of Human Subjects and the Institutional Review Board (IRB). To simplify the experiment and implementation of the device, measurements were conducted on hairless areas, such as the forehead. The total illumination power was within the American National Standards Institute (ANSI) laser safety standards for maximum skin exposure of a 785 nm laser beam.

A total of fifty-three subjects were enrolled. Three subjects were excluded from the

analysis following quality control for raw data noise and artifact levels and significant movement during the recording. The final dataset encompasses 160 breath-holding entries from 50 subjects. According to the prior questionnaire, the mean(std) ages of the low and higher risk groups were 31(5) and 60(4) years old respectively, 33 subjects were Female and 17 were Male. Traditional stroke risk assessment was performed using the Cleveland Stroke Risk Calculator, which provides a probability stroke risk score ranging from 1 to 10, with lower scores indicating lower risk. Among the 50 subjects, 25 scored 1, 6 scored 4, 10 scored 5, and 9 scored between 6 and 7 in the Cleveland Stroke Risk Calculator.

Compact SCOS device

The experimental configuration of the wearable SCOS device is shown in Fig. 5.1A. It includes a laser source for illumination and a board camera for detection. See Ref. [36] for a more detailed presentation of the apparatus. For this study, we used a single-mode continuous wave λ = 785 nm laser diode [Thorlabs L785H1] which can deliver up to 200 mW. To ensure control over the illumination spot size and prevent undesirable laser light reflections, we housed the laser diode within a 3D-printed mount [36]. The laser source and detecting units were positioned on one side of the participants' foreheads (see Fig. 5.1). The forehead was chosen as the device location, as SCOS devices works better on hairless areas. The laser diode was set 5 mm away from the skin of participants such that the illumination spot diameter was 5 mm. The total illumination power was limited to 45 mW to ensure that the laser light intensity level of the area of illumination is well within the American National Standards Institute (ANSI) laser safety standards for maximum permissible exposure (2.95 mW/mm2) for skin exposure to a laser beam at 785 nm [42]. We used a USB-board camera [Basler daA1920-160um (sensor Sony IMX392)]. For optimal performance and stability, we typically operated the camera at a framerate of 60 frames-per-second (fps) and with a global shutter setting recording 12-bit images. The camera featured a pixel pitch of 3.4 μm, which offers a balance between the average intensity per pixel and the number of speckles per pixel [43].

The source injects coherent laser light into the head of the participant. At a S-D distance from the illumination spot on the scalp, a 60 frames per second camera captured the light that traveled through the brain. The S-D distance was set at 3.2 cm for 43 subjects and 4.0 cm for 7 subjects, with larger distances used when possible to optimize brain sensitivity. The S-D distance was chosen based on a benchmark measurement before the breath-holding experiment. Cerebral blood

flow index (CBFI) and cerebral blood volume index (CBVI) were recorded at 3.2 cm and 4.0 cm over 20 seconds, and analysis of these time traces identified the optimal S-D distance by checking for a clear heart rate peak in the Fourier transform of the CBFI and CBVI traces and distinct peaks P1, P2, and P3 in the CBFI cardiac pulse. It is important to note that scalp and skull thickness can vary among individuals, affecting the ideal S-D distance for each subject [27].

Brain blood flow and volume calculations

The brain blood volume was extracted from the camera images by calculating the ratio of the mean time-varying intensity $\langle I(t)\rangle$ over the baseline intensity I_0 calculated by taking the mean image intensity of the first 60 seconds, subsequently referred to as the cerebral blood volume index (CBVI) [24]:

$$\mathrm{CBVI}(t) = \frac{\langle I(t)\rangle}{I_0}, \tag{5.1}$$

where in Eq. (5.1) I_0 is the intensity at baseline and $I(t)$ is the intensity recorded by the camera image at time t. The intensity baseline is measured with the subject at rest over the first 60 seconds. The brain blood flow was extracted from the camera images by calculating the cerebral blood flow index (CBFI) as [30, 36]:

$$\mathrm{CBFI}(t) = \frac{1}{K^2_{\mathrm{adjusted}}(t)}, \tag{5.2}$$

where in Eq. (5.2) K^2_{adjusted} is the adjusted speckle contrast obtained by subtracting the raw speckle contrast K^2_{raw} by all sources of noise [36]. The noise sources included variance contributions from the shot noise K^2_{shot} which depend on the mean intensity $\mu(I)$ and the analog to digital conversion ratio, quantization noise K^2_{quant} which depend on the mean intensity, and the camera's readout noise and dark noise K^2_{cam} measured experimentally. See Ref. [36] for detailed calculations and precise definitions of each noise source. The raw speckle contrast is defined as:

$$K^2_{\mathrm{raw}}(t) = \frac{\sigma^2(I(t))}{\mu^2(I(t))}, \tag{5.3}$$

where in Eq. (5.3) $\sigma^2(I)$ is the variance and $\mu(I)$ the mean of the recorded image I at time t. See Refs. [30, 36] for more details about speckle contrast and CBFI calculations from the recorded camera images. In all the results of this paper, we

utilize the normalized CBFI and CBVI relative metrics for enhanced comparability across measurements [36]. The CBFI accounts for the volume of blood moving per unit of time while the CBVI accounts for the volume of blood present at the given time. The ratio between CBFI and CBVI serves as a proxy for relative mean arterial blood pressure measurement [41, 44]. Any alterations in the blood pressure can be attributed to changes in the blood flow or changes in the diameter of the blood vessel (i.e. blood volume), which can both be measured with the compact SCOS device.

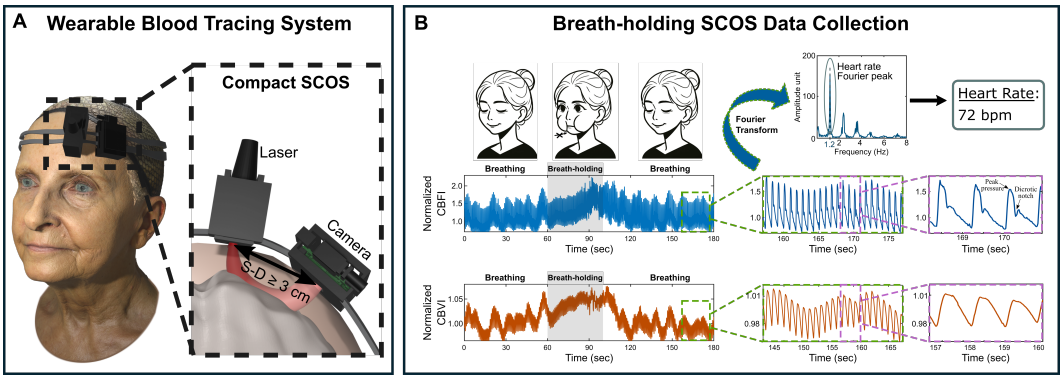


Figure 5.1: Infrared laser cerebrovascular perfusion measures during breath-holding. (A) Compact speckle contract optical spectroscopy (SCOS) device for blood flow and blood volume simultaneous measurements. (B) Breath-holding cerebral blood flow and blood volume data collection. The heart rate is extracted from the blood flow via Fourier transform.

5.3 Breath holding SCOS results

Typical cerebral blood flow, blood volume, and heart rate measurements recorded during voluntary breath-holding by our compact SCOS device is shown in Fig. 5.1B. The breath-holding protocol was as follows: the total duration was 180 seconds: 60 seconds of normal respiration, followed by voluntary breath-holding with a self-selected duration as tolerable by the subject, then a recovery period and normal respiration until the 180th second. The participants were asked to exhale before holding their breath and were reminded not to hold their breath beyond their comfortable limits. The participants were also asked to remain steady and to avoid head movement during the measurement. All the measurements were conducted on hairless areas, i.e. on the forehead region (Fig. 5.1A).

A marked increase of the CBFI and CBVI can be observed during the participant's breath retention as shown in Fig. 5.1B, attributed to the increased brain's demand for blood to transport oxygen and carbon dioxide until breath retention stops. During

breath retention, the brain enters a heightened state of alert, triggering a sequence of protective mechanisms to ensure a stable regulation of carbon dioxide and oxygen [24, 45, 46]. This maintenance mechanism is accomplished by mobilizing and diverting oxygen and nutrients from other parts of the body to the brain, achieved through an accelerated circulation of blood and thus an increase in blood flow [47] together with an increase in blood volume in the brain through dilation of blood vessels [48]. Consequently, a rapid increase in CBFI and CBVI traces can be observed with some fluctuations. For a few seconds after the end of the breath holding, the cerebrovascular reactivity still exhibits a reactive increase in CBFI and CBVI before returning to baseline. Note that the large fluctuations in the CBFI and CBVI traces in Fig. 5.1B are not noise but represent blood pulsations as shown in the insets. These pulsations are observable in both CBFI and CBVI traces with similar overall shape and frequency. However, the dynamic features such as the dicrotic notch and peak systole are only discernable in the CBFI trace (Fig. 5.1B). This underscores the significance of separately measuring blood flow and blood volume, as they each convey distinct information. The heart rate of the participant can also be extracted by Fourier transforming the CBFI signal and measuring the frequency of the heart rate peak [27, 36]. In Fig. 5.1B, the heart rate was estimated at a frequency of 1.2 Hz (72 beats per minute).

We aim to develop a biomarker which can classify participants at low and high risk for stroke using the CBFI, CBVI, and heart rate time series recorded during breath-holding (Fig. 5.2). As a reference, we used the traditional stroke risk assessment method, shown in Fig. 5.2A, which is based on the Cleveland Clinic Stroke Risk Calculator [8]. This questionnaire relies on indirect markers for stroke risk estimation, such as demographics and comorbidities including age, smoking and low physical activity lifestyle-related factors, diabetes, hypertension, along with previous history of stroke or TIA. This widely recognized questionnaire is used to estimate an individual's risk of having a stroke within the next ten years. Based on the questionnaire input, a 10-year stroke risk probability ranging between 0.7% and 13.4% is computed. The probability score is divided into a scale risk from 1 to 10 where the lower the scale, the lower the risk. A score of 1st decile corresponds to a low risk (0.7% probability) of having a stroke in the next ten years. See the original paper's Supplementary Material for more information about the Cleveland stroke risk questionnaire.

For this study, we enrolled 50 participants divided equally into two groups of 25

subjects each by using the Cleveland Clinic Stroke Risk Calculator. The cohort consisted of subjects with diverse ages, genders, races, and varying levels of stroke risk factors, see Methods section for more details. This study received approval from the Caltech Committee for the Protection of Human Subjects and the Institutional Review Board (IRB). One group was at low risk for stroke (the low-risk group) and corresponded to participants who scored 1st decile (0.7% probability). Typically, participants in the low-risk group were individuals younger than 40 years of age and in good health. The second group was at higher risk for stroke (higher-risk group) and corresponded to participants who scored in the 4th decile or greater (3% probability or higher). Typically, participants in the higher-risk group were individuals older than 55 years of age and with at least one of the following: history of stroke/TIA, high blood pressure, high blood sugar or diabetes, smoking, history of cardiovascular events, or poor health. Participants with a stroke risk score of 2 or 3 were excluded from this study. The participant with the highest stroke risk score in this study had a score of 7.

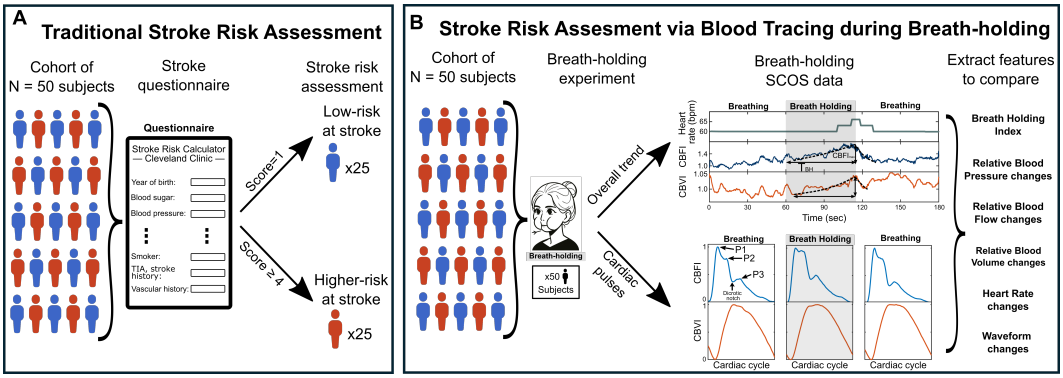


Figure 5.2: Stroke risk assessment via brain perfusion measurements during breath-holding. (A) Traditional stroke risk assessment based on a questionnaire. (B) Proposed stroke risk assessment via perfusion dynamics during breath-holding.

Figure 5.2B shows the proposed stroke risk assessment via brain perfusion measures during breath-holding (as in Fig. 5.1B) with the same cohort of participants as in Fig. 5.2A. A typical example of the heart rate, CBFI, and CBVI time traces are depicted in Fig. 5.2B. The heart rate was determined by Fourier transforming a sliding window of 20 seconds in the CBFI time trace. The method provided a heart rate resolution of 3 BPM (1 / 20 sec = 0.05 Hz), resulting in a discretized nature of the heart rate curve shown in Fig. 5.2B. The choice of the 20-second sliding windows was justified to optimize the accuracy of detecting changes of heart rate during the breath holding period.

As shown in Fig. 5.2B, the heart rate increase during breath-holding aligns well with the CBFI and CBVI increases. For the best visualization and extraction of features from CBFI and CBVI time traces, the temporal resolution was smoothened by a two-second temporal averaging filter. From those, we extracted different features outlined below to compare across the two groups (Fig. 5.2). Our expectation is to observe a statistically significant difference between the two groups (low-risk vs higher-risk) and correlate back our results with the risk probabilities estimated by the Cleveland Clinic stroke risk calculator, indicating that it is possible to estimate the risk of having a stroke in near future via brain perfusion measurements during breath-holding.

The first set of features was the breath-holding index (BHI) defined as the maximal change from baseline value during breath-holding divided by the duration of breath-holding T_{BH} [24, 49]. We defined a breath-holding index (BHI) for CBF, CBV, and flow to volume ratio as:

$$\mathrm{BHI}_{\mathrm{CBF}} = 100 \cdot \frac{\mathrm{CBFI}_{\mathrm{max}} - \mathrm{CBFI}_0}{\mathrm{CBFI}_0 \cdot T_{\mathrm{BH}}}, \tag{5.4a}$$

$$\mathrm{BHI}_{\mathrm{CBV}} = 100 \cdot \frac{\mathrm{CBVI}_{\mathrm{max}} - \mathrm{CBVI}_0}{\mathrm{CBVI}_0 \cdot T_{\mathrm{BH}}}, \tag{5.4b}$$

$$\text{Flow to volume ratio} = \frac{\mathrm{BHI}_{\mathrm{CBF}}}{\mathrm{BHI}_{\mathrm{CBV}}}, \tag{5.4c}$$

where $\mathrm{CBFI}_{\mathrm{max}}$, $\mathrm{CBVI}_{\mathrm{max}}$ denote the maximum value of CBFI, CBVI during breath-holding, CBFI_0, CBVI_0 are the CBFI, CBVI baseline value before breath-holding when the subject is at rest, and T_{BH} is the duration (seconds) of breath-holding. The $\mathrm{BHI}_{\mathrm{F}}$ and $\mathrm{BHI}_{\mathrm{V}}$ assess the cerebrovascular reactivity by measuring the percentage change per second of BFI and BVI and have a unit of percent per second [49, 50]. The flow to volume ratio in Eq. (5.4c) serves as an estimate of changes in mean arterial pressure.

The second set of features was extracted by fitting the CBFI (or CBVI) changes during and after breath-holding using exponential functions:

$$f_1 = 1 + \mathrm{CBFI}_{\mathrm{max}} e^{(T_i - T_{\mathrm{start}})/\tau_{\mathrm{growth}}}, \tag{5.5a}$$

$$f_2 = 1 + \mathrm{CBFI}_{\mathrm{max}} e^{(T_j - T_{\mathrm{max}})/\tau_{\mathrm{decay}}}, \tag{5.5b}$$

where $\mathrm{CBFI}_{\max}$ is the maximum value of CBFI during breath-holding, $T_{\max}$ is the time after breath-holding at which CBFI is maximal (i.e. right before CBFI starts decreasing), T_i are times from the start of breath-holding until $T_{\max}$ and T_j are times from $T_{\max}$ until the CBFI returns to the baseline level, τ_{growth} is the growth factor and τ_{decay} is the decay factor. Both τ_{growth} and τ_{decay} are measured from the fits f_1 and f_2. Our expectation is that the low-risk group exhibit different τ_{growth} and τ_{decay} factors than the higher-risk group. The time $T_{\max}$ typically corresponds to the sum of T_{start} (time at which breath-holding starts) plus T_{BH} (the duration of breath-holding). The resting heart rate and maximal heart rate changes during breath-holding were also compared between the two groups, see the original paper's Supplementary Material.

The CBFI and CBVI time traces were also segmented by each cardiac cycle (Fig. 5.2B) and the waveforms before, during, and after breath-holding were compared. As shown in Fig. 5.2B, the typical CBFI cardiac pulse is composed of three distinct peaks P1, P2, P3, and one dip (dicrotic notch), related to arterial waveform. Although our method for measuring blood flow is based on a different principle than arterial pressure measurements, we observed similarities between our measurements and arterial pressure map tracings found in the literature [51]. Specifically, peaks P1, P2, and P3 can be associated with changes in arterial pressures during the cardiac cycle. The first peak P1 corresponds to the rapid ejection of blood (systole). The second peak P2 corresponds reflected waves from the vascular tree [51]. After the ventricular ejection, the pressure within the ventricles drops further marking the end of systole, producing a dip in the CBFI, i.e. dicrotic notch (beginning of diastole). The third peak P3 corresponds to the closing of the aortic valve preventing backflow into the heart, causing a brief momentary rise in the CBFI (diastole). Interruption of the diastolic downstroke caused by P3 produces the dicrotic notch. It has been shown that these peaks may help quantify aortic stiffness and cardiovascular health condition [52]. Furthermore, as shown in Fig. 5.2B, the waveform of the CBFI cardiac cycle, specifically the relative height of the P1, P2, and P3 peaks changes before and during breath-holding, as observed in Ref. [24]. Note that the peaks P1, P2, P3, and the dicrotic notch are not present in the CBVI cardiac cycle. To quantitatively evaluate the relative height of the P1 and P2 peaks, we calculated the cardiac peaks height ratio peaks ratio = $\mathrm{BFI}_{\mathrm{P2}}/\mathrm{BFI}_{\mathrm{P1}}$ from the normalized CBFI pulses. As reported in Ref. [24], we found that the ratio increased during breath-holding.

Figure 5.3 summarizes the results from the breath-holding experiment conducted on the cohort of 50 participants. For each participant, between two to five datasets

of breath-holding were recorded, depending on the subject's performance in the breathing exercise. From each dataset (such as the one shown in Fig. 5.2B), features such as BHI (Eqs. (5.4a-5.4c)), τ_{growth} (Eq. (5.5a)), τ_{decay} (Eq. (5.5b)), $T_{\max}$ and T_{BH} were extracted. Then, for each subject, the extracted features were averaged across all realizations. The averaged features for each subject are presented in Fig. 5.3. Subjects were categorized into two groups: low-risk and higher-risk groups. As shown, statistically significant differences can be observed between the low-risk group and the higher-risk group. Figure 5.3A shows the typical CBFI and CBVI breath-holding time traces of each risk group, obtained by averaging the features in the f_1 and f_2 fit across all subjects of each risk group. As shown, the higher-risk group exhibits a higher and slightly faster increase in blood flow during breath-holding than the low-risk group. On the contrary, the higher-risk group exhibits a lower and slightly slower increase of blood volume during breath-holding. Note that both risk groups have similar $T_{\max}$, i.e. similar duration of breath-holding T_{BH}. These findings align with our expectations: during breath-holding among those at elevated stroke risk, less flexible blood vessels impede dilation, prompting accelerated blood flow in response to the brain's heightened demand for oxygen caused by carbon dioxide buildup. As a consequence, reactive blood pressure increases more for the higher-risk group than the low-risk group due to the shear effect and lower capability of the older population to dilate vessels, indicative of lower vascular compliance.

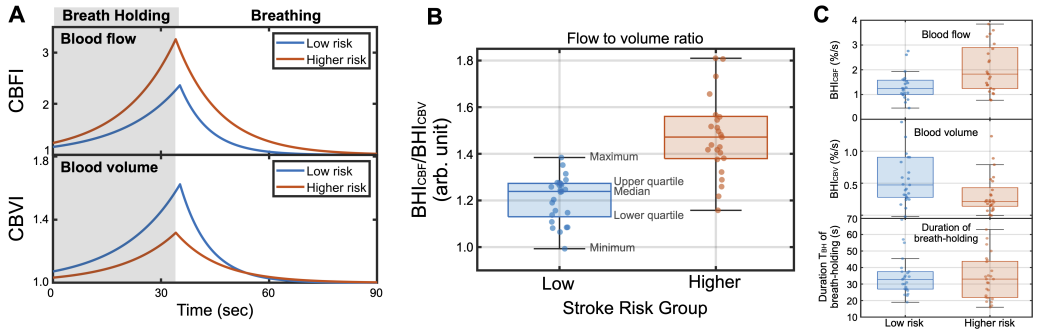


Figure 5.3: Breath-holding features comparison between the low-risk and higher-risk groups. (A). Illustrative breath-holding changes in CBFI and CBVI during breath-holding for each group. (B). Flow to volume pressure ratio breath-hold index comparison. (C). Relative blood flow and blood volume breath-hold index comparison and breath-holding duration comparison. See Table 1 for p-values and significance levels.

Those results are further validated in Fig. 5.3B by looking at the distribution of the flow to volume pressure ratio $\text{BHI}_{\text{CBF}}/\text{BHI}_{\text{CBV}}$ defined in Eq. (5.4c). In Figs. 5.3B-

C, the data is presented using a box plot, where each data point corresponds to each subject. The top and bottom edges of the box correspond to the upper and lower quartiles, the line inside the box corresponds to the median and the outside lines correspond to the maximum and minimum in the data set excluding any outliers. Outliers are data points that significantly differ from the rest of the dataset and are defined as data points whose values are larger than 1.5 times the interquartile of the top or bottom of the box. As expected, the median and quartiles of the flow to volume ratio are higher for the higher-risk group than the low-risk group, with a statistically significant difference (p-value = 0.000001) and a large effect size (d' = -1.686) as shown in Table 5.1. Figure 5.3C shows the BHI distributions for the CBFI and CBVI. We also show the distribution of the duration of breath-holding T_{BH} for both groups in Fig. 5.3C, where no statistical difference between the two groups was observed, indicating that both groups perform similar breath-holding exercise. We also compared other features such as the resting heart rate (p-value = 0.467) and maximal heart rate (p-value = 0.005) between the two groups, see Table 5.1 and Supplementary Material. We then compared and correlated the results of Fig. 5.3 to those obtained using a blood pressure cuff located on the upper arm, see Supplementary Material.

The mean and standard deviation of the features are presented in Table 5.1, along with the corresponding p-values, statistical significance, and effect sizes. We note that when comparing multiple variables between groups, a correction on the alpha p-value threshold (i.e. the significance level) is necessary to account for the potential increase of false positives. Using the Bonferroni correction method, we determined our significance levels to be *:0.0063, **:0.0013, ***:0.00013, and ****:0.000013 for single variable features and *:0.0018, **:0.00036, ***:0.000036, and ****:0.0000036 for double variable features. As shown in Table 5.1, the breath-holding duration T_{BH} was similar across both groups. There is also no significant difference in the time constants τ_{growth} and τ_{decay} between both groups. Notably, the higher-risk group exhibited, on average, greater flow changes but smaller volume changes during breath-holding compared to the low-risk group. We attribute this difference to the likelihood that individuals in the higher-risk group may have lower vascular elasticity than those in the low-risk group. Note that the BHI ratio BHI_{CBF}/BHI_{CBV} exhibits a more pronounced difference between the two groups, as shown by a lower p-value and very large effect size (p=0.000001, d' = -1.686) in comparison to the BHI_{CBF} or BHI_{CBV} feature. Additionally, the higher-risk group has a higher standard deviation for BHI_{CBF}/BHI_{CBV} than the low-risk group, which

we attribute to a more diverse range of health conditions within this group. Results indicate that the flow to volume ratio (BHI_{CBF}/BHI_{CBV}) is the most robust discriminator among the features listed in Table 5.1.

We also analyzed the changes in the vascular peaks height ratio (peaks ratio = $CBFI_{P2}/CBFI_{P1}$) between peaks P1 and P2 (Fig. 5.2B), which was found to increase during breath-holding [53]. For the peak analysis, data from nine subjects were removed due to lack of consistency between cardiac periods in the processed CBFI, determined through visual inspection and assessment. After removal, the cohort size was 41 subjects (17 in the low-risk and 24 in the higher-risk group). We first segmented the CBFI time trace into individual cardiac cycles and applied a min-max normalization to ensure each cycle's CBFI was in the range [0, 1] (Fig. 5.2B), refer to original paper's supplementary material for more details. Subsequently, we measured the relative heights of the two peaks P1 and P2 (see Fig. 5.2B), and calculated their ratio. The detailed peak extraction algorithm is explained in the original paper's supplementary material (S4). We then compared the peaks ratio at rest (peaks $ratio_{resting}$) and during breath-holding (peaks $ratio_{BH}$) between the two risk groups. As shown in Table 5.1, statistically significant differences between the two risk groups were observed for peak ratio at rest, with the peak ratio for the higher-risk group being higher than that for low-risk group, as similarly observed in Ref. [52] by recording Doppler waveforms in 286 participants on the carotid artery. Finally, we compared the ratio between peaks $ratio_{BH}$/peaks $ratio_{resting}$ but could not find any statistically significant differences among the two risk groups. Overall, these results indicate that our device can be a valuable tool for assessing cerebralvascular health conditions. Its high sampling rate allows for the acquisition of many cardiac pulses during a single breath-holding sequence, ideal for input into deep learning methods that require larger sample sizes. Refer to original paper's supplementary material for additional discussion on other features comparisons between the two groups.

Feature	**Low-Risk Group mean (std)**	**Higher-Risk Group mean (std)**	**p-value**	**Significance level**	**Effect Size**
Stroke risk score	1 (0)	5 (1)		–	
S-D distance	3.4 (0.3)	3.3 (0.2)		–	
T_{BH} (s)	35 (12)	34 (13)	0.797	ns	0.073
τ_{growth} (s)	16.3 (8.6)	15.0 (8.3)	0.593	ns	0.152
τ_{decay} (s)	8.0 (6.1)	12.1 (17.5)	0.280	ns	-0.311
$CBFI_{change}$ (%)	44 (16)	63 (25)	0.003	*	-0.891
$CBVI_{change}$ (%)	20 (14)	9 (8)	0.001	*	0.976
BHI_{CBF} (%/s)	1.36 (0.57)	2.26 (1.62)	0.014	ns	-0.741
BHI_{CBV} (%/s)	0.62 (0.49)	0.32 (0.30)	0.011	ns	-0.757
BHI_{CBF}/BHI_{CBV} (arb. u.)	1.21 (0.10)	1.50 (0.23)	0.000001	****	-1.686
Resting heart rate (bpm)	68 (9)	66 (8)	0.467	ns	0.207
Maximum heart rate (bpm)	84 (10)	76 (10)	0.005	*	0.829
$T^{max}_{CBVI} - T^{max}_{CBFI}$ (s)	1.4 (2.3)	1.0 (2.6)	0.601	ns	0.084
Peaks $ratio_{resting}$ (arb. u.)	0.84 (0.13)	1.05 (0.23)	0.003	*	-1.064
Peaks $ratio_{BH}$ (arb. u.)	1.04 (0.14)	1.22 (0.23)	0.009	ns	-0.927
Peaks $ratio_{BH}$/Peaks $ratio_{resting}$	1.24 (0.08)	1.18 (0.11)	0.0517	ns	0.617

Table 5.1: Mean and standard deviation of the different features extracted from the breath-holding dataset, comparing the low-risk and higher-risk groups. P-values were calculated from the Welch's t-test. Significance level has been through Bonferroni correction. For single variable metrics, the significance levels are indicated by stars as where ns: not significant, *: $p < 0.0063$, **: $p < 0.00133$, ***: $p < 0.00013$, and ****: $p < 0.000013$. For metrics comprised with two variables: *: $p < 0.0018$, **: $p < 0.0004$, ***: $p < 0.00004$, and ****: $p < 0.000004$. Effect size reveals additional information about difference between the two groups.

The difference in vascular reactivity between the two risk groups was expected given the statistically significant age difference between groups and the known effects of age on cerebrovascular health. However, a similar trend was observed when the higher-risk group was subdivided into three smaller subgroups, Fig. 5.4 of the manuscript, where subjects of each three smaller subgroups had similar age range but different comorbidities. We subdivided the distribution of $\mathrm{BHI_{CBF}/BHI_{CBV}}$ within the higher-risk group into risk score groups of 4, 5, and 6-7, using the Cleveland Score Risk score. The low-risk group (score risk of 1) had a sample size of $N_1 = 25$ subjects, while the higher-score risk subgroups 4, 5, and 6-7 had a sample size of $N_4 = 6$, $N_5 = 10$, and $N_{6-7} = 9$ subjects, respectively. As shown in Fig. 5.4, those with higher risk scores showed a more pronounced increase in brain blood volume and a lower increase in blood flow. The rather small sample size within each risk subgroups (6 to 10 subjects per subgroups risk) would need a further study with a larger cohort (e.g. 25 subjects per subgroups risk) to statistically validate these observations. Despite the limited sample sizes hindering statistically significant conclusions, the data in Fig. 5.4 shows an increasing trend in the $\mathrm{BHI_{CBF}/BHI_{CBV}}$ ratio together with the risk score, showing a correlation with the Cleveland Stroke Risk Calculator. Notably, Fig. 5.4 includes one instance of an abnormally high flow to volume ratio $\mathrm{BHI_{CBF}/BHI_{CBV}}$ (labeled Outlier) in the risk group 6-7. We anticipate that this subject may have a potentially higher risk of stroke compared to the rest of the cohort, however, this conclusion remains tentative due to the small sample size. Moving forward, we plan to expand our sample size. For more information about all the features' mean and standard deviation across stroke risk subgroups, refer to the original paper's supplementary material (Tables S2 and S3), where the means and standard deviations as well as ANOVA and Spearman correlation test results for all features risk subgroups are detailed.

5.4 Preventative screening, looking forward and what is next?

We combined a compact and cost-effective laser-powered device (compact SCOS) with a breath-holding exercise for assessing cerebrovascular reactivity via measurement of blood blow and blood volume changes on a cohort of 50 participants stratified into two groups (low-risk vs higher-risk for stroke). The compact SCOS device consisted of only two components: a laser diode and a CMOS-based board camera [36]. The collected breath-holding data showed a highly significant group difference (*Welch's t-test*, p-value = 0.000001, d' = -1.686) when comparing the BHI_{CBF}/BHI_{CBV} ratios. The higher-risk group exhibited a greater increase in

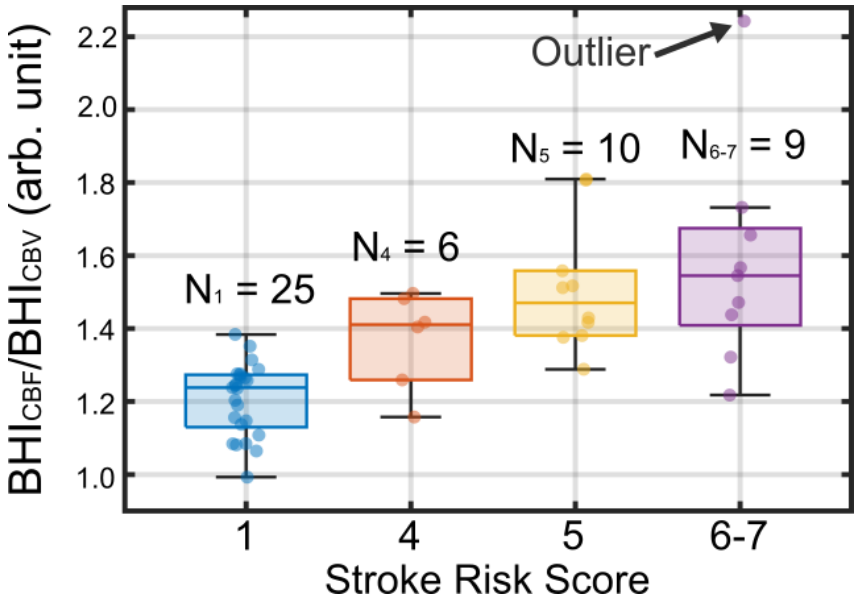


Figure 5.4: Distribution of the flow-to-volume ratio BHI_{CBF}/BHI_{CBV} during breath-holding across stroke risk groups (scores 1, 4, 5, and 6-7). The box plot shows the distribution of the flow to volume ratio for different stroke risk score groups, indicating a trend where a higher risk score corresponds to a higher ratio.

brain blood volume (effect size) and a lower increase in blood flow during breath-holding (p-value = 0.014). Our breath-holding data revealed a statistically significant difference between the two groups when comparing changes in either blood flow or blood volume. Notably, individuals at low risk for stroke showed a higher increase in brain blood volume, while subjects at higher risk for stroke exhibited a greater rise in brain blood flow rates.

The results were consistent with those obtained using a blood pressure cuff located on the upper arm. These findings align with our expectations that during breath-holding among those at elevated stroke risk, less flexible blood vessels impede dilation, prompting accelerated blood flow in response to the brain's heightened demand for oxygen and clearance of carbon dioxide buildup. Future work could focus on characterizing the dynamic brain responses to breath-holding, including the extent of changes in CBFI and CBVI and the speed at which the brain returns to a baseline level of activity, to objectively quantify the cerebrovascular health of a participant and evaluate their individualized risk of experiencing a cerebrovascular disease such as stroke. Due to the portability and cost-effectiveness of the compact SCOS device, it is worth underscoring the potential of deploying the device and incorporating the breath-holding maneuver in various geographical settings to

provide quantitative feedback for stroke pre-diagnosis and prevention, especially in resource-limited populations that are disproportionately more affected by stroke and its sequelae. Compared to other methods for measuring cerebral blood changes, the approach of simultaneously measuring both blood flow and volume provides additional information for potential stroke evaluation. These two measurements would enable the monitoring of cerebral perfusion pressure [41, 54, 55].

In conclusion, this study, involving 50 participants, demonstrated a statistically significant difference in cerebrovascular responses during breath-holding between low-risk and higher-risk stroke groups. Specifically, the higher-risk group exhibited a greater increase in brain blood volume and a smaller increase in blood flow during breath-holding. A similar trend was observed when the higher-risk group was subdivided into three smaller subgroups, where those with higher risk scores showed a more pronounced increase in brain blood volume and a lower increase in blood flow. However, the relatively small sample size of these subgroups, ranging from 6 to 10 subjects, limits the statistical conclusions that can be drawn about these findings. It is recognized that a larger and more diverse cohort would enhance the validation of these results. This would not only improve the generalizability of the findings but also allow for a more detailed, multivariate investigation of the method's effectiveness across different demographics and comorbidity profiles. Additionally, a larger sample size would enable addressing potential biases and confounding factors more comprehensively through advanced statistical analyses.

Future research directions could involve expanding the sample size and incorporating machine learning to refine data processing and analysis, facilitating more detailed and quantitative categorization of stroke risk. A broader dataset across varying stroke risk scores would also allow for the determination of an optimal threshold for further longitudinal studies. Moreover, a larger cohort would improve the ability to conduct controlled comparisons that account for age and other factors, further validating the observed correlation between metrics like the BHI_{CBF}/BHI_{CBV} ratio and stroke risk. Additionally, exploring the long-term clinical outcomes of patients assessed using the proposed method could provide further validation of its utility in stroke prevention and intervention.

References

[1] Jiahui Fan et al. "Global Burden, Risk Factor Analysis, and Prediction Study of Ischemic Stroke, 1990-2030". eng. In: *Neurology* 101.2 (July 2023), e137–e150. DOI: 10.1212/WNL.0000000000207387.

[2] Valery L Feigin et al. “World Stroke Organization (WSO): Global Stroke Fact Sheet 2022”. en. In: *International Journal of Stroke* 17.1 (Jan. 2022), pp. 18–29. DOI: 10.1177/17474930211065917.

[3] Kathryn M. Rexrode et al. “The Impact of Sex and Gender on Stroke”. In: *Circulation Research* 130.4 (Feb. 2022). Publisher: American Heart Association, pp. 512–528. DOI: 10.1161/CIRCRESAHA.121.319915.

[4] Bruce Dopler. “Stroke Prevention”. en. In: *Delaware Journal of Public Health* 9.3 (Aug. 2023), pp. 6–10. DOI: 10.32481/djph.2023.08.003.

[5] James F. Meschia et al. “Guidelines for the primary prevention of stroke: a statement for healthcare professionals from the American Heart Association/American Stroke Association”. eng. In: *Stroke* 45.12 (Dec. 2014), pp. 3754–3832. DOI: 10.1161/STR.0000000000000046.

[6] Gregory Y.H. Lip et al. “Refining Clinical Risk Stratification for Predicting Stroke and Thromboembolism in Atrial Fibrillation Using a Novel Risk Factor-Based Approach”. en. In: *Chest* 137.2 (Feb. 2010), pp. 263–272. DOI: 10.1378/chest.09-1584.

[7] Yongjun Wang et al. “Clopidogrel with Aspirin in Acute Minor Stroke or Transient Ischemic Attack”. en. In: *New England Journal of Medicine* 369.1 (July 2013), pp. 11–19. DOI: 10.1056/NEJMoa1215340.

[8] *Stroke Risk Calculator*. en.

[9] Amelia K. Boehme, Charles Esenwa, and Mitchell S.V. Elkind. “Stroke Risk Factors, Genetics, and Prevention”. en. In: *Circulation Research* 120.3 (Feb. 2017), pp. 472–495. DOI: 10.1161/CIRCRESAHA.116.308398.

[10] Kimberly Dwyer Hollender. “Screening, Diagnosis, and Treatment of Post-Stroke Depression”. en-US. In: *Journal of Neuroscience Nursing* 46.3 (June 2014), p. 135. DOI: 10.1097/JNN.0000000000000047.

[11] D. G. Hackam et al. “Most stroke patients do not get a warning: a population-based cohort study”. In: *Neurology* 73.13 (Sept. 2009). Publisher: Wolters Kluwer, pp. 1074–1076. DOI: 10.1212/WNL.0b013e3181b9c8e5.

[12] P. A. Wolf et al. “Probability of stroke: a risk profile from the Framingham Study”. eng. In: *Stroke* 22.3 (Mar. 1991), pp. 312–318. DOI: 10.1161/01.str.22.3.312.

[13] Mustafa Cetin et al. “Prediction of coronary artery disease severity using CHADS2 and CHA2DS2-VASc scores and a newly defined CHA2DS2-VASc-HS score”. eng. In: *The American Journal of Cardiology* 113.6 (Mar. 2014), pp. 950–956. DOI: 10.1016/j.amjcard.2013.11.056.

[14] Christopher G Favilla et al. “Portable cerebral blood flow monitor to detect large vessel occlusion in patients with suspected stroke”. en. In: *Journal of NeuroInterventional Surgery* (Mar. 2024), jnis–2024–021536. DOI: 10.1136/jnis-2024-021536.

[15] Tianxin Gao et al. “Stroke analysis and recognition in functional near-infrared spectroscopy signals using machine learning methods”. In: *Biomedical Optics Express* 14.8 (July 2023), pp. 4246–4260. DOI: 10.1364/BOE.489441.

[16] Y. Okudaira et al. “Evaluation of the acetazolamide test. Vasoreactivity and cerebral blood volume”. eng. In: *Stroke* 26.7 (July 1995), pp. 1234–1239. DOI: 10.1161/01.str.26.7.1234.

[17] K. H. Kang, H. S. Kim, and S. Y. Kim. “Quantitative Cerebrovascular Reserve Measured by Acetazolamide-Challenged Dynamic CT Perfusion in Ischemic Adult Moyamoya Disease: Initial Experience with Angiographic Correlation”. en. In: *American Journal of Neuroradiology* 29.8 (Sept. 2008). Publisher: American Journal of Neuroradiology Section: BRAIN, pp. 1487–1493. DOI: 10.3174/ajnr.A1129.

[18] A. S. Vagal et al. “The acetazolamide challenge: techniques and applications in the evaluation of chronic cerebral ischemia”. eng. In: *AJNR. American journal of neuroradiology* 30.5 (May 2009), pp. 876–884. DOI: 10.3174/ajnr.A1538.

[19] Jiali Sun et al. “Predicting acute ischemic stroke using the revised Framingham stroke risk profile and multimodal magnetic resonance imaging”. English. In: *Frontiers in Neurology* 14 (Sept. 2023). Publisher: Frontiers. DOI: 10.3389/fneur.2023.1264791.

[20] Daniel F. Arteaga et al. “Cerebral blood flow territory instability in patients with atherosclerotic intracranial stenosis”. eng. In: *Journal of magnetic resonance imaging: JMRI* 50.5 (Nov. 2019), pp. 1441–1451. DOI: 10.1002/jmri.26737.

[21] Georgios Tsivgoulis, Andrei V. Alexandrov, and Michael A. Sloan. “Advances in transcranial Doppler ultrasonography”. eng. In: *Current Neurology and Neuroscience Reports* 9.1 (Jan. 2009), pp. 46–54. DOI: 10.1007/s11910-009-0008-7.

[22] Jawad Naqvi et al. “Transcranial Doppler ultrasound: a review of the physical principles and major applications in critical care”. eng. In: *International Journal of Vascular Medicine* 2013 (2013), p. 629378. DOI: 10.1155/2013/629378.

[23] C. K. Willie et al. “Utility of transcranial Doppler ultrasound for the integrative assessment of cerebrovascular function”. eng. In: *Journal of Neuroscience Methods* 196.2 (Mar. 2011), pp. 221–237. DOI: 10.1016/j.jneumeth.2011.01.011.

[24] Christopher G. Favilla et al. “Validation of the Openwater wearable optical system: cerebral hemodynamic monitoring during a breath-hold maneuver”. In: *Neurophotonics* 11.01 (Mar. 2024). DOI: 10.1117/1.NPh.11.1.015008.

[25] Stefan A. Carp, Mitchell B. Robinson, and Maria A. Franceschini. “Diffuse correlation spectroscopy: current status and future outlook”. In: *Neurophotonics* 10.01 (Jan. 2023). DOI: 10.1117/1.NPh.10.1.013509.

[26] Gary E. Strangman, Zhi Li, and Quan Zhang. “Depth Sensitivity and Source-Detector Separations for Near Infrared Spectroscopy Based on the Colin27 Brain Template”. en. In: *PLoS ONE* 8.8 (Aug. 2013), e66319. DOI: 10.1371/journal.pone.0066319.

[27] Simon Mahler et al. “Assessing depth sensitivity in laser interferometry speckle visibility spectroscopy (iSVS) through source-to-detector distance variation and cerebral blood flow monitoring in humans and rabbits”. In: *Biomed. Opt. Express* 14.9 (Sept. 2023), pp. 4964–4978. DOI: 10.1364/BOE.498815.

[28] Stefan A. Carp et al. “Diffuse correlation spectroscopy measurements of blood flow using 1064 nm light”. In: *Journal of Biomedical Optics* 25.9 (Sept. 2020). Publisher: SPIE, p. 097003. DOI: 10.1117/1.JBO.25.9.097003.

[29] Meir Nitzan, Itamar Nitzan, and Yoel Arieli. “The Various Oximetric Techniques Used for the Evaluation of Blood Oxygenation”. en. In: *Sensors* 20.17 (Aug. 2020), p. 4844. DOI: 10.3390/s20174844.

[30] Byungchan Kim et al. “Measuring human cerebral blood flow and brain function with fiber-based speckle contrast optical spectroscopy system”. en. In: *Communications Biology* 6.1 (Aug. 2023), p. 844. DOI: 10.1038/s42003-023-05211-4.

[31] Yaniv Eliezer. “Controlling Nonlinear Interaction in a Many-Mode Laser by Tuning Disorder”. In: *Physical Review Letters* 128.14 (2022). DOI: 10.1103/PhysRevLett.128.143901.

[32] Simon Mahler et al. “Fast laser speckle suppression with an intracavity diffuser”. en. In: *Nanophotonics* 10.1 (Jan. 2021). Publisher: De Gruyter, pp. 129–136. DOI: 10.1515/nanoph-2020-0390.

[33] Ronen Chriki. “Spatiotemporal supermodes: Rapid reduction of spatial coherence in highly multimode lasers”. In: *Physical Review A* 98.2 (2018). DOI: 10.1103/PhysRevA.98.023812.

[34] David A. Boas and Andrew K. Dunn. “Laser speckle contrast imaging in biomedical optics”. en. In: *Journal of Biomedical Optics* 15.1 (2010), p. 011109. DOI: 10.1117/1.3285504.

[35] Tanja Dragojević et al. “Compact, multi-exposure speckle contrast optical spectroscopy (SCOS) device for measuring deep tissue blood flow”. EN. In: *Biomedical Optics Express* 9.1 (Jan. 2018). Publisher: Optica Publishing Group, pp. 322–334. DOI: 10.1364/BOE.9.000322.

[36] Yu Xi Huang et al. “Compact and cost-effective laser-powered speckle contrast optical spectroscopy fiber-free device for measuring cerebral blood flow”. In: *Journal of Biomedical Optics* 29.6 (2024), p. 067001. DOI: 10.1117/1.JBO.29.6.067001.

[37] Zhenyu Dong et al. “Non-invasive laser speckle contrast imaging (LSCI) of extra-embryonic blood vessels in intact avian eggs at early developmental stages”. en. In: *Biomedical Optics Express* 15.8 (Aug. 2024), p. 4605. DOI: 10.1364/BOE.530366.

[38] Claudia P. Valdes et al. “Speckle contrast optical spectroscopy, a non-invasive, diffuse optical method for measuring microvascular blood flow in tissue”. en. In: *Biomedical Optics Express* 5.8 (Aug. 2014), p. 2769. DOI: 10.1364/BOE.5.002769.

[39] Jian Xu, Ali K Jahromi, and Changhuei Yang. “Diffusing wave spectroscopy: A unified treatment on temporal sampling and speckle ensemble methods”. en. In: *APL Photonics* 6.1 (Jan. 2021). Publisher: AIP Publishing, p. 016105. DOI: 10.1063/5.0034576.

[40] Yu Xi Huang et al. “Interferometric speckle visibility spectroscopy (iSVS) for measuring decorrelation time and dynamics of moving samples with enhanced signal-to-noise ratio and relaxed reference requirements”. In: *Opt. Express* 31.19 (Sept. 2023), pp. 31253–31266. DOI: 10.1364/OE.499473.

[41] P Schumann. “Evaluation of the ratio of cerebral blood flow to cerebral blood volume as an index of local cerebral perfusion pressure [published erratum appears in Brain 1998 Oct;121(pt 10):2027]”. In: *Brain* 121.7 (July 1998), pp. 1369–1379. DOI: 10.1093/brain/121.7.1369.

[42] *ANSI Z136.1-2014 - American National Standard for Safe Use of Lasers*.

[43] Sharvari Zilpelwar et al. “Model of dynamic speckle evolution for evaluating laser speckle contrast measurements of tissue dynamics”. en. In: *Biomedical Optics Express* 13.12 (Dec. 2022), p. 6533. DOI: 10.1364/BOE.472263.

[44] Masashi Kameyama et al. “A Novel Proposal for an Index for Regional Cerebral Perfusion Pressure – A Theoretical Approach Using Fluid Dynamics”. English. In: *Frontiers in Neurology* 12 (Jan. 2022). Publisher: Frontiers. DOI: 10.3389/fneur.2021.765463.

[45] Wenjun Zhou et al. “Functional interferometric diffusing wave spectroscopy of the human brain”. en. In: *Science Advances* 7.20 (May 2021), eabe0150. DOI: 10.1126/sciadv.abe0150.

[46] Rachel J. Skow et al. “The ins and outs of breath holding: simple demonstrations of complex respiratory physiology”. In: *Advances in Physiology Education* 39.3 (Sept. 2015). Publisher: American Physiological Society, pp. 223–231. DOI: 10.1152/advan.00030.2015.

[47] Andreas Kastrup et al. “Cerebral Blood Flow–Related SignalChanges during Breath-Holding”. In: *AJNR: American Journal of Neuroradiology* 20.7 (July 1999), pp. 1233–1238.

[48] Manus J. Donahue et al. “Hemodynamic Changes Following Visual Stimulation and Breath-holding Provide Evidence for an Uncoupling of Cerebral Blood Flow and Volume from Oxygen Metabolism”. In: *Journal of cerebral blood flow and metabolism : official journal of the International Society of Cerebral Blood Flow and Metabolism* 29.1 (Jan. 2009), pp. 176–185. DOI: 10.1038/jcbfm.2008.109.

[49] Mauro Silvestrini. “Impaired Cerebral Vasoreactivity and Risk of Stroke in Patients With Asymptomatic Carotid Artery Stenosis”. en. In: *JAMA* 283.16 (Apr. 2000), p. 2122. DOI: 10.1001/jama.283.16.2122.

[50] Kyu-On Jung, Seung-Jae Lee, and Tae-Kyeong Lee. “A Breath-Holding Index Applied to the Internal Carotid Artery Siphon in Transcranial Doppler Studies”. en. In: *Journal of Neuroimaging* 30.6 (Nov. 2020), pp. 862–866. DOI: 10.1111/jon.12752.

[51] Jonathan B. Mark. *Atlas of cardiovascular monitoring*. eng. New York: Churchill Livingstone, 1998.

[52] Junichiro Hashimoto, Berend E. Westerhof, and Sadayoshi Ito. “Carotid Flow Augmentation, Arterial Aging, and Cerebral White Matter Hyperintensities: Comparison With Pressure Augmentation”. en. In: *Arteriosclerosis, Thrombosis, and Vascular Biology* 38.12 (Dec. 2018), pp. 2843–2853. DOI: 10.1161/ATVBAHA.118.311873.

[53] Christopher G. Favilla et al. *Validation of the Openwater wearable optical system: cerebral hemodynamic monitoring during a breath hold maneuver*. en. Pages: 2023.10.11.23296612. Oct. 2023. DOI: 10.1101/2023.10.11.23296612.

[54] Bruce C.V. Campbell et al. “Cerebral Blood Flow Is the Optimal CT Perfusion Parameter for Assessing Infarct Core”. In: *Stroke* 42.12 (Dec. 2011). Publisher: American Heart Association, pp. 3435–3440. DOI: 10.1161/STROKEAHA.111.618355.

[55] G. Sette et al. “Local brain haemodynamics and oxygen metabolism in cerebrovascular disease: position emission tomography”. In: *Brain* 112.4 (Aug. 1989), pp. 931–951. DOI: 10.1093/brain/112.4.931.

Chapter 6

NEXT THINGS TO EXPLORE

Our journey through the development and application of interferometric Speckle Visibility Spectroscopy (iSVS) and Speckle Contrast Optical Spectroscopy (SCOS) has taken us from the fundamental challenges of sensitivity and signal-to-noise ratio to the expansion of modularity with multi-channel systems, and finally to a tangible clinical application. While these advancements represent significant strides in non-invasive cerebral blood flow (CBF) monitoring, the horizon of possibility remains vast and ripe for exploration. The following outlines several exciting avenues for future research that promise to further refine and expand the capabilities of this technology.

Advanced on-device camera calibration

A critical area for advancement lies in the refinement of camera calibration. Our current work has demonstrated the potential of leveraging the inherent non-correlation between cerebral blood volume (CBV) and CBF to retrospectively calibrate noise and mitigate artifacts. However, this approach relies on a physiological prior that may not hold true in all pathological states. To create a more robust and universally applicable system, the development of on-device, rapid gain calibration is paramount. This would involve creating a standardized, pre-measurement routine that can quickly characterize the unique noise profile of the camera system in its current state, accounting for factors like temperature and component aging. Such a "push-button" calibration, performed just before data acquisition, would eliminate the reliance on physiological assumptions and ensure a higher fidelity of CBF measurements from the outset.

The dawn of neuro-waveform analysis with neural networks

The rich, dynamic waveforms generated by SCOS are replete with information about cerebrovascular health. The application of sophisticated machine learning models, particularly neural networks, opens up a new frontier for interpreting these signals. Neural networks could be trained to recognize subtle, yet significant, patterns within the CBF and CBV waveforms that are correlated with specific physiological symptoms or disease states. For instance, a trained model might identify unique

morphological features in the pulsatile waveform that are indicative of increased stroke risk, or detect early signs of vasospasm following a traumatic brain injury. This approach could move beyond simple amplitude and timing metrics to a more holistic, pattern-based understanding of cerebrovascular dynamics, potentially uncovering novel biomarkers for a range of neurological conditions.

Expanding the clinical frontier: the power of big data

The promising results from our initial clinical application underscore the immense potential of SCOS as a diagnostic and monitoring tool. However, to fully realize this potential, a concerted effort to acquire more extensive and diverse clinical datasets is essential. Expanding the applicational front to include a wider range of patient populations, pathologies, and longitudinal studies will be crucial for validating the clinical utility of SCOS-derived biomarkers. Larger datasets will not only strengthen the statistical power of our findings but also provide the necessary training data for the development of robust neural network models. Collaborative efforts with clinical centers to integrate SCOS into routine monitoring protocols will be key to amassing the "big data" needed to translate this technology into a widespread clinical reality.

Redefining sensitivity: a gradient-based approach to depth

While we have demonstrated that increasing the source-detector (S-D) distance enhances sensitivity to cerebral signals, a more nuanced understanding of depth resolution is attainable. The development and use of a long, customized strip of CMOS camera sensor would allow for quasi-continuous sampling of the backscattered light across a range of S-D distances simultaneously. By analyzing the gradient, or the rate of change, of the speckle contrast along this strip, it may be possible to differentiate between the distinct optical properties of the scalp, skull, and different layers of the brain, such as gray and white matter. This "gradient analysis" could provide a more precise, data-driven method to isolate and remove the influence of superficial tissue layers from the signals obtained at longer S-D distances. This would allow for the use of closer S-D distances while still achieving high brain specificity, thereby improving the overall signal-to-noise ratio.

The interferometric frontier: depth-resolved signal enhancement

Finally, the principles of interferometry, which we initially explored for signal-to-noise ratio enhancement, could be reimagined to achieve depth-resolved measurements, akin to Optical Coherence Tomography (OCT). By employing a light source

with a short coherence length, it is possible to selectively amplify the signal from photons that have traveled a specific path length, and therefore, to a specific depth. This technique, often referred to as interferometric diffusing wave spectroscopy (iDWS), could be integrated with SCOS to provide a powerful tool for selectively probing blood flow dynamics within different layers of the cerebral cortex. This would represent a paradigm shift from a global measure of CBF to a depth-resolved map of cerebral perfusion, offering unprecedented insights into the laminar organization of neurovascular coupling and the layer-specific effects of disease.

In conclusion, the foundation laid by the work in this thesis opens the door to a host of exciting and impactful future research directions. From refining the core technology through advanced calibration and sensor design to unlocking new clinical insights with the power of artificial intelligence and expanding the scope of its applications, the journey to fully harness the potential of SCOS for understanding and improving brain health is just beginning.